University of Southampton

Faculty of Environmental and Life Sciences

Ocean and Earth Science

Topographic Control of Southern Ocean Gyres and the Antarctic Circumpolar Current

by

Ryan Declan Patmore

ORCID ID 0000-0002-5571-9229

Thesis for degree of Doctor of Philosophy

July 2018

University of Southampton

Abstract

Faculty of Environmental and Life Sciences
Ocean and Earth Science
Doctor of Philosophy

Topographic Control of Southern Ocean Gyres and the Antarctic Circumpolar Current
by Ryan Declan Patmore

The large-scale circulation of the Southern Ocean is determined by the underlying topography. The topography of the Southern Ocean is characterised by a series of ridges and basins. This thesis investigates the role of the submarine ridges in the steering of the Antarctic Circumpolar Current and the formation of Southern Ocean gyres. This investigation is carried out through the use of idealised barotropic numerical simulations. Each mechanism has been analysed in terms of both momentum and vorticity.

It is shown that the appearance and strength of Southern Ocean gyres are highly dependent on the gradients in topography along their western boundary. Gyres only appear when topographic gradients are sufficiently high along the eastern flank of a meridional ridge.

It is also found that the volume transport of the Antarctic Circumpolar Current is dependent on the geometric properties of ridges. The width, meridional asymmetry and meridional alignment of a ridge all affect volume transport.

Contents

UNIVERSITY OF Southampton

Research Thesis: Declaration of Authorship

Print name:	

Title of thesis:	

I declare that this thesis and the work presented in it is my own and has been generated by me as the result of my own original research.

I confirm that:

1. This work was done wholly or mainly while in candidature for a research degree at this University;
2. Where any part of this thesis has previously been submitted for a degree or any other qualification at this University or any other institution, this has been clearly stated;
3. Where I have consulted the published work of others, this is always clearly attributed;
4. Where I have quoted from the work of others, the source is always given. With the exception of such quotations, this thesis is entirely my own work;
5. I have acknowledged all main sources of help;
6. Where the thesis is based on work done by myself jointly with others, I have made clear exactly what was done by others and what I have contributed myself;
7. Either none of this work has been published before submission, or parts of this work have been published as: [please list references below]:

Signature:		Date:	

Acknowledgements

The production of this thesis has been quite the journey and I would like to thank and acknowledge the people who have helped make it possible.

I, first of all, would like to thank my supervisors, Paul, Alberto, Dave S and Mike for their guidance and support throughout. In particular, I would like to thank Paul, who has questioned and challenged my every thought with the utmost scrutiny. Many important debates and discussions have occurred along the way and without this my work would not have reached the quality at which it stands. I would like to thank Dave M, for all the valuable advice on MITgcm and the many hours spent staring at equations.

I would like to thank Tom, Ailsa and Jess for all the support they have given me throughout the final stages of the process. Lifesavers. I feel Cecilia and Leyre should also have a mention, there from the start, they have made for an enjoyable four years, I couldn't have hoped for better house-mates. Lastly, I would like to thank my parents who continue to support me at every stage of life.

Abbreviations

AABW	Antarctic Bottom Water
ACC	Antarctic Circumpolar Current
CDW	Circumpolar Deep Water
ENSO	El Niño Southern Oscillation
MITgcm	Massachusetts Institute of Technology General Circulation Model
SAM	Southern Annular Mode

1 Introduction

The Southern Ocean is unique in that it exists at all longitudes and is the main communication between the Atlantic, Indian and Pacific Oceans. Figure 1.1 gives an overview of the key Southern Ocean circulations. Flow in the Southern Ocean is characterised by the Antarctic Circumpolar Current (ACC) and several significant subpolar gyres that lie between the ACC and Antarctica. The ACC is a zonal current which envelops Antarctica with a volume transport of 173.3 $\pm$ 10.7 Sv [Donohue et al., 2016] (1 Sv = $10^6 m^3\ s^{-1}$). The two largest gyres which occur in the Southern Ocean are the Ross Gyre in the Pacific sector and Weddell Gyre in the Atlantic sector. The positions of these gyres are shown in Figure 1.1.

The formation of the ACC and Southern Ocean gyres results in regional differences around Antarctica with processes that take place in gyre regions being distinct from those that occur in the ACC. Ocean forcing is thought to play a role in the melting of ice-sheets [Jenkins et al., 2016] and regions where the ACC passes close to the Antarctic continental shelf are coincident with elevated ice-sheet loss [Pritchard et al., 2012]. Regions where gyres develop are important for the formation of Antarctic Bottom Water (AABW) [Jacobs et al., 1970], a water mass which is of global importance and is exported into the abyssal ocean. Recent evidence indicates that winds over the Southern Ocean are changing, with anticipated implications for Southern Ocean circulation [Langlais et al., 2015, Armitage et al., 2018]. Variability in the wind is suggested to affect regional processes through alterations of the path and strength of both the ACC and gyres [Langlais et al., 2015, Armitage et al., 2018, Dotto et al., 2018]. Understanding what sets the path and strength of Southern Ocean flow provides insight into these changes.

There is a wealth of knowledge on ACC dynamics. The mean flow of the ACC has been estimated from observations in many studies, for example by Gordon et al. [1978], Gille [2003] and Sokolov and Rintoul [2009]. The Southern Ocean has many significant topographic features, with the path of the ACC largely determined by the extensive ridges and troughs that are present [Gordon et al., 1978, Killworth, 1992, Gille, 2003]. Similarly, subpolar gyres are observed to be topographically constrained by large topographic features lying along their western boundaries [Wolff et al., 1991, Ishida, 1994, Krupitsky et al., 1996, LaCasce and Isachsen, 2010, Nadeau and Ferrari, 2015]. To the west of the Weddell Gyre lies the Antarctic Peninsula and to the west of the Ross Gyre is the Pacific-Antarctic Ridge. Fewer investigations, however, have been made into the dynamics of the gyres which appear in the Southern Ocean.

Improving the knowledge of the large scale dynamics of the Southern Ocean is key for

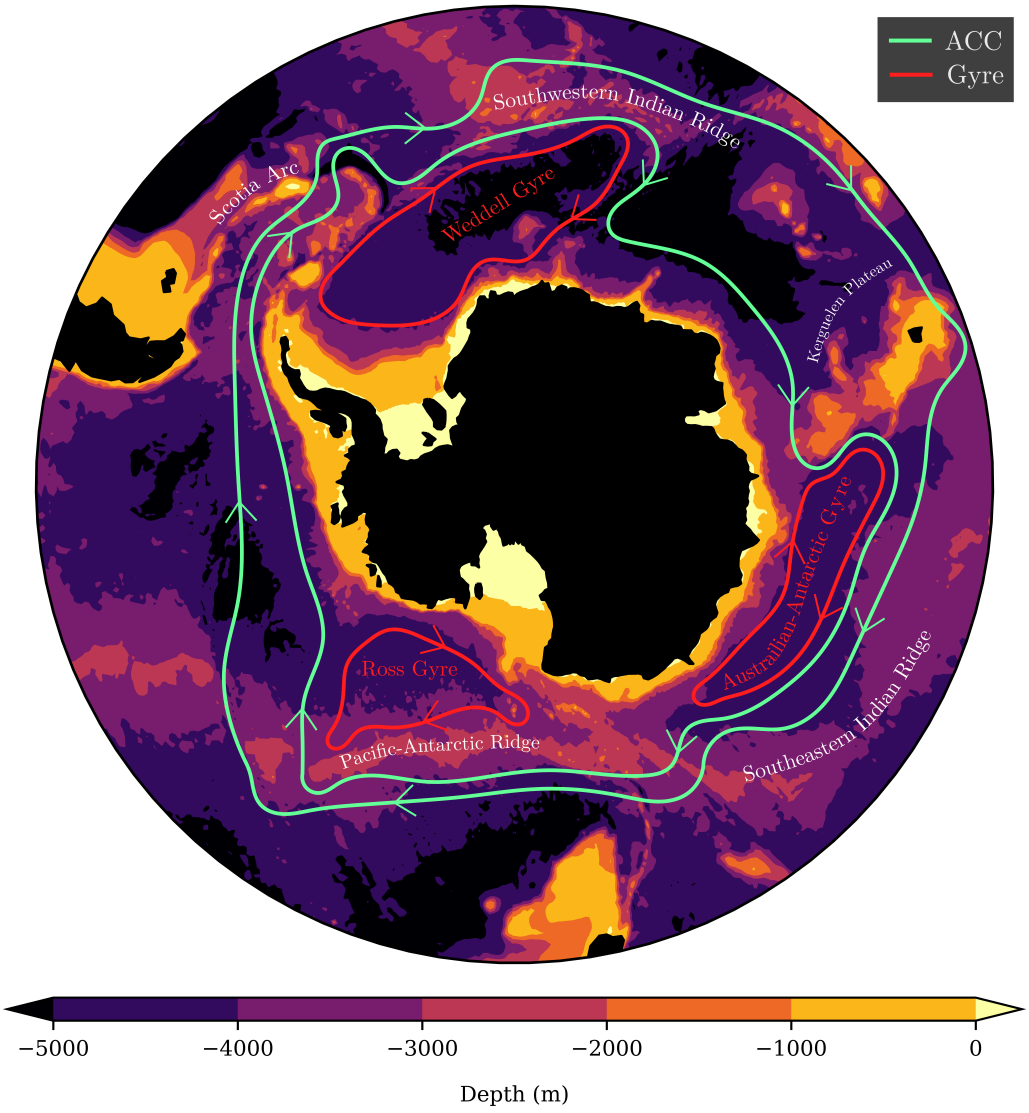

Figure 1.1: Indications of the major Southern Ocean circulations overlaid on bathymetry. The green lines represent the Antarctic Circumpolar Current. The red lines represent gyre circulations.

gaining an insight into future, past and present climate changes. The research here addresses this by investigating the control that the seabed topography features around Antarctica have on the over-lying ACC and subpolar gyres. The remainder of this chapter will give a broader introduction to the ACC, subpolar gyres and topographic features of the Southern Ocean; provides a more in depth outline of the motivation for this research and concludes with a summary of the following chapters of this thesis. This introduction is written to be broad and only a general overview of mechanisms is given. A more detailed description of governing equations and relevant processes is provided in Chapters 2 and 3.

1.1 Southern Ocean Wind Forcing

Figure 1.2 shows the mean sea level pressure averaged over the ten year period spanning 2008 to 2017 overlaid on bathymetry. The contours of mean sea level pressure indicate the wind forcing over the Southern Ocean with prevailing winds following these contours. The winds are almost entirely zonal and are westerly in direction over the majority of the Southern Ocean. These westerly winds are the primary driving force of the ACC. South of the westerlies is a region of low pressure which lies over most of the Antarctic coastline. This low pressure creates a reversal in the wind stress and forces the Antarctic Slope Current, a circumpolar flow which aligns with the continental shelf and flows westward rather than eastward [Armitage et al., 2018]. The Antarctic Slope Current is thought to form the southern boundary of the subpolar gyres.

The winds over the Southern Ocean vary on multiple time-scales. The strength and position of the winds have been linked to two prominent modes of variability; the Southern Annular Mode (SAM) and the El Niño-Southern Oscillation (ENSO) [Marshall, 2003, Langlais et al., 2015]. These modes oscillate on both annual and inter-annual time scales. It has been shown that the Ross Gyre exhibits significant annual variability in both strength and area due to the ENSO [Dotto et al., 2018]. The SAM also varies on annual time-scales [Marshall, 2003] but it is additionally thought to be the cause of changes over a much longer time-scale. There is a long term trend in the westerlies toward a southward shift causing intensifying winds owing to a positive phase in the SAM [Marshall, 2003]. This positive phase in the SAM is thought to be producing long term changes in Southern Ocean circulation, the ACC in particular [Böning et al., 2008, Sallée et al., 2008, Graham et al., 2012, Gille, 2014, Langlais et al., 2015, Armitage et al., 2018].

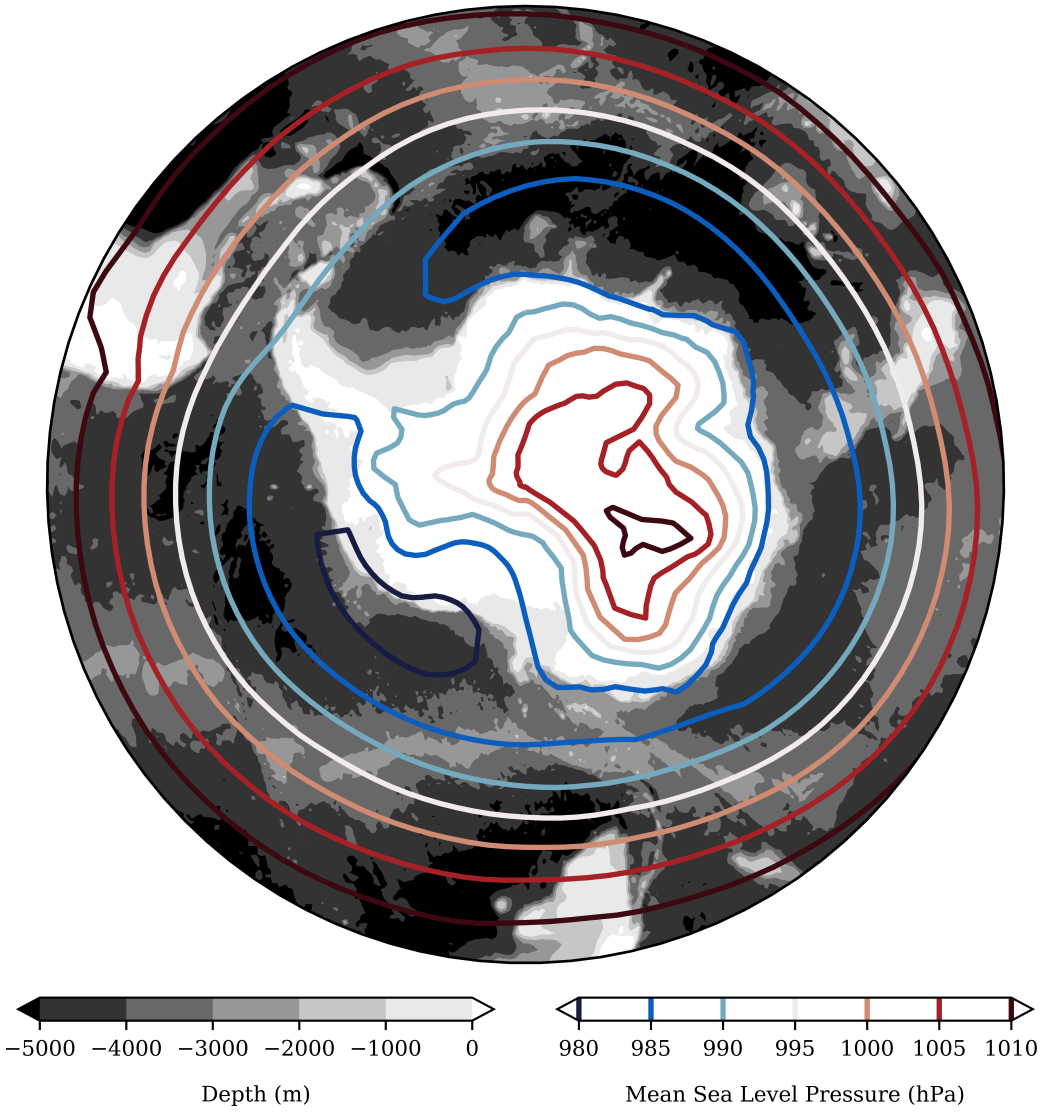

Figure 1.2: Bathymetry of the Southern Ocean over-laid with contours of mean sea level pressure. Mean sea level pressure is calculated on a 3° by 3° grid and is averaged over the ten year period 2008-2017. The mean sea level pressure data is taken from ERA-interim [Dee et al., 2011].

1.2 The Antarctic Circumpolar Current

Knowing what controls the path and strength of the ACC aids many important discussions about the impacts of climate change. The path and strength of the ACC are determined by multiple factors. The ACC is predominantly forced by the westerly winds which dominate the Southern Ocean. As a result, the volume transport of the ACC is associated with these winds. The ACC volume transport is also linked to generation of eddies. Eddies which originate from the ACC have a tendency to dampen its mean flow and limit its volume transport [Meredith and Hogg, 2006, Meredith et al., 2012, Langlais et al., 2015]. The path of the ACC is primarily controlled by bottom topography. Large scale features in the seabed act to steer the ACC, deviating from the path of the wind and taking large meridional deflections around ridges [Gordon et al., 1978]. This subsection gives details regarding the general structure of the ACC and its key drivers and controls.

1.2.1 Structure

The ACC is often described as a broad and unified current but it has long been acknowledged that the ACC is composed of several circumpolar jet filaments [Nowlin et al., 1977, Orsi et al., 1995, Hughes and Ash, 2001, Sokolov and Rintoul, 2007, 2009]. These jets arise as narrow regions of intensified flow and are associated with large density gradients in the horizontal. The frontal structure of the ACC allows individual jets to be defined through water mass properties and unique closed paths can be identified based on this criteria [Orsi et al., 1995]. More recently, it has been recognised that the jets can be mapped through peaks in dynamic topography [Hughes and Ash, 2001, Sokolov and Rintoul, 2007, 2009]. The path of the ACC is constrained by the bottom topography and is steered by several significant topographic features [Gordon et al., 1978]. Figure 1.3 shows a time-mean view of the ACC's frontal structure. Each ACC front aligns with a large-scale structure that appears in the bathymetry.

The ACC is steered around five major topographic features: the Pacific-Antarctic Ridge; the Scotia Arc; the Southwestern Indian Ridge, the Kerguelen Plateau and the Southeastern Indian Ridge [Orsi et al., 1995]. For geographical locations refer to Figure 1.1. In some locations, the fronts of the ACC converge as they approach these topographic features and diverge as their path descends towards deeper regions. An example of this is in the Pacific region where the ACC flow deviates northward, ascending the partially meridionally aligned Pacific-Antarctic Ridge. The flow converges towards the Udintsev Fracture Zone before taking a southward turn into the Southeast Pacific Basin and broadening [Gordon et al., 1978]. The Kerguelen Plateau is also meridionally aligned, though it is far steeper

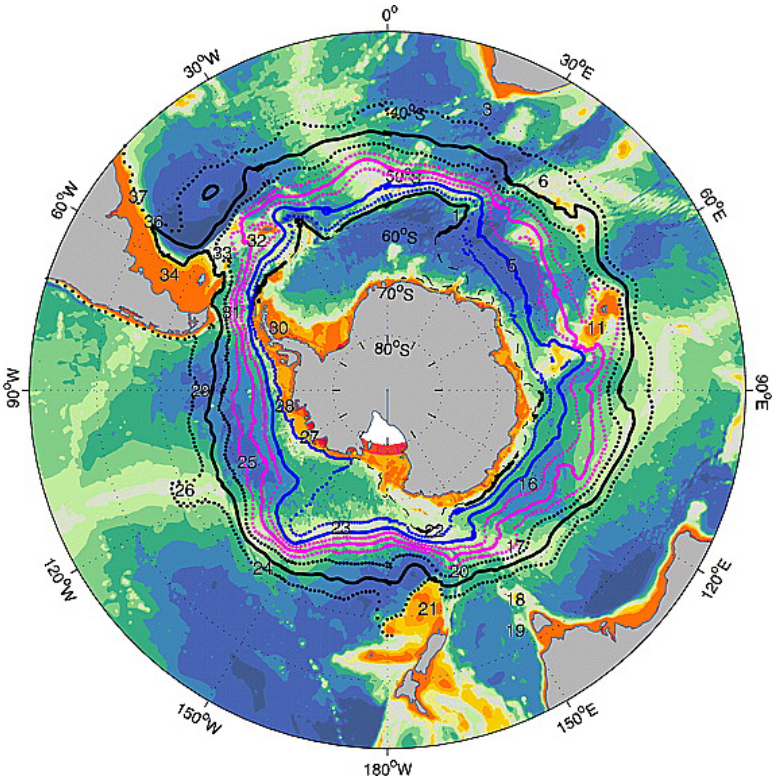

Figure 1.3: ACC front positions calculated from satellite altimetry, taken from Sokolov and Rintoul [2009].

and protrudes to much shallower depths than the Pacific-Antarctic ridge. The result of this difference in geometry is that much of the ACC is obstructed by this feature and is deflected around the base of the plateau [Orsi et al., 1995]. On the other hand, the zonal alignment of the Southeastern and Southwestern Indian Ridges result in smaller meridional deviations of the ACC in these regions and in places the fronts span both sides of the ridge crests.

1.2.2 Barotropic Structure

The ACC is observed to have an equivalent barotropic structure [Killworth, 1992]. The direction of the current is uniform with depth but the magnitude in the velocities is depth dependent with velocities generally reducing with depth. This equivalent barotropic structure of the ACC is attributed to its large eastward velocities and is associated with Rossby wave propagation [Hughes et al., 1998]. In studies of basin flow, in the sub-tropics, the short wavelength, baroclinic Rossby waves propagate westward relative to the time-mean flow and permit a baroclinic flow to develop [Anderson and Gill, 1975]. The effects of baroclinicity on the flow is less important where baroclinic Rossby waves travel eastward. The direction of travel for the baroclinic waves is dependent on eastward velocities. High eastward velocities can carry the westward propagating Rossby waves eastward in absolute terms [Rossby, 1939]. The propagation of baroclinic Rossby waves is slower at high latitudes [Lighthill, 1969] meaning a lower eastward velocity is required for the occurrence of eastward travelling baroclinic Rossby waves near the poles. The eastward velocities of the ACC are large enough for eastward travelling baroclinic Rossby waves to occur, resulting in a deep penetrating, equivalent barotropic current [Hughes et al., 1998].

1.2.3 Topographic Steering

In the absence of variable topography, ACC flow would be strictly zonal. Many major topographic features cause significant meridional deflection of the flow [Gordon et al., 1978]. Topographic steering of the flow is characterised by contours of f/H, where f represents planetary rotation and H is the water column thickness. Flow aligns with contours of f/H in order to conserve potential vorticity (see Chapters 2 and 3). f is monotonic and varies with latitude only. Meridional gradients in f/H are smaller when H is large. As a result, contours of f/H converge towards shallower regions and diverge towards deeper regions, accounting for the divergence and convergence structure observed in parts of the ACC.

The ACC generally aligns with contours of f/H but it is not strictly determined by this quantity. There is a degree of deviation of the ACC from contours of f/H. Topographic in-

fluence on large scale flow is reduced by stratification [Marshall, 1995a,b, Krupitsky et al., 1996, Gille, 2003]. Further, processes that are able to add or remove vorticity can influence the alignment of flow with contours of f/H. Thus, the topographic effects are also obscured by the wind forcing [Hughes et al., 1999], bottom drag [Neumann, 1960, McCartney, 1976] and inertial influences [Porter and Rattray, 1964, McCartney, 1976], which all act as sources and sinks of vorticity. Below, each effect is considered separately.

Stratification. Gradients in isopycnals can often oppose those of the sea surface, creating a baroclinic flow where geostrophic transport decreases with depth. In regions of high stratification, this effect can confine wind forced flow to shallow regions, acting to 'shield' flow from variations in topography. In the baroclinic limit, where velocities decrease with depth, the shielding of flow causes it to align with contours of f rather than f/H. The Southern Ocean has some degree of stratification. The dynamics of the ACC lies somewhere intermediate to a barotropic limit where flow follows contours of f/H and this baroclinic limit where flow follows contours of f [Marshall, 1995b]. The baroclinic limit and the associated shielding of bottom topography appears only where baroclinic Rossby waves are permitted to propagate westward [Anderson and Killworth, 1977]. As discussed above, the strong eastward flow and slow propagation of baroclinic Rossby waves in the Southern Ocean gives the ACC an equivalent barotropic structure. This results in significant topographic steering of the current and is indicative of a low influence of baroclinicity on the ACC, with flow aligning closer with contours of f/H than contours of f. The equivalent barotropic structure and thus topographic steering is shown to have a spatially non-uniform influence, with shallower topography being a larger determinant of the flow [Gille, 2003, Peña-Molino et al., 2014]. Nonetheless, surface waters are observed to be steered by deep topography and coherent, depth-uniform structures are present throughout the ACC [Gordon et al., 1978, Killworth, 1992].

Inertia and bottom drag. Inertia and bottom drag both act to deflect flow from contours of f/H over regions of variable topography through associated sources and sinks of vorticity [Neumann, 1960, Porter and Rattray, 1964, McCartney, 1976]. Bottom drag causes a net poleward deviation of streamlines from contours of f/H [Neumann, 1960, McCartney, 1976]. Although inertia causes a similar deviation over topography, unlike bottom drag there is no net deflection of streamlines along a closed contour of f/H [Porter and Rattray, 1964, McCartney, 1976]. These terms become integral to processes described in Chapter 5 and details will be given therein.

Wind forcing. Sverdrup balance is a process in which wind stress curl adds vorticity to the ocean [Sverdrup, 1947] and, in response, flow is advected across contours of f/H. This mechanism occurs to conserve potential vorticity. The addition of vorticity by the wind

stress must be locally balanced by another process which generates vorticity. The advection of flow to a region with a different value of f/H provides the required vorticity to balance the wind stress. In the context of gyres, this mechanism for the meridional displacement of flow is commonly referred to as Sverdrup balance [Sverdrup, 1947]. Additionally, this process is also known to displace the ACC from contours of f/H [Hughes et al., 1999]. To the south of the wind stress maximum Sverdrup balance acts to displace flow southwards and north of this position the displacement is northwards.

1.2.4 Form Stress

The topographic features in the Southern Ocean not only act to steer the flow but also form the primary sink of momentum imparted by the westerly winds [Munk and Palmén, 1951, Stevens and Ivchenko, 1997, Masich et al., 2015]. This topographic momentum sink is termed *topographic form stress* and arises from flow passing over topography.

In the Southern Ocean the westerly winds impart an eastward momentum into the underlying ocean, forcing the eastward ACC. As the ACC passes over topographic features, the flow is meridionally deflected generating zonal gradients in sea surface height. Gradients in the sea surface height over topography lead to a different pressure force on each flank of a topographic feature. Form stress arises due to this pressure difference over variable topography. The ocean puts a downward pressure force on the seabed. This pressure force is transferred to a horizontal force by topography. Fluid overlying the western flank of a meridional ridge creates a sink of eastward momentum and fluid overlying the eastern flank creates a source of eastward momentum. Generally in the Southern Ocean, the pressure force on the western flank is larger than the eastern flank and an overall sink of momentum is generated. Form stress is expressed though the sea surface height due to the equivalent barotropic structure of the Southern Ocean [Stewart and Hogg, 2017]. Further, this momentum sink is isolated to a few large topographic features of the Southern Ocean, such as the Kerguelen Plateau at 70°E, Macquarie Ridge and Campbell Plateau at 170°E, and Drake Passage at 60°W [Gille, 1997].

1.2.5 Volume Transport

The ACC is predominantly forced by the westerly winds which dominate the Southern Ocean, transferring momentum to the ocean surface. The volume transport of the ACC is associated with this source of momentum and it is a function of the entire combined circumpolar wind forcing [Wearn and Baker, 1980]. As a result, circumpolar transport is estimated in specific locations and the volume transport of the ACC is often quantified

by transport through the Drake Passage [Wearn and Baker, 1980, Whitworth et al., 1982, Donohue et al., 2016]. Measuring volume transport from this position removes the influence of flow leaving and entering from the basins to the north. For a given wind stress there are multiple factors that can affect the resulting volume transport. Three significant processes that have a control on the volume transport are: eddy generation due to isopycnal tilt [Meredith and Hogg, 2006, Meredith et al., 2012, Langlais et al., 2015], Sverdrup balance [Hughes et al., 1999] and topographic form stress [Munk and Palmén, 1951].

Eddy generation. The westerly winds over the ACC lead to a tilting of isopycnals. Tilting isopycnals results in the generation of baroclinic eddies which oppose the response of the wind forcing and act to flatten the isopycnals. The eddies which form in this way can both enhance and dampen the mean flow of the ACC depending on eddy geometry [Youngs et al., 2017]. There is an observed tendency for these eddies to dampen the mean flow of the ACC and limit its response to an increase in wind forcing [Meredith and Hogg, 2006, Meredith et al., 2012, Langlais et al., 2015]. This mechanism is often termed *eddy compensation.*

Sverdrup balance. Sverdrup balance is introduced above as a mechanism that can deflect flow from contours of f/H. Sverdrup balance is thought to contribute to the volume transport of the ACC [Hughes et al., 1999]. Flow can freely develop over contours of f/H which form a closed curve and are not blocked by any landmasses. These unblocked contours of f/H are present in the Southern Ocean and a proportion of them form a closed loop around Antarctica. These contours represent a 'free mode' along which ACC can flow and whose dynamics are equivalent to a flat bottom re-entrant channel [Hughes et al., 1999]. Some contours of f/H in the Southern Ocean do not form a closed loop around Antarctica as they are blocked by landmasses, inhibiting the development of circumpolar flow over these regions. Drake Passage is a region where many contours of f/H are blocked [Hughes et al., 1999] with South America emerging as a barrier for the flow. Although flow is restricted from developing, the ACC is observed to flow over these regions of blocked contours of f/H. It is thought that Sverdrup balance plays a role in permitting the ACC to flow in these regions of blocked contours of f/H [Hughes et al., 1999]. Sverdrup balance acts to shift this flow which aligns with blocked contours of f/H onto unblocked contours of f/H further downstream, increasing the capacity of the wind to force the ACC.

Topographic form stress. In the early studies of ocean circulation, wind forcing was thought to be balanced by drag from the bottom or side boundaries of the ocean [Stommel, 1948, Munk, 1950]. However, extending this balance to the Southern Ocean leads to a requirement of an unrealistic flow field [Munk and Palmén, 1951]. For frictional drag to balance the momentum imparted by the surface wind forcing the ACC transport would

need to be an order of magnitude larger than what is observed [Munk and Palmén, 1951]. Munk and Palmén [1951] hypothesised that significant topographic features were instead responsible for the majority of the momentum sink in the Southern Ocean through topographic form stress. This indicates that form stress plays a role in the volume transport of the ACC and without it the ACC volume transport would be notably higher. It has been found that there is a non-uniform form stress contribution with depth [Stevens and Ivchenko, 1997, Masich et al., 2015]. Approximately, in the upper 3700 metres of the water column form stress provides a momentum sink. Below this depth, the characteristics can vary and in parts of the Southern Ocean, form stress can be a momentum source [Stewart and Hogg, 2017]. This source of momentum is attributed to the formation of AABW which is is exported along the eastern flank of meridional ridges [Stewart and Hogg, 2017]. This export of AABW results in a pressure difference across the topography at depth, with higher pressure to the east creating a westward force [Stewart and Hogg, 2017]. This contribution is thought to permit an increased volume transport in the ACC [Stewart and Hogg, 2017].

1.3 Southern Ocean Gyres

Subpolar gyres of the Southern Ocean form in regions between the southern boundary of the ACC and the coastline of Antarctica [Gordon et al., 1978, Orsi et al., 1995]. They form under topographic constraints and are forced by the same westerly winds which drive the ACC. These gyres are important for understanding the changing climate. However, there is a particular lack of knowledge surrounding the gyres. They are poorly represented in models, with substantial disparity between simulations [Wang and Meredith, 2008, Rickard et al., 2010]. There is also a lack of observations in the regions where the gyres form. The gyres are coincident with extensive sea ice cover and are difficult to observe over large spatial or time-scales. This is a primary cause for the lack of literature on these subpolar gyres in comparison to the ACC. Historically, satellite altimetry has failed to observe the gyres but recent advances in altimetry methods have resulted in the first approximations of dynamic topography in regions of high ice concentrations [Kwok and Morison, 2016, Armitage et al., 2018, Dotto et al., 2018]. There is still a particular lack of in-situ observations in the subpolar gyres. This subsection gives an overview of the gyres which form in the Southern Ocean.

1.3.1 The Formation of Subpolar Gyres

Subpolar gyres are cyclonic circulations which are forced by wind stress curl. Most knowledge of gyres has stemmed from studies of the North Atlantic gyre. In the classical setting gyres are forced by a wind stress curl over a flat basin. A meridional flow is induced through Sverdrup balance in the ocean interior to balance the input of vorticity via the wind stress curl [Sverdrup, 1947]. The fluid which is advected meridionally via this process is returned along a western boundary to conserve mass. The westerly winds that occur over the Southern Ocean forcing the ACC are also responsible for forcing the subpolar gyres. The wind stress profile has a curl and inputs negative vorticity on the poleward side of the peak of the wind stress. This negative input of vorticity is conducive to supporting the subpolar gyres. There is a divergence of flow from the centre of these subpolar gyres, setting an Ekman suction which creates a dip in the sea surface height towards the centre of the gyres.

1.3.2 Structure

Although there are a lack of observations of gyres which form in the Southern Ocean, attempts have been made to summarise these circulations from the sparse dataset which is available. Studies have been published with summaries of the path and volume transport in the Weddell [Gordon et al., 1981, Gouretski and Danilov, 1993], Ross [Locarnini, 1994, Gouretski, 1999] and Australian-Antarctic [McCartney and Donohue, 2007] gyres.

Ross Gyre. Figure 1.4a shows the bathymetry in the region of the Ross Gyre. The Ross Gyre lies in the Ross Sea and its position is determined by local topography [Gouretski, 1999]. The south of the gyre is bounded by the Antarctic continent. To the north west lies the Pacific-Antarctic Ridge, forming the north-western boundary of the Ross Gyre, with the ACC flowing on the equatorward side of the ridge crest [Gouretski, 1999]. At approximately 140°W the ACC passes east through a narrow fracture zone, the Udintsev Fracture Zone [Gouretski, 1999]. Through the fracture zone the ACC is narrow and intense. Downstream of this feature the ACC broadens, with its southern limb turning southward [Gordon et al., 1978, Orsi et al., 1995, Gouretski, 1999]. The southern boundary of the ACC forms the northern and eastern boundaries of the Ross Gyre. There is a westward flow following topography along the Antarctic continental shelf. Much of this westward flow forms the southern limb of the Ross Gyre and is directed northward by the Pacific-Antarctic ridge. However, this ridge does not intersect with the Antarctic continent and a gap exists for some flow to continue westward out of the Ross Sea. The Ross Gyre has been estimated to have a baroclinic volume transport of 5-9 Sv [Locarnini, 1994, Gouretski, 1999].

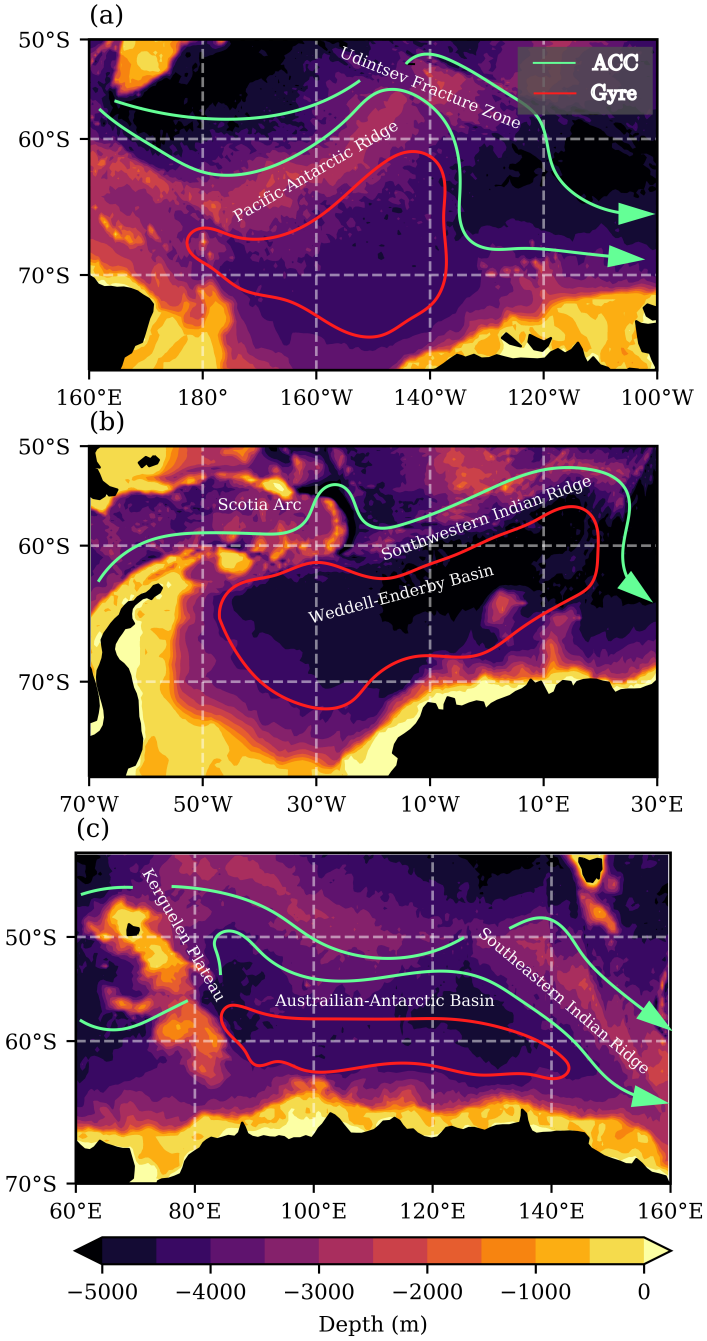

Figure 1.4: The bathymetry in the regions of the Ross, Weddell and Australian-Antarctic gyres. (a) The South Pacific sector of the Southern Ocean centered on the Ross Sea, where the Ross Gyre forms. (b) The South Atlantic sector of Southern Ocean centered on the Weddell Sea, where the Weddell Gyre forms. (c) The Indian Sector of the Southern Ocean, where the Australian-Antarctic Gyre forms.

The transport in the Ross Gyre appears to be highly barotropic and there is a degree of alignment of deep and surface flow [Gouretski, 1999]. As the gyres are indicated to have an equivalent barotropic structure it is likely that the above volume transports are underestimations [Park and Gamberoni, 1995, Wang and Meredith, 2008]. An estimate from satellite altimetry, based on depth uniform flow, inferred from gradients in the sea surface height show the Ross Gyre to have a transport of $\sim 23 \pm 8$ Sv [Dotto et al., 2018]. It is unlikely that the Ross Gyre is strictly depth-uniform indicating that this is an overestimate of the gyre transport. It is indicated that modelling studies also overestimate the gyre strength with estimates exceeding the observations. The total gyre transport, which includes both baroclinic and barotropic components of the flow, estimated by model simulations stands at 22-33 Sv [Rickard et al., 2010].

Weddell Gyre. Figure 1.4b shows the bathymetry in the region of the Weddell Gyre. The Weddell Gyre forms in the Weddell-Enderby basin. This basin is bounded to the south and west by the Antarctic continent, to the north by the Scotia Arc and Southwestern Indian Ridge and to the east by the Kerguelen Plateau. The north, south and western limits of the gyre are aligned with the basin boundaries but the gyre does not extend out to the Kerguelen Plateau [Gordon et al., 1981]. Similar to the southward turn of the ACC at the Udintsev Fracture Zone, the ACC turns south and broadens after passing through a gap in the Southwestern Indian Ridge at around 20-30°E [Gordon et al., 1978, 1981, Orsi et al., 1995, Sokolov and Rintoul, 2009]. Despite the relatively small variance in topography poleward of the Southwestern Indian Ridge, it has been suggested that this southward flow is a result of topographic steering [Gouretski and Danilov, 1993]. The poleward limit of the ACC at this southward turn, near 20-30°E, forms the eastern boundary of the Weddell Gyre [Gordon et al., 1981]. The volume transport of the Weddell Gyre, estimated from by the northern limb along the Prime Meridian, is approximately 45 Sv [Klatt et al., 2005].

Australian-Antarctic Gyre. A third large cyclonic circulation named the Australian-Antarctic Gyre is observed to the east of the Kerguelen Plateau and forms in the Australian-Antarctic Basin [Park and Gamberoni, 1995, McCartney and Donohue, 2007]. Figure 1.4c shows the bathymetry in the region of this gyre. The southern half of Kerguelen Plateau bounds the gyre to the west, Antarctica bounds the gyre to the south and the Southeastern Indian Ridge bounds it to the east. The boundary to the north is approximately set by the peak wind stress [McCartney and Donohue, 2007]. The line of peak wind stress is characterised by zero wind stress curl. North of this line the wind stress curl is positive. The Australian-Antarctic gyre is cyclonic thus forms south of the peak in wind stress. The Australian-Antarctic Gyre is approximated to have a volume transport of 76 Sv [McCartney and Donohue, 2007]. Though this seems high given the estimates of the more promi-

nent Ross and Weddell Gyres.

1.3.3 The Western Boundary

Gyre formation requires a western boundary to permit the meridional return flow of fluid which is advected by Sverdrup balance. The Weddell Gyre forms under similar conditions to the North Atlantic gyre, with Sverdrup balance acting in the interior and the Antarctic Peninsula supporting a western boundary current for the flow to return north. Differences from the classical case arises however, for both the Ross and Australian-Antarctic Gyres. These two gyres have no land masses to the west, yet western boundary currents are supported. Submarine topography is able to replace the role of a continent in this situation, supporting an equatorward return flow.

The lack of a continental boundary permits the ACC to form. This means that submarine topography such as Kerguelen Plateau and the Pacific-Antarctic Ridge support both gyre circulation and the ACC. The balance between ACC and gyre flow in the Southern Ocean has been studied by Nadeau and Ferrari [2015]. This work will be discussed in more detail later in this thesis.

1.4 Regional Disparity

Southern Ocean circulation plays an important role in sea ice production and transporting water masses. The regional distribution of these processes are largely associated with the path and strength of the large-scale circulation. Gyre regions are the predominant location for the formation of AABW, a water mass created through the formation of sea ice [Jacobs et al., 1970]. Furthermore, along both the eastern limb of these gyres and the ACC there is an upwelling of Circumpolar Deep Water (CDW), a warm and highly saline water mass which has been associated with the melting of ice shelves [Jenkins et al., 2016].

1.4.1 Circumpolar Deep Water

CDW originates at depth and is upwelled to the surface in the Southern Ocean. The upwelling of CDW stems from the westerly winds driving a geostrophic flow through Ekman transport, forming the large-scale circulation. The process is depicted in Figure 1.5a. Surface Ekman transport in the Southern Ocean, set by the westerly winds, drives an advection of surface waters perpendicular to the mean barotropic transport. The westerly winds force a surface Ekman transport towards the north leading to a tilting of isopycnals [Meredith and Hogg, 2006]. The northward Ekman transport is balanced by a southward transport at depth and isopycnals become sloped up towards Antarctica, outcropping at

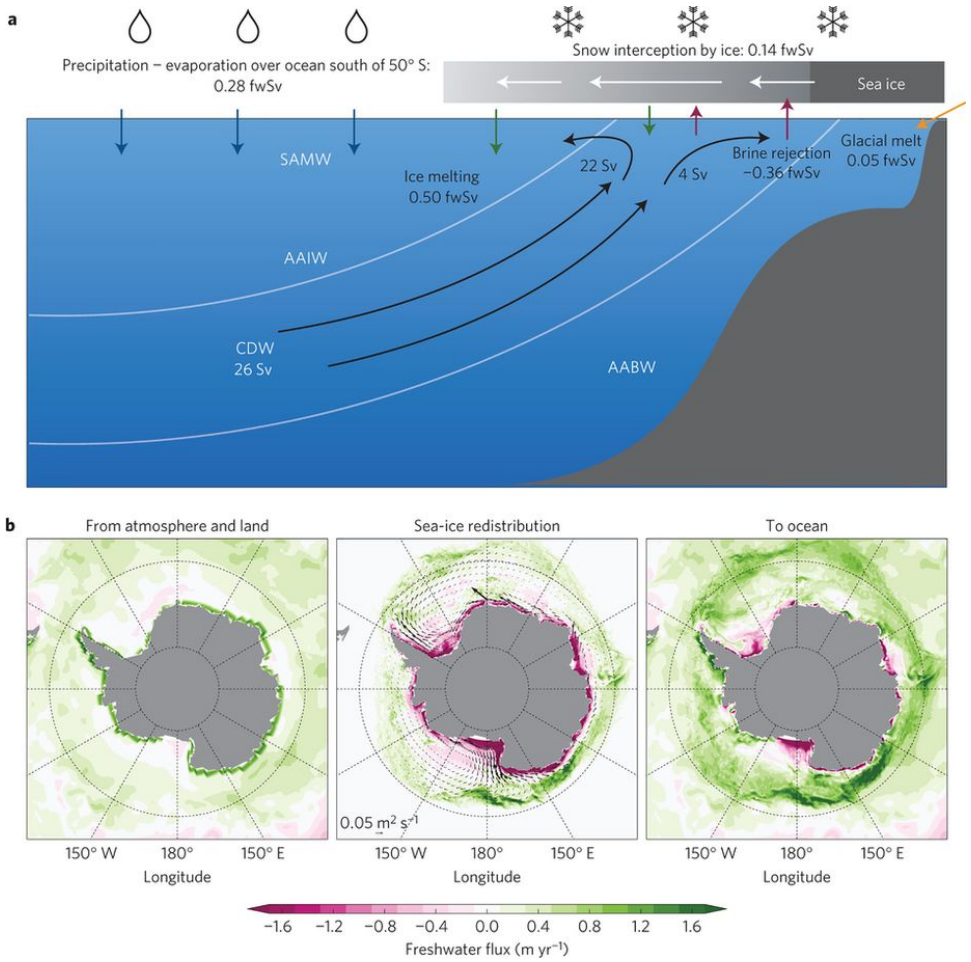

Figure 1.5: Surface buoyancy fluxes of the Southern Ocean taken from Abernathey et al. [2016]. (a) Schematic of density surfaces of the Southern Ocean with surface flux estimates. (b: left) Fresh water flux leaving the atmosphere and land. (b: centre) The difference betweeen the fresh water flux leaving the atmosphere and land and the fresh water flux to the Southern Ocean, representing the redistribution of fresh water via the advection of sea ice. (b: right) Fresh water flux to the Southern Ocean

the ocean surface [Meredith and Hogg, 2006]. The curl in the wind stress forms a divergence in the northward Ekman transport and where this divergence occurs water is drawn up from depth, following the tilted isopycnals. A large proportion of the upwelled water mass is CDW [Orsi et al., 1995, Gouretski, 1999]. Figure 1.5a displays a southward surface Ekman transport to the south of the upwelling. This Ekman transport stems from the easterly winds which lie close to the Antarctic coastline driving the Antarctic Slope Current.

The location of upwelled CDW is associated with the path of both the ACC and subpolar gyres [Gouretski and Danilov, 1993, Orsi et al., 1995, Gouretski, 1999]. The southward flow on the eastern limb of the subpolar gyres advects CDW towards the Antarctic coastline [Gouretski and Danilov, 1993, Orsi et al., 1995, Gouretski, 1999]. In some locations downstream of the gyres, such as along the west of the Antarctic Peninsula, the ACC draws close to the coast, also advecting CDW towards the continental shelf [Orsi et al., 1995]. The advection of CDW towards the Antarctic continent forms a link between ice shelf melt and the large scale circulations of the Southern Ocean [Jenkins et al., 2016].

1.4.2 Sea Ice

At particular locations near the Antarctic continental shelf, a production of sea ice occurs. Regional differences which are associated with the large scale circulations also occur in sea ice production. Figure 1.5b shows the annual-mean fresh water flux distribution for the Southern Ocean. This indicates a net flux of fresh water to sea ice in the southern part of gyre regions which is much less pronounced elsewhere. Thus, there is a net sea ice formation confined to the southern regions of the subpolar gyres.

AABW production is linked to sea ice formation and regional disparity also arises in the presence of AABW. Shelf Water is formed during sea ice production [Jenkins et al., 2016]. Inflowing CDW from the open ocean is often mixed with this saline Shelf Water to form the highly dense AABW [Jacobs et al., 1970, Orsi et al., 1995] and is subducted towards the deep ocean [Jacobs et al., 1970]. A limited amount of Shelf Water is situated along the western side of the Antarctic Peninsula [Orsi et al., 1995]. The limited Shelf Water is associated with the lower sea ice production in this region. Thus where sea ice production is high, such as within the gyre circulations, AABW production is also high.

1.5 The Role of Southern Ocean Circulation in Climate

As the ACC and subpolar gyres are associated with regional differences in water mass properties and ice-ocean processes, changes in these circulations have significant implications on

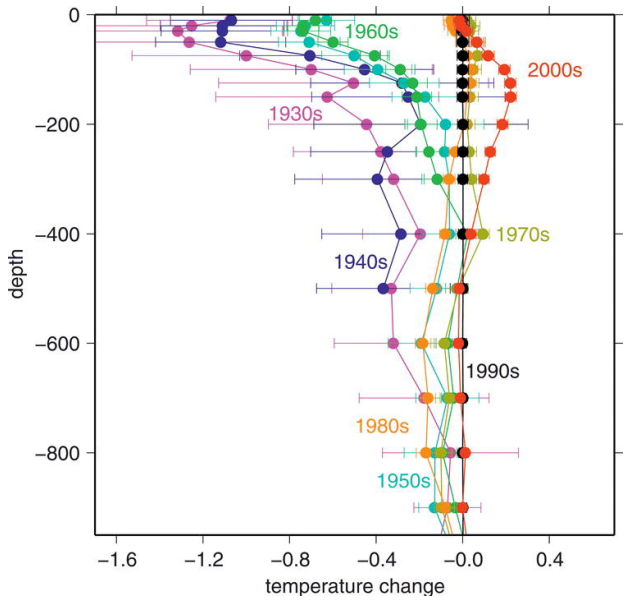

Figure 1.6: Depth profile of the mean difference in temperature of the Southern Ocean over the period 1930-2006, referenced to observations taken in 1990-2000. Figure is taken from Gille [2008].

the climate. It has been suggested that these large-scale circulations have played an important role in observed changes in Southern Ocean heat content [Böning et al., 2008] and ice-sheet loss over the continent [Jenkins et al., 2016].

1.5.1 Southern Ocean Warming

Figure 1.6 shows the depth profile of the mean difference in temperature of the Southern Ocean over the period 1930-2006, referenced to observations taken in 1990-2000. The Southern Ocean is observed to have warmed at a significant rate over the 20th Century [Gille, 2002, 2008]. Numerous studies propose that the observed warming is linked to changes in winds associated with the trend in the SAM [Gille, 2002, Böning et al., 2008], with the proposed mechanisms involving changes in both path and strength of the ACC. One hypothesis is that the warming stems from a response in the ACC to shift southward matching the changes in the wind, drawing warm water further south [Gille, 2002, 2008]. An alternative mechanism given for the observed warming is an increased eddy heat flux through eddy compensation [Böning et al., 2008].

Shift of the ACC. A possible southward shift in the ACC, associated with the observed southward shift in the westerly winds could explain the warming of the Southern Ocean

[Gille, 2002, 2008]. However, a southward shift in the ACC is largely absent in both model simulations [Graham et al., 2012] and data [Sallée et al., 2008, Gille, 2014]. Although the path of the ACC is observed to have some response to changes in wind forcing, this relationship is non-uniform across the Southern Ocean [Sallée et al., 2008, Graham et al., 2012]. The strong topographic influence on the ACC results in the current being insensitive to changes in wind forcing where gradients in f/H are large [Sallée et al., 2008]. In flat-bottom regions, with weaker topographic control, there is a greater sensitivity in the ACC to changes in winds [Sallée et al., 2008]. However the influence of the SAM is variable, with some regions exhibiting an opposing northward shift of the ACC with a positive phase of the SAM [Sallée et al., 2008]. The complexity in the response of the ACC over the flat-bottom regions and the observed insensitivity of the flow over variable topography leaves the shift in the fronts an unlikely candidate for the Southern Ocean warming.

Eddy Compensation. Eddy compensation is observed across the ACC and possibly contributes to Southern Ocean warming [Böning et al., 2008]. The strengthening of the winds associated with a positive SAM has not induced the anticipated increase in ACC strength through a steepening of isopycnals. This observation has been attributed to increased eddy activity linked to eddy compensation [Meredith and Hogg, 2006]. As the wind strengthens over the Southern Ocean, surface Ekman flow drives both a barotropic and baroclinic response, steepening both sea surface height gradients and isopycnals respectively. As isopycnals steepen, eddies are formed which act to relax the isopycnal gradients, counteracting the effects of the winds. The warming of the Southern Ocean has been attributed to this eddy compensation mechanism [Böning et al., 2008]. The increased eddy activity acts to drive a southward heat flux from warmer waters to the north, preferentially raising the temperatures of the Southern Ocean south of the ACC.

The Role of Topography in Eddy Dynamics. Adding to the complexity, it has also been shown that this southward eddy flux of warm water is not zonally uniform and is enhanced by meanders in the lee of large scale topography [Thompson and Naveira Garabato, 2014]. As wind stress increases, most of the increase in isopycnal tilt is confined upstream of topographic features. In the lee of the ridge, this enhanced isopycnal tilt is reduced through eddy generation producing a southward flux of heat. The topographic enhancement of eddying reduces vertical stratification, further enhancing the barotropic structure of flow over topography, as noted by Killworth [1992]. It has been observed that the resulting meanders occur over barotropic length scales [Hughes, 2005]. The increased heat flux is a result of an increased *eddy efficiency* rather than an increase in the occurrences of eddies [Abernathey and Cessi, 2014]. The eddy efficiency is heightened with an enhancement of curvature and density gradients across a standing meander, both of which are associated with increased

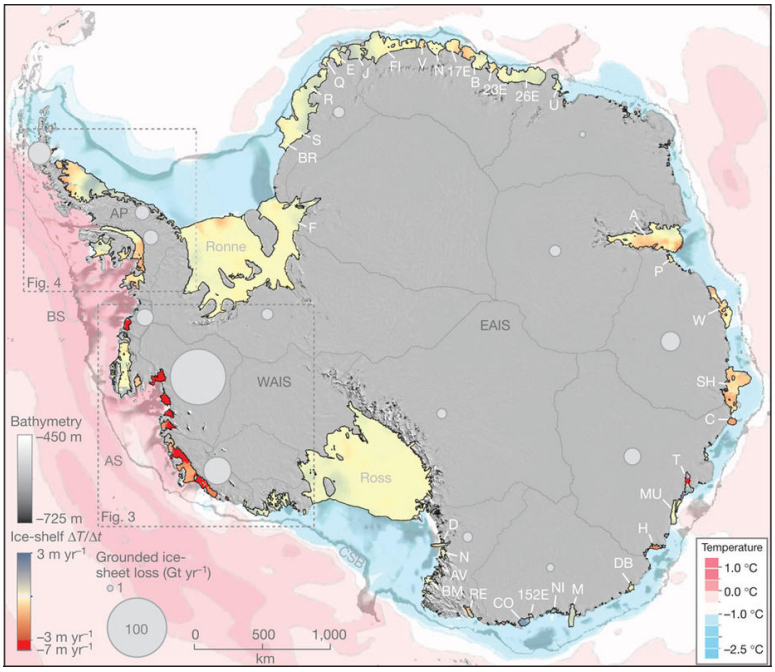

Figure 1.7: Ocean temperatures at the seabed and changes in ice-sheet loss between 2003-2008 around Antarctica. Figure is taken from Pritchard et al. [2012].

wind forcing. As a result, flow over topography is indicated to play a vital role in Southern Ocean warming.

1.5.2 Regional Ice-Sheet Melt

The regional disparity in the circulations that bound Antarctica are associated with regional differences in processes that occur on the ice-sheet. Figure 1.7 shows mean ocean temperatures at the seabed and regional ice-sheet loss for the period 2003-2008. Regions where the warm CDW is brought close to the coastline, such as the western side of the Antarctic Peninsula, coincide with larger magnitudes of ice-sheet loss. The ocean circulation has implications for ice-sheet processes with decadal variability, linked to the ENSO, playing key role [Jenkins et al., 2016].

1.6 This Study

It has been shown that the large scale circulation of the Southern Ocean plays a key role in climate processes. Together, the gyre circulations and the ACC cause significant regional differences in processes and properties of the ocean and cryosphere. Thus, the path and

strength of these currents are of primary interest.

The path and strength of the large-scale flow in the Southern Ocean is largely controlled by seabed topography. Understanding the dynamics behind topographic steering of Southern Ocean circulation is important for gaining insight into what controls the path of these flows. Improved knowledge of what sets the path and strength of the ACC and Southern Hemisphere subpolar gyres will aid the comprehension of the observed changes attributed to climate change.

Large topographic features act to steer the ACC and have a control on its volume transport. These same topographic features appear to support the western boundaries of the large gyre circulations such as the Ross Gyre and Australian-Antarctic Gyre. The mechanism for these gyres to be supported through submarine ridges rather than the coastlines of continents is poorly understood. This thesis investigates the influence of these large topographic features on the gyres and the ACC in a barotropic context. The majority of the analysis is done through the use of idealised computer simulations.

Chapter 2 gives an overview of the methods, outlining the model used and providing a detailed derivation of the governing equations for subsequent analysis. Chapter 3 provides an in-depth introduction into existing gyre theory. This begins with classical theory centered on understanding the North Atlantic gyre then extends to the current knowledge on Southern Ocean gyres. The background in Chapter 3 has been largely neglected in the introduction as it can be better explained through the use of equations derived in Chapter 2 and model simulations. Chapter 4 shows results of the effects of topographic gradients on Southern Ocean gyres, shedding new light on the influence of topography on gyre formation in the Southern Ocean. Chapter 5 then focuses the analysis on the ACC and analyses the effects of the topographic variations on the ACC alone. Section 6 shows further relevant forms of topographic variations which have an effect on the ACC flow. Results in Chapter 6 are a work in progress and will require extended analysis to fully understand the effects. Finally, in Chapter 7 conclusions are provided of the full study, summarising the main outcomes of this research.

2 Methods

This chapter describes the tools used to address questions highlighted by the introduction. A large proportion of the work here makes use of numerical simulations, so an outline is provided of the model that is used. The analysis of the model results involves various equations that can be derived from the momentum equation. A derivation is given here for all the relations required in subsequent chapters. In order to conduct the analysis for this work using the derived equations, modifications of the model output are required. Details are given in this chapter of the numerical methods developed for undertaking these modifications, providing documentation for possible replication. Lastly, a base model case is presented to give the reader an appreciation of the geometries and forcing applied to the model runs, with a table of all model variants used in this thesis for reference.

In general, the Navier-Stokes equations are used to analyse the dynamics of fluids. The model used for simulations in this study is the the Massachusetts Institute of Technology general circulation model (MITgcm, [Marshall et al., 1997a,b]), which is capable of simulating the full Navier-Stokes equations. For this thesis, the interest is in the barotropic component of the flow so simplifications are made to the MITgcm's default set-up. Velocities are taken to be uniform in the vertical, achieved by using a grid with one layer in the vertical. Variable seabed topography is factored in using partial cells. The density is taken to be constant everywhere meaning there is no buoyancy forcing or variation in temperature and salinity.

2.1 Governing Equations

For a fluid with uniform density, the Navier-Stokes equations are given by:

$$\rho_0\left(\frac{D\boldsymbol{u}}{Dt} + f\boldsymbol{k}\times\boldsymbol{u}\right) = -\boldsymbol{\nabla}p + \frac{\partial\boldsymbol{\tau}}{\partial z} + \mu\boldsymbol{\nabla}^2\boldsymbol{u}, \tag{2.1}$$

$$\boldsymbol{\nabla}\cdot\boldsymbol{u} = 0, \tag{2.2}$$

where ρ_0 is the reference density; $D\boldsymbol{u}/Dt = \partial\boldsymbol{u}/\partial t + \boldsymbol{u}\cdot\boldsymbol{\nabla}\boldsymbol{u}$ is the Lagrangian derivative; $\boldsymbol{u} = \{u, v, w\}$, the velocity vector where u, v and w are the velocities in the x, y and z directions respectively; f is the Coriolis parameter; $\boldsymbol{k}$ is the unit vector pointing upwards; p is the pressure; $\boldsymbol{\tau}$ is the external forcing; μ is the molecular dynamic viscosity coefficient and $H = h+\eta$ is the water column thickness, h is distance from the resting ocean surface to the bottom topography and η is the sea surface height. The definition of the water column in these equations is highlighted by Figure 2.1. For convenience u will be referred to as the

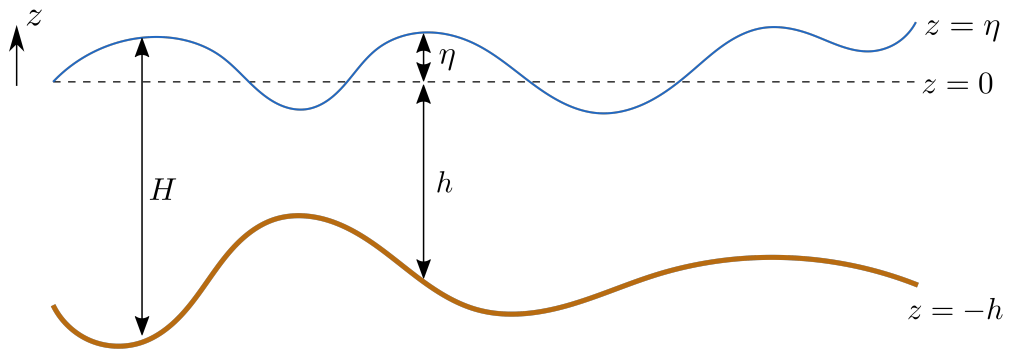

Figure 2.1: An illustration of the definition of water column thickness: $H = h + \eta$ where h is distance from the resting ocean surface to the bottom topography and η is the sea surface height relative to the resting surface.

eastward velocity and v the northward velocity.

The analysis in this thesis makes use of four forms derived from equation (2.1). The derivations for these equations are outlined in the following subsections. The four derived forms are named:

- Barotropic Momentum Equation - This is the depth integral of the momentum equation. It encompasses the effects of topographic variations into the momentum equations.
- Barotropic Vorticity Equation - Achieved through taking the curl of the barotropic momentum equations. This is useful for decomposing the dynamical contributions within gyres. It also provides a view of the eddying effects on the time-mean flow.
- Form Stress Equation - This is the zonal integral of the barotropic zonal momentum equation. Within channels this can be used to find the total zonal momentum at each latitude. The key zonal momentum sink often arises from topographic variations and is termed topographic form stress.
- Potential Vorticity Equation - A vorticity equation found by taking the curl of the momentum equations rather than the barotropic momentum equations. This is the more classical equation for discussing gyre dynamics and is a useful alternative to the

barotropic vorticity equation. It provides an additional way of describing the vorticity in a system that also highlights the effects of topographic steering.

The potential vorticity equation is primarily used for describing analytical concepts. Model results of vorticity are mostly shown in terms of the barotropic vorticity equation. The form stress equation is used both for discussing analytical concepts and displaying model results.

As the interest is restricted to the barotropic component of the flow, the shallow-water approximation is made to equations (2.2) and (2.1). By the shallow-water approximation, the fluid is assumed to be in hydrostatic balance and the vertical component of the momentum equations is neglected from (2.1). Additionally, the horizontal velocities are taken to be depth-independent, the sea surface height is variable and vertical velocities are retained. As a result, the water column thickness is directly related to the vertical velocities:

$$w_\eta - w_{-h} = \frac{DH}{Dt}. \tag{2.3}$$

2.1.1 Barotropic Momentum Equation

The barotropic momentum equation is found by taking the depth-integral of the shallow-water approximation of equations (2.1) and (2.2), given by:

$$\rho_0\left(\int_{-h}^{\eta} \frac{D\boldsymbol{u}}{Dt}\,dz + \int_{-h}^{\eta} f\boldsymbol{k}\times\boldsymbol{u}\,dz\right) = -\int_{-h}^{\eta} \boldsymbol{\nabla} p\,dz + \int_{-h}^{\eta} \frac{\partial \boldsymbol{\tau}}{\partial z}\,dz + \mu\int_{-h}^{\eta} \boldsymbol{\nabla}^2\boldsymbol{u}\,dz, \tag{2.4}$$

$$\int_{-h}^{\eta} \boldsymbol{\nabla}\cdot\boldsymbol{u}\,dz = 0. \tag{2.5}$$

Before evaluating these integrals, common steps will be outlined. As velocities are depth-uniform:

$$\int_{-h}^{\eta} u\,dz = Hu, \tag{2.6}$$

$$\int_{-h}^{\eta} v\,dz = Hv. \tag{2.7}$$

Through the use of these relations and the Leibniz integral rule the following hold:

$$\int_{-h}^{\eta} \frac{\partial u}{\partial x}\,dz = \frac{\partial}{\partial x}\int_{-h}^{\eta} u\,dz - u\frac{\partial \eta}{\partial x} - u\frac{\partial h}{\partial x} = \frac{\partial (uH)}{\partial x} - u\frac{\partial H}{\partial x}, \tag{2.8}$$

$$\int_{-h}^{\eta} \frac{\partial v}{\partial y}\,dz = \frac{\partial}{\partial y}\int_{-h}^{\eta} v\,dz - v\frac{\partial \eta}{\partial y} - v\frac{\partial h}{\partial y} = \frac{\partial (vH)}{\partial y} - v\frac{\partial H}{\partial y}. \tag{2.9}$$

The Leibniz integral rule makes use of the velocities at the boundaries, which are usually different on the surface and the bottom boundaries. Depth-uniform velocities allow for the combination of the boundary components in equations (2.8) and (2.9). The depth-integrated vertical velocity gradient is evaluated as:

$$\int_{-h}^{\eta} \frac{\partial w}{\partial z}\, dz = w_\eta - w_{-h} = \frac{DH}{Dt}. \tag{2.10}$$

Making use of (2.8), (2.9) and (2.10), the depth-integrated continuity equation, (2.5), is then evaluated,

$$\begin{aligned}\int_{-h}^{\eta} \boldsymbol{\nabla}\cdot\boldsymbol{u}\, dz =& \int_{-h}^{\eta} \frac{\partial u}{\partial x} + \frac{\partial v}{\partial y} + \frac{\partial w}{\partial z}\, dz \\ =& \frac{\partial (uH)}{\partial x} - u\frac{\partial H}{\partial x} + \frac{\partial (vH)}{\partial y} - v\frac{\partial H}{\partial y} + \frac{DH}{Dt}.\end{aligned} \tag{2.11}$$

Using (2.3), equation (2.11) can be further reduced,

$$\begin{aligned}&\frac{\partial (uH)}{\partial x} - u\frac{\partial H}{\partial x} + \frac{\partial (vH)}{\partial y} - v\frac{\partial H}{\partial y} + \frac{DH}{Dt} \\ =&\frac{\partial (uH)}{\partial x} - u\frac{\partial H}{\partial x} + \frac{\partial (vH)}{\partial y} - v\frac{\partial H}{\partial y} + \frac{\partial H}{\partial t} + u\frac{\partial H}{\partial x} + v\frac{\partial H}{\partial y} \\ =&\frac{\partial H}{\partial t} + \frac{\partial (uH)}{\partial x} + \frac{\partial (vH)}{\partial y} \\ =&\frac{\partial H}{\partial t} + \boldsymbol{\nabla}\cdot(H\boldsymbol{u}).\end{aligned} \tag{2.12}$$

Thus, the depth-integrated continuity equation, (2.5), is given as:

$$\int_{-h}^{\eta} \boldsymbol{\nabla}\cdot\boldsymbol{u}\, dz = \frac{\partial H}{\partial t} + \boldsymbol{\nabla}\cdot(H\boldsymbol{u}) = 0. \tag{2.13}$$

Each integral term of (2.4) will now be evaluated independently. The Lagrangian derivative is expanded as follows,

$$\int_{-h}^{\eta} \frac{D\boldsymbol{u}}{Dt}\, dz = \int_{-h}^{\eta} \frac{\partial \boldsymbol{u}}{\partial t}\, dz + \int_{-h}^{\eta} u\frac{\partial \boldsymbol{u}}{\partial x}\, dz + \int_{-h}^{\eta} v\frac{\partial \boldsymbol{u}}{\partial y}\, dz. \tag{2.14}$$

The first term on the right-hand side of (2.14) is expanded as

$$\int_{-h}^{\eta} \frac{\partial \boldsymbol{u}}{\partial t}\, dz = \frac{\partial (\boldsymbol{u}H)}{\partial t} - \boldsymbol{u}\frac{\partial H}{\partial t} = \boldsymbol{u}\frac{\partial H}{\partial t} + H\frac{\partial \boldsymbol{u}}{\partial t} - \boldsymbol{u}\frac{\partial H}{\partial t}. \tag{2.15}$$

As depth-uniform velocities result in $\partial \boldsymbol{u}/dz = 0$, through integration by parts,

$$\begin{aligned}\int_{-h}^{\eta} u\frac{\partial \boldsymbol{u}}{\partial x}\,dz =& u\frac{\partial(\boldsymbol{u}H)}{\partial x} - u\boldsymbol{u}\frac{\partial H}{\partial x} - \int_{-h}^{\eta}\frac{\partial u}{\partial z}\left(u\frac{\partial(\boldsymbol{u}H)}{\partial x} - u\boldsymbol{u}\frac{\partial H}{\partial x}\right)dz \\ =& u\frac{\partial(\boldsymbol{u}H)}{\partial x} - u\boldsymbol{u}\frac{\partial H}{\partial x},\end{aligned} \tag{2.16}$$

$$\begin{aligned}\int_{-h}^{\eta} v\frac{\partial \boldsymbol{u}}{\partial x}\,dz =& v\frac{\partial(\boldsymbol{u}H)}{\partial x} - v\boldsymbol{u}\frac{\partial H}{\partial x} - \int_{-h}^{\eta}\frac{\partial v}{\partial z}\left(v\frac{\partial(\boldsymbol{u}H)}{\partial x} - v\boldsymbol{u}\frac{\partial H}{\partial x}\right)dz \\ =& v\frac{\partial(\boldsymbol{u}H)}{\partial x} - v\boldsymbol{u}\frac{\partial H}{\partial x}.\end{aligned} \tag{2.17}$$

Substituting (2.15), (2.16) and (2.17) into (2.14) gives

$$\begin{aligned}&\int_{-h}^{\eta}\frac{\partial \boldsymbol{u}}{\partial t}\,dz + \int_{-h}^{\eta} u\frac{\partial \boldsymbol{u}}{\partial x}\,dz + \int_{-h}^{\eta} v\frac{\partial \boldsymbol{u}}{\partial y}\,dz \\ =&\boldsymbol{u}\frac{\partial H}{\partial t} + H\frac{\partial \boldsymbol{u}}{\partial t} - \boldsymbol{u}\frac{\partial H}{\partial t} + u\frac{\partial(\boldsymbol{u}H)}{\partial x} - u\boldsymbol{u}\frac{\partial H}{\partial x} + v\frac{\partial(\boldsymbol{u}H)}{\partial x} - v\boldsymbol{u}\frac{\partial H}{\partial x} \\ =&H\frac{\partial \boldsymbol{u}}{\partial t} + Hu\frac{\partial \boldsymbol{u}}{\partial x} + Hv\frac{\partial \boldsymbol{u}}{\partial y} \\ =&H\frac{D\boldsymbol{u}}{Dt}.\end{aligned} \tag{2.18}$$

Thus, the depth-integrated Lagrangian derivative is given as:

$$\int_{-h}^{\eta}\frac{D\boldsymbol{u}}{Dt}\,dz = H\frac{D\boldsymbol{u}}{Dt}. \tag{2.19}$$

The depth-integrated Coriolis term is evaluated as:

$$\int_{-h}^{\eta} f\boldsymbol{k}\times\boldsymbol{u}\,dz = f\boldsymbol{k}\times\int_{-h}^{\eta}\boldsymbol{u}\,dz = f\boldsymbol{k}\times(\boldsymbol{u}H). \tag{2.20}$$

The pressure is defined as $p = p_a + \rho_0 g(\eta + z)$ where p_a is the atmospheric pressure exerted on the ocean surface and g is gravity. Pressure exerted on the bottom topography will be a common term from here on and is defined as $p_b = p_a + \rho_0 g(\eta + h) = p_a + \rho_0 gH$. Following the assumptions made by Hughes and De Cuevas [2001] atmospheric pressure is taken to be negligible and $p_a \simeq 0$. This assumption simplifies the pressure terms to $p = \rho_0 g(\eta + z)$ and $p_b = \rho_0 gH$. With this, the depth integrated pressure term is expanded through the use

of the Leibniz integral rule,

$$\begin{aligned}
-\int_{-h}^{\eta} \boldsymbol{\nabla} p \, dz =& -\boldsymbol{\nabla} \int_{-h}^{\eta} p \, dz + p_b \boldsymbol{\nabla} h + p_a \boldsymbol{\nabla} \eta \\
=& -\boldsymbol{\nabla} \int_{-h}^{\eta} p \, dz + p_b \boldsymbol{\nabla} h \\
=& -\rho_0 g \boldsymbol{\nabla} \int_{-h}^{\eta} (\eta + z) \, dz + p_b \boldsymbol{\nabla} h \\
=& -\rho_0 g \boldsymbol{\nabla} \left(\eta^2 + \eta h - \frac{\eta^2}{2} + \frac{h^2}{2} \right) + p_b \boldsymbol{\nabla} h \\
=& -\rho_0 g \boldsymbol{\nabla} \left(\frac{H^2}{2} \right) + p_b \boldsymbol{\nabla} h \\
=& -\frac{1}{2} \boldsymbol{\nabla} (H p_b) + p_b \boldsymbol{\nabla} h.
\end{aligned} \tag{2.21}$$

The external external stresses exist at the sea surface and seabed only. As a result, the depth-integrated external forcing is evaluated as:

$$\int_{-h}^{\eta} \frac{\partial \boldsymbol{\tau}}{\partial z} \, dz = \boldsymbol{\tau}_w - \boldsymbol{\tau}_b, \tag{2.22}$$

where $\boldsymbol{\tau}_w$ is the surface wind forcing and $\boldsymbol{\tau}_b$ is the bottom drag. Evaluating the final term on the right-hand side of (2.4) requires further relations to be outlined. The zonal and meridional components of the depth-integrated Laplacian can be expanded in the following way,

$$\begin{aligned}
\int_{-h}^{\eta} \frac{\partial^2 u}{\partial x^2} \, dz =& \frac{\partial}{\partial x} \left(\int_{-h}^{\eta} \frac{\partial u}{\partial x} \, dz \right) - \frac{\partial u}{\partial x} \frac{\partial \eta}{\partial x} - \frac{\partial u}{\partial x} \frac{\partial h}{\partial x} \\
=& \frac{\partial^2 (uH)}{\partial x^2} - \frac{\partial u}{\partial x} \frac{\partial H}{\partial x} - \frac{\partial}{\partial x} \left(u \frac{\partial H}{\partial x} \right) \\
=& \frac{\partial^2 (uH)}{\partial x^2} - 2 \frac{\partial u}{\partial x} \frac{\partial H}{\partial x} - u \frac{\partial^2 H}{\partial x^2},
\end{aligned} \tag{2.23}$$

$$\begin{aligned}
\int_{-h}^{\eta} \frac{\partial^2 v}{\partial y^2} \, dz =& \frac{\partial}{\partial y} \left(\int_{-h}^{\eta} \frac{\partial v}{\partial y} \, dz \right) - \frac{\partial v}{\partial y} \frac{\partial \eta}{\partial y} - \frac{\partial v}{\partial y} \frac{\partial h}{\partial y} \\
=& \frac{\partial^2 (vH)}{\partial y^2} - \frac{\partial v}{\partial y} \frac{\partial H}{\partial y} - \frac{\partial}{\partial y} \left(v \frac{\partial H}{\partial y} \right) \\
=& \frac{\partial^2 (vH)}{\partial y^2} - 2 \frac{\partial v}{\partial y} \frac{\partial H}{\partial y} - v \frac{\partial^2 H}{\partial y^2}.
\end{aligned} \tag{2.24}$$

There also exists a vector identity, which for any scalar, λ, and vector, $\boldsymbol{A}$, combination:

$$\lambda \boldsymbol{\nabla}^2 \boldsymbol{A} = \boldsymbol{\nabla}^2(\lambda \boldsymbol{A}) - 2\boldsymbol{\nabla}\boldsymbol{A} \cdot \boldsymbol{\nabla}\lambda - \boldsymbol{A} \cdot \boldsymbol{\nabla}^2\lambda. \tag{2.25}$$

By (2.23), (2.24) and the vector identity (2.25) the depth-integrated Laplacian in the viscosity term is evaluated as

$$\begin{aligned}
\int_{-h}^{\eta} \boldsymbol{\nabla}^2 \boldsymbol{u}\, dz =& \left(\int_{-h}^{\eta} \frac{\partial^2 u}{\partial x^2}\, dz, \int_{-h}^{\eta} \frac{\partial^2 v}{\partial y^2}\, dz \right) \\
=& \left(\frac{\partial^2 (uH)}{\partial x^2} - 2\frac{\partial u}{\partial x}\frac{\partial H}{\partial x} - u\frac{\partial^2 H}{\partial x^2}, \frac{\partial^2 (vH)}{\partial y^2} - 2\frac{\partial v}{\partial y}\frac{\partial H}{\partial y} - v\frac{\partial^2 H}{\partial y^2} \right) \\
=& \boldsymbol{\nabla}^2(H\boldsymbol{u}) - 2\boldsymbol{\nabla}\boldsymbol{u} \cdot \boldsymbol{\nabla} H - \boldsymbol{u} \cdot \boldsymbol{\nabla}^2 H \\
=& H\boldsymbol{\nabla}^2 \boldsymbol{u}.
\end{aligned} \tag{2.26}$$

Leaving the depth-integrated viscosity term as:

$$\mu \int_{-h}^{\eta} \boldsymbol{\nabla}^2 \boldsymbol{u}\, dz = \mu H \boldsymbol{\nabla}^2 \boldsymbol{u}. \tag{2.27}$$

Finally, substituting (2.19), (2.20), (2.21), (2.22) and (2.27) into (2.4) gives the barotropic momentum equation,

$$\rho_0 \left(H \frac{D\boldsymbol{u}}{Dt} + f\boldsymbol{k} \times (H\boldsymbol{u}) \right) = -\frac{1}{2}\boldsymbol{\nabla}(H p_b) + p_b \boldsymbol{\nabla} h + \boldsymbol{\tau}_w - \boldsymbol{\tau}_b + \mu H \boldsymbol{\nabla}^2 \boldsymbol{u} \tag{2.28}$$

and the divergence equation,

$$\frac{\partial H}{\partial t} + \boldsymbol{\nabla} \cdot (H\boldsymbol{u}) = 0. \tag{2.29}$$

2.1.2 Barotropic Vorticity Equation

The barotropic vorticity equation is found by taking the vertical component of the curl of (2.28). The curl of a gradient is zero, thus,

$$\boldsymbol{k} \cdot \boldsymbol{\nabla} \times (\boldsymbol{\nabla}(H p_b)) = 0. \tag{2.30}$$

Additionally,

$$\begin{aligned} \boldsymbol{k}\cdot\boldsymbol{\nabla}\times(p_b\boldsymbol{\nabla}h) &= \boldsymbol{k}\cdot\boldsymbol{\nabla}p_b\times\boldsymbol{\nabla}h, && (2.31)\\ \boldsymbol{k}\cdot\boldsymbol{\nabla}\times(H\boldsymbol{\nabla}^2\boldsymbol{u}) &= \boldsymbol{k}\cdot\boldsymbol{\nabla}H\times\boldsymbol{\nabla}^2\boldsymbol{u}+H\boldsymbol{k}\cdot\boldsymbol{\nabla}\times(\boldsymbol{\nabla}^2\boldsymbol{u}) && (2.32)\\ &= \boldsymbol{k}\cdot\boldsymbol{\nabla}H\times\boldsymbol{\nabla}^2\boldsymbol{u}+H\boldsymbol{\nabla}^2\zeta. \end{aligned}$$

where $\zeta = dv/dx - du/dy$ is the relative vorticity. It is assumed here that $\boldsymbol{k}\cdot\boldsymbol{\nabla}H\times\boldsymbol{\nabla}^2\boldsymbol{u}$ is negligible in comparison to $H\boldsymbol{\nabla}^2\zeta$. Model output in this study is of the full term given by (2.32), however notation hereafter is simplified to

$$\boldsymbol{k}\cdot\boldsymbol{\nabla}\times(H\boldsymbol{\nabla}^2\boldsymbol{u}) = H\boldsymbol{\nabla}^2\zeta. \tag{2.33}$$

Therefore, taking the vertical component of curl of (2.28) gives:

$$\begin{aligned} \rho_0\boldsymbol{k}\cdot\boldsymbol{\nabla}\times\left(H\frac{D\boldsymbol{u}}{Dt}+f\boldsymbol{k}\times(H\boldsymbol{u})\right) = \\ \boldsymbol{k}\cdot\boldsymbol{\nabla}p_b\times\boldsymbol{\nabla}h \;+\; \boldsymbol{k}\cdot\boldsymbol{\nabla}\times(\boldsymbol{\tau}_w-\boldsymbol{\tau}_b)+\mu H\boldsymbol{\nabla}^2\zeta. \end{aligned} \tag{2.34}$$

Given $\boldsymbol{A}$ and $\boldsymbol{B}$ are arbitrary vectors, using the vector identity,

$$\boldsymbol{\nabla}\times(\boldsymbol{A}\times\boldsymbol{B}) = \boldsymbol{A}(\boldsymbol{\nabla}\cdot\boldsymbol{B})+\boldsymbol{B}\cdot\boldsymbol{\nabla}\boldsymbol{A}-\boldsymbol{B}(\boldsymbol{\nabla}\cdot\boldsymbol{A})-\boldsymbol{A}\cdot\boldsymbol{\nabla}\boldsymbol{B}, \tag{2.35}$$

the second curl term on the left hand side of (2.34) can be expanded as follows:

$$\begin{aligned} \boldsymbol{k}\cdot\boldsymbol{\nabla}\times\left(f\boldsymbol{k}\times(H\boldsymbol{u})\right) =& \boldsymbol{k}\cdot\left(f\boldsymbol{k}(\boldsymbol{\nabla}\cdot(H\boldsymbol{u}))+H\boldsymbol{u}\cdot\boldsymbol{\nabla}f\boldsymbol{k}-H\boldsymbol{u}(\boldsymbol{\nabla}\cdot f\boldsymbol{k})-f\boldsymbol{k}\cdot\boldsymbol{\nabla}(H\boldsymbol{u})\right)\\ =& \boldsymbol{k}\cdot\left(f\boldsymbol{k}(\boldsymbol{\nabla}\cdot(H\boldsymbol{u}))+H\boldsymbol{u}\cdot\boldsymbol{\nabla}f\boldsymbol{k}\right)\\ =& f(\boldsymbol{\nabla}\cdot(H\boldsymbol{u}))+H\boldsymbol{u}\cdot\boldsymbol{\nabla}f, \end{aligned} \tag{2.36}$$

where $H\boldsymbol{u}(\boldsymbol{\nabla}\cdot f\boldsymbol{k}) = 0$ and $f\boldsymbol{k}\cdot\boldsymbol{\nabla}(H\boldsymbol{u}) = 0$ due to $\partial f/\partial z = 0$ and depth-independent velocities respectively. Substitution of the continuity equation (2.13) into (2.36) leaves the

simplified form,

$$\begin{aligned}\boldsymbol{k}\cdot\boldsymbol{\nabla}\times\left(f\boldsymbol{k}\times(H\boldsymbol{u})\right) &= f(\boldsymbol{\nabla}\cdot(H\boldsymbol{u}))+H\boldsymbol{u}\cdot\boldsymbol{\nabla}f\\ &= -f\frac{\partial H}{\partial t}+H\boldsymbol{u}\cdot\boldsymbol{\nabla}f\\ &= -f\frac{\partial H}{\partial t}+H\beta v,\end{aligned} \tag{2.37}$$

where the Cartesian coordinate system dictates that $\beta = \partial f/\partial y$. Finally, this form can be substituted back into (2.34) to give the barotropic vorticity equation:

$$\begin{aligned}\rho_0\left(\boldsymbol{k}\cdot\boldsymbol{\nabla}\times\left(H\frac{D\boldsymbol{u}}{Dt}\right)-f\frac{\partial H}{\partial t}+H\beta v\right) =\\ \boldsymbol{k}\cdot\boldsymbol{\nabla}p_b\times\boldsymbol{\nabla}h\;+\;\boldsymbol{k}\cdot\boldsymbol{\nabla}\times(\boldsymbol{\tau}_w-\boldsymbol{\tau}_b)+\mu H\boldsymbol{\nabla}^2\zeta.\end{aligned} \tag{2.38}$$

2.1.3 Time-Averaging

An instantaneous view of a dynamical system is not necessarily representative of the key relationships that arise. In a system which is highly oscillatory in time, a snapshot could provide a view of a state which sits as an outlier in comparison to the rest of the dataset. For this reason, once the system has reached statistical equilibrium, the interest is in the mean state, so the time-mean equations are required. For a linear function, evaluating the time-mean is straight-forward, the time-mean of the function is equal to the function of time-mean variables, i.e.,

$$\overline{f(x)} = f(\overline{x}). \tag{2.39}$$

For a non-linear term however this does not necessarily hold. For any two terms, a and b, which co-vary,

$$\overline{ab} \neq \overline{a}\,\overline{b}. \tag{2.40}$$

Most terms in the momentum equation (2.1) are linear, however, the Lagrangian derivative has a non-linear component, the inertial term, $\boldsymbol{u}\cdot\boldsymbol{\nabla}\boldsymbol{u}$. The time-mean of a non-linear term requires a Reynolds decomposition to be calculated. The Reynolds decomposition is defined as:

$$\boldsymbol{u} = \overline{\boldsymbol{u}} + \boldsymbol{u}', \tag{2.41}$$

where the over bars represent the time-mean and dashes represent the deviation from the time-mean. Taking the Reynolds decomposition of the inertial term gives

$$\boldsymbol{u}\cdot\boldsymbol{\nabla u}=\overline{\boldsymbol{u}}\cdot\boldsymbol{\nabla}\overline{\boldsymbol{u}}+\boldsymbol{u'}\cdot\boldsymbol{\nabla u'}+\overline{\boldsymbol{u}}\cdot\boldsymbol{\nabla u'}+\boldsymbol{u'}\cdot\boldsymbol{\nabla}\overline{\boldsymbol{u}}. \tag{2.42}$$

It holds that $\overline{a'}=0$ and $\overline{a\bar{b}}=\bar{a}\bar{b}$. Thus, taking the time-mean of the (2.42) gives

$$\overline{\boldsymbol{u}\cdot\boldsymbol{\nabla u}}=\overline{\boldsymbol{u}}\cdot\boldsymbol{\nabla}\overline{\boldsymbol{u}}+\overline{\boldsymbol{u'}\cdot\boldsymbol{\nabla u'}}. \tag{2.43}$$

The $\overline{\boldsymbol{u'}\cdot\boldsymbol{\nabla u'}}$ term is named the Reynolds stress and it arises due to turbulent motions in the fluid.

2.1.4 Depth Integrated Time-Averaging

The term $\boldsymbol{u}\cdot\boldsymbol{\nabla u}$ is the only term in (2.1) that is non-linear and produces extra terms when taking the time-mean. The depth integrated form (2.28), however, is complicated by the time-dependent water column thickness, $H=h+\eta$. η is variable in time so it produces deviations from the mean. This results in further second and third order correlation terms arising when a time-mean is taken of (2.28). Following the Reynolds decomposition above for these extra correlation terms, the time-mean of (2.28) is

$$\rho_0\left(\overline{H\frac{D\boldsymbol{u}}{Dt}}+\overline{f\boldsymbol{k}\times(H\boldsymbol{u})}\right)=\frac{1}{2}\overline{\boldsymbol{\nabla}(Hp_b)}+\overline{p}_b\boldsymbol{\nabla}h+\overline{\boldsymbol{\tau}}_w-\overline{\boldsymbol{\tau}}_b+\overline{H\boldsymbol{\nabla}^2\boldsymbol{u}}, \tag{2.44}$$

where

$$\begin{aligned}\overline{H\frac{D\boldsymbol{u}}{Dt}}&=\overline{H'\frac{\partial\boldsymbol{u'}}{\partial t}} \\ &\quad+\overline{H}\overline{\boldsymbol{u}}\cdot\boldsymbol{\nabla}\overline{\boldsymbol{u}}+\overline{H}\overline{\boldsymbol{u'}\cdot\boldsymbol{\nabla u'}}+\overline{\boldsymbol{u}}\overline{H'\cdot\boldsymbol{\nabla u'}}+\overline{H'\boldsymbol{u'}}\cdot\boldsymbol{\nabla}\overline{\boldsymbol{u}}+\overline{H'\boldsymbol{u'}\cdot\boldsymbol{\nabla u'}},\end{aligned} \tag{2.45}$$

$$\overline{f\boldsymbol{k}\times(H\boldsymbol{u})}=f\boldsymbol{k}\times(\overline{H}\overline{\boldsymbol{u}})+f\boldsymbol{k}\times(\overline{H'\boldsymbol{u'}}), \tag{2.46}$$

$$\overline{\boldsymbol{\nabla}Hp_b}=\boldsymbol{\nabla}\overline{H}\overline{p}_b++\overline{H'\boldsymbol{\nabla}p'_b}, \tag{2.47}$$

$$\overline{H\boldsymbol{\nabla}^2\boldsymbol{u}}=\overline{H}\boldsymbol{\nabla}^2\overline{\boldsymbol{u}}+\overline{H'\boldsymbol{\nabla}^2\boldsymbol{u'}}. \tag{2.48}$$

The complexity of this relation makes it complicated to diagnose from the model outputs. In an effort to simplify the problem a consideration is taken to reduce this set of equations.

The H' term in the above relation arises due to turbulent motions and is often small in comparison to $\overline{H}$. In a highly turbulent system H' is large enough to make significant contributions to the budget. However, there is only a contribution from terms that include H' if there is a co-variance with each part within the term. The level of co-variance in each H' term of (2.45)–(2.48) that occurs in a turbulent system is unknown. Although interesting to investigate, this is noted but not explored in this study. Despite implementing turbu-

lent simulations in this study, it will be assumed that the covariance of H' with other terms remains significantly small and solely the $\overline{H}$ component of the equations will be explored. Under this condition (2.45)-(2.48) are significantly simplified and (2.44) reduces to:

$$\rho_0\left(\overline{H}\overline{\boldsymbol{u}}\cdot\boldsymbol{\nabla}\overline{\boldsymbol{u}}+\overline{H\boldsymbol{u}'\cdot\boldsymbol{\nabla}\boldsymbol{u}'}+f\boldsymbol{k}\times(\overline{H}\overline{\boldsymbol{u}})\right)=\frac{1}{2}\boldsymbol{\nabla}(\overline{H}\overline{p}_b)+\overline{p}_b\boldsymbol{\nabla}h+\overline{\boldsymbol{\tau}}_w-\overline{\boldsymbol{\tau}}_b+\overline{H}\boldsymbol{\nabla}^2\overline{\boldsymbol{u}}. \quad (2.49)$$

All results of this research have been simplified in this manner.

2.1.5 Steady Barotropic Vorticity Equation

The time-averaged barotropic vorticity equation is evaluated under the same assumptions as above. Using the tools relations outlined in Section 2.1.2, the time-averaged barotropic vorticity equation is found taking the curl of (2.49):

$$\begin{aligned}\rho_0\left(\boldsymbol{k}\cdot\boldsymbol{\nabla}\times\left(\overline{H}\overline{\boldsymbol{u}}\cdot\boldsymbol{\nabla}\overline{\boldsymbol{u}}+\overline{H\boldsymbol{u}'\cdot\boldsymbol{\nabla}\boldsymbol{u}'}\right)+f\frac{\partial\overline{H}}{\partial t}+\overline{H}\beta\overline{v}\right)=\\ \boldsymbol{k}\cdot\boldsymbol{\nabla}\overline{p}_b\times\boldsymbol{\nabla}h+\boldsymbol{k}\cdot\boldsymbol{\nabla}\times(\overline{\boldsymbol{\tau}}_w-\overline{\boldsymbol{\tau}}_b)+\mu\overline{H}\boldsymbol{\nabla}^2\overline{\zeta}.\end{aligned} \quad (2.50)$$

Here, the system is taken to be statistically steady. Thus, the unsteady term, $\partial\overline{H}/\partial t$, is assumed to be zero everywhere. This means (2.50) can be simplified to

$$\begin{aligned}\rho_0\left(\boldsymbol{k}\cdot\boldsymbol{\nabla}\times\left(\overline{H}\overline{\boldsymbol{u}}\cdot\boldsymbol{\nabla}\overline{\boldsymbol{u}}+\overline{H\boldsymbol{u}'\cdot\boldsymbol{\nabla}\boldsymbol{u}'}\right)+\overline{H}\beta\overline{v}\right)=\\ \boldsymbol{k}\cdot\boldsymbol{\nabla}\overline{p}_b\times\boldsymbol{\nabla}h+\boldsymbol{k}\cdot\boldsymbol{\nabla}\times(\overline{\boldsymbol{\tau}}_w-\overline{\boldsymbol{\tau}}_b)+\mu\overline{H}\boldsymbol{\nabla}^2\overline{\zeta}.\end{aligned} \quad (2.51)$$

2.1.6 Eddy Dynamics

The dynamical effect of eddies on the time-mean flow occurs through the inertial term, $\boldsymbol{u}\cdot\boldsymbol{\nabla}\boldsymbol{u}$. Following Hughes and Ash [2001] these eddy forces can be analysed in a time-mean sense by using a vector identity to split the inertial term into two components,

$$\boldsymbol{u}\cdot\boldsymbol{\nabla}\boldsymbol{u}=\zeta\boldsymbol{k}\times\boldsymbol{u}+\frac{1}{2}\boldsymbol{\nabla}(\boldsymbol{u}\cdot\boldsymbol{u}). \quad (2.52)$$

This is the vector invariant form of the inertial term, which is not only useful for eddy diagnosis but it is also invariant under coordinate transformations. Applying the Reynolds decomposition to (2.52) and taking the time-mean gives,

$$\overline{\boldsymbol{u}}\cdot\boldsymbol{\nabla}\overline{\boldsymbol{u}}+\overline{\boldsymbol{u}'\cdot\boldsymbol{\nabla}\boldsymbol{u}'}=\overline{\zeta}\boldsymbol{k}\times\overline{\boldsymbol{u}}+\frac{1}{2}\boldsymbol{\nabla}(\overline{\boldsymbol{u}}\cdot\overline{\boldsymbol{u}})+\overline{\zeta'\boldsymbol{k}\times\boldsymbol{u}'}+\frac{1}{2}\boldsymbol{\nabla}(\overline{\boldsymbol{u}'\cdot\boldsymbol{u}'}). \quad (2.53)$$

The importance of this form is highlighted in Hughes and Ash [2001] and further discussed by Thompson and Richards [2011]. The rotational Reynolds stress term, $\overline{\zeta' \boldsymbol{k} \times \boldsymbol{u}'}$, provides the forcing of mean flow by eddies in the system. This term may be re-formed as $\overline{\zeta' \boldsymbol{k} \times \boldsymbol{u}'} = \boldsymbol{k} \times \overline{\zeta' \boldsymbol{u}'}$, where $\overline{\zeta' \boldsymbol{u}'}$ is commonly termed the eddy vorticity flux.

The vorticity which eddies contribute to the system is diagnosed in the barotropic vorticity equation with use of the decomposition in (2.53). The irrotational terms of equation (2.53) are eliminated by taking the curl,

$$\boldsymbol{k} \cdot \boldsymbol{\nabla} \times \left(\frac{1}{2} \boldsymbol{\nabla} (\overline{\boldsymbol{u}} \cdot \overline{\boldsymbol{u}}) + \frac{1}{2} \boldsymbol{\nabla} (\overline{\boldsymbol{u}' \cdot \boldsymbol{u}'}) \right) = 0. \tag{2.54}$$

This gives the relation

$$\begin{aligned} \boldsymbol{k} \cdot \boldsymbol{\nabla} \times \left(\overline{\boldsymbol{u}} \cdot \boldsymbol{\nabla} \overline{\boldsymbol{u}} + \overline{\boldsymbol{u}' \cdot \boldsymbol{\nabla} \boldsymbol{u}'} \right) &= \boldsymbol{k} \cdot \boldsymbol{\nabla} \times \left(\overline{\zeta} \boldsymbol{k} \times \overline{\boldsymbol{u}} + \overline{\zeta' \boldsymbol{k} \times \boldsymbol{u}'} \right) \\ &= \boldsymbol{\nabla} \cdot (\overline{\boldsymbol{u}} \overline{\zeta}) + \boldsymbol{\nabla} \cdot (\overline{\boldsymbol{u}' \zeta'}). \end{aligned} \tag{2.55}$$

Using (2.55), the time-averaged Lagrangian derivative of the barotropic vorticity equation, (2.38), is expanded as:

$$\begin{aligned} &\boldsymbol{k} \cdot \boldsymbol{\nabla} \times (\overline{H} \overline{\boldsymbol{u}} \cdot \boldsymbol{\nabla} \overline{\boldsymbol{u}} + \overline{H} \overline{\boldsymbol{u}' \cdot \boldsymbol{\nabla} \boldsymbol{u}'}) \\ =&\overline{H} \left(\boldsymbol{k} \cdot \boldsymbol{\nabla} \times \left(\overline{\boldsymbol{u}} \cdot \boldsymbol{\nabla} \overline{\boldsymbol{u}} + \overline{\boldsymbol{u}' \cdot \boldsymbol{\nabla} \boldsymbol{u}'} \right) \right) + \boldsymbol{k} \cdot \boldsymbol{\nabla} \overline{H} \times \left(\overline{\boldsymbol{u}} \cdot \boldsymbol{\nabla} \overline{\boldsymbol{u}} + \overline{\boldsymbol{u}' \cdot \boldsymbol{\nabla} \boldsymbol{u}'} \right) \\ =&\overline{H} \left(\boldsymbol{\nabla} \cdot (\overline{\boldsymbol{u}} \overline{\zeta}) + \boldsymbol{\nabla} \cdot (\overline{\boldsymbol{u}' \zeta'}) \right) + \boldsymbol{k} \cdot \boldsymbol{\nabla} \overline{H} \times \left(\overline{\boldsymbol{u}} \cdot \boldsymbol{\nabla} \overline{\boldsymbol{u}} + \overline{\boldsymbol{u}' \cdot \boldsymbol{\nabla} \boldsymbol{u}'} \right). \end{aligned} \tag{2.56}$$

The primed term, $\boldsymbol{\nabla} \cdot (\overline{\boldsymbol{u}' \zeta'})$, is the divergence of the eddy vorticity flux, where a convergence and divergence causes an addition of positive and negative vorticity to the system respectively. This term is derived by Williams et al. [2007] to show the eddy forcing of jets in the ocean and atmosphere. The terms $\boldsymbol{k} \cdot \boldsymbol{\nabla} \times (\overline{H} \overline{\boldsymbol{u}} \cdot \boldsymbol{\nabla} \overline{\boldsymbol{u}})$ and $\boldsymbol{k} \cdot \boldsymbol{\nabla} \times (\overline{H} \overline{\boldsymbol{u}' \cdot \boldsymbol{\nabla} \boldsymbol{u}'})$ are independently diagnosed in the model output shown in the subsequent chapters. In the absence of variable topography, these terms simplify to:

$$\boldsymbol{k} \cdot \boldsymbol{\nabla} \times (\overline{H} \overline{\boldsymbol{u}} \cdot \boldsymbol{\nabla} \overline{\boldsymbol{u}}) = \overline{H} \boldsymbol{\nabla} \cdot (\overline{\boldsymbol{u}} \overline{\zeta}) \tag{2.57}$$

$$\boldsymbol{k} \cdot \boldsymbol{\nabla} \times (\overline{H} \overline{\boldsymbol{u}' \cdot \boldsymbol{\nabla} \boldsymbol{u}'}) = \overline{H} \boldsymbol{\nabla} \cdot (\overline{\boldsymbol{u}' \zeta'}), \tag{2.58}$$

showing that $\boldsymbol{k} \cdot \boldsymbol{\nabla} \times (\overline{H} \overline{\boldsymbol{u}' \cdot \boldsymbol{\nabla} \boldsymbol{u}'})$ represents the vorticity contribution from eddies in the flat bottom regions of the results that follow.

2.1.7 Form Stress Equation

As outlined in Chapter 1, form stress is a sink of momentum which arises from pressure acting on topography due to the fluid which lies above it. The form stress term can be derived from the depth-integrated momentum equation (2.28). Similar to Section 2.1.6, a vector identity can be applied to the time-mean, depth-integrated Lagrangian derivative:

$$\begin{aligned}\overline{H\frac{D\boldsymbol{u}}{Dt}} &= \overline{H}\left(\overline{\boldsymbol{u}}\cdot\boldsymbol{\nabla}\overline{\boldsymbol{u}} + \overline{\boldsymbol{u}'\cdot\boldsymbol{\nabla}\boldsymbol{u}'}\right) \\ &= \overline{H}\left(\overline{\zeta}\boldsymbol{k}\times\overline{\boldsymbol{u}} + \frac{1}{2}\boldsymbol{\nabla}(\overline{\boldsymbol{u}}\cdot\overline{\boldsymbol{u}}) + \overline{\zeta'\boldsymbol{k}\times\boldsymbol{u}'} + \frac{1}{2}\boldsymbol{\nabla}(\overline{\boldsymbol{u}'\cdot\boldsymbol{u}'})\right).\end{aligned} \tag{2.59}$$

Substituting (2.59) into equation (2.49) and taking $\overline{H}$ outside of the Coriolis term gives

$$\begin{aligned}\rho_0\overline{H}\left(\overline{\zeta}\boldsymbol{k}\times\overline{\boldsymbol{u}} + \frac{1}{2}\boldsymbol{\nabla}(\overline{\boldsymbol{u}}\cdot\overline{\boldsymbol{u}}) + \overline{\zeta'\boldsymbol{k}\times\boldsymbol{u}'} + \frac{1}{2}\boldsymbol{\nabla}(\overline{\boldsymbol{u}'\cdot\boldsymbol{u}'}) + f\boldsymbol{k}\times\overline{\boldsymbol{u}}\right) = \\ \frac{1}{2}\boldsymbol{\nabla}(\overline{H}\overline{p}_b) + \overline{p}_b\boldsymbol{\nabla}h + \overline{\boldsymbol{\tau}}_w - \overline{\boldsymbol{\tau}}_b + \overline{H}\boldsymbol{\nabla}^2\overline{\boldsymbol{u}}.\end{aligned} \tag{2.60}$$

By grouping the first and last terms on the left-hand side of (2.60),

$$\begin{aligned}\rho_0\overline{H}\left((f+\overline{\zeta})\boldsymbol{k}\times\overline{\boldsymbol{u}} + \frac{1}{2}\boldsymbol{\nabla}(\overline{\boldsymbol{u}}\cdot\overline{\boldsymbol{u}}) + \overline{\zeta'\boldsymbol{k}\times\boldsymbol{u}'} + \frac{1}{2}\boldsymbol{\nabla}(\overline{\boldsymbol{u}'\cdot\boldsymbol{u}'})\right) = \\ \frac{1}{2}\boldsymbol{\nabla}(\overline{H}\overline{p}_b) + \overline{p}_b\boldsymbol{\nabla}h + \overline{\boldsymbol{\tau}}_w - \overline{\boldsymbol{\tau}}_b + \overline{H}\boldsymbol{\nabla}^2\overline{\boldsymbol{u}}.\end{aligned} \tag{2.61}$$

The zonal component of (2.61) is

$$\begin{aligned}\rho_0\overline{H}\left((f+\overline{\zeta})\overline{v} + \overline{\zeta'v'} + \frac{1}{2}\frac{\partial(\overline{u}^2)+(\overline{v}^2)}{\partial x} + \frac{1}{2}\frac{\partial(u'^2+v'^2)}{\partial x}\right) = \\ -\frac{1}{2}\frac{\partial(\overline{H}\overline{p}_b)}{\partial x} + \overline{p}_b\frac{\partial h}{\partial x} + \overline{\tau}^x_w - \overline{\tau}^x_b + \mu\overline{H}\boldsymbol{\nabla}^2\overline{u}.\end{aligned} \tag{2.62}$$

The Southern Ocean is often described as a zonally periodic channel. In this setting, due to continuity, the zonal integral of fvH is zero. The same is true for the the first term on the right hand side [Olbers, 1998, Masich et al., 2015]. This means that the zonal integral of (2.62) in a zonally periodic channel is

$$\begin{aligned}\rho_0\left(\oint \overline{H}(\overline{\zeta}\overline{v} + \overline{\zeta'v'})\,dx + \oint \frac{\overline{H}}{2}\frac{\partial(\overline{u}^2+\overline{v}^2)}{\partial x}\,dx + \oint \frac{\overline{H}}{2}\frac{\partial(u'^2+v'^2)}{\partial x}\,dx\right) = \\ \oint \overline{p}_b\frac{\partial h}{\partial x}\,dx + \oint \overline{\tau}^x_w\,dx - \oint \overline{\tau}^x_b\,dx + \mu\oint \overline{H}\boldsymbol{\nabla}^2\overline{u}\,dx,\end{aligned} \tag{2.63}$$

where $\oint$ is used to represent the periodicity of the domain. This equation is used for diagnosing form stress where $\oint \overline{p}_b(dh/dx)\,dx$ is the form stress term. The form stress term becomes important in Chapter 5 where an investigation is made into the geometrical effects of topography on mean net zonal flow.

2.1.8 Potential Vorticity

The potential vorticity equation can be derived from the vector invariant momentum equation:

$$\rho_0\left(\frac{\partial \boldsymbol{u}}{\partial t} + (\zeta + f)\boldsymbol{k} \times \boldsymbol{u}\right) = -\boldsymbol{\nabla}\left(p + \frac{\rho_0}{2}(\boldsymbol{u} \cdot \boldsymbol{u})\right) + \frac{\partial \boldsymbol{\tau}}{\partial z} + \mu \boldsymbol{\nabla}^2 \boldsymbol{u}, \tag{2.64}$$

which is equivalent to (2.1) with a decomposition of the inertial term using relation (2.52). The potential vorticity equation is not used to describe numerical results but is used as an analytical tool to describe the numerical results displayed via the previous equations outlined above. The time-mean is not required for this type of analysis. Taking the curl of equation (2.64) gives

$$\rho_0\left(\frac{\partial \zeta}{\partial t} + \boldsymbol{\nabla} \cdot (\boldsymbol{u}(f + \zeta))\right) = \boldsymbol{\nabla} \times \frac{\partial \boldsymbol{\tau}}{\partial z} + \mu \boldsymbol{\nabla}^2 \zeta, \tag{2.65}$$

where the gradient term on the right hand side of (2.64) has vanished as the curl of a gradient is zero. The second term on the left hand side of (2.65) can then be expanded to give

$$\rho_0\left(\frac{\partial \zeta}{\partial t} + \boldsymbol{u} \cdot \boldsymbol{\nabla}(f + \zeta) + (f + \zeta)(\boldsymbol{\nabla} \cdot \boldsymbol{u})\right) = \boldsymbol{\nabla} \times \frac{\partial \boldsymbol{\tau}}{\partial z} + \mu \boldsymbol{\nabla}^2 \zeta. \tag{2.66}$$

The continuity equation (2.13) can be rearranged as

$$\frac{DH}{Dt} + H(\boldsymbol{\nabla} \cdot \boldsymbol{u}) = 0. \tag{2.67}$$

Rearranging (2.67) gives

$$\boldsymbol{\nabla} \cdot \boldsymbol{u} = -\frac{1}{H}\frac{DH}{Dt}. \tag{2.68}$$

Substituting (2.68) into (2.66) leaves

$$\rho_0\left(\frac{\partial \zeta}{\partial t} + \boldsymbol{u} \cdot \boldsymbol{\nabla}(f + \zeta) - \frac{(f + \zeta)}{H}\frac{DH}{Dt}\right) = \boldsymbol{\nabla} \times \frac{\partial \boldsymbol{\tau}}{\partial z} + \mu \boldsymbol{\nabla}^2 \zeta. \tag{2.69}$$

Since $\partial f/\partial t = 0$ then $D(f+\zeta)/Dt = \partial\zeta/\partial t + \boldsymbol{u}\cdot\boldsymbol{\nabla}(f+\zeta)$. Using this relation it can be written that

$$\rho_0 H\left(\frac{1}{H}\frac{D(f+\zeta)}{Dt} - \frac{(f+\zeta)}{H^2}\frac{DH}{Dt}\right) = \boldsymbol{\nabla}\times\frac{\partial\boldsymbol{\tau}}{\partial z} + \mu\boldsymbol{\nabla}^2\zeta. \tag{2.70}$$

Using the quotient rule it results that

$$\frac{1}{H}\frac{D(f+\zeta)}{Dt} - \frac{(f+\zeta)}{H^2}\frac{DH}{Dt} = \frac{D}{Dt}\left(\frac{f+\zeta}{H}\right). \tag{2.71}$$

Thus, equation (2.70) can be written as

$$\rho_0 H\frac{D}{Dt}\left(\frac{f+\zeta}{H}\right) = \boldsymbol{\nabla}\times\frac{\partial\boldsymbol{\tau}}{\partial z} + \mu\boldsymbol{\nabla}^2\boldsymbol{\zeta}. \tag{2.72}$$

The depth-average of (2.72) is

$$\rho_0 H\frac{D}{Dt}\left(\frac{f+\zeta}{H}\right) = \boldsymbol{\nabla}\times\left(\frac{\boldsymbol{\tau}_w - \boldsymbol{\tau}_b}{H}\right) + \mu\boldsymbol{\nabla}^2\boldsymbol{\zeta}, \tag{2.73}$$

which is commonly termed the Potential Vorticity equation. In the absence of inertial effects this simplifies to

$$\rho_0 H\frac{D}{Dt}\left(\frac{f}{H}\right) = \boldsymbol{\nabla}\times\left(\frac{\boldsymbol{\tau}_w - \boldsymbol{\tau}_b}{H}\right) + \mu\boldsymbol{\nabla}^2\boldsymbol{\zeta}. \tag{2.74}$$

2.2 Model Outline

The majority of the analysis undertaken to investigate dynamics here is done using idealised modeling. The model chosen for this work is the MITgcm, version number c65k. This model was developed to simulate flows of the ocean and atmosphere over multiple scales. The hydrostatic, Cartesian form of this model is employed. The model is applied with one layer in the vertical and no density variations or buoyancy forcing. Topography is implemented through the use of partial cells in the vertical. A non-linear free surface is also applied. Under these conditions the governing equations of the model are equivalent to the shallow-water approximation of (2.1) and (2.2) outlined above. Where the stress term, τ, is written explicitly, these equations are:

$$\rho_0\left(\frac{D\boldsymbol{u}}{Dt} + f\boldsymbol{k}\times\boldsymbol{u}\right) = -\boldsymbol{\nabla}p + \frac{\boldsymbol{\tau}_w}{H} - \rho_0 C_d\frac{|\boldsymbol{u}|\boldsymbol{u}}{H} + \mu\boldsymbol{\nabla}^2\boldsymbol{u}, \tag{2.75}$$

$$\frac{\partial H}{\partial t} + \boldsymbol{\nabla}\cdot(H\boldsymbol{u}) = 0. \tag{2.76}$$

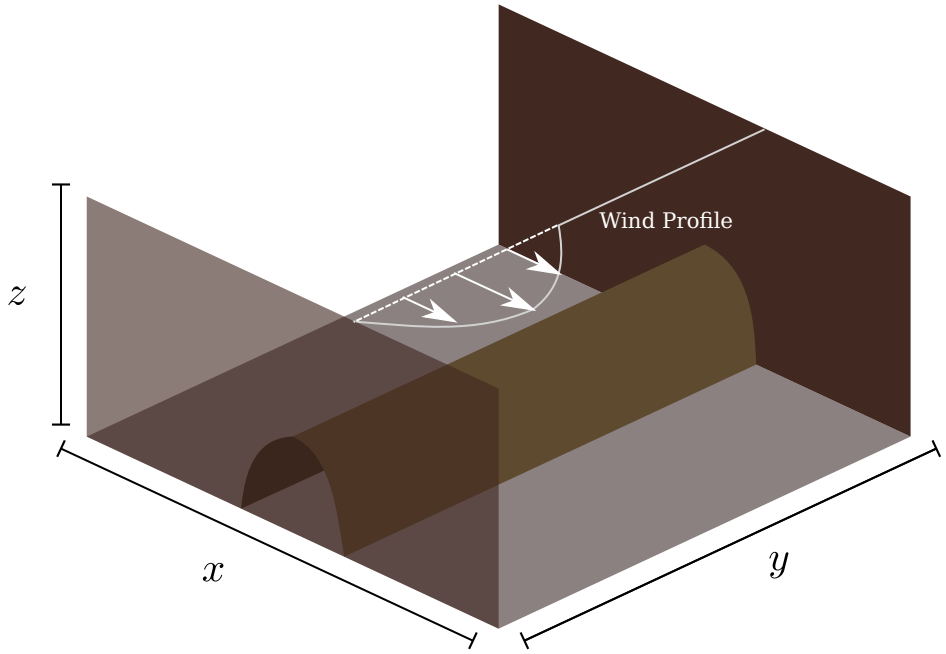

Figure 2.2: Three-dimensional representation of model 24 in Table 3. The white line represents the zonally uniform surface wind forcing. A 2000 metre high meridional ridge lies in the centre of the domain. The domain is zonally periodic and has walls to the north and south.

where C_d is the quadratic bottom drag coefficient. The wind stress, $\boldsymbol{\tau}_w$, is given as a constant forcing and is not calculated relative to sea surface velocities.

In this study various model geometries and forms of forcing are used. This section outlines the base case and the main variants. For reference, a list of all models and their setups is given by Table 3 in the Appendix. An example schematic, representative of model 24, with a meridional ridge, sinusoidal wind stress and a symmetric domain with zonal and meridional lengths of 7200 km is given by Figure 2.2.

2.2.1 Base Model

All simulations are based on a 1-layer channel of 5000 m depth, to which a variety of ridge geometries are added. The initial domain has size: $L_x = 7200$ km and $L_y = 3600$ km, where L_x and L_y represent the length of the domain in the zonal and meridional directions respectively. All models have a zonally uniform surface wind stress. The initial results have

a 'sinusoidal' wind stress which varies in the meridional direction governed by $0.5\tau_0(1 + \cos(2\pi y/L_y))$, where $\tau_0 = 0.144$ Nm^{-2} is the peak wind stress. This wind stress profile is denoted by 'curl' in Table 3.

The base horizontal grid spacing is 12.5 km. At this resolution the grid spacing is sufficiently small to resolve some of the turbulent motions created by shear in velocity profiles. The time-step used for the 12.5 km grid is 3600 seconds. All simulations are run for 10 years. Diagnostics are output for the final year to sample the model data. The output is recorded as snapshots at a frequency of 24 hours. All results are averaged over the snapshots from the final simulation year, where the model is statistically steady. The model is approximated to a tangent-plane, resulting in an approximation of the Coriolis parameter to $f = f_0 + \beta y$ where $f_0 = 2\omega \sin\phi_0$ and $\beta = (2\omega \cos\phi_0)/a$ is the Rossby parameter where $\omega = 7.2921 \cdot 10^{-5}$ s^{-1} is the angular velocity of the Earth, ϕ_0 is a fixed latitude and $a = 6371$ km is the Earth's radius. In all model simulations the southern latitudinal boundary of the model is set to $\phi_0 = -60.85°$ such that $f_0 = -1.27393 \cdot 10^{-4}$ s^{-1} and $\beta = 1.1144 \cdot 10^{-11}$ m^{-1} s^{-1}. The model is of constant density with $\rho_0 = 999.8$ kg m^{-3} as the reference density. The hydrostatic approximation means that $p = p_a + \rho_0 g(\eta + z)$ with $g = 9.8$ m s^{-2}, the gravitational acceleration. All solid lateral boundaries have a free slip condition. The upper boundary is governed by a non-linear free surface, the lower by a quadratic drag with drag coefficient of $C_d = 2.5 \cdot 10^{-3}$ and there is a constant viscosity coefficient of $\mu = 10$ Pa s. As the grid resolution is not of molecular scale the viscosity must act to represent some of the unresolved motions in the system. Table 2 gives a summary of the set-up used for the base simulation.

Model List	
Parameter	Value
Horizontal resolution	12.5 km
Time step	3600 s
Reference density, ρ_0	999.8 kg m^{-3}
Gravity, g	9.8 m s^{-2}
Bottom drag	Quadratic
Bottom drag coefficient, C_d	$2.5 \cdot 10^{-3}$
Horizontal viscosity	Constant
Horizontal viscosity coefficient, μ	10 Pa s
Coriolis parameter, f_0	$-1.27393 \cdot 10^{-4}$ s^{-1}
Rossby parameter, β	$1.1144 \cdot 10^{-11}$ m^{-1}

Table 2: List of the key parameters and settings for the base model.

2.2.2 A Note on Model Variations

The topography, domain size and wind forcing are all varied in the results. A large number of ridge geometries are investigated. The different variants in ridge topography used are introduced with their respective results.

The domain is set with periodic boundary conditions to the east and west, forming a channel. In some simulations a meridional wall is placed along the central longitude of the domain and in cases with topography this wall lies along the peak of the topography. When this wall is implemented, the domain is equivalent to a closed box simulation with walls on all sides and no periodic boundary conditions. Flow can span the periodic boundary but no net zonal flow can exist.

Another variant on the base case is the domain size. Some models have a meridional extent which is doubled to $L_y = 7200$ km. In this case f_0 remains fixed and the resulting meridional extension is equivalent to moving the northern boundary equator-ward whilst keeping the southern boundary fixed in position. The southern half of the domain has the same wind forcing as the base case and the northern half, the area of 'new' domain, has no wind forcing applied.

Wind variations are also made. Some models have a wind stress with zero curl, these are denoted by 'flat' in wind column of Table 3. The curl-free wind stress is set through applying a uniform wind stress on the entire domain with a strength equal to the peak of the base, sinusoidal wind stress, $\tau_0 = 0.144$ N m^{-2}.

2.2.3 Model Grid

A uniform horizontal grid spacing is used. The model uses the 'c' grid defined by Arakawa and Lamb [1977]. The horizontal grid is shown in Figure 2.3. Data on the grid is represented on one of four points consisting of u-velocity, v-velocity, mass and vorticity points (as blue, yellow, pink and black respectively in Figure 2.3). The distances between these points are labeled individually. The definition for each distance in the x and y directions respectively are defined as: Δx_f and Δy_u for the distance between u-velocity points; Δx_v and Δy_f for the distance between v-points; Δx_c and Δy_c for the distance between mass points; Δx_g and Δy_g for the distance between vorticity points. The choice to use a uniform grid here leads these distances to all be of the same length. Despite this, a choice has been made to differentiate between them for consistency with notation used in MITgcm.

Topography in the model is implemented using partial cells [Adcroft et al., 1997]. The treatment of the grid in three dimensions is shown in Figure 2.4. The height of a cell is given by Δr_f and topography is then represented through scaling factors of Δr_f: h_c, h_w

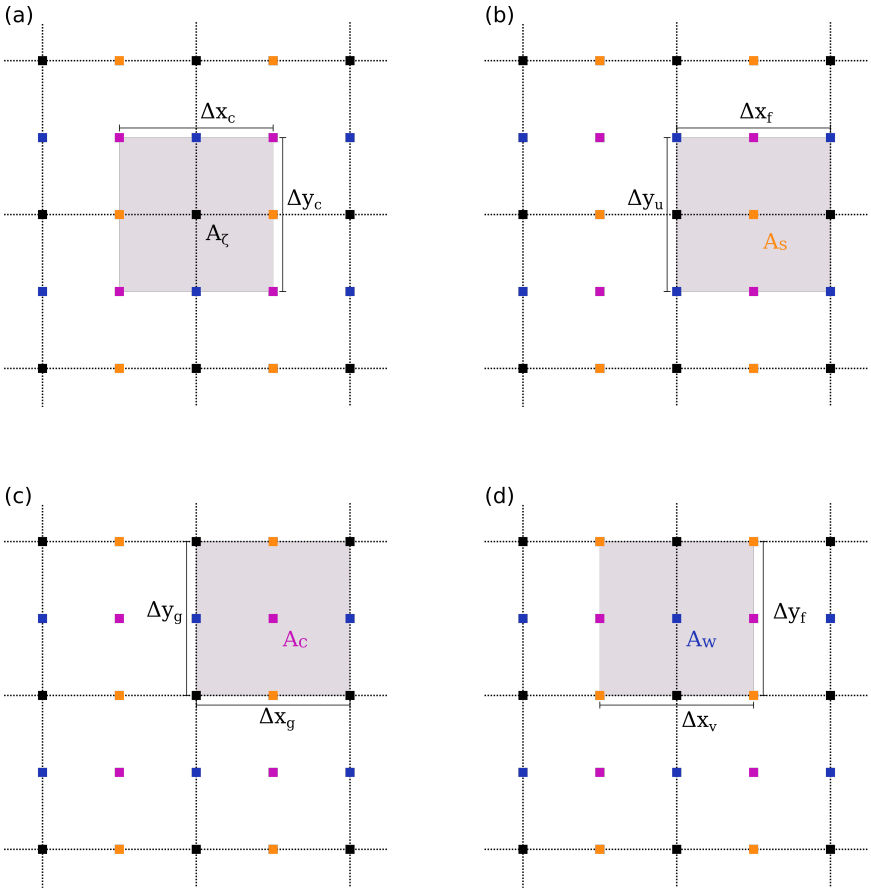

Figure 2.3: A plan view of the four grid horizontal cell definitions in MITgcm. (a) The ζ cell, centred on vorticity points with a zonal length of Δx_c meridional length of Δy_c and area of A_ζ; (b) The v cell, centred on v-velocity points with a zonal length of Δx_f meridional length of Δy_u and area of A_s; (c) The mass cell, centred on mass points with a zonal length of Δx_g meridional length of Δy_g and area of A_c; (d) The u cell centred on u-velocity points with a zonal length of Δx_v meridional length of Δy_f and area of A_w.

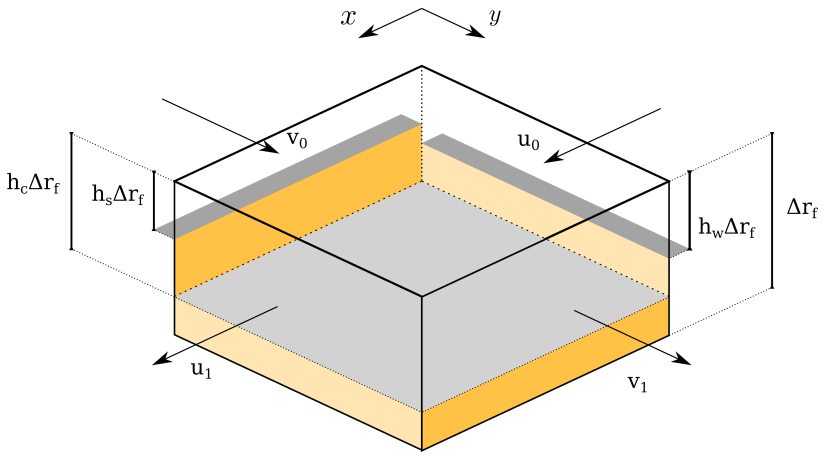

Figure 2.4: A three-dimensional view of a grid cell in MITgcm showing the implementation of topography in the model. u_0 and u_1 are the zonal velocities entering and exiting the cell respectively. v_0 and v_1 are the meridional velocities entering and exiting the cell respectively. Δr_f is the height of the cell in the vertical. h_c, h_w and h_s are then the scale factors defining the vertical proportion of the cell which is defined as ocean, the neighbouring cell to the west and the neighbouring cell to the south respectively.

and h_s. $h_c\Delta r_f$ is the depth of the cell, $h_w\Delta r_f$ is the depth of the cell to the west and $h_s\Delta r_f$ is the depth of the cell to the south. These definitions are useful in defining the flux of fluid in and out of each surface of the grid cell. There is an additional vertical scale factor for a grid cell, h_ζ, defined for the vorticity points. A given $h_\zeta^{i,j}$ term, with i, j representing position in the zonal and meridional directions respectively, is calculated by taking the minimum of neighbouring scale factors: $h_w^{i,j}$, $h_w^{i,j-1}$, $h_s^{i,j}$ and $h_s^{i-1,j}$.

2.3 Model Diagnostic Development

MITgcm has an integrated package for outputting a large number of diagnostics from the model at run-time in specified intervals. This package has some limitations and some further off-line diagnostics are required in order to calculate all terms of the equations derived in Section 2.1.

2.3.1 Reynolds Stress Terms

The sole focus of this work is on statistically steady results. A proportion of the analysis involves using the Reynolds decomposition of the non-linear, inertial term of the momentum equation, described in Section 2.1.3. There is a framework available in the MITgcm diagnostics package to output time-averaged diagnostics. However, this averaging does not take into account the additional Reynolds stress terms generated when time-averaging any non-linear terms. Thus, it is required that these missing terms are calculated in post-processing in order to satisfy the time-mean momentum balance. The interest is in both the irrotational and rotational components of the advection term so a calculation is made of the fully expanded relation given by (2.53). In order to find the terms of (2.53) regular snapshots of its constituents, $\boldsymbol{u}$ and ζ, are required. A calculation is made of the mean for both of these: $\overline{\boldsymbol{u}}$ and $\overline{\zeta}$. The two rotational terms of (2.53), $\overline{\zeta}\boldsymbol{k}\times\overline{\boldsymbol{u}}$ and $\overline{\zeta'\boldsymbol{k}\times\boldsymbol{u}'}$, which arise from the time-averaging, are found using the following discretised numerical scheme:

$$v_{flux}^{i,j} = v^{i,j}\cdot\Delta x_g^{i,j}\cdot h_s^{i,j}, \tag{2.77}$$

$$(v\zeta)^{i,j} = \frac{1}{4\Delta x_c^{i,j}}\left((v_{flux}^{i,j}+v_{flux}^{i-1,j})\frac{\zeta^{i,j}}{h_{i,j}^\zeta}+(v_{flux}^{i,j+1}+v_{flux}^{i-1,j+1})\frac{\zeta^{i,j+1}}{h_{i,j+1}^\zeta}\right), \tag{2.78}$$

$$u_{flux}^{i,j} = u^{i,j}\cdot\Delta y_g^{i,j}\cdot h_w^{i,j}, \tag{2.79}$$

$$-(u\zeta)^{i,j} = \frac{-1}{4\Delta y_c^{i,j}}\left((u_{flux}^{i,j}+u_{flux}^{i,j-1})\frac{\zeta^{i,j}}{h_{i,j}^\zeta}+(u_{flux}^{i+1,j}+u_{flux}^{i+1,j-1})\frac{\zeta^{i+1,j}}{h_{i+1,j}^\zeta}\right), \tag{2.80}$$

where i, j represent the zonal and meridional positions and $v\zeta$ and $-u\zeta$ are the zonal and meridional components of $\zeta\boldsymbol{k}\times\boldsymbol{u}$ respectively. The $v\zeta$ and $-u\zeta$ terms lie on u and v-points of the grid respectively. This scheme is in line with the Sadourny energy conserving calculation within MITgcm [Sadourny, 1975]. In this study, both the time-mean term, $\overline{\zeta}\boldsymbol{k}\times\overline{\boldsymbol{u}}$, and the Reynolds stress term, $\overline{\zeta'\boldsymbol{k}\times\boldsymbol{u'}}$ are calculated offline from these numerical schemes. Each component of the time-mean term is found by averaging u and ζ,

$$(\overline{\zeta}\boldsymbol{k}\times\overline{\boldsymbol{u}})^{i,j}=\big((\overline{v}\overline{\zeta})^{i,j},\,-(\overline{u}\overline{\zeta})^{i,j}\big). \tag{2.81}$$

Each component of the Reynolds stress term is calculated using a combination of the snapshots and the time mean term,

$$(\overline{\zeta'\boldsymbol{k}\times\boldsymbol{u'}})^{i,j}=\big(\overline{(v\zeta)^{i,j}-(\overline{v}\overline{\zeta})^{i,j}},\,\overline{(\overline{u}\overline{\zeta})^{i,j}-(u\zeta)^{i,j}}\big). \tag{2.82}$$

The numerical discretisation for the irrotational terms in (2.53), $\boldsymbol{\nabla}(\overline{\boldsymbol{u}}\cdot\overline{\boldsymbol{u}})/2$ and $\boldsymbol{\nabla}(\overline{\boldsymbol{u'}\cdot\boldsymbol{u'}})/2$, is then:

$$\mathrm{KE}^{i,j}=\frac{1}{2}((u^{i,j}\cdot u^{i+1,j})+(v^{i,j}+v^{i,j+1})), \tag{2.83}$$

$$\left(\frac{d((\boldsymbol{u}\cdot\boldsymbol{u})/2)}{dx}\right)^{i,j}=\frac{1}{\Delta x_c^{i,j}}(\mathrm{KE}^{i,j}-\mathrm{KE}^{i-1,j}), \tag{2.84}$$

$$\left(\frac{d((\boldsymbol{u}\cdot\boldsymbol{u})/2)}{dy}\right)^{i,j}=\frac{1}{\Delta y_c^{i,j}}(\mathrm{KE}^{i,j}-\mathrm{KE}^{i,j-1}), \tag{2.85}$$

where KE is defined on mass-points. The time-mean and Reynolds stress components of the irrotational term are then calculated similar to above. Each component of the time-mean term is found by averaging u and ζ,

$$\left(\frac{1}{2}\boldsymbol{\nabla}(\overline{\boldsymbol{u}}\cdot\overline{\boldsymbol{u}})\right)^{i,j}=\left(\left(\frac{d((\overline{\boldsymbol{u}}\cdot\overline{\boldsymbol{u}})/2)}{dx}\right)^{i,j},\left(\frac{d((\overline{\boldsymbol{u}}\cdot\overline{\boldsymbol{u}})/2)}{dy}\right)^{i,j}\right). \tag{2.86}$$

Then each component of the Reynolds stress term is calculated using a combination of the snapshots and the time mean term,

$$\begin{aligned}\left(\frac{1}{2}\boldsymbol{\nabla}(\overline{\boldsymbol{u'}\cdot\boldsymbol{u'}})\right)^{i,j}=\Bigg(&\left(\frac{d((\boldsymbol{u}\cdot\boldsymbol{u})/2)}{dx}\right)^{i,j}-\left(\frac{d((\overline{\boldsymbol{u}}\cdot\overline{\boldsymbol{u}})/2)}{dx}\right)^{i,j},\\&\left(\frac{d((\boldsymbol{u}\cdot\boldsymbol{u})/2)}{dy}\right)^{i,j}-\left(\frac{d((\overline{\boldsymbol{u}}\cdot\overline{\boldsymbol{u}})/2)}{dy}\right)^{i,j}\Bigg).\end{aligned} \tag{2.87}$$

2.3.2 Depth-Integrated Terms

The staggering of the horizontal grid in MITgcm means that the terms of the momentum equation are calculated at different positions in the horizontal. In order to calculate the momentum budget MITgcm implements a scheme in which terms are spatially averaged to a common point. Point-wise, the momentum budget (2.1) closes without complication as the model itself is balanced. However, this is not the case when taking a depth integral in the presence of variable topography. In order to exactly close the depth-integrated momentum budget, a depth-integral would be required before spatial averaging is implemented. There is currently no method for this within the MITgcm framework. The errors produced by this phenomenon are relatively small when examining the depth-integrated momentum budget but in the zonally integrated barotropic momentum budget errors accumulate. The primary errors arise in the the Coriolis term, $f\boldsymbol{k} \times \boldsymbol{u}$ and the pressure gradient term, $\boldsymbol{\nabla} p$. In this study, an offline correction is made to these two terms in order to account for the errors produced by depth-integrating and improve accuracy.

A method for avoiding errors in the Coriolis term exists in MITgcm but was not designed for this purpose and has not been implemented in this research. This method is outlined by Jamart and Ozer [1986] and has the primary purpose of reducing the occurrence of spurious boundary flows that occur in three dimensional models. This implementation happens to prevent the integrating error in the Coriolis term by including the partial cell scale factors in the spatial averaging. The spurious boundary flows which the Jamart and Ozer [1986] method is designed to prevent do not occur on a two dimensional grid. Although this method is not used for simulations here, the note has been made to highlight its possible utility in future investigations.

In the default momentum equations of MITgcm, terms are averaged to common velocity points without taking partial cells in the vertical grid into account. Figure 2.5 depicts the grid layout of the components used for calculating the zonal component of the Coriolis term and the pressure gradient term in (2.1). The numerical scheme used to calculate the Coriolis term in MITgcm is:

$$v^{i,j}_{flux} = v^{i,j} \cdot \Delta x^{i,j}_g, \tag{2.88}$$

$$(vf\boldsymbol{k})^{i,j} = \frac{1}{4\Delta x^{i,j}_c}((v^{i,j}_{flux} + v^{i-1,j}_{flux}) f^{i,j}_g + (v^{i,j+1}_{flux} + v^{i-1,j+1}_{flux}) f^{i,j+1}_g), \tag{2.89}$$

where f_g is the Coriolis parameter on the vorticity-points. Then the scheme for the pres-

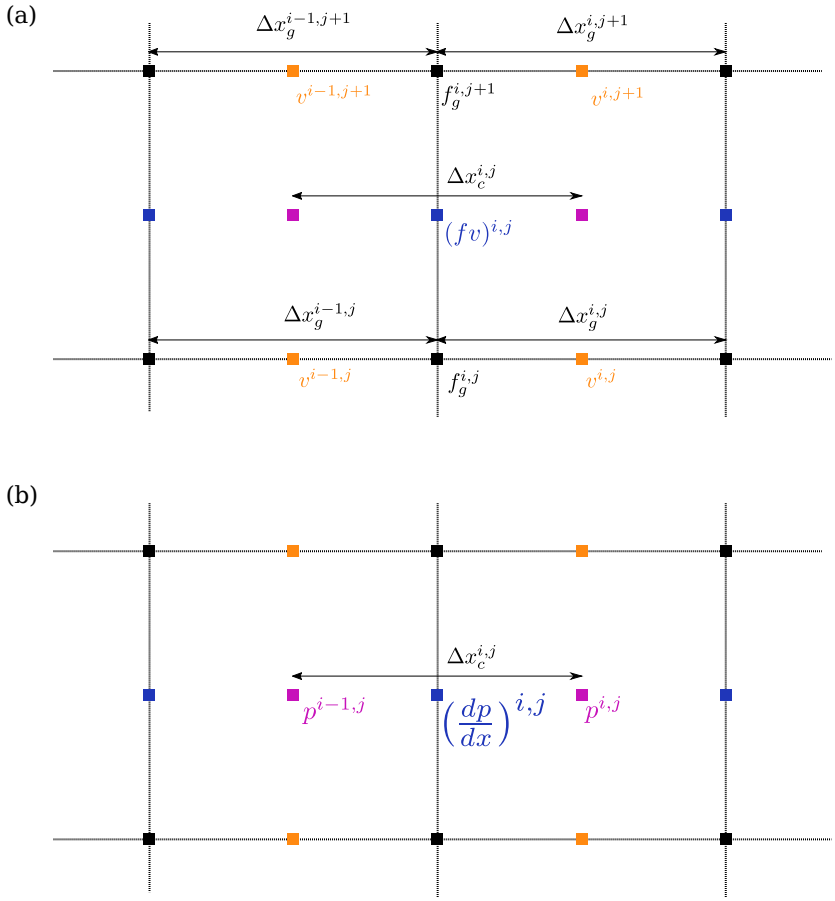

Figure 2.5: Gridding for the calculation of the zonal Coriolis term, fv, and zonal pressure gradient term dp/dx. The colour coding of grid points is the same as in Figure 2.3. The zonal and meridional grid positions are represented by i and j respectively. (a) shows the gridding for fv where f_g is the Coriolis parameter on vorticity points and the meridional velocity, v, is given on v-velocity points. (b) shows the gridding for the calculation of dp/dx where the pressure values are given on mass points.

sure gradient in MITgcm is:

$$\left(\frac{dp}{dx}\right)^{i,j} = \frac{1}{\Delta x_c^{i,j}}(p^{i,j} - p^{i-1,j}). \tag{2.90}$$

In this case, terms are averaged onto the u-points of the cells. The zonal Coriolis term is taken from a composition of the average of velocities on four v-points and Coriolis values on two ζ points. The pressure gradient term is calculated from pressure values on the mass points. Taking the depth-integral on the velocity points to which the terms are averaged disregards the effect of partial cells on the points from which terms are averaged. There are two ways to account for this in the analysis. The first is to multiply the terms by an average of the appropriate scale factors. For example, the depth-integrated Coriolis term is calculated using the average of four h_s values rather than h_w,

$$\left(\int_{-h}^{\eta} vf\boldsymbol{k}\, dz\right)^{i,j} = (vf\boldsymbol{k})^{i,j} \cdot \Delta r_f^{i,j} \cdot \frac{1}{4}(h_s^{i,j} + h_s^{i-1,j} + h_s^{i,j+1} + h_s^{i-1,j+1}). \tag{2.91}$$

Whereas the depth integral of the pressure term is taken over the zonal average of h_c rather than h_w,

$$\left(\int_{-h}^{\eta} \frac{dp}{dx}\, dz\right)^{i,j} = \frac{1}{2}(h_c^{i,j} + h_c^{i-1,j}) \cdot \Delta r_f^{i,j} \cdot \frac{1}{\Delta x_c^{i,j}}(p^{i,j} - p^{i-1,j}). \tag{2.92}$$

As noted above, this results in a correction rather than an exact calculation. The second method calculates the depth-integral exactly. To do this, each component is required to be multiplied by its associated partial cell scale factor. As an example, the exact calculation of the pressure term is:

$$\left(\int_{-h}^{\eta} \frac{dp}{dx}\, dz\right)^{i,j} = \Delta r_f^{i,j} \cdot \frac{1}{\Delta x_c^{i,j}}(h_c^{i,j} \cdot p^{i,j} - h_c^{i-1,j} \cdot p^{i-1,j}). \tag{2.93}$$

For this research, the correction method of (2.91) and (2.92) is utilised.

3 Existing Results in Model Framework

Most knowledge of gyres has arisen from studies of the North Atlantic, which poses a very different setting to the Southern Ocean. This chapter outlines the classical theory of gyre formation in a basin, forming a basis for the extension of these ideas to the Southern Ocean in the subsequent chapter. The concept of geostrophic contours is introduced, providing a convenient context in which to make this comparison between dynamics in these two geographical locations. For clarity, this is all conveyed through the use of model results.

3.1 Classical Gyre Theory

A typical gyre is characterised by a broad meridional current in the interior and an intense western boundary current flowing in the opposing direction. In early theory this gyre flow was understood to require three things:

1. A wind forcing with meridional variation, i.e. a non-zero curl in the wind stress
2. A Coriolis parameter with meridional variation, i.e. a beta effect must be present
3. A closed, flat bottom domain

These criteria are explained with the use of the barotropic vorticity equation (see Section 2.1 for derivation):

$$\rho_0\left(\boldsymbol{k}\cdot\boldsymbol{\nabla}\times(\overline{H}\overline{\boldsymbol{u}}\cdot\boldsymbol{\nabla}\overline{\boldsymbol{u}}+\overline{H}\overline{\boldsymbol{u}'\cdot\boldsymbol{\nabla}\boldsymbol{u}'})+\overline{H}\beta\overline{v}\right)= \boldsymbol{k}\cdot\boldsymbol{\nabla}\overline{p}_b\times\boldsymbol{\nabla}h+\boldsymbol{k}\cdot\boldsymbol{\nabla}\times(\overline{\boldsymbol{\tau}}_w-\overline{\boldsymbol{\tau}}_b)+\mu\overline{H}\boldsymbol{\nabla}^2\overline{\zeta}. \tag{3.1}$$

A zonal wind forcing with a meridional variation exhibits a curl which acts to input vorticity into the system. In order to conserve vorticity there must be a sink of vorticity, opposite in sign to the wind stress, which balances the wind stress curl. According to Sverdrup [1947], the balancing term is the advection of planetary vorticity, $\beta\overline{v}$, which creates a meridional flow in the interior. This is defined as Sverdrup balance:

$$\rho_0\overline{H}\beta\overline{v}=\boldsymbol{k}\cdot\boldsymbol{\nabla}\times\overline{\boldsymbol{\tau}}_w. \tag{3.2}$$

Through Sverdrup balance the global wind stress curl field relates to an ocean flow which is equator-ward for subtropical gyres and poleward for subpolar gyres. As gyres are defined as closed circulations there must be a return flow in the opposing direction to ensure

conservation of mass. Meridional flow is generally zonally asymmetric in gyres with the occurrence of an intense western return flow. Stommel [1948] shows that f varying with latitude is responsible for a zonal asymmetry in the meridional flow in gyres. Where f varies meridionally the return flow occurs as an intense western boundary current, however, if f is taken to be constant meridional flow is zonally symmetric. The asymmetry in the case with variable f is set by vorticity constraints imposed by Sverdrup balance. In the case where f is constant $\beta\overline{v}$ is zero and Sverdrup balance no longer holds.

For the case where f is variable, flow is zonally asymmetric due to the presence of $\beta\overline{v}$. Sverdrup balance acts to force flow meridionally in the interior. In the return flow, Sverdrup balance breaks down as $\beta\overline{v}$ takes the opposite sign and acts together with the wind stress as a source of vorticity. Alternative sinks of vorticity must act to balance the input from both the wind stress and advection of planetary vorticity. In Stommel's analytical model, bottom drag is the balancing term for the input of vorticity by the western boundary current [Stommel, 1948]. Alternatively, Munk [1950] later showed that it is possible to balance this vorticity via horizontal viscous effects. The mechanisms by which these sinks act to balance the vorticity lead to the intense return flow. In order for both bottom drag and horizontal viscous effects to generate a sink of vorticity there must be a curl in the profile of the flow. The flow returns as intense boundary current to create a shear in the flow which in turn provides the necessary curl in the flow.

A simplified view of the vorticity balance in gyres has been provided in Böning [1986]. Due to conservation of mass, the volume of fluid passing north over a line of latitude is matched by the volume flowing south over the same line. This means when taking an area integral of (3.1) between two bounding lines of latitude the $\beta\overline{v}$ term is negligible. Over an area bounded by a streamline the mean inertial term, $\rho_0 \boldsymbol{k} \cdot \boldsymbol{\nabla} \times (\overline{H}\overline{\boldsymbol{u}} \cdot \boldsymbol{\nabla}\overline{\boldsymbol{u}})$, integrates to zero [Böning, 1986]. Therefore, the domain integral of (3.1) leaves

$$\begin{aligned} &\int\int_A \boldsymbol{k} \cdot \boldsymbol{\nabla} \times \overline{\boldsymbol{\tau}}_w \, dA = \\ &\int\int_A \boldsymbol{k} \cdot \boldsymbol{\nabla} \times \overline{\boldsymbol{\tau}}_b \, dA + \mu \int\int_A \overline{H} \boldsymbol{\nabla}^2 \overline{\zeta} \, dA - \rho_0 \int\int_A \boldsymbol{k} \cdot \boldsymbol{\nabla} \times \left(\overline{H} \overline{\boldsymbol{u}' \cdot \boldsymbol{\nabla} \boldsymbol{u}'} \right) dA, \end{aligned} \tag{3.3}$$

where A denotes the domain area over which the integral is taken. In this perspective $\beta\overline{v}$ does not provide an input of torque and is only responsible for communicating the spatially separated sources and sinks of vorticity. In the early gyre studies, model resolution was too low to produce eddies and their complexity meant that they were left from the analytical

studies. As a result, equation (3.3) took a simplified form and is reduced in these studies to

$$\int\int_A \boldsymbol{k}\cdot\boldsymbol{\nabla}\times\overline{\boldsymbol{\tau}}_w\,dA = \int\int_A \boldsymbol{k}\cdot\boldsymbol{\nabla}\times\overline{\boldsymbol{\tau}}_b\,dA + \mu\int\int_A \overline{H}\boldsymbol{\nabla}^2\overline{\zeta}\,dA. \tag{3.4}$$

Equation (3.4) provides a direct relationship for the conclusions of Stommel [1948] and Munk [1950] that the input of vorticity via the wind stress is removed by bottom drag or horizontal viscous effects.

The remainder of this section discusses the dynamics within the western boundary current. As the classical studies are given in the context of the North Atlantic gyre the description will be given in the context of a sub-tropical gyre, where the western boundary current is poleward. The same results hold for sub-polar gyres except the direction of the meridional currents are in the opposite direction, so the western boundary current is equatorward.

An analytical model by Fofonoff [1954] outlines the effect of inertia within a gyre. In this publication an analytical method is used to form two counter rotating gyres in a system with uniform depth where both bottom drag and viscosity were neglected. It is shown that due to potential vorticity constraints, under these conditions absolute vorticity, $f+\zeta$, is a conserved property meaning it must be constant along a streamline. For a sub-tropical gyre, flow in the western boundary current is in the poleward direction. A poleward current results in an increase in f along a streamline. In order to maintain a constant absolute vorticity in the western boundary current there must be a large input of negative relative vorticity, ζ. The input of relative vorticity is achieved through a zonal convergence of the flow as it heads poleward and the zonal shear in the flow increases towards the pole. Fofonoff [1954] showed that these vorticity constraints are not only responsible for an intensifying poleward current but also the intensity of the eastward return flow. The absence of dissipative effects means that the flow retains its relative vorticity as it leaves the western boundary and flows eastward towards the interior. As a result, the flow overshoots the western boundary and is returned to the interior as an intense eastward jet.

In the presence of bottom drag in the Stommel case or viscosity in the Munk case relative vorticity is dissipated and the inertial overshoot is limited. In the limit where bottom drag or viscosity dominates, the western boundary current is symmetric in the meridional direction with peak relative vorticity in western boundary current aligning with the central latitude of the gyre [Veronis, 1966b, Böning, 1986]. As inertial terms become more influential relative to the dissipative terms in the system, the dynamics tend towards the Fofonoff system. The higher inertial influence means that a larger distance is required for the relative vorticity to dissipate and the peak relative vorticity position moves poleward. With a

large enough poleward shift in this position the flow overshoots and a eastward jet occurs along the gyre boundary [Veronis, 1966b, Böning, 1986].

The vorticity sink generated by viscosity and bottom drag are both dependent on relative vorticity. Viscosity requires a larger relative vorticity field in order to generate an equal vorticity sink to that produced by bottom drag [Böning, 1986]. This means that a stronger or narrower western boundary current is required to balance the vorticity source from the wind forcing in the Munk case relative to the Stommel case [Böning, 1986]. The Munk case is more sensitive to inertial effects and a smaller increase in inertia is needed to create the inertial overshoot which generates the eastward jet of the Fofonoff system [Böning, 1986].

The β effect causes the western return flow in a gyre to be confined to a narrow band. The width of this current is dependent on parameter choice. For the two model set-ups discussed, the Munk and Stommel models, the parameters which affect the width of the return flow are different in each case. The Reynolds number is a non-dimensional parameter given as: $\rho uL/\mu$ where u is the flow velocity and L is characteristic length scale of the flow. The Reynolds number is the parameter which dictates the width scale of the return flow for the Munk case [Bryan, 1963]. Whereas the coefficient of bottom drag, C_d, determines this for the Stommel case [Veronis, 1966a]. For a fixed geometry and wind stress the required sink of vorticity remains the same. If μ or C_d is increased the relative vorticity required to generate the same vorticity sink reduces. Two possible dynamical responses to a reduced relative vorticity are either to reduce the flow velocities or to increase the width of the current. The increase of these two parameters leads to the increase in width of the return current [Bryan, 1963, Veronis, 1966a]. From here on the bottom drag and horizontal viscous terms will be grouped under the name *frictional terms*.

3.2 Classical Gyre Theory in Model Results

It is possible to highlight some of the early theories outlined above through model results. Contrary to previous investigations, the simulations here are carried out for the Southern Hemisphere for consistency with the Southern Hemisphere focus of this study. Figure 3.1d shows the barotropic streamfunction for a simulation with a domain and forcing similar to the analytical model described in Stommel [1948]. The result is for a flat bottom domain which is forced by a eastward, sinusoidal wind stress. The domain is zonally periodic with a meridional wall in the centre and walled boundaries to the north and south. This case is equivalent to a closed basin. This unusual set-up is used so that the important features of resulting flow lie in the centre of the domain. For further details on the model set-up see

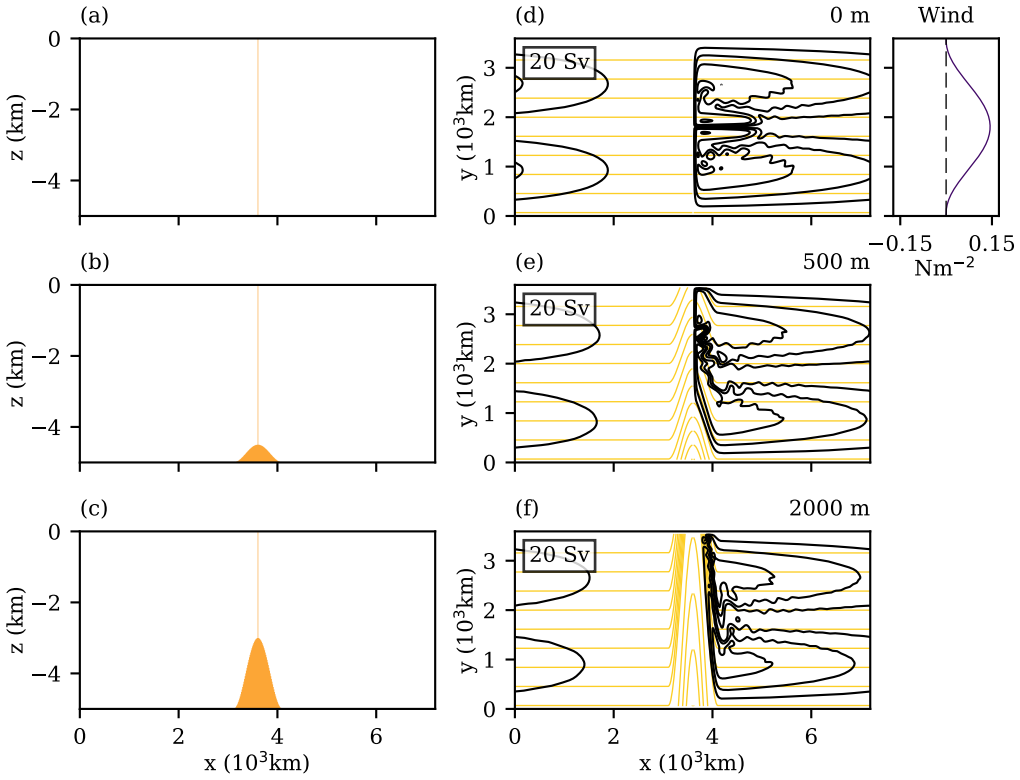

Figure 3.1: Plan view of barotropic simulations with a meridional wall and a ridge that varies in height. A side profile from the south is shown in (a)-(c) to highlight the topography. The ridge heights are: d) 0 m e) 500 m f) 2000 m. Streamlines are shown in black. Orange lines signify contours of f/h. The box to the top-left of each panel signifies the contour spacing for each streamfunction. (d)-(f) are results from models 01, 03 and 08 respectively.

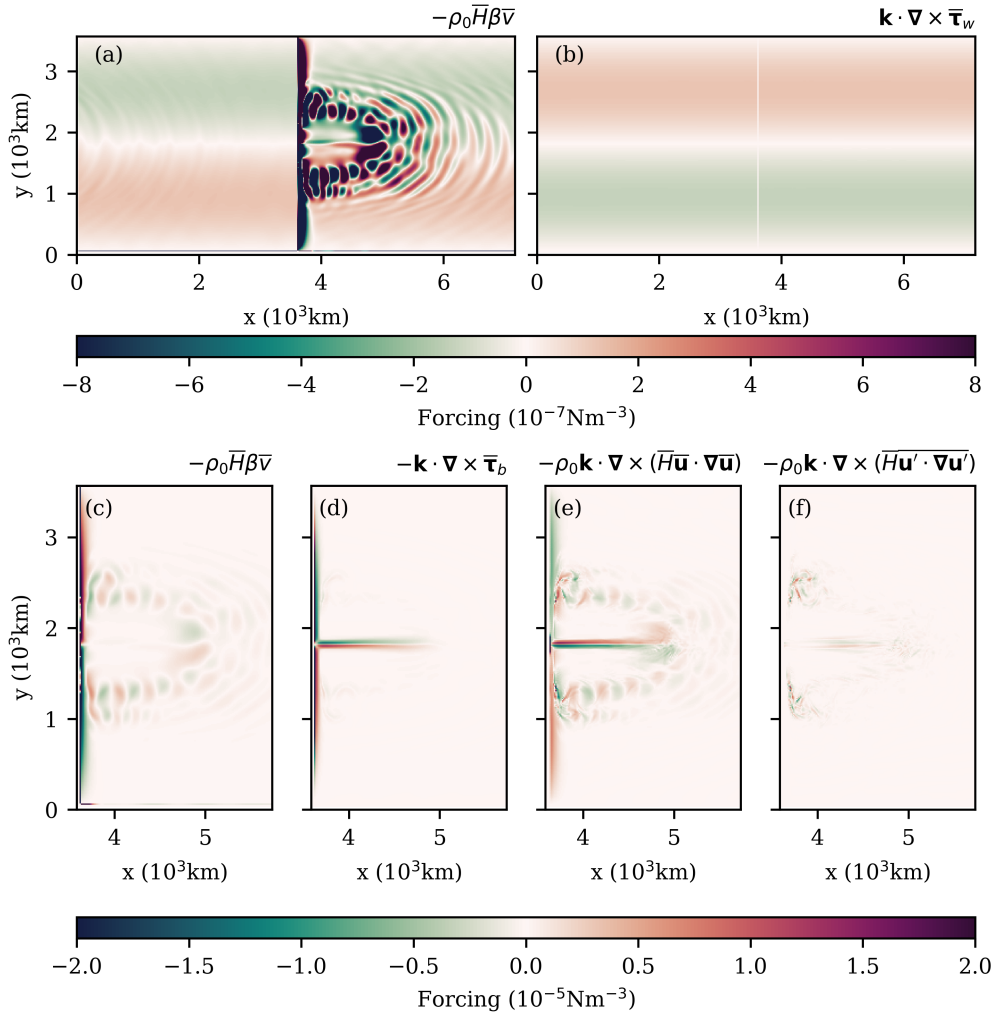

Figure 3.2: Terms of the barotropic vorticity balance for model 01 with a meridional wall in the centre and no bottom topography, as in Figure 3.1d. (a) and (b) show the entire domain whereas (c)-(f) show a zoomed in view of the western boundary current. The colour scales of (a) and (b) differ from (c)-(f) to emphasize the different balances.

section 2.2 and Appendix, model 01.

The streamfunction in Figure 3.1d shows two counter rotating gyres with a central zonal jet emerging between the gyres. Figure 3.2 shows terms of the vorticity equation for this simulation. Figures 3.2a and 3.2b reveal the presence of Sverdrup balance, (3.2), over most of the domain interior. The remaining contribution in the domain interior arises from the inertial terms shown in Figures 3.2e and 3.2f. The vorticity from the inertial terms appears due to the combination of relatively high resolution and low viscosity used here. The viscosity term has been neglected from this plot as its vorticity contributions is negligible. As this set-up is similar to the Stommel solution, in a domain integral sense bottom drag is the main balance of the vorticity input by the wind stress. This can be seen by the narrow band in bottom drag vorticity partially balancing $\beta\overline{v}$ in Figures 3.2c and 3.2d. The model is defined with free-slip boundary conditions on the walls. No slip boundary conditions are a key requirement for a viscous vorticity sink described by Munk [1950]. This results in no possible contribution from the Munk type balance of vorticity described above. The narrow vorticity sink from bottom drag extends into the interior of the domain where a eastward jet develops. As with the results of Veronis [1966b], the occurrence of this zonal jet is down to the large influence from the inertial terms. The inertial terms balance the vorticity arising from the bottom drag in this zonal jet. There is an increased tendency for this kind of zonal jet in a Stommel set-up when inertial influences are increased [Veronis, 1966b].

The vorticity arising from the mean inertial term in the interior of the domain (Figure 3.2e) results from stationary Rossby waves forming in the eastward flow. Stationary Rossby waves are governed by the short barotropic Rossby wave dispersion relation:

$$\omega = uk - \frac{\beta k}{K^2}, \tag{3.5}$$

where ω is the wave frequency; $K^2 = k^2 + l^2$ with k and l the zonal and meridional wave numbers respectively; u is eastward velocity. For a stationary Rossby wave, $\omega = 0$ and (3.5) simplifies to $u = \beta/K^2$. With β fixed, the wave number of the stationary Rossby wave is proportional to u. Stationary Rossby waves are generated when the velocity of eastward flow is equal to the phase velocity of a westward propagating Rossby wave. The presence a stationary Rossby wave is determined by the zonal velocities.

The steady result in Figure 3.1a shows a strong eastward jet forming in the confluence zone in the centre of the domain. The zonal jet velocities reduce and the current turns increasingly meridional at roughly 1000 km from the wall. There is a fixed limit of the zonal flow velocity at which continue Rossby waves propagate westward. This limit is proportional to the value β. In the region of the jet in Figure 3.1a, zonal velocities are faster than

any of the westward phase velocities of the high wave-number Rossby waves and there is no significant sign of a stationary wave. Where the jet velocities are reduced, u tends towards a velocity comparable to higher wave-number barotropic Rossby wave phase velocities and a stationary wave is visible. The dominant wave-like structure of flow in Figure 3.2a is due to the dependence of stationary Rossby waves on eastward velocities over much of the domain. Stationary waves are also present in regions of lower, positive u to the north and south of the jet. Rossby waves do not occur when $u < 0$. As a result, there are no wave-like features in the westward flow near the northern and southern boundaries.

3.3 Variable Topography and Geostrophic Contours

Seabed topography has an important influence on flow. Results in Figures 3.1e and 3.1f show the barotropic streamfunction for the closed domain used for the result in Figure 3.1d except with the addition of topography of differing heights (500 m and 2000 m) on either side of the meridional wall. This topography is of sinusoidal shape taking the form $h_0(\cos(x/w_0) + 1)/2$, $x \in \{-\pi w_0, \pi w_0\}$, where $x = 0$ represents the position of the meridional wall, h_0 is the ridge height and w_0 is the ridge width. The introduction of variable topography alters the balances that occur in gyre formation. In order to effectively describe the impact of topography it is useful to present the concept of geostrophic contours, which arises from potential vorticity constraints.

In an inviscid, unforced, linear fluid the potential vorticity equation (2.74) reduces to

$$\frac{D}{Dt}\left(\frac{f}{H}\right) = 0. \tag{3.6}$$

It follows from (3.6) that flow is directed along lines of constant f/H to conserve planetary potential vorticity. The sea surface height contribution to H is small, so hereafter unless stated otherwise the discussion will revolve around contours of f/h rather than f/H. Contours of f/h will be referred to as geostrophic contours. In the flat-bottom, closed domain considered above (Figure 3.1d), all geostrophic contours are zonal and blocked by the meridional wall. In Figures 3.1e and 3.1f topography is introduced at the meridional wall. As the simulation is representative of the Southern Hemisphere, values of f/h become more negative for decreasing depth. This means that geostrophic contours are deflected northward over a rising topography. The deflection happens to the point where the contours become blocked by the northern boundary rather than the meridional wall in Figure 3.1f. The geostrophic contours also show greater convergence towards the boundary as the slope is raised. As contour spacing at the boundary reduces, the gradient in f/h increases.

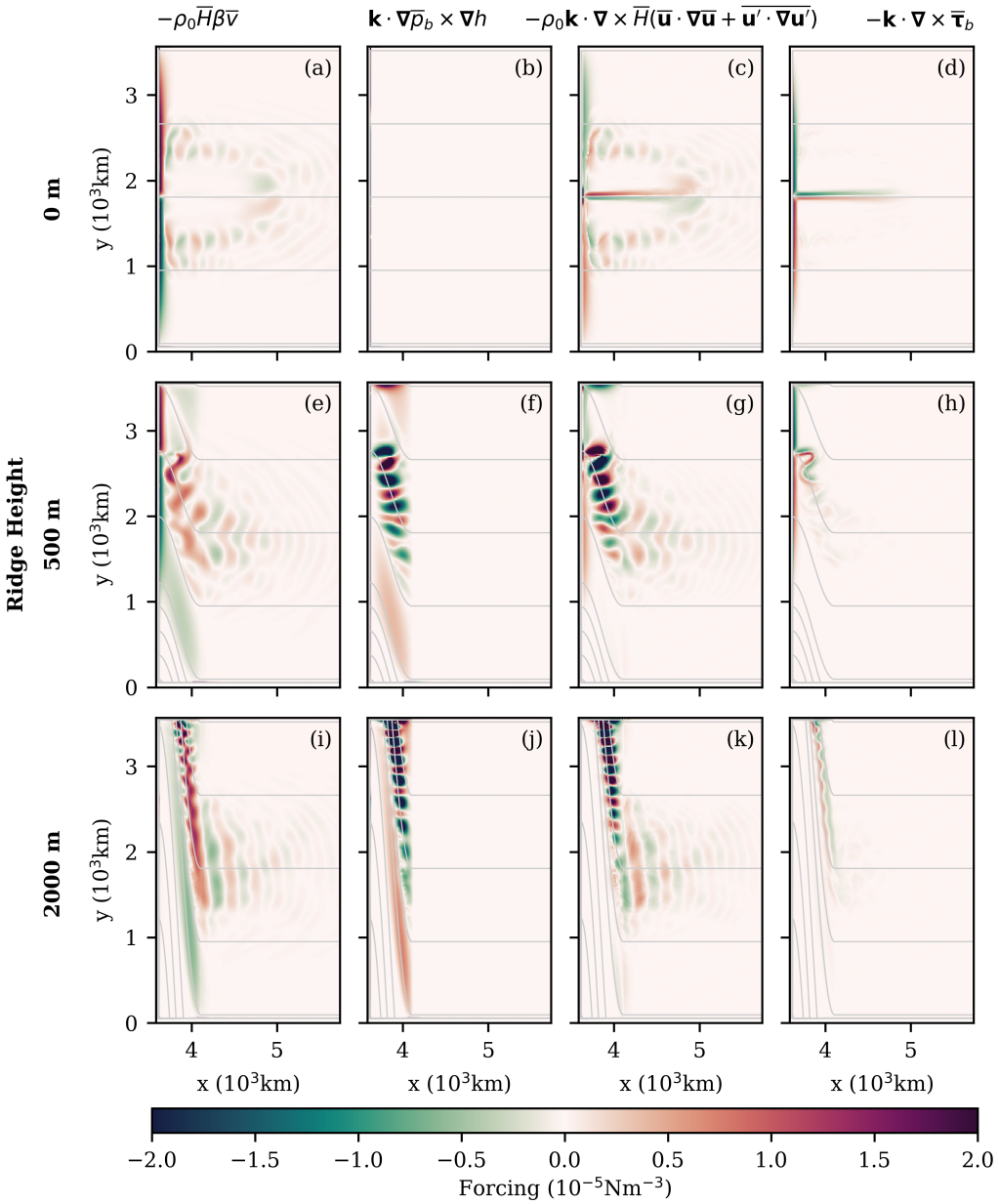

Figure 3.3: Terms of the barotropic vorticity balance for three simulations with a meridional wall and varying ridge height: (a)-(d) for no bottom topography, (e)-(h) for 500 m high topography and (i)-(l) for 2000 m high topography. These plots are zoomed to the same region and have the same colour scale as Figure 3.2c-f. The grey lines indicate the geostrophic contours. Results are from models 01, 03 and 08.

The streamlines in Figure 3.1 show that the flow responds to the change in topography by aligning with the deflected geostrophic contours. The balances in barotropic vorticity are altered with this change in flow. Figure 3.3 shows vorticity terms in the western boundary currents for these differing topographies. With the introduction of topography comes the addition of the bottom pressure torque term, $\boldsymbol{k} \cdot \boldsymbol{\nabla} \overline{p}_b \times \boldsymbol{\nabla} h$. It is this term which causes the flow to align with geostrophic contours over topography [Jackson et al., 2006]. The bottom pressure torque becomes an important part of the vorticity balance in the western boundary current as a result. It is reported by Holland [1972], Hughes and De Cuevas [2001] and Jackson et al. [2006] that this term is the major balance for the meridional flow over topography. As a result, the primary vorticity balance over topography becomes between $\boldsymbol{k} \cdot \boldsymbol{\nabla} \overline{p}_b \times \boldsymbol{\nabla} h$ and $\beta \overline{v}$. The results in Figure 3.3 broadly agree but the highly inertial character of the model means that in some regions this result is masked by the inertial terms.

In the two simulations with topography of 2000 m and 500 m the counter rotating gyres form a pressure field which gives a symmetric pattern in the bottom pressure torque with respect to geostrophic contours (Figure 3.3). The symmetric pattern appears over the topography in these simulations. The symmetry is formed of a wave-like feature aligned with the central geostrophic contour then a signal of positive vorticity along both higher and lower values of f/h. In each domain, there is a westward flow towards the northern and southern boundaries. Where this flow meets the topography it turns north, following the geostrophic contours. Once both flows have reached the top of the slope the currents turn towards each other, crossing geostrophic contours. There is then a confluence at which the flow returns back down the slope to the interior. There is an addition of positive vorticity by the bottom pressure torque as a fluid parcel moves up the slope. The role of bottom pressure torque in the return flow is is a little less clear due to the inertial waves which appear. In a less inertial system, the bottom pressure torque is shown to be a source of negative vorticity in this return flow down the slope [Jackson et al., 2006]. The inertia is distorting the bottom pressure torque, however, it is indicated by the $\beta \overline{v}$ term (Figures 3.3e and 3.3i) that the combined effect of both inertia and bottom pressure torque is to add negative vorticity. This agrees with the previous findings and suggests that bottom pressure torque acts as a source of negative vorticity where the flow is returning to the interior.

Equation (3.6) dictates that fluid can flow freely along geostrophic contours in the case where they are un-blocked. However, along blocked geostrophic contours, flow is restricted by the intersection with a boundary and no mean flow emerges in the case where equation (3.6) holds. Contrary to this conclusion, in Figures 3.1d-f flow develops in regions where geostrophic contours are blocked due to the presence of the wall. In this case, terms ne-

glected from (3.6) permit flow to cross geostrophic contours, allowing for a circulation in a region of blocked geostrophic contours. This will be further discussed below.

3.4 Frictional Effects

In order for flow to develop in a region of blocked geostrophic contours an alternative form of equation (3.6) must be considered. An introduction of forcing and 'frictional' terms (bottom drag and viscosity) to equation (3.6) results in the dynamics being governed by:

$$\rho_0 H \frac{D}{Dt}\left(\frac{f}{H}\right) = \boldsymbol{\nabla} \times \frac{\boldsymbol{\tau}_w - \boldsymbol{\tau}_b}{H} + \mu \boldsymbol{\nabla}^2 \zeta, \tag{3.7}$$

which is derived in Section 2.1.8. Equation (3.7) shows that the wind stress, bottom drag and viscosity permit flow to cross geostrophic contours, akin to the dynamics described in Section 3.1.

It has been shown in the previous section that the 'frictional' terms are no longer dominant in the barotropic vorticity balance with the introduction of topography. Despite this it is given by (3.7) that the 'frictional' terms are vital for the observed dynamics. It is highlighted by Salmon [1992] that whilst geostrophic contours are key for the meridional deflection of the flow it is the 'frictional' terms at the point where these contours intersect with a boundary that enable return flow into the interior. A parcel of fluid will follow geostrophic contours over topography until those contours are blocked. At a boundary, 'frictional' terms will take over, moving the fluid across geostrophic contours parallel to the boundary. The fluid then returns along a different geostrophic contour, into the interior whereby Sverdrup balance takes over in a flat-bottomed region. The bottom pressure torque deflects geostrophic contours and the 'frictional' terms allow flow to cross them.

When moving across the geostrophic contours at a boundary, the range of f/h that the fluid crosses matches the range of f/h crossed in the interior. This means that the gyre strength is limited by the ability of both wind forcing and the 'frictional' terms to add vorticity, forcing the flow across geostrophic contours.

The 'frictional' effect described by Salmon [1992] is the same mechanism that was described for the flat bottom case in terms of barotropic vorticity in Section 3.2. 'Frictional' terms act to balance the vorticity input from the wind stress and contribute to the formation of an intense return current. The 'frictional' effects in the simulations of this study are predominantly provided by bottom drag. The adjustment of the bottom drag term to the introduction of topography can be seen in Figure 3.3. This 'frictional' vorticity sink is confined to the same range of geostrophic contours between the varying topographies.

The greater convergence of geostrophic contours as topography becomes steeper results in this 'frictional' balance acting across a smaller space. There is also a northward shift in this 'frictional' balance. It has previously been shown by Holland [1967] that increasing topographic height leads to an equatorward shift in this 'frictional' balance. Figure 3.3 shows that this northward shift is a result of the northward deflection of geostrophic contours as topographic height increases. The results of Holland [1967] are for the Northern Hemisphere leading a relationship in the opposite direction. Increased topographic height in Holland [1967] gives a southward shift in the 'frictional' balance relating to the southward deflection of geostrophic contours.

The local frictional balance also changes with varying topography. In the case with no topography all geostrophic contours intersect with the western boundary and flow is parallel with the boundary. The meridional alignment of the flow results in a local balance between $\beta\overline{v}$ and bottom drag. As topography is introduced, the geostrophic contours are deflected northwards and the point where they intersect with the boundary changes. In the case with topography of 500 m in height some of the geostrophic contours intersect with the western boundary and the remainder intersect with the northern boundary. Where the geostrophic contours intersect with the western boundary, the vorticity balance is unchanged compared with the no topography case. The balance is altered where contours intersect with the northern boundary. In this region, in order for flow to cross geostrophic contours at the boundary it must flow in the zonal direction. The absence of $\overline{v}$ in this flow means that an alternative vorticity balance must arise. It is indicated in Figure 3.3 that a balance between bottom pressure torque and inertia emerges where geostrophic contours intersect with the northern boundary. In the case with 2000 m topography all geostrophic contours intersect with the northern boundary and the balance between $\beta\overline{v}$ and bottom drag at the western boundary is entirely absent. In the case with no topography this balance plays a primary role in the formation of gyres yet they still form in the case with 2000 m topography. There is a shift in the underlying mechanism allowing flow to return across geostrophic contours in the presence of topography at the western boundary. In Figure 3.3l there is a presence of bottom drag in return flow. This return flow is further investigated below and it is indicated that this is the important structure for permitting gyres in the topographic case.

3.5 Inertial Modulation of Frictional Effects

In the theory presented so far, 'frictional' terms act as a vorticity sink, balancing the vorticity input from the wind stress. As summarised by (3.7), this 'frictional' vorticity sink

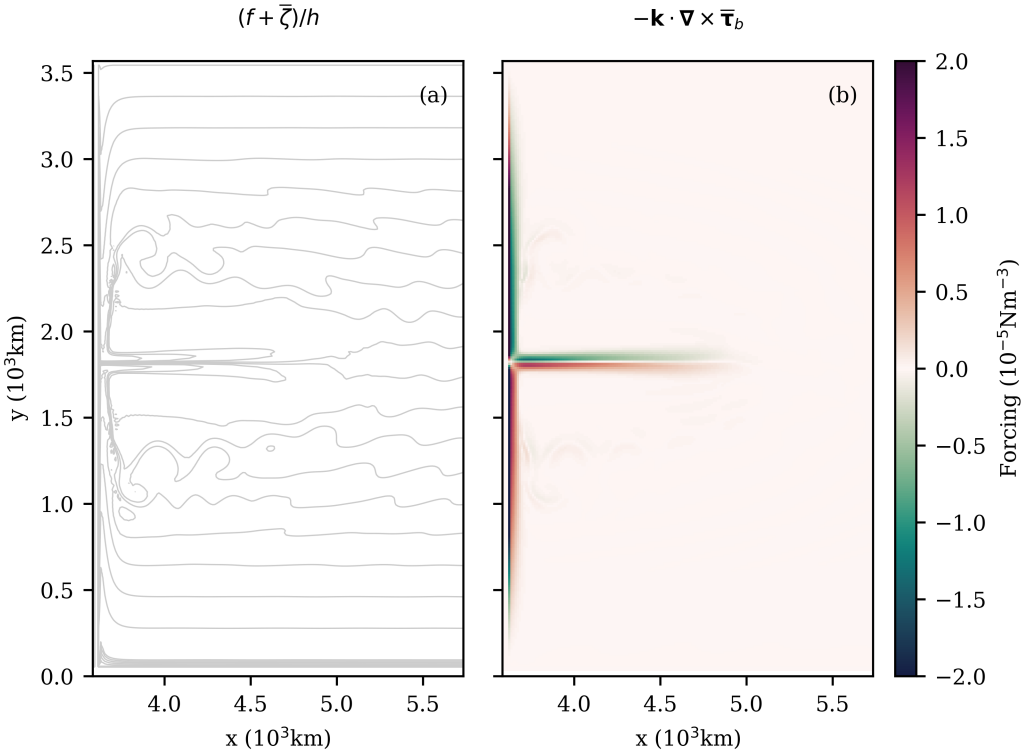

Figure 3.4: Vorticity for the walled domain with no bottom topography, model 01. Plots are zoomed to east of the meridional wall. (a) contours of $(f + \overline{\zeta})/h$. (b) The bottom drag contribution to the barotropic vorticity budget.

permits flow to cross contours of f/h. This theory is drawn under the assumption that inertia is small, however, the simulations presented in this study are significantly inertial. Inertia acts to introduce jets which can modulate frictional effects [Veronis, 1966b, Böning, 1986]. This behavior has already been observed in the flat bottom closed domain presented above. Figure 3.2 shows the vorticity for this simulation. A jet extends away from the boundary with a vorticity balance between bottom drag and inertia. It is expected from (3.4) that the bottom drag in the jet extension plays a role in balancing the wind stress curl. Figure 3.3d shows that in this jet extension the bottom drag is acting to flux vorticity along geostrophic contours and not across them. This indicates that the jet does not contribute to returning flow across geostrophic contours, thus does not act to balance the wind stress curl. However, this is a discussion of an inertial jet under a non-inertial mechanism. Under an inertial system (3.7) is extended to:

$$\rho_0 H \frac{D}{Dt}\left(\frac{f+\zeta}{H}\right) = \boldsymbol{\nabla} \times \frac{\boldsymbol{\tau}_w - \boldsymbol{\tau}_b}{H} + \mu \boldsymbol{\nabla}^2 \boldsymbol{\zeta}. \tag{3.8}$$

The introduction of ζ means that 'frictional' terms act across contours of $(f+\zeta)/h$ in order to balance the wind stress curl. Figure 3.4 shows $(f+\overline{\zeta})/h$ and $-\boldsymbol{k} \cdot \boldsymbol{\nabla} \times \overline{\boldsymbol{\tau}}_b$ for the same flat bottomed simulation as in Figure 3.2. Contours of $(f+\overline{\zeta})/h$ differ considerably to f/h in the region of the jet extension. It is shown that contours of $(f+\overline{\zeta})/h$ pass across the jet rather than align with it. This suggests that the bottom drag does in fact act as a balance for wind stress curl in regions of high inertia, supporting gyre circulations.

Recall that from equation (3.4), the absence of $\beta\overline{v}$ suggests it is a transport term for the sources and sinks of vorticity rather than a source or sink itself. Inertia is also absent in (3.4) indicating that it takes a similar role to $\beta\overline{v}$ in transporting the vorticity. The appearance of the eastward jet represents a spatial shift in the vorticity balance where a proportion of bottom drag sink shifts downstream and is balanced by inertia rather than the $\beta\overline{v}$ term. It remains the bottom drag which allows flow to return to the interior. In regions of highly inertial flow the linear theory of f/h may not apply and an extension to $(f+\overline{\zeta})/h$ is required.

3.6 Wind Forcing Under the Introduction of Topography

Under the introduction of topography, geostrophic contours are distorted which alters the vorticity balance. This adjustment has implications on gyre transport. Figure 3.5 shows gyre strength for the ridge variations shown in Figure 3.1 with a larger range of topographic heights. For the southern gyre there is a clear asymptotic trend. For the lower heights, the

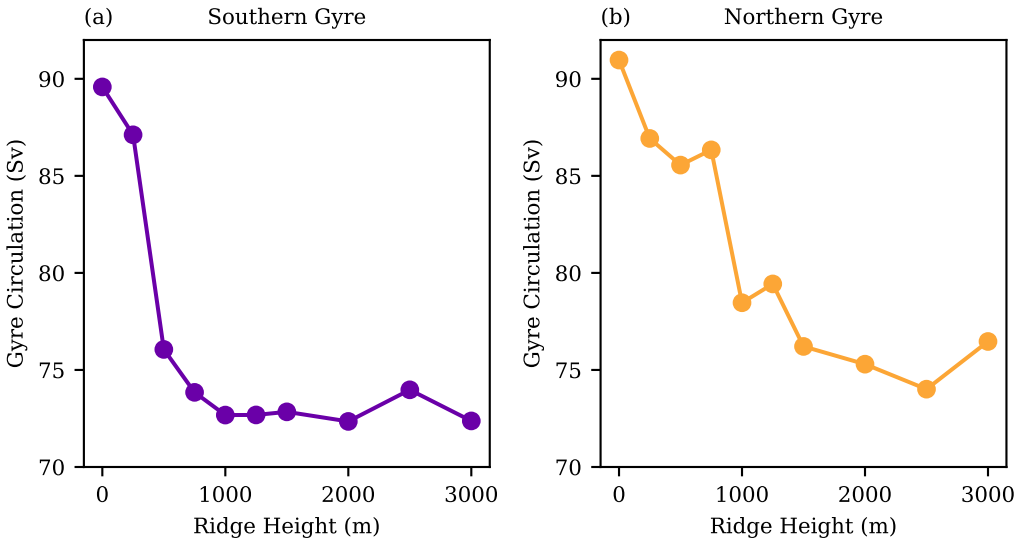

Figure 3.5: Gyre strength in Sverdrups for differing ridge heights. The results are from models 01-10.

gyre strength has a sharp reduction for increased topographic height. As ridge height exceeds 1000 m, the trend levels off and there is little change with ridge height variation. Although the northern gyre shows more variability and has less of an asymptotic tendency, it does also display a similar relationship; there is a general reduction in the northern gyre strength with increased ridge height.

As the gyre strength is largely set by the input of vorticity by the wind stress curl and the sink of vorticity arising from 'frictional' terms the relationship in gyre transport can be investigated through the vorticity balance. Although the wind stress is kept constant between results shown in Figure 3.5 it will be shown here the input of vorticity via the wind stress is altered for changing topography. The gyre strength is associated with this adjustment in the vorticity through Sverdrup balance.

Sverdrup balance takes a different form in the presence of variable topography. Where water column thickness varies, Sverdrup balance is distorted to act across geostrophic contours rather than lines of latitude. In this situation the balance is termed *topographic Sverdrup balance*. The extension to topographic Sverdrup balance is derived by Holland [1967] under the assumption of a linear, homogeneous and inviscid ocean and is defined as:

$$H\rho_0 u\frac{d}{dx}\left(\frac{f}{H}\right)+v\frac{d}{dy}\left(\frac{f}{H}\right)=-\frac{\boldsymbol{\nabla}\times\boldsymbol{\tau}_w}{H}. \tag{3.9}$$

Gyre strength is largely linked to the ability of flow to cross geostrophic contours. Through topographic Sverdrup balance, flow is permitted to cross geostrophic contours by an input of vorticity from wind stress. If this input of vorticity over a gyre changes, the gyre strength will adjust. Model results of Nadeau and Ferrari [2015] show this relationship in a channel domain with both an ACC and counter-rotating gyres. In these simulation the zonal length of the domain is varied, adjusting the area over which Sverdrup balance can act. The results show that as the domain is extended the gyre strength is significantly increased. It is possible to calculate the total influence of Sverdrup balance on gyres by integrating the wind stress curl which forces them.

Figure 3.6 shows the wind stress lying over each gyre which formed in simulations presented by Figure 3.1. The northern and southern gyres represent subtropical and subpolar gyres respectively. The northern and southern gyre boundaries occur between geostrophic contours which align with the contours of zero wind stress curl in the flat bottom interior [Veronis, 1966b]. This means that the boundary between the gyres lies along geostrophic contours which pass through the central latitude of the domain interior. In the case with no topography the total input of vorticity by the wind stress is equal for both gyres. This is not the case for the simulations with 500 and 2000 m topography. The geostrophic contours are deflected northward and the southern gyre flow passes through a region of opposing wind stress curl. Where flow travels through a region of opposite wind stress curl the total integral of Sverdrup balance over the gyre is reduced.

Figure 3.7a shows the area integral of the gyre forcing from the wind stress curl between the bounding geostrophic contours of each gyre. It appears, for the lower heights, that the wind forcing decreases with increased ridge height. From Figure 3.6 it is shown that this is due to a decreased flat bottom area over which the wind forcing acts. The forcing of the southern gyre is reduced much more for the same ridge variation in this range. This can be attributed to the area of opposite curl which the southern gyre passes through. When the ridge height is increased the area of opposite curl which the southern gyre passes through increased and the contribution from the opposed wind stress curl is heightened. For the southern gyre, the total wind stress curl shows an increase for increased ridge height above 1000 m. As the geostrophic contours become blocked by the northern boundary the area of opposite curl which the southern gyre passes through is reduced. The small increase in forcing could be attributed to this change in geostrophic contours.

Figure 3.7b shows the relationship of gyre strength to ridge height for ridge same ridge height variations. Though there are clearly other processes involved, the general decrease in gyre strength with increased ridge height suggests that the change in wind stress curl forcing has an effect on the gyre strength.

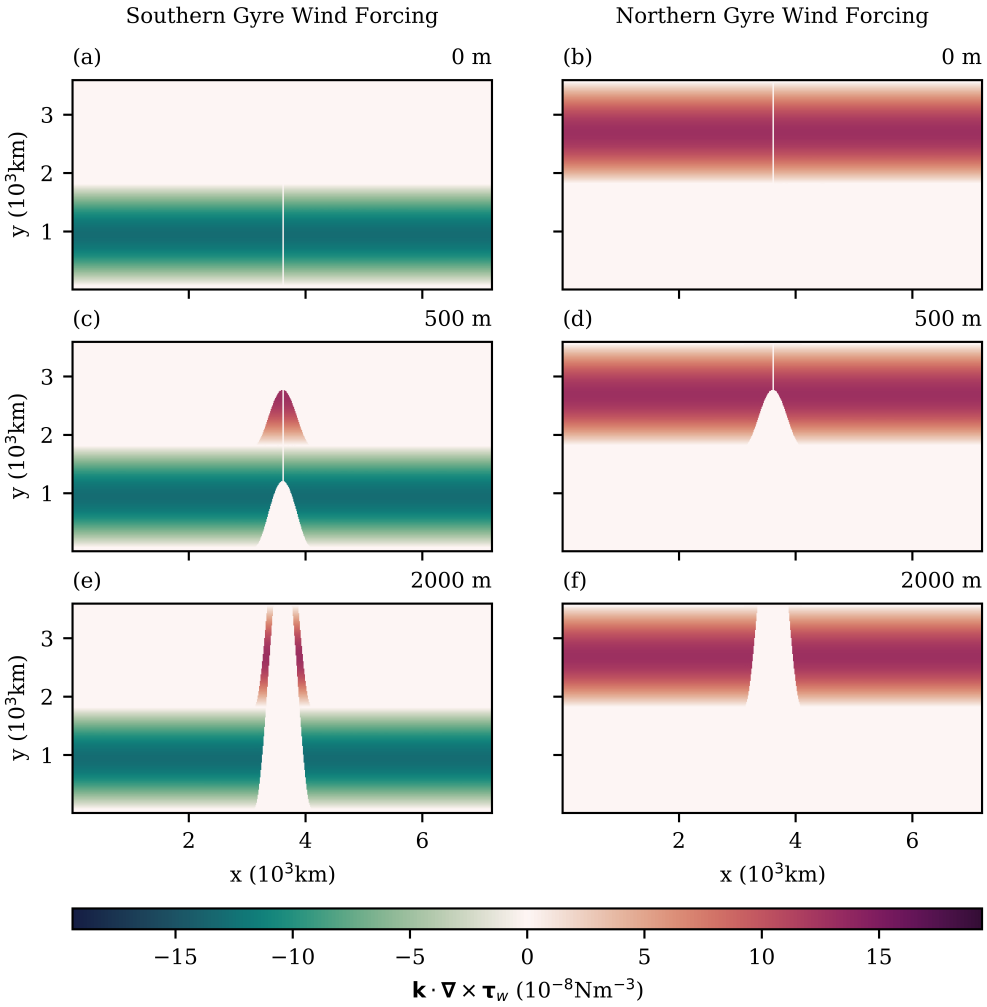

Figure 3.6: Wind forcing over each gyre for varying topographic height. (a): Southern gyre forcing for a case with no bottom topography. (b): Northern gyre forcing for a case with no bottom topography. (c): Southern gyre forcing for a domain with topography of 500 m in height. (d): Northern gyre forcing for a domain with topography of 500 m in height. (e): Southern gyre forcing for a domain with topography of 2000 m in height. (f): Northern gyre forcing for a domain with topography of 2000 m in height. Results are from models 01, 03 and 08.

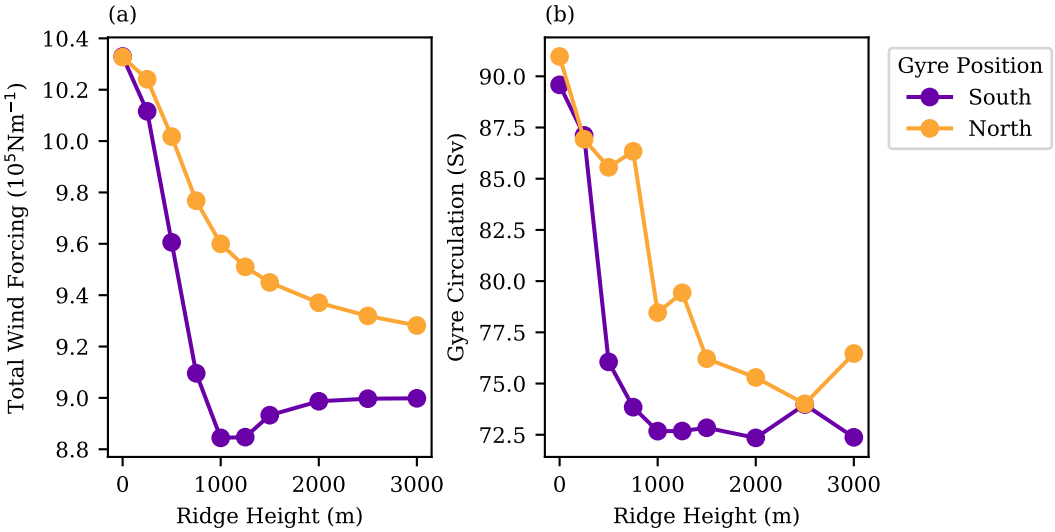

Figure 3.7: Wind forcing over each gyre and the resulting gyre circulation volume transport. Purple and orange represent the southern and northern gyres respectively (a): The area integral of wind forcing fields for each ridge width shown in Figure 3.6. (b): The gyre circulation for each ridge width. Results are from models 01, 03 and 08.

3.7 Topographic Effects on the Frictional Balance

The introduction of topography not only affects the gyre strength but it also creates a transition in the vorticity dynamics of the frictional terms. Figure 3.8 shows terms of the vorticity budget for the three variants of topography presented above in Figure 3.1. In the case with no topography, the bottom drag is balanced by $\beta\overline{v}$ along the western boundary. As topography is introduced and increased, the shift in geostrophic contours causes transition in the balance. Where geostrophic contours intersect with the northern boundary the primary balance is between inertia and bottom pressure torque. This transition is described in Section 3.4.

It has been noted for the case with no topography that it's not just bottom drag at the boundary which is important for gyre circulation. The jet extension towards the interior, which has a vorticity balance between bottom drag and mean inertia also contributes to supporting a gyre circulation. The jet remains aligned with the geostrophic contours as the contours shift with changes in topography. It appears from Figure 3.8 that the bottom drag term becomes more important in this jet region than at the boundary for the topography of 2000 m.

The bottom drag is not the only 'frictional' term which is able to balance the wind

stress curl. Both viscosity and the eddy inertial term are also capable of providing the required vorticity sink. Figure 3.8 shows a breakdown of bottom drag, viscosity, the eddy inertial term and the inertial term associated with mean flow. In all three simulations the viscosity is negligible due to use of a low viscosity coefficient and a free slip boundary condition. It is possible that the eddy inertial term is influencing the system but the lack of coherence in the vorticity makes it difficult to diagnose. The response of these terms associated with varying topography is further investigated below.

3.8 Two Dynamical Regimes of the Frictional Effects

The transition in the vorticity budget for the variations in topography has implications for the dynamics and two regimes emerge. Figure 3.9 shows the response of the gyre transport in model domains with no topography and 2000 m high topography to changes in bottom drag coefficient. Bottom drag is a function of velocity and increasing the bottom drag coefficient means that lower velocities are requred to match the same vorticity sink. It may be expected that gyre strength reduces in with increasing bottom drag coefficient. In a flat bottom domain, gyre strength is shown to decrease for increasing bottom drag coefficient [Veronis, 1966b, Böning, 1986]. For the case with no topography in Figure 3.9 the results are in agreement with expectation, increasing the bottom drag coefficient tends to decrease the gyre transport. On the other hand, the gyre transport in the 2000 m case is insensitive to the increased drag coefficient.

Figure 3.10 shows vorticity terms for the 0 m simulation which are able to provide a balance for the wind stress and influence gyre transport. As before, the viscosity is negligible. The eddy inertial term is also irrelevant. The last two terms show that increasing the drag coefficient causes a retraction of the jet. Bottom drag is a function of velocity and when the bottom drag coefficient is increased, lower velocities are required to match the same vorticity sink. The current slows, damping the inertia. This jet extension arises from inertia. It is shown above that the jet extension is responsible for a spatial redistribution of the bottom drag effects. The retraction of the jet is thus association with a shift of the bottom drag sink into the western boundary. The change in gyre transport is linked to the reduced velocities which occur with increased bottom drag coefficient.

Figure 3.11 shows the same vorticity terms for the 2000 m case. In this situation, both inertial terms reduce with increased drag coefficient. Increasing bottom drag tends to reduce variability in flow causing a reduction in eddy formation. This causes the eddy inertial term to reduce in magnitude with increasing drag coefficient. There is little change in the magnitude and spatial distribution of the bottom drag term as the inertia reduces

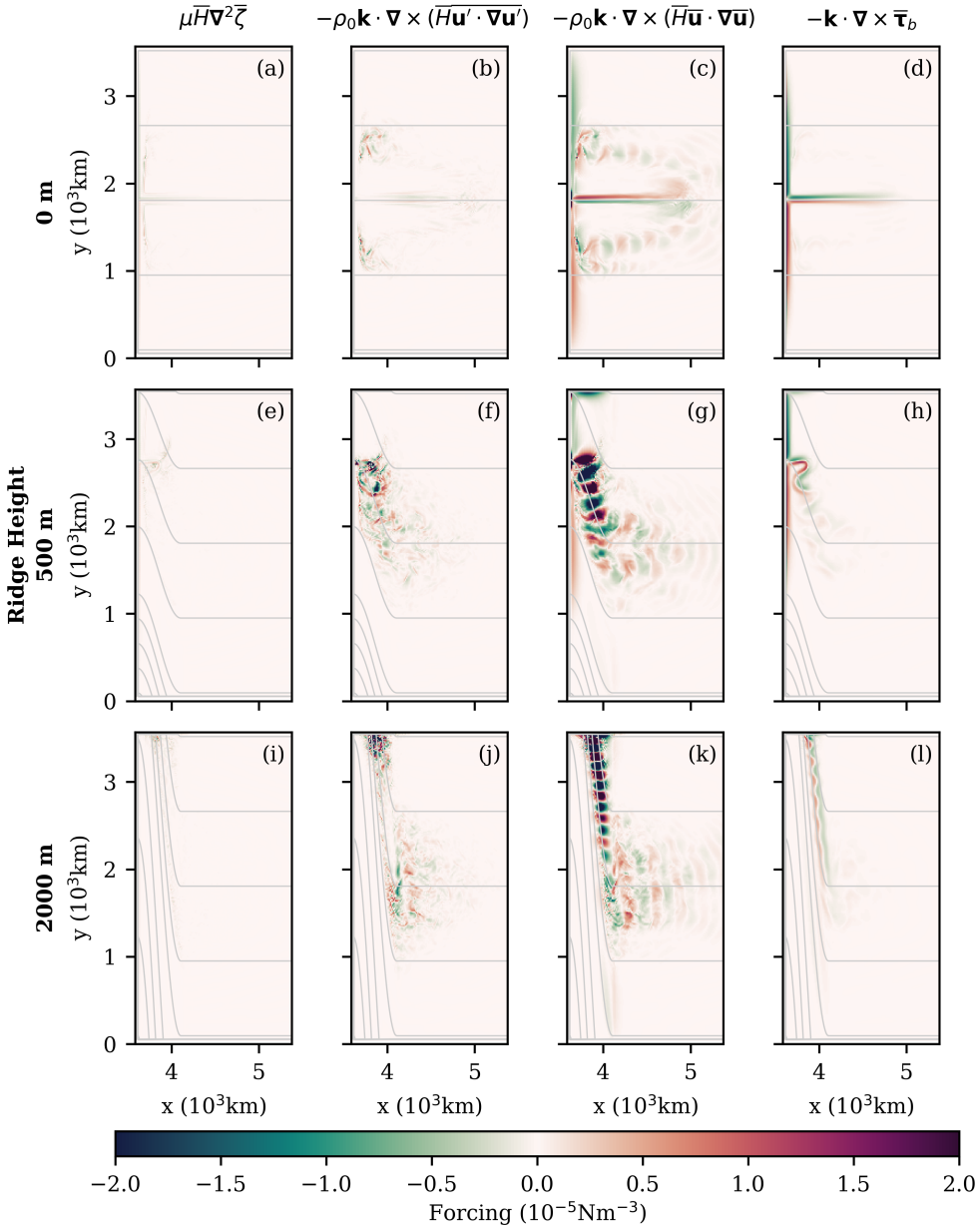

Figure 3.8: Terms of the barotropic vorticity equation for differing ridge heights in domains with the meridional wall. Rows are associated with particular ridge heights (0 m, 500 m and 2000 m). Columns represent differing barotropic vorticity terms (viscosity, eddy inertial term, mean inertial term and the bottom drag). Models shown are 01, 03 and 08.

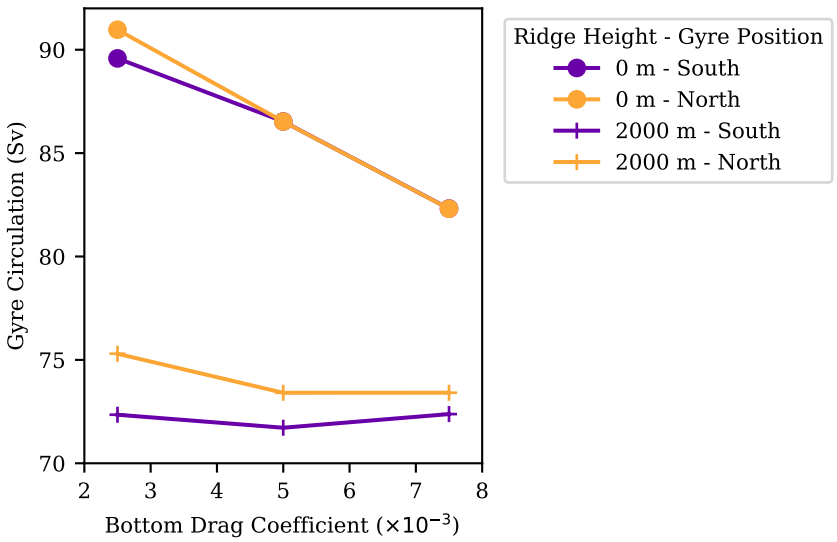

Figure 3.9: Gyre strength in Sverdrups for differing drag coefficients and topography. Results are from models 01, 08, 11, 12, 13 and 14.

suggesting that the bottom drag vorticity sink is not coupled with inertia over topography. The decoupling suggests that, unlike the case with no bottom topography, inertia is not balancing the vorticity in the bottom drag term in this jet extension. This suggests that the jet becomes dependent on the topography in place of the inertial effects. An increased gradient in f/h is related to smaller spacing between geostrophic contours and leads to higher velocities in the flow [Smith and Fandry, 1978]. As topography is introduced, gradients in f/h increase supporting the generation of a jet and introducing bottom pressure torques. Bottom drag arises to dissipate the relative vorticity generated by the topographic jet.

In the case with topography the magnitudes in the bottom drag remain unchanged in the jet for increased bottom drag coefficient. Bottom drag is dependent on velocities, as the bottom drag coefficient is increased a lower relative vorticity is required to generate the same bottom drag. The constant magnitudes in the bottom drag for increased bottom drag coefficient indicates that the relative vorticity is reducing. A reduction in relative vorticity can manifest in two ways, either through lowered velocity magnitudes or a broadening of the current. Figure 3.12 shows the bottom drag in 3.11 on a different scale. The space over which the vorticity sink occurs increases with increasing bottom drag coefficient. This suggests that the current broadens as the bottom drag coefficient increases. A broadening

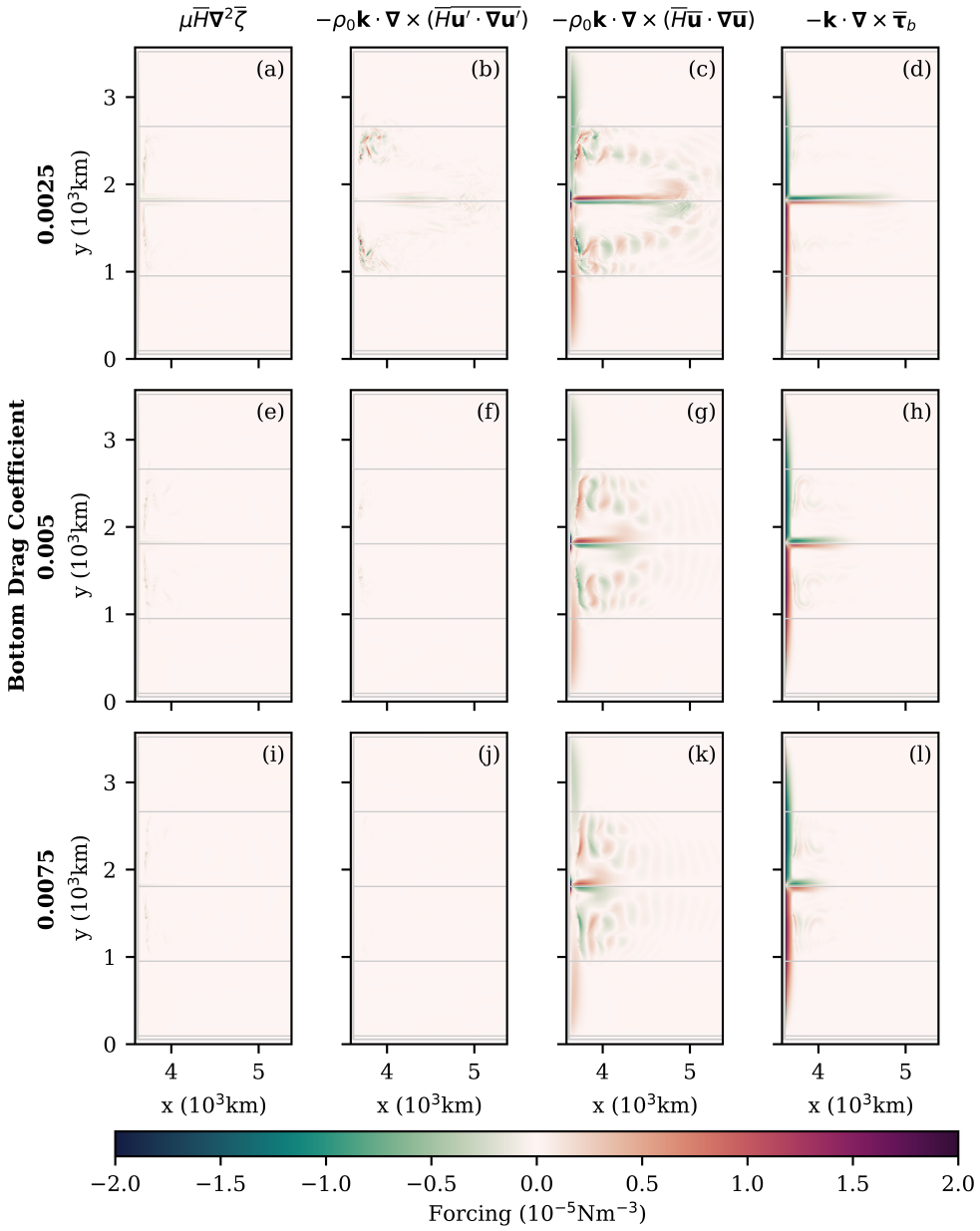

Figure 3.10: Terms of the barotropic vorticity equation for differing bottom drag coefficients in a domain with a meridional wall and no bottom topography. Rows are associated with particular bottom drag coefficients (0.0025, 0.005 and 0.0075). Columns represent differing barotropic vorticity terms (viscosity, eddy inertial term, mean inertial term and the bottom drag). Models shown are 01, 11 and 12.

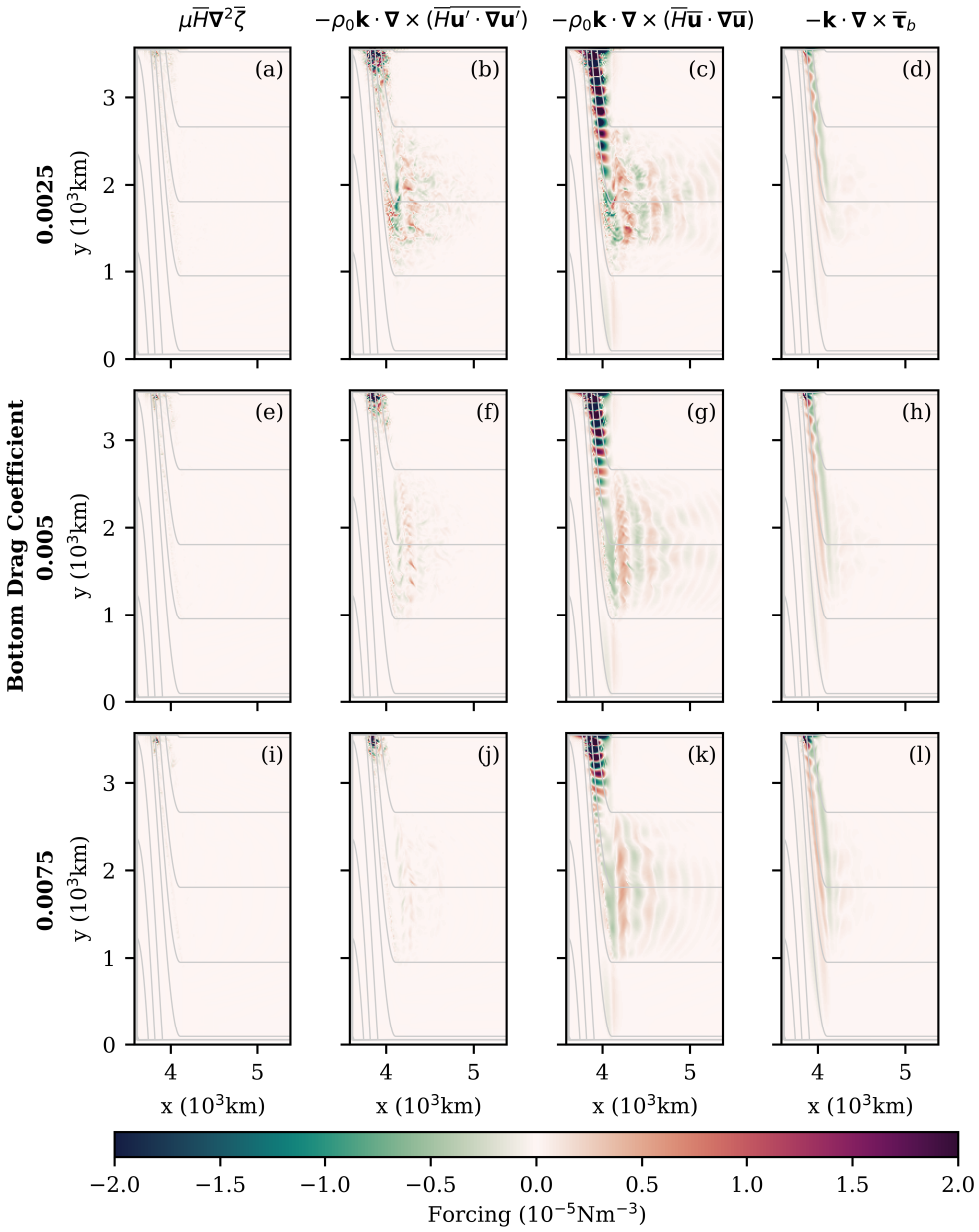

Figure 3.11: Terms of the barotropic vorticity equation for differing bottom drag coefficients in a domain with a meridional wall and 2000 m high bottom topography. Rows are associated with particular bottom drag coefficients (0.0025, 0.005 and 0.0075). Columns represent differing barotropic vorticity terms (viscosity, eddy inertial term, mean inertial term and the bottom drag). Models shown are 08, 13 and 14.

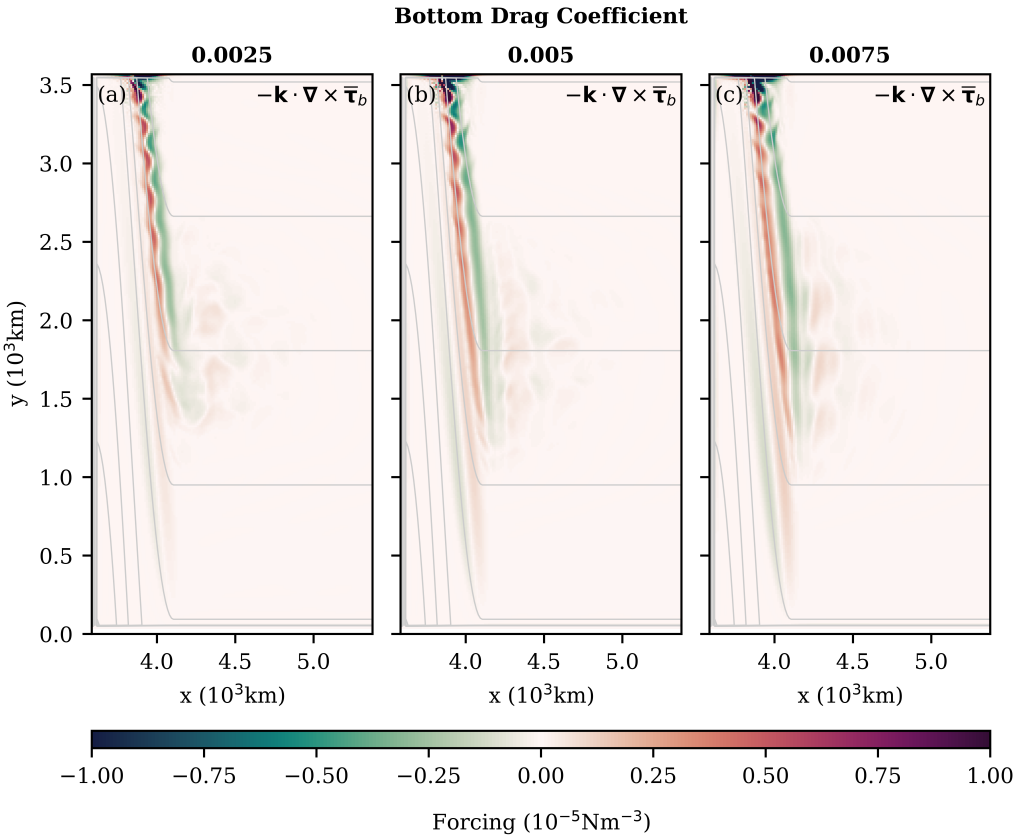

Figure 3.12: The bottom drag contribution to the barotropic vorticity budget for differing bottom drag coefficients in a domain with a meridional wall and 2000 m high bottom topography. (a) Bottom drag coefficients of 0.0025. (b) Bottom drag coefficients of 0.005. (c) Bottom drag coefficients of 0.0075. Models shown are 08, 13 and 14.

of the jet would result in an increased volume transport in the gyre. Thus, the flow must maintain the observed constant volume transport by also reducing velocity magnitudes.

3.9 Topographic Lee Waves

Figure 3.13 shows the 500 m and 2000 m high topography results shown in Figure 3.1 zoomed to the topographic region east of the central meridional wall. For both cases the geostrophic contours converge over the topography with an increasing gradient in f/h as the water column shallows. As the flow follows these geostrophic contours it also converges up-slope and diverges as it returns eastward down the slope. The convergence and divergence of the flow affects the resulting velocities. A convergence of the flow increases its velocity

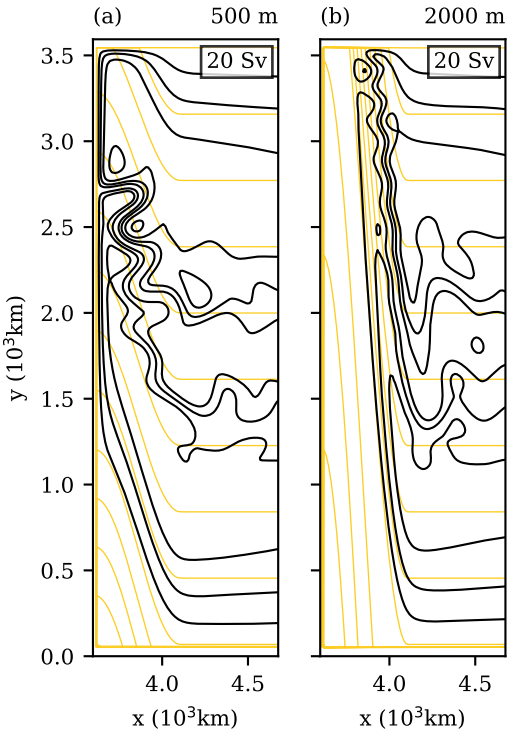

Figure 3.13: Plan view of barotropic simulations with a meridional wall and a ridge that varies in height. Results shown are zoomed to the topographic region east of the central meridional wall. (a) model 03 with 500 m high topography. (b) model 08 with 2000 m high topography. Streamlines are shown in black. Orange line signify contours of f/h. The box to the top-right of each panel signifies the the contour spacing for each streamfunction.

and divergence has the opposing effect. This means that velocities are generally enhanced over the topography in comparison to the interior flow. The geostrophic contours are more closely spaced over the topography for the 2000 m case compared with the 500 m case. This means that the topographic enhancement of the velocities is greater for the case with 2000 m high topography.

Both results in Figure 3.13 show a non-uniform inertial response. A stationary meander develops in the flow returning eastward to the interior which is aligned with geostrophic contours. Yet, no such inertial effects are present in the up-slope, westward flow. The non-uniformity also shows up in the barotropic vorticity equation in Figure 3.3. The stationary meander results in a generation of vorticity in the eastward flow which leads to the distortion of the bottom pressure torque. This distortion is not present for the westward flow. Analysis by Holland [1967] suggests that the non-uniform flow pattern is a result of Rossby waves. As shown above through (3.5), stationary Rossby waves only develop in eastward flow. The up-slope flow has no eastward component, however, the zonal component of the down-slope flow is eastward, permitting Rossby waves to form.

The characteristics of the topography has a bearing over the resulting stationary Rossby wave that develops. The wave number of a stationary Rossby wave is dependent on the eastward flow velocities. As topographic height can influence the eastward velocities of the flow through gradients in f/h, it can have an impact on the stationary meander which forms. The wave number of a stationary Rossby wave which develops on the eastern side of a topographic feature increases significantly for an increased topographic height [Anderson and Killworth, 1977]. The increase in topographic height from 500 metres to 2000 metres in Figure 3.13 results in faster eastward velocities confined to a smaller space. The enhanced velocities with a higher topographic feature indicate a stationary Rossby wave of smaller amplitude but higher wave number, aligned with geostrophic contours.

Stationary Rossby waves which form in the lee of topographic features are usually referred to as topographic lee waves. Hughes [2005] observed topographic lee wave meanders in the Southern Ocean and indicated that they are barotropic in nature due to the length scales over which the meanders occur.

3.10 Summary

This chapter provides an outline of the dynamics behind gyre circulation in a closed basin and introduces some key concepts with which to discuss gyres. Gyres form under the basis of wind stress curl forcing flow across geostrophic contours to a different value of f/h and 'frictional' terms permitting flow to return back to a position with the original value

of f/h. Topography distorts dynamical balances within gyres. With the introduction of topography, geostrophic contours are deflected and the effectiveness of the wind stress curl to force gyre flow is altered. Changes in topography lead to a change in gyre transport.

In a highly inertial system a zonal jet forms in the return flow towards the interior of a domain. The bottom drag which occurs within the inertial jet contributes to the 'frictional' balance of the wind stress curl. A similar jet arises in the case with variable topography. This jet has a different dynamical balance to the case where there is a uniform water column depth. In the case of the flat bottom, the jet is formed by an inertial overshoot and responds to changes in bottom drag coefficient dampening inertial effects. Over variable topography a change in the bottom drag coefficient has little affect on the jet suggesting it is not formed by under the same dynamics. It is indicated that the jet in this case forms due the topography creating a convergence of flow. Both of these jets give rise to bottom drag which acts as sink of vorticity and permits gyres to form.

4 The Dynamics of Southern Ocean Gyres

The discussion so far has focused on the theory of Gyre formation in closed basins. This is representative of circulations such as the North Atlantic gyre which are bounded by continents to the east and west. The primary interest of this study is the Southern Ocean dynamics and not all of the North Atlantic (closed basin) concepts necessarily apply. In this chapter, attention is directed to the Southern Ocean and an investigation is made into relevance of classical Gyre theory to Southern Ocean gyres. The first part of this chapter discusses the current knowledge on Southern Ocean gyre dynamics. In the latter part, new results are presented on a topographic balance that is unique to many of the Southern Ocean gyres.

4.1 Existing Theories of Southern Ocean Gyres

Investigations into the formation of Southern Ocean gyres are sparse in comparison to the North Atlantic gyre. In past studies, research on gyres has been generally down weighted in favor of the ACC. The appearance of gyres in numerical simulations of the Southern Ocean is variable and where they do appear in results they are usually neglected from dynamical discussion.

4.1.1 Examples of Gyres in Existing Results

Examples of gyres occurring in simulations of the Southern Ocean are given by Wolff et al. [1991], Ishida [1994], Krupitsky et al. [1996] and Jackson et al. [2006]. The existence of gyres in these models is attributed to the blocking of geostrophic contours [LaCasce and Isachsen, 2010]. This is the same mechanism by which gyres form in the theory representative of the North Atlantic, presented in Chapter 3. In simulations of Ishida [1994] geostrophic contours are blocked with a meridionally aligned wall. On the other hand, in Krupitsky et al. [1996], where no meridional wall exists, geostrophic contours are blocked by the northern boundary. These two variations in model set-up are much like the topographic variations shown in Figure 3.1. In a closed basin with no variable topography (Figure 3.1d) all geostrophic contours are blocked with a western boundary. In a closed basin with a large topographic feature (Figure 3.1f) they are blocked with the northern boundary. Moreover, under the premise that the gyres form due to the blocking of geostrophic contours, the dynamics of these channel and basin set-ups are the same.

Figure 4.1 shows results of the removal of the meridional wall for Figure 3.1f, creating a channel domain similar to Krupitsky et al. [1996]. The flow follows almost the same pat-

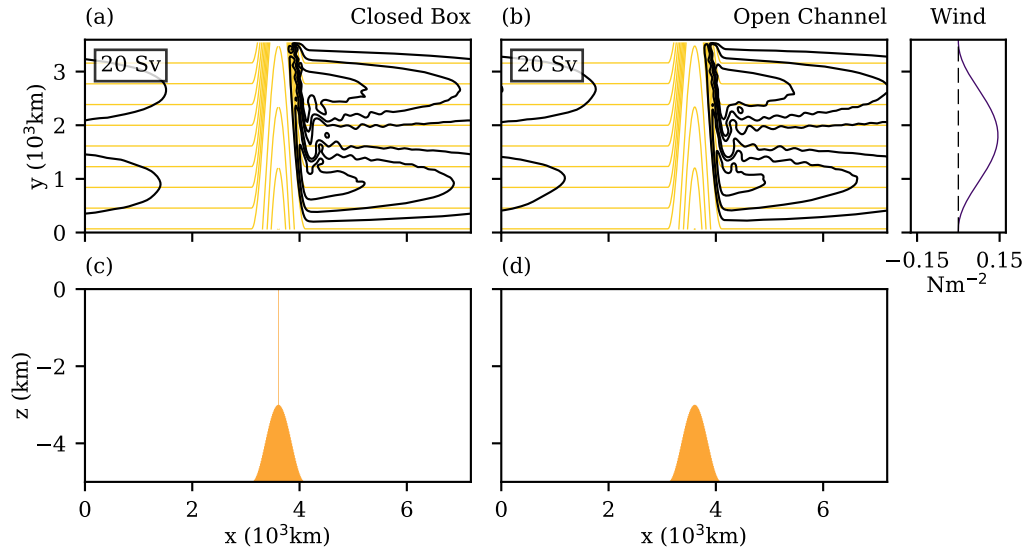

Figure 4.1: Plan view of the barotropic streamfunction for two simulations. A side profile from the south is shown in (c) and (d) to highlight the topography. (a): A closed domain with a meridional wall with sloping topography of 2000 m either side (model 08). (b): Same as (a) but with the meridional wall removed becoming an open channel set-up (model 15). Streamlines are shown in black. Orange lines represent geostrophic contours. The box to the top-left signifies the contour spacing of the streamfunction in Sverdrups.

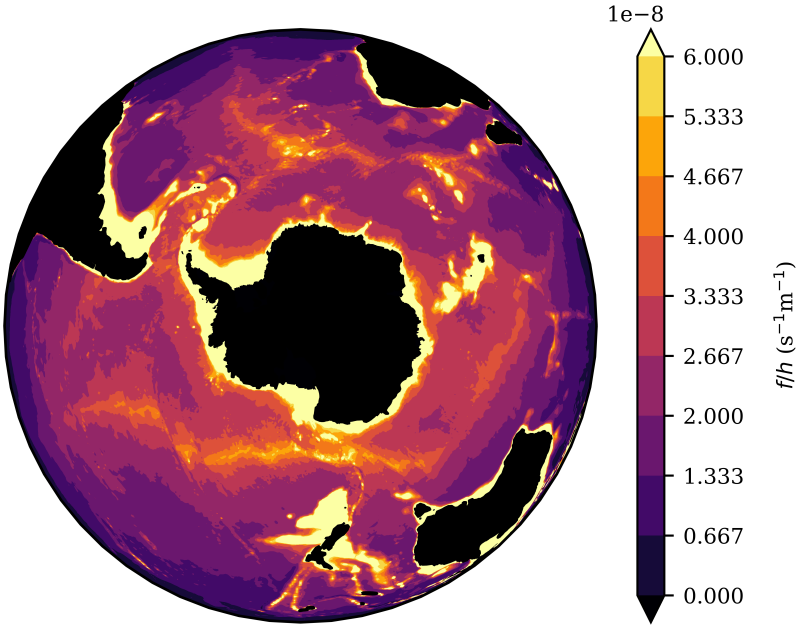

Figure 4.2: f/h for the Southern Hemisphere calculated on a 0.5 degree grid.

tern regardless of the presence of the meridional wall. The total eastward volume transport transitions from 0 Sv for the closed domain to ∼2 Sv for the channel domain. Figure 4.1 confirms both the northern boundary influence on the gyre formation here and the equivalency between closed basins and channels with blocked geostrophic contours.

Figure 4.2 shows f/h for the Southern Ocean. It could be argued that features such as the Weddell Gyre appear under dynamics akin to the North Atlantic gyre. There is the Antarctic Peninsula to the west and no clear path for geostrophic contours through Drake Passage to the north. This means that the dynamics could be similar to that of a closed basin, where all geostrophic contours are blocked by a western continental boundary. In this situation investigations such as Ishida [1994] may be appropriate. It is clear that some subpolar gyres of the Southern Hemisphere form under a different dynamical scenario to the closed basin with a western boundary. Gyres such as the Ross Gyre and the Kerguelen Gyre form in the absence of a meridional wall. This makes the Krupitsky et al. [1996] simulations a more appropriate representation of these gyres.

4.1.2 The Influence of Blocked and Unblocked Geostrophic Contours

The Southern Ocean flow is composed of both closed gyre circulations and circumpolar flow (the ACC). The channel model in Figure 4.1b shows gyre formation but fails to show any signs of a circumpolar flow. This is because all geostrophic contours are blocked; generally circumpolar flow occurs along unblocked geostrophic contours [Krupitsky et al., 1996, Hughes et al., 1999]. It is possible to have both a circumpolar flow and gyres in a channel by having both blocked and unblocked geostrophic contours in the domain. Nadeau and Ferrari [2015] show that, in a channel model, the existence and size of the gyres that form are dependent on the range of blocked f/h by the northern boundary and the strength of circumpolar flow is dependent on the range of unblocked f/h. The range of blocked geostrophic contours is larger for a higher ridge. In Figure 4.3 the ridge height is progressively reduced in a domain with no meridional wall. The flow transitions from a scenario where there are two counter rotating gyres and little net zonal transport to a regime dominated by net eastward flow. The northward deflection of the geostrophic contours decreases with a decreasing ridge height, so the range of unblocked geostrophic contours (orange fill) increases. Since the gyres here are dependent on the range of blocked geostrophic contours, a reduction in ridge height decreases gyre strength. At the same time, a net zonal transport is formed in the newly unblocked region. As these unblocked contours pass through the entire domain in a zonal sense, a zonal flow is forced through the channel. The Southern Ocean has a combination of a dominant zonal flow, the ACC, and series of subpolar gyres that lie between the ACC and the Antarctic continent. Figure 4.3b has a combination of blocked and unblocked geostrophic contours permitting both a subtropical gyre and zonal flow. However, Figure 4.4 shows the same simulation with different contouring of the streamlines and there is no sign of a cyclonic, subpolar gyre in the south of the domain. Under the theory presented so far, the absence of a subpolar gyre is due to the presence of unblocked geostrophic contours occupying the space where such a gyre would preferentially develop. However, results presented by Nadeau and Ferrari [2015] show the formation of a southern gyre in a region of unblocked geostrophic contours. The occurrence of this gyre is not discussed in Nadeau and Ferrari [2015]. The dynamics behind the formation of gyres in regions of unblocked geostrophic contours will be discussed in the latter part of this chapter.

4.1.3 The Vorticity Balance for Blocked and Unblocked Geostrophic Contours

There is a distinct dissimilarity between flow that occurs in a region of blocked and unblocked geostrophic contours. Here the barotropic vorticity equation is used to build intu-

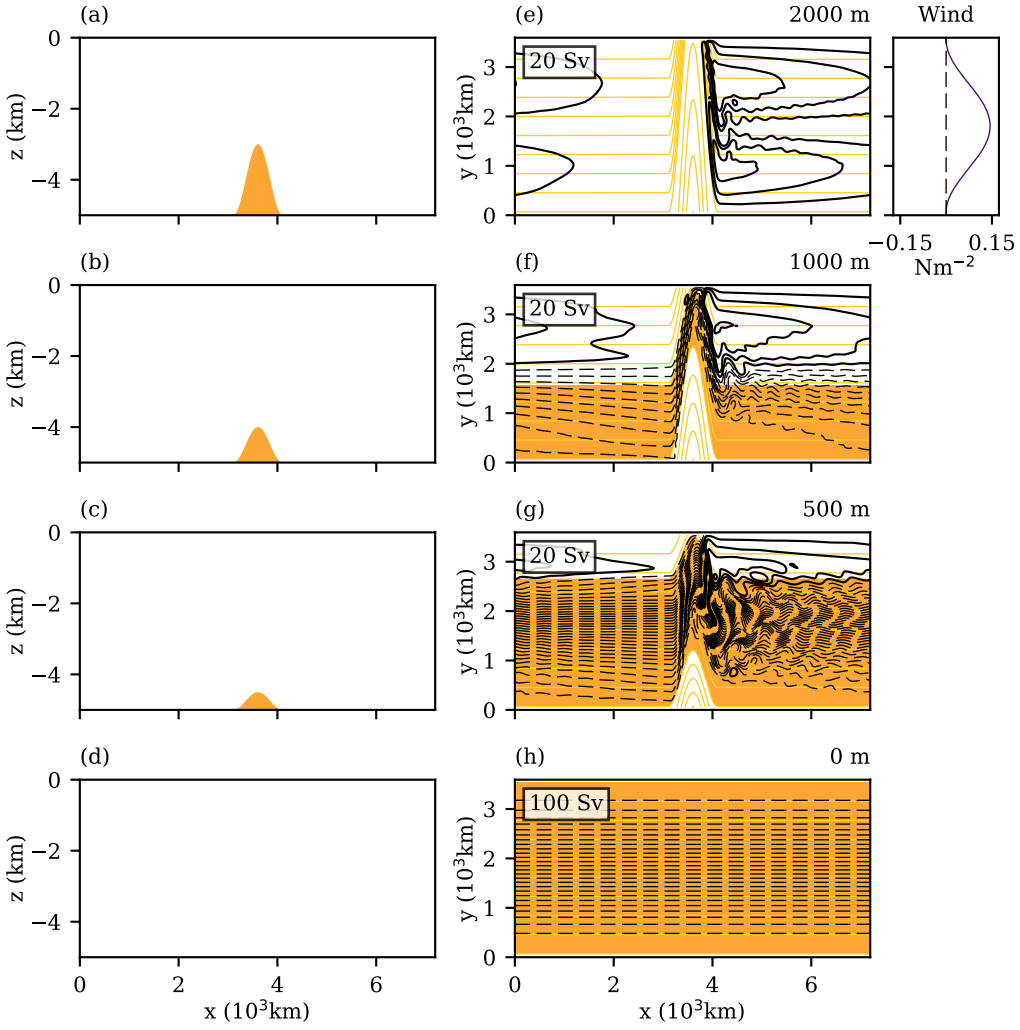

Figure 4.3: Plan view of the barotropic streamfunction for channel simulations with a meridional ridge topography varying in height. A side profile from the south is shown in (a)-(d) to highlight the topography. The ridge heights are: (a,e) 2000 m, (b,f) 1000 m, (c,g) 500 m and (d,h) 0 m. Results are from models 15-18. The box to the top-left of (e)-(h) signifies the contour spacing of the streamfunction in Sverdrups. Streamlines are shown in black; dashed lines cover the entire domain (representing an ACC), solid lines do not cover the domain (representing gyres or stationary eddies). Yellow lines are geostrophic contours. The yellow fill represents any region of unblocked geostrophic contours, whereby contours do not intersect with a zonal boundary.

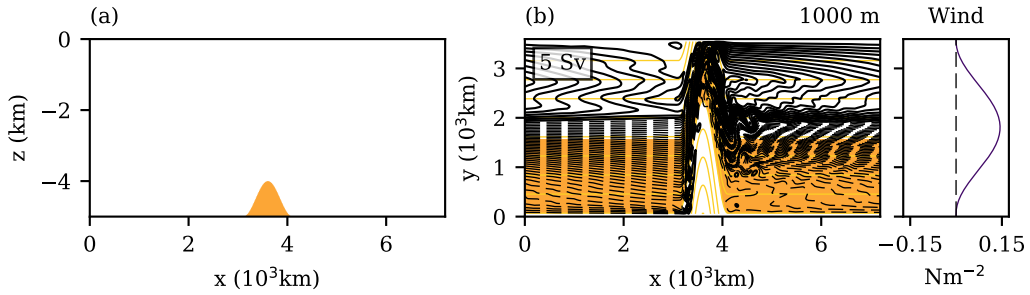

Figure 4.4: Plan view of the barotropic streamfunction for channel simulations with a meridional ridge topography of 1000 metres in height (model 16). A side profile from the south is shown in (a) to highlight the topography. For colouring and contouring see Figure 4.3.

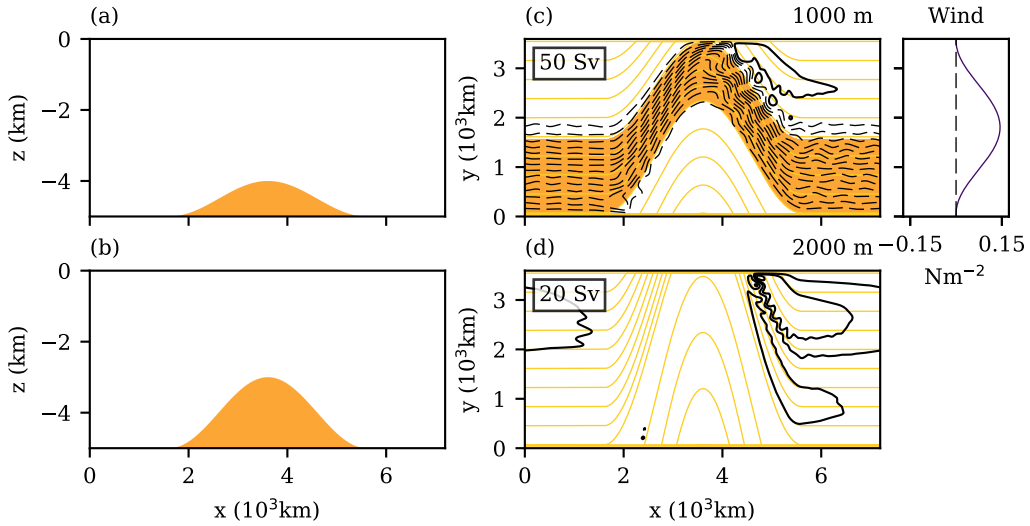

Figure 4.5: Plan view of two barotropic channel simulations with a 4000 km wide ridge. The wind forcing profile is plotted to the right and topography profiles to the left. (a): 1000 m ridge height (model 19). (b): 2000 m ridge height (model 20). For colouring and contouring see Figure 4.3.

ition and highlight the dynamical differences that occur between each characteristic flow pattern. Figure 4.5 shows streamlines for two simulations with differing ridge heights, 1000 m and 2000 m. The ridges are wider than in previous simulations, a choice made to exaggerate the different flow characteristics over the topography. Gyres are dominant in the 2000 m ridge case and net zonal flow is dominant for the 1000 m ridge. In the 2000 m case all geostrophic contours are blocked whereas the 1000 m case has significant area of unblocked geostrophic contours. Figure 4.6 shows the important vorticity terms of (3.1) for both the 1000 m and 2000 m ridge height cases. There is a clear adjustment in the barotropic vorticity balance between the two simulations.

The barotropic vorticity budget shows that away from the ridge, for both ridge heights, the flow is dominantly in Sverdrup balance. This is comparable to the closed domain with a meridional wall (Figures 4.6c, 4.6d, 4.6g and 4.6h). The vorticity input from the curl in the wind stress is balanced by a meridional flow. Due to the variable topography, topographic Sverdrup balance (see Section 3.4) should be the relevant balance of the wind stress here, however, the response is simplified in the flat interior. Although the meridional component of the flow due to Sverdrup balance is more recognisable in the 2000 m case there is still a clear meridional influence with the smaller, 1000 m ridge.

For both cases, the northward excursion of geostrophic contours over the ridge creates a vorticity balance between $\beta\overline{v}$, $\boldsymbol{k}\cdot\boldsymbol{\nabla}\times\overline{H}(\overline{\boldsymbol{u}}\cdot\boldsymbol{\nabla}\overline{\boldsymbol{u}}+\overline{\boldsymbol{u}'\cdot\boldsymbol{\nabla}\boldsymbol{u}'})$ and $\boldsymbol{k}\cdot\nabla\overline{p}_b\times\nabla h$, the bottom pressure torque. This balance is consistent with results from Hughes and De Cuevas [2001]. The inertial contribution to this balance arises from the topographic Rossby waves distortion discussed in Chapter 3. This vorticity balance has a different spatial pattern for each ridge height. For the 1000 metre ridge height case, the unblocked geostrophic contours cause the flow to pass over the ridge, creating a zonal dipole in $\beta\overline{v}$ and an equal and opposite dipole in the bottom pressure torque (modulated by the inertia). In the 2000 m ridge height case, however, the blocked geostrophic contours restrict cross-ridge flow and cause a different vorticity pattern. This balance bears a close similarity to the case with the ridge and meridional wall (Figures 3.3i-l). The flow moves meridionally in the interior due to Sverdrup balance. As flow cannot cross the ridge it must return meridionally in the opposing direction to conserve mass. This return flow occurs via a western boundary current on the east of the ridge. The vorticity input by the meridional flow in the western boundary current is also supported by the bottom pressure torque. Where the flow meets with the northern boundary it is forced back across geostrophic contour via frictional effects (not shown).

The main dynamical difference between the two scenarios is the means by which flow is returned across geostrophic contours. In both cases fluid is advected meridionally via

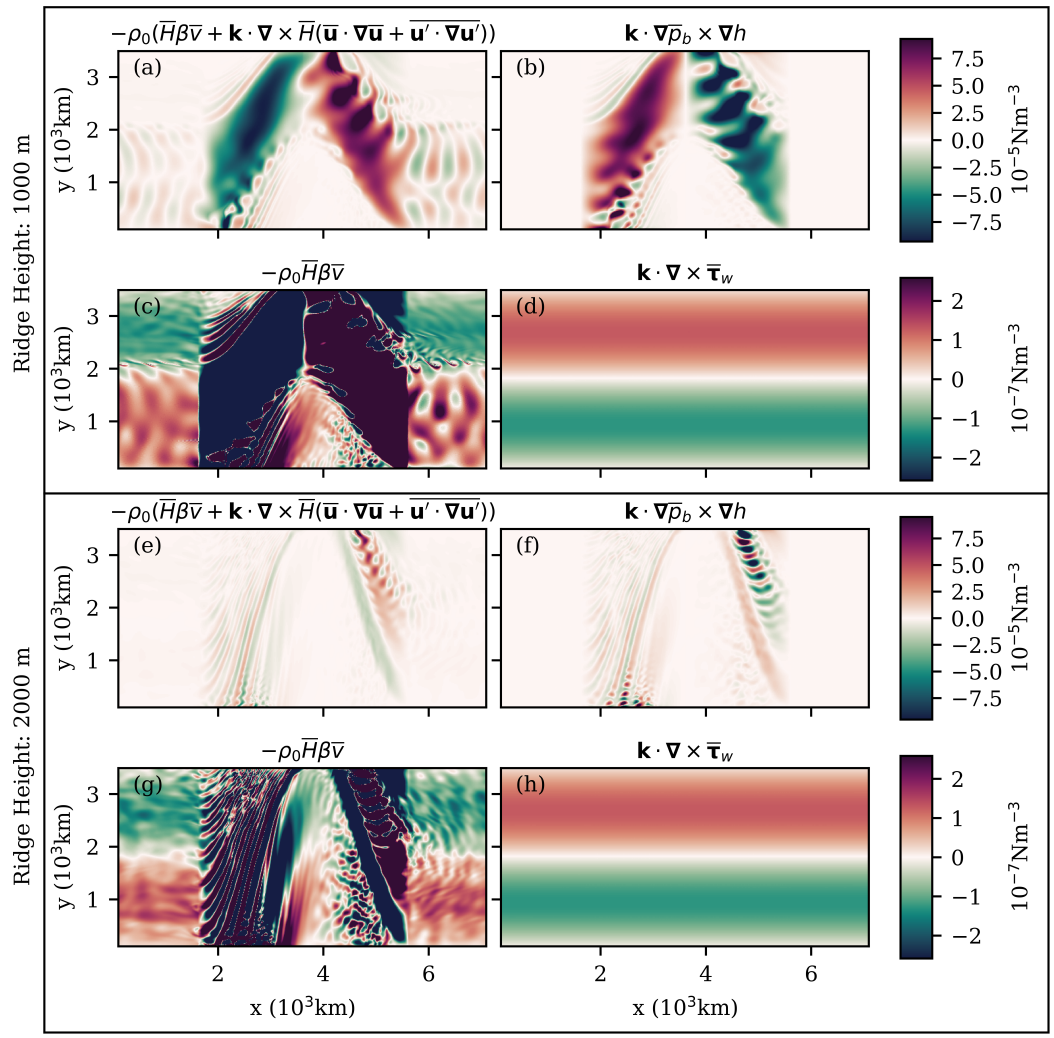

Figure 4.6: Terms of the barotropic vorticity balance for two model runs (a)-(d) for a 1000 metre ridge height (model 19) and (e)-(f) for a 2000 m ridge height (model 20). The panels are plotted on two colour scales: (a), (b), (e) and (f) are scaled to the bounds of $\boldsymbol{k}\cdot\nabla\overline{p}_b\times\nabla h$; (c), (d), (g) and (h) are scaled to the bounds of $\boldsymbol{k}\cdot\boldsymbol{\nabla}\times\boldsymbol{\tau}_w$.

topographic Sverdrup balance to a different value of f/h. In the 2000 m case, gyres form and flow is returned to its original value of f/h through frictional effects at the point where the geostrophic contours are blocked. However, gyres are absent in the 1000 m case. The flow which is advected meridionally by topographic Sverdrup balance is returned across geostrophic contours by a mechanism which does not involve a western boundary current.

4.2 The Influence of Topographic Gradients on Gyres

Thus far, gyre formation has been linked to the blocking of geostrophic contours [Nadeau and Ferrari, 2015]. This theory does not strictly apply as results are shown by Nadeau and Ferrari [2015] in which gyres form in regions of unblocked geostrophic contours. A discussion is given below showing that the formation of gyres due to blocked geostrophic contours may also be inadequate to explain features such as the Ross Gyre. It is clear that topography plays a central role in the formation of gyres in the Southern Ocean, yet the mechanisms behind their formation are not fully understood. The analysis in this subsection explores a new avenue, providing further insight into the formation of gyres in the Southern Ocean. In particular, an investigation is made into the effects of topographic gradients on the characteristics of gyre formation.

4.2.1 The Control of Ridge Width on the Vorticity Balance

To test the effect of ridge width on gyre circulation Figure 4.7 shows the streamfunction for three simulations where ridge width is varied. All geostrophic contours are blocked by the northern boundary so there is little net zonal transport in all three simulations and gyres dominate. Further, as it is only ridge width that varies, the range of f/h which intersects with the boundaries is fixed between simulations. The results show that a wider ridge leads to a decreased gyre transport. As ridge width increases there is a decreased gradient in f/h over the topography.

In the previous chapter it was shown that the inertial influence over the spatial distribution for the bottom drag vorticity sink is diminished with the introduction of topography. Over variable topography the bottom pressure torque takes over the role of bottom drag in being the primary balancing term for the vorticity generated by the inertia. This transition results in gyre transport becoming insensitive to changes in bottom drag coefficient. Figure 4.8 shows terms of the vorticity budget for the three simulations shown in 4.7. The vorticity balance shows that with higher gradients in f/h there is an increased downstream extension of the bottom drag term (Figures 4.8d, 4.8h and 4.8l). This relationship supports the idea that over variable topography the extension in the bottom drag

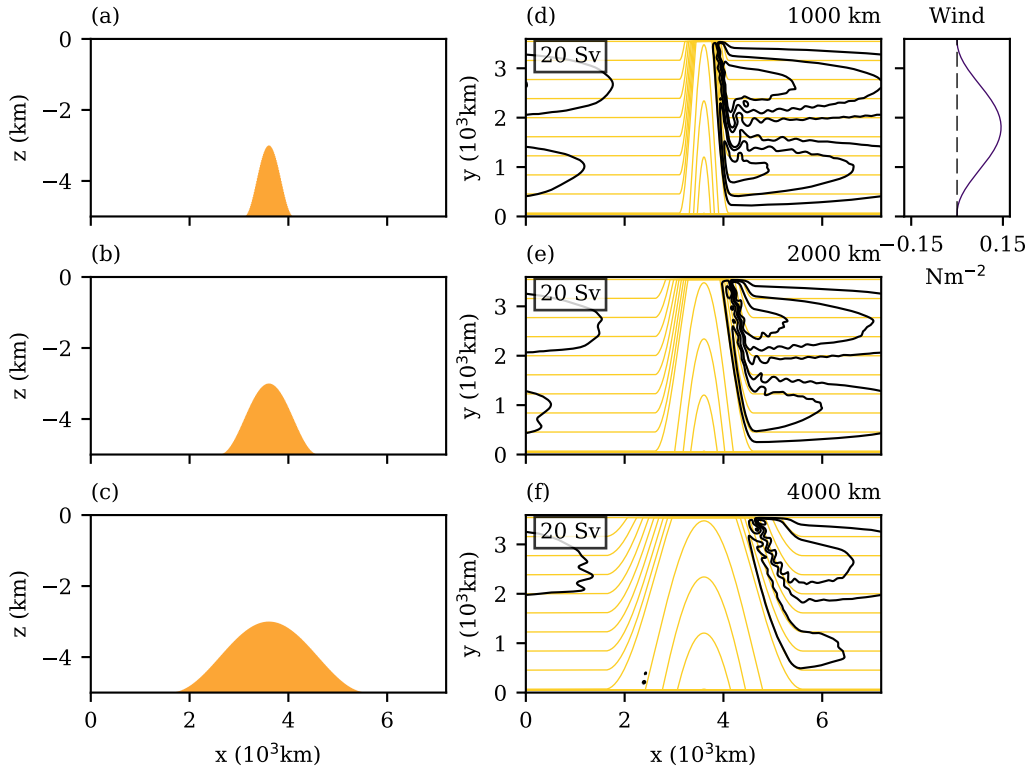

Figure 4.7: Plan view of the barotropic streamfunction for channel simulations with a ridge height of 2000 m. The ridge width varies for each simulation and a side profile highlighting the topography is displayed in panels (a)-(c). The results shown are from models 15, 20 and 21. The ridge widths are: (d) 1000 km, (e) 2000 km and (f) 4000 km. For colouring and contouring see Figure 4.3.

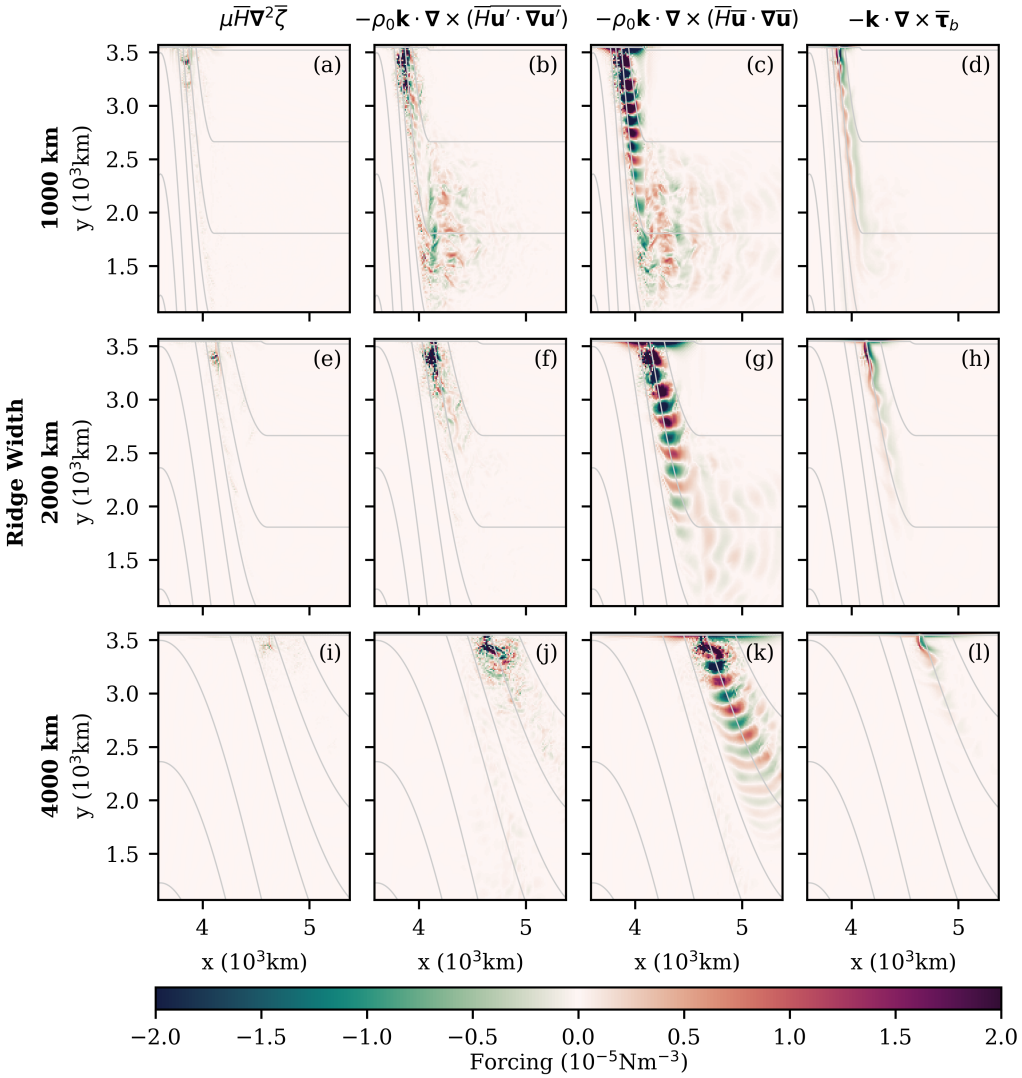

Figure 4.8: Terms of the barotropic vorticity equation for simulations with a meridional ridge of 2000 m in height and of varying ridge widths. Rows are associated with particular ridge widths (1000 km, 2000 km and 4000 km). Columns represent differing barotropic vorticity terms (viscosity, inertial term, mean inertial term and the bottom drag). Models shown are 15, 20 and 21.

term away from the boundary is supported by gradients in f/h rather than inertia. As the ridge width decreases the gradients in f/h are increased resulting in lowered velocities in the return flow and hence a lowered effect on vorticity from the bottom drag.

Figure 4.8 also shows that a change in ridge width affects the eddy inertial term. The decreased ridge width results in an increased eddying. The argument for this effect is similar to that of the changes seen in the bottom drag. The decreased ridge width leads to larger shear in the flow which generally gives heightened instability. From these simulations alone it difficult to assess the role that these eddies have on the system. Variations in resolution would be required to to further investigate their effect.

The discussion here has been purely about the vorticity terms which are able to balance the input of vorticity input by the wind stress. Although these vorticity balances have some bearing on the volume transport they are not responsible for the observed leading-order change in gyre transport. Similar to results in Chapter 3, it will be shown in the next subsection that the dominant factor is the changing vorticity input from the wind stress.

4.2.2 The Influence of Topography on Wind Forcing

In Chapter 3 a theory is outlined in which the wind forcing of a gyre changes depending on the bottom topography. Gyres are primarily confined to flow between two bounding geostrophic contours. The bounding contours are set by the sign of the wind stress curl over the region which is in Sverdrup balance. The bounding contours generally lie where the wind stress curl changes sign or at the domain boundary. This means the gyre extent is controlled by geostophic contours rather than lines of latitude. A change in topography can affect the path of the gyre. An adjustment of the topography can steer gyre flow into regions of opposite signed wind stress curl or shrink the bounding area of the gyre, altering the integral forcing of the gyre. Figure 4.9 shows the wind stress lying over each gyre which formed in simulations presented by Figure 4.7. For the northern gyre (Figures 4.9b, 4.9d and 4.9f), there is a clear relationship between the wind forcing and the change in topography. As the ridge is widened, the area over which the gyre is forced is reduced. The relationship for the southern gyre (Figures 4.9a, 4.9c and 4.9e) is a little more complex. The majority of the wind forcing in each case is has a negative curl. However, there is an additional region of positive curl where the flow is deflected northward. As the ridge width is increased, the area of forcing decreases and the proportion of this wind forcing which is of positive curl is increased. These two effects work in the same way, reducing the southern gyre wind stress curl forcing as the ridge width increases.

Figure 4.10a shows the area integral of the gyre forcing from the wind stress curl for

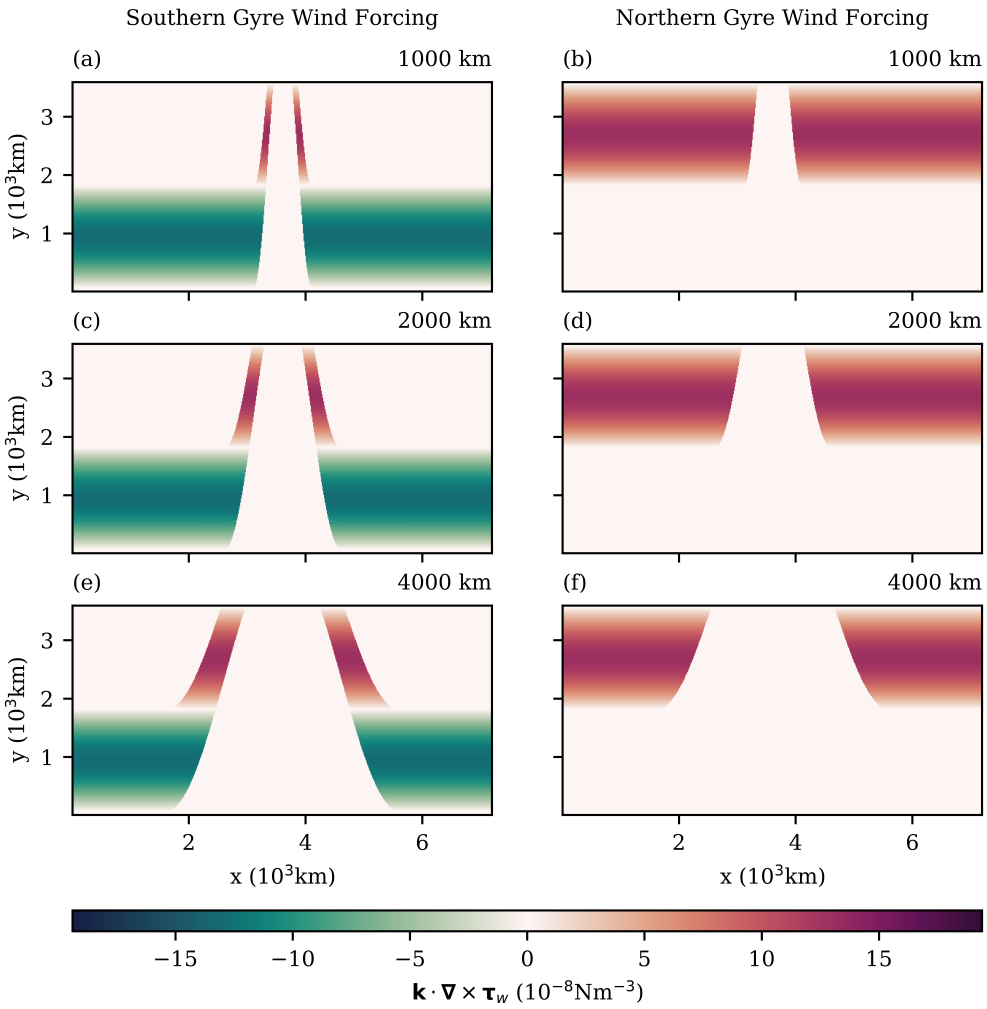

Figure 4.9: Wind forcing over each gyre for varying ridge width. (a): Southern gyre forcing for a 1000 km wide ridge. (b): Northern gyre forcing for a 1000 km wide ridge. (c): Southern gyre forcing for a 2000 km wide ridge. (d): Northern gyre forcing for a 2000 km wide ridge. (e): Southern gyre forcing for a 4000 km wide ridge. (f): Northern gyre forcing for a 4000 km wide ridge. Results are from models 15, 20 and 21.

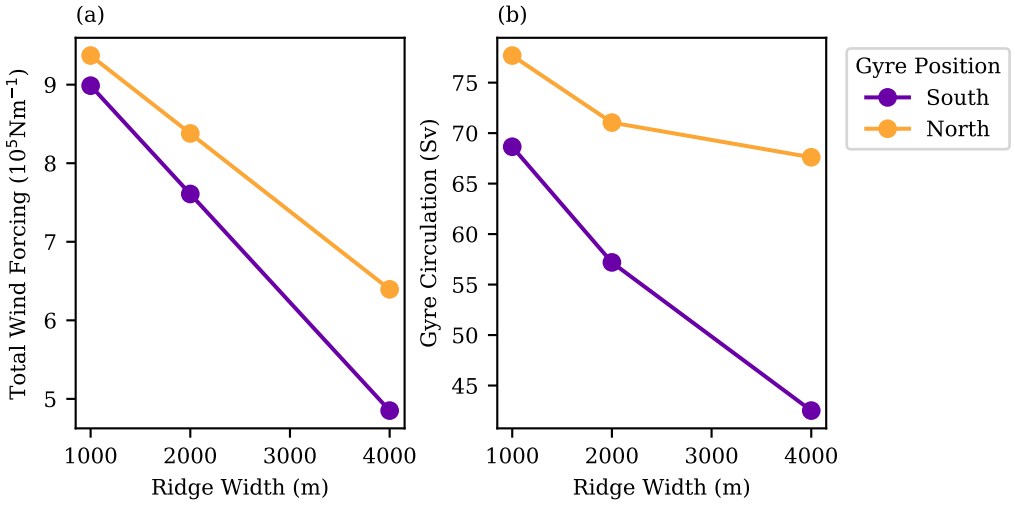

Figure 4.10: Wind forcing over each gyre and the resulting gyre circulation volume transport. Purple and orange represent the southern and northern gyres respectively (a): The area integral of wind forcing fields for each ridge width shown in Figure 4.9. (b): The gyre circulation for each ridge width. Results are from models 15, 20 and 21.

both the southern and northern gyres presented by Figure 4.7. There is a reduction in the total wind forcing of each gyre with a larger reduction in the southern gyre for the same change in topography. This result fits with the description above. The area of forcing for each gyre is reducing. The southern gyre forcing exhibits a greater reduction in the total forcing due to the enlarged area of opposite sign wind stress curl which occurs with a increased ridge width.

Figure 4.10b shows the relationship in gyre strength for the same ridge width variations. The change in forcing aligns with the change in volume transport. As the ridge width increases, the gyre strength decreases with a greater reduction in the southern gyre for the same variation in topography. This indicates that the response in the wind forcing to changes in topography has a primary control on the observed gyre strength.

This highlights the importance of using wind forcing over geostrophic contours as a metric for gyre flow. Gyre strength can be largely determined by topographic steering. The steering of gyre flow into regions of opposite wind stress curl can have significant effects on the resulting gyre transport.

4.2.3 The Northern Boundary Influence on Gyres

The model experiments in Figure 4.3 and Nadeau and Ferrari [2015] investigate the balance of net zonal transport versus gyre formation. Gyre formation in these results are dependant on the blocking of geostrophic contours with a northern boundary. Figure 4.2 shows that the degree to which geostrophic contours are blocked in the Southern Ocean is a complicated picture. Contrary to the representations of gyre formation in the models, there exists no significant northern boundary by which geostrophic contours can be blocked. This implies that the results by Nadeau and Ferrari [2015] are not relevant to understanding gyre formation in the Southern Ocean.

Although there are no major northern land masses, the theory of gyres forming due to blocked geostrophic contours could hold for areas with a western land mass. This could either be treated as an abstraction of results of Nadeau and Ferrari [2015] or an application of Ishida [1994]. In the Southern Ocean, the region with the highest level of blocked geostrophic contours is Drake Passage. Thus, theories of gyre formation due to blocked geostrophic contours are most applicable in this region. When topography creates a region of blocked geostrophic contours, a gyre develops to the east of this topographic feature. Under this constraint, a gyre is dependent on locally blocked geostrophic contours to the west of its formation. The formation of the Weddell gyre to the east of Drake Passage could be due to blocked geostrophic contours.

Most of the range of f/h which is found in the region of the ACC is not present in Drake Passage. Only geostrophic contours which lie close to the continent around the rest of the Southern Ocean pass through Drake Passage. Under barotropic theory, the ACC is largely unable to pass through Drake Passage and it is partially diverted into the Pacific Ocean [Marshall, 1995b]. Local dynamics allow deviations from geostrophic contours which permits flow on the northern limb of the ACC to pass through Drake Passage [Marshall, 1995b, Hughes et al., 1999]. A combination of local baroclinic effects [Marshall, 1995b] and topographic Sverdrup balance [Marshall, 1995b, Hughes et al., 1999] permits the ACC to continue its path around Antarctica. As a result, the concept of blocked geostrophic contours does not necessarily apply in this specific location. Although the Weddell Gyre lies within a region of blocked geostrophic contours, the observation that the ACC is shifted to align with a significant range of these blocked geostrophic contours renders many of them equivalently unblocked. Therefore, results given by Nadeau and Ferrari [2015] and Ishida [1994] showing gyres forming due blocked geostrophic contours may also not apply to the Weddell gyre where geostrophic contours are blocked.

Aside from the Weddell Sea, in other regions where gyres form in the Southern Ocean

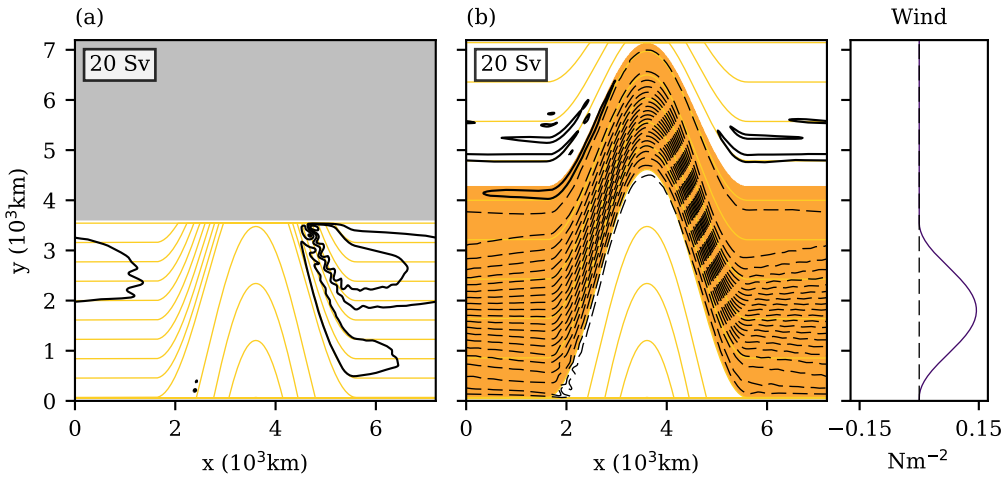

Figure 4.11: Plan view of two barotropic channel simulations with variation of the meridional extent. (a) 2000 m ridge height with 3600 km meridional extent (model 15). The grey section signifies land. (b) 2000 m ridge height height with 7200 km meridional extent (model 24). (Right) meridional profile of the zonal wind stress for both cases. For colouring and contouring see Figure 4.3.

there are no major obstacles by which geostrophic contours can be blocked. In the Ross Sea, for example, there is no land mass by which geostrophic contours are blocked yet the Ross Gyre forms here. This is a further suggestion that the representation of gyre formation via blocked geostrophic contours is not entirely appropriate for gyres of the Southern Ocean. There must be an alternative mechanism by which gyres form, which is different from any theories which have been proposed so far.

In order to investigate the dynamics of gyres and zonal flow in the real Southern Ocean the leading-order influence of the northern boundary in the channel simulations must be removed. In Figure 4.11 the meridional extent (L_y) is doubled for a domain with no meridional wall and ridge topography of 2000 m in hight. Doubling L_y creates a large region of unblocked geostrophic contours. The forcing is fixed and remains over the same latitude band. In the new domain almost the entire forcing is over regions of unblocked geostrophic contours. Through the emergence of this unblocked region and the removal of the dependency on the northern boundary gyres no longer form and a large net zonal transport develops. So the question remains, what characteristic of Southern Ocean ridges supports gyre formation?

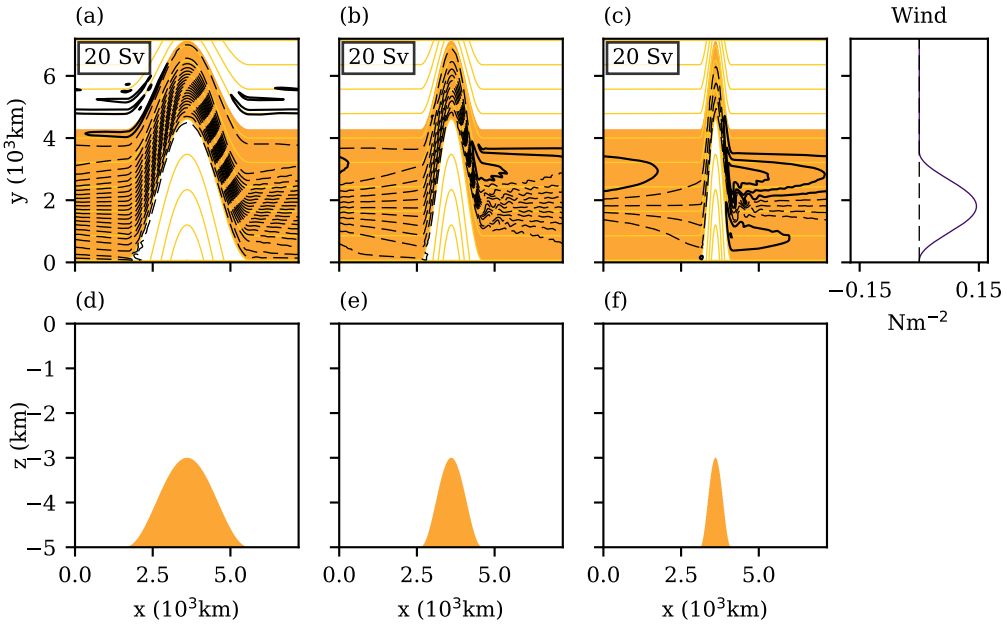

Figure 4.12: Plan view of barotropic channel simulations for a 2000 m high ridge, with variation of wind stress and ridge width. The wind forcing profile is plotted to the right. Side profiles of the bathymetry for each simulation is given in (d)-(f). (a): 4000 km ridge width. (b): 2000 km ridge width. (c): 1000 km ridge width. Results are from models 22, 23 and 24. For colouring and contouring see Figure 4.3.

4.2.4 The Control of Topographic Gradients on Gyres

In regions of unblocked geostrophic contours the preference of flow is to align geostrophic contours and in a periodic channel domain a net zonal flow is generated. In the real Southern Ocean it is indicated that gyres form in regions of unblocked geostrophic contours. In order for these gyres to form there must be a mechanism by which the preference of the flow is cross geostophic contours rather than align with them. It is found here that large gradients in ridge topography is a sufficient condition for flow to cross geostrophic contours and for gyres to form.

Topographic gradients have a bearing on characteristics of the geostrophic contours. An increased topographic gradient increases the gradients in f/h, causing geostrophic contours to bunch together. Examples of increased gradients in topography have been given above through the variation of topographic height and width in model simulations. These variations were shown to have significant effects on gyre volume transport in a closed domain.

Topographic gradients have also been explored in channel simulations through varying topographic height. It is difficult to single out the gradient effects in these channel results due to the simultaneous change in blocking of geostrophic contours. Varying the width of a topographic feature creates changes in topographic gradients without affecting the range of blocked geostrophic contours. Figure 4.12 explores various topographic gradients by varying the width of a ridge which is 2000 m in height. In Figures 4.12a-c, an increase in the topographic gradient leads to an introduction of two counter-rotating gyres. Contrary to existing results [Nadeau and Ferrari, 2015], these gyres do not form due to blocked geostrophic contours. This leaves steep topographic gradients as an alternative explanation for the formation of gyres in the Southern Ocean.

Results in Section 4.2.2 indicate that the gyre strength increases with decreasing ridge width in Figure 4.12 due to the response of the wind forcing to changes in topography. This wind response could explain the change in volume transport in Figure 4.12 but it does not provide a mechanism for the existence of the gyres.

The remainder of this chapter investigates the dynamics behind the existence of gyres in regions of unblocked geostrophic contours.

4.2.5 Vorticity Budgets

Gyres exist under the vorticity constraints introduced in Chapter 3. Thus, the vorticity budgets are a useful tool for diagnosing the formation of gyres in a region of unblocked geostrophic contours.

In Section 4.1.3 a discussion is provided of the transition in the vorticity balance that occurs when gyres form due to the introduction of blocked geostrophic contours. Figure 4.13 shows the key terms of the barotropic vorticity equation for the 4000 km wide ridge case and the 1000 km wide ridge case shown in Figure 4.12. As gyres are introduced, there is a similar response in the bottom pressure torque and the advection of planetary vorticity to the results in Section 4.1.3. In the 4000 km case the vorticity balance shows the zonal dipole in the advection of planetary vorticity (Figure 4.13a) and the bottom pressure torque (Figure 4.13c) with equal and opposite contributions. In the 1000 km case, where both the gyre circulations and the ACC is present, these terms remain the leading order balance but there is a change in the spatial pattern associated with the presence of the gyres. The zonal dipole associated with the ACC persists. However, an additional feature arises to the north and south of the vorticity sink in the bottom pressure torque (Figure 4.13d, green) on the eastern ridge flank. The additional feature is a source of vorticity in the bottom pressure torque (Figure 4.13d, red) associated with up-slope gyre flow on the

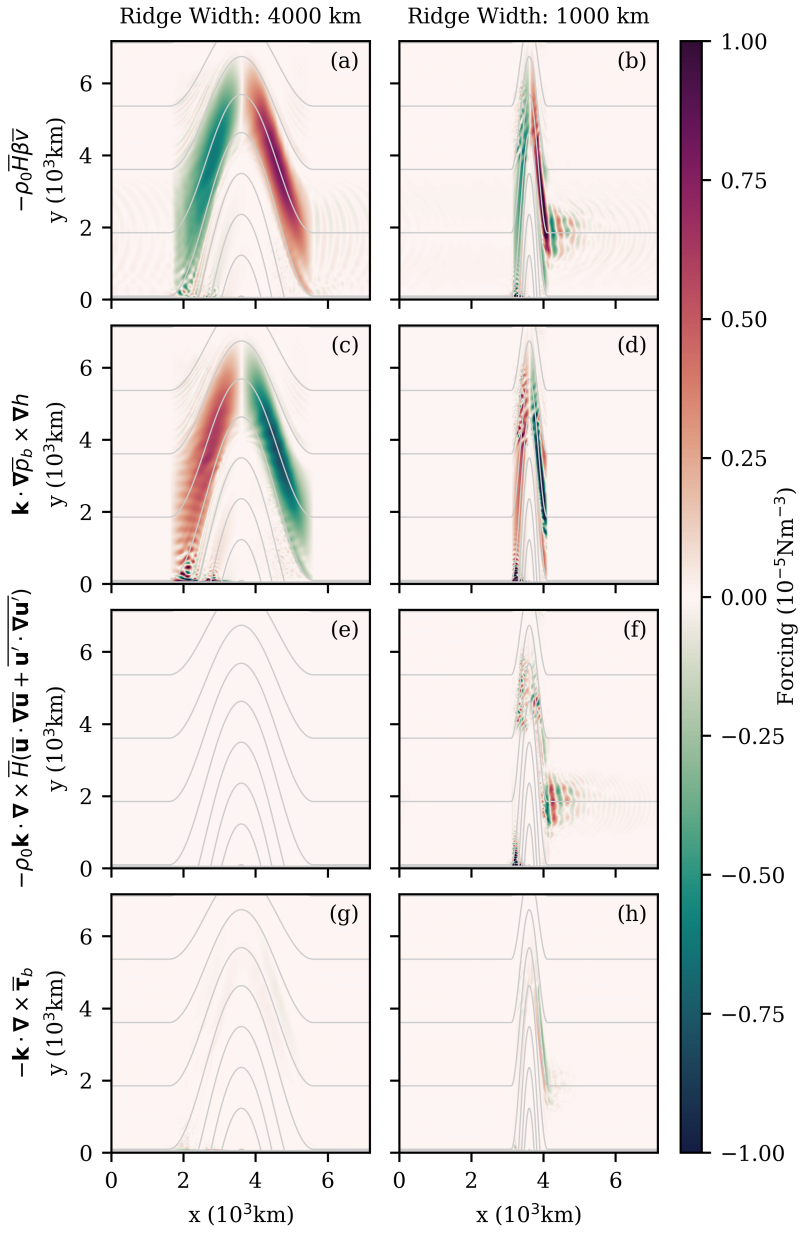

Figure 4.13: Terms of the barotropic vorticity equation for simulations with a meridional ridge of 2000 m in height and of varying ridge widths. Columns shown results for the 4000 and 1000 km ridge width. Rows are associated with each vorticity term. The grey lines indicate the geostrophic contours. Results are from models 22 and 24.

eastern ridge flank.

The contributions from inertial effects (Figure 4.13e) and bottom drag (Figure 4.13g) for the 4000 km case are negligible. Whereas these terms have a visible contribution for 1000 km case (Figures 4.13f and 4.13h). The change in the visible contribution in these terms is associated with adjustment in the geostrophic contours. For the 4000 km case the flow over the ridge is broad and is steered in a smooth manner. In the 1000 km case there is both increased gradient and curvature in f/h leading to a narrower current and a more abrupt steering of the flow. These changes result in a greater influence of inertia. It is noted in the previous chapter that bottom drag over topography is largely set by gradients in geostrophic contours. This indicates that the increased gradient in f/h for the 1000 km case also leads to contribution of bottom drag to the vorticity shown in Figure 4.13g.

4.2.6 Frictional Pinching

Gyres occur in the presence of a curl in the wind forcing, setting a Sverdrup balance in which flow is advected across geostrophic contours and a vorticity term permitting the flow to return. The necessary wind forcing for the occurrence of gyres is present in all simulations shown in Figure 4.12. This means that the missing feature for gyre formation in the case with a 4000 km wide ridge is the appropriate vorticity term to permit return flow. In the simulations presented here the return flow can either be set by bottom drag, viscosity or the eddy inertial term.

In previous results above, bottom drag arose to permit gyres in response to the blocking of geostrophic contours. Salmon [1992] provides a mechanism whereby it is possible to form gyres without the presence of blocked geostrophic contours. Results are given in which two counter rotating gyres form in a domain representative of the North Atlantic where geostrophic contours do not intersect with a boundary. Salmon [1992] suggests that frictional terms take over the role of blocked geostrophic contours. It is described that where large gradients in f/h occur frictional terms take over, 'pinching' off the flow. This pinching forces flow across geostrophic contours in a similar way to the blocked geostrophic contour situation. This indicates that the generation of vorticity in response to an increase of gradients in f/h permits the formation of gyres in regions of unblocked geostrophic contours. As the ridge is narrowed the gradient f/h increases and reaches a threshold at which the pinching effect can occur. Bottom drag is not the only term which can provide the necessary vorticity for this pinching effect. It could also be possible that the eddy inertial term or viscosity act in a similar way to bottom drag in pinching off the flow. Results in Figure 4.13 suggest that either inertia or bottom drag could be responsible for gyre formation in

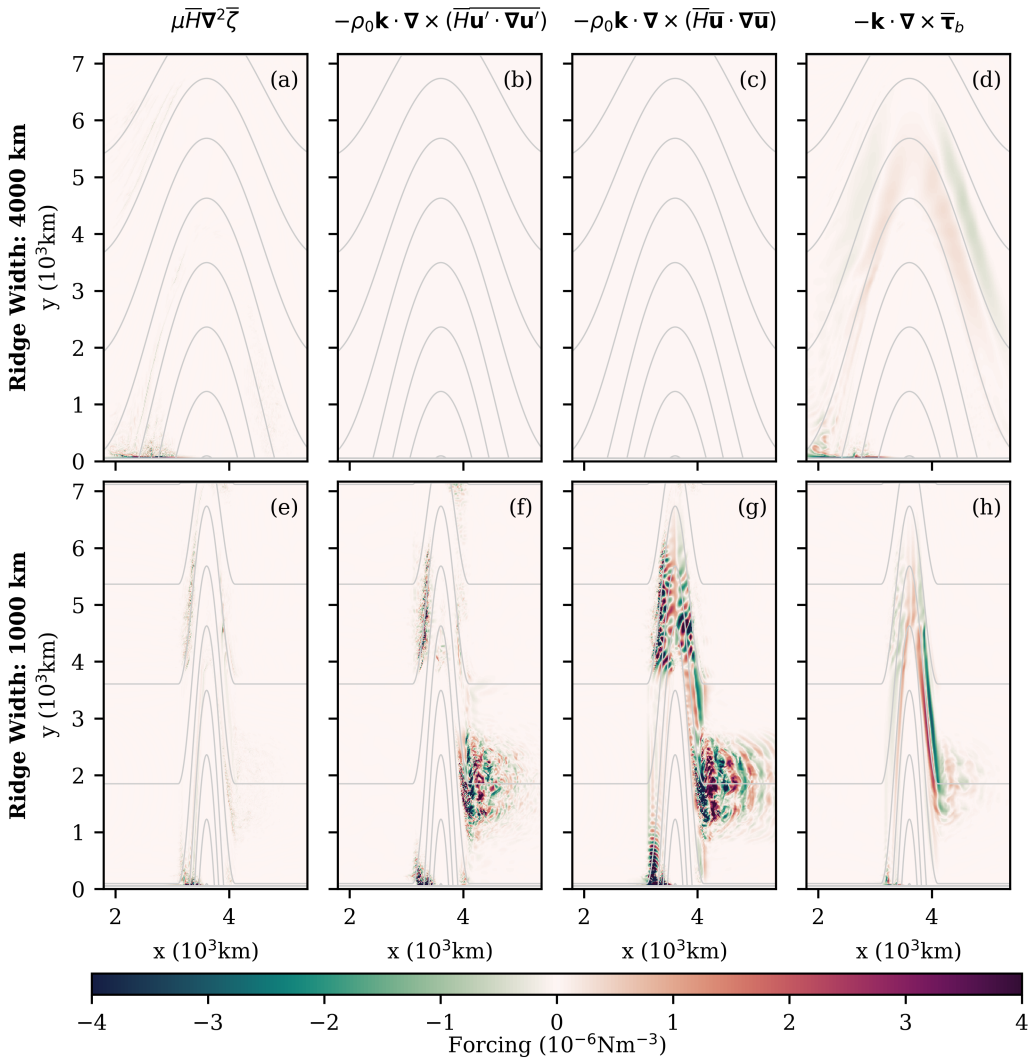

Figure 4.14: Terms of the barotropic vorticity equation for simulations with a meridional ridge of 2000 m in height and of varying ridge widths. Rows are associated with particular ridge widths (4000 km and 1000 km). Columns represent differing barotropic vorticity terms (viscosity, eddy inertial term, mean inertial term and the bottom drag). Simulations shown are 22 and 24.

the 1000 km case.

Figure 4.14 shows the vorticity generated by viscosity, eddy inertial terms, mean inertial terms and bottom drag for the same 4000 km and 1000 km wide ridge simulations, on a different scale to that of Figure 4.13. The viscosity terms are negligible in both simulations. As indicated previously, both the mean and eddy inertial terms are negligible for the 4000 km case but the adjustment in ridge geometry causes a contribution from these terms in the 1000 km case. There is a small contribution from bottom drag in the 4000 km which increases as the ridge is narrowed to 1000 km. The change in both the eddy inertial term and the bottom drag indicates that either of these terms could be associated with the gyre formation. In next subsection it is shown that bottom drag is the more important than the eddy inertial term in the formation of gyres in regions of unblocked geostrophic contours.

4.2.7 The Details of Fictional Pinching

It is shown that the appearance of gyres in regions of unblocked geostrophic contours is dependent on the gradients in f/h. The gyres form in Figure 4.12 due to the increased influence of either the eddy inertal term or bottom drag with decreased ridge width, pinching off the flow. It is possible to determine which of these terms is more important to the gyre formation by adjusting the bottom drag coefficient for the model simulations shown in Figure 4.12. In the previous chapter it is shown that where flow is returned across geostrophic contours over topography via bottom drag, changes in the bottom drag coefficient have no effect on gyre transport. However, the length scale over which bottom drag acts is proportional to its drag coefficient [Veronis, 1966a,b, Salmon, 1992]. The pinching effect can occur over weaker gradients in f/h if the frictional length scale is increased. Thus, in contradiction to the flat bottom case, an increase in gyre transport with increased bottom drag coefficient would suggest bottom drag is the key term for the return flow and therefore the pinching effect. On the other hand, an increase in bottom drag coefficient reduces eddy inertial terms by damping the variability in the flow and increases the influence of the bottom drag. This means that an decrease in gyre flow with increased bottom drag coefficient would indicate that inertia is the dominant pinching term. Figure 4.15 shows a comparison of three ridge width variations run with two different drag coefficients, 0.0025 and 0.005. The results show that the increased bottom drag coefficient causes stronger gyre transport. This indicates that the bottom drag term is the crucial term in these simulations for pinching the flow and permitting the gyres to form in regions of unblocked geostrophic contours.

As a side note, the relationship in the ACC flow is less clear for results in Figure 4.15. For the simulations with drag coefficient of 0.0025, the net zonal transport decreases with

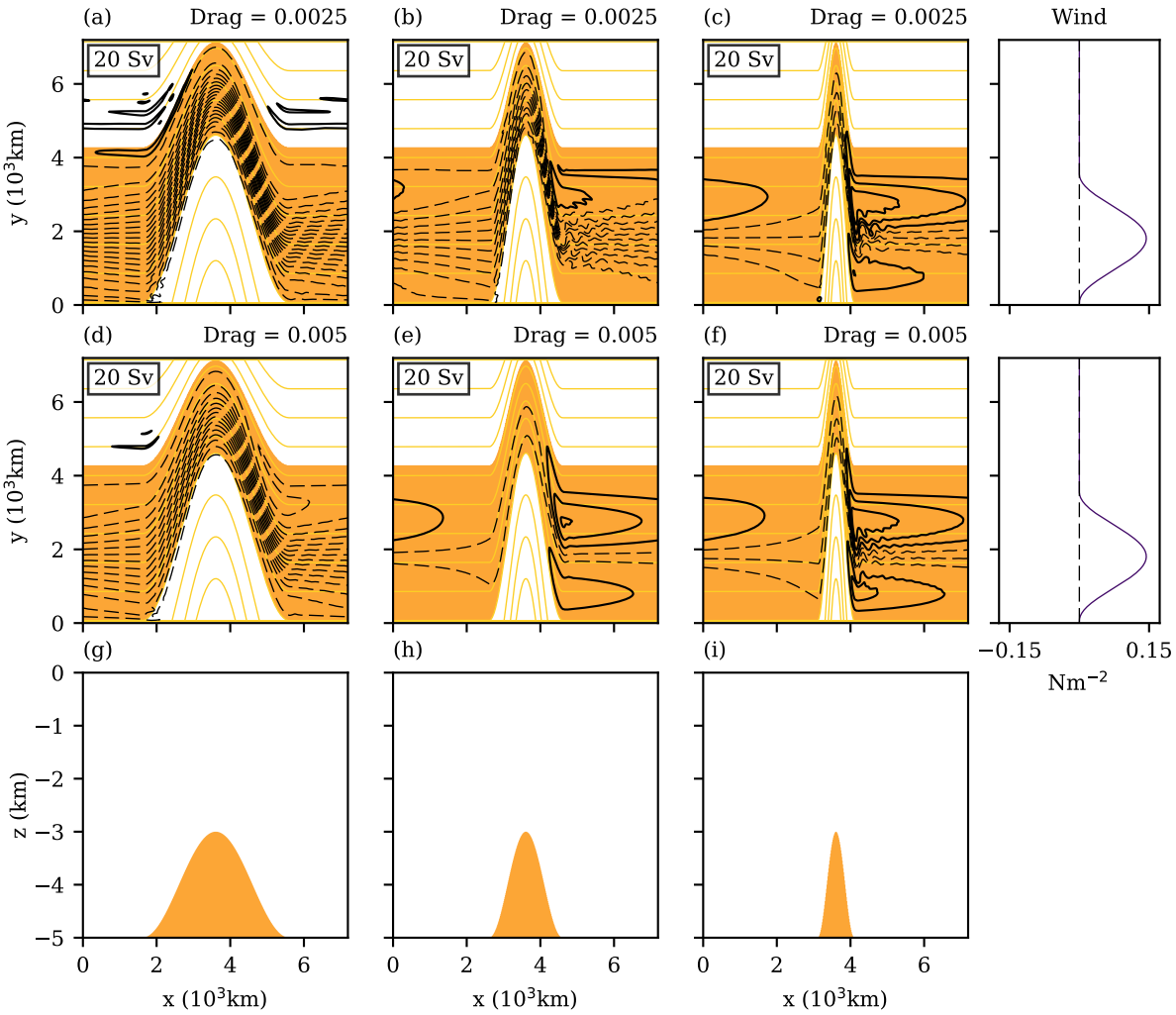

Figure 4.15: Plan view of barotropic channel simulations for a 2000 m high ridge, with variation of quadratic bottom drag coefficient and ridge width. Respective wind forcing profiles are plotted to the right. (a): 4000 km ridge width, drag coefficient 0.0025. A side profile of the topography is shown in (g)-(i). (b): 2000 km ridge width, drag coefficient 0.0025. (c): 1000 km ridge width, drag coefficient 0.0025. (d): 4000 km ridge width, drag coefficient 0.005. (e): 2000 km ridge width, drag coefficient 0.005. (f): 1000 km ridge width, drag coefficient 0.005. Results shown are from models 22-27. For colouring and contouring see Figure 4.3.

decreasing ridge width. The same relationship holds for results in Figures 4.15e and 4.15f where the drag coefficient is 0.005. However, with the further reduction in ridge width between Figures 4.15d and 4.15e the opposite relationship is observed, the net zonal volume transport increases with a decrease in ridge width. This anomalous response is not formally investigated in this study. However, theory provided in the next chapter shows the response of the ACC to changes in ridge geometry and further insight is provided on the dynamics of the net zonal flow.

The pinching effect is further investigated in Figure 4.16. This shows the sink of vorticity provided by the bottom drag for each simulation shown in Figure 4.15. The important changes occur on the eastern flank of the ridge so results are zoomed to this area. The largest signal arises from the intense south-eastward, down-slope flow. Whilst this flow is far weaker for the lower panels (d-f) the increased drag coefficient determines that the magnitude of the vorticity sink is much the same. Overall, the results for both drag coefficients are very similar. The biggest disparity in the vorticity arises for the cases with the 2000 km wide ridge, where the differences in the gyre circulations are most noticeable. For this geometry, the low drag case has little sign of a southern gyre whereas there is a clear southern gyre circulation for the high drag case. The length scale over which bottom drag acts is larger for the 0.005 coefficient (Figure 4.16e) than for the 0.0025 coefficient (Figure 4.16b). Moreover, it appears that the presence of a southern gyre is associated with a vorticity forcing dipole that is separate to the dipole arising from the jet across the ridge. This vorticity pattern is most prominent in the model grid between 0-1500 km on the y-axis and 4000-4500 km on the x-axis. It also has the opposite orientation to the vorticity of the jet with negative vorticity to the south of positive vorticity implying a link to up-slope flow. Although the signal is weaker, all other cases concur with the additional vorticity appearing along with southern gyre flow. The vorticity pattern is present for both 1000 km geometries but absent for the 4000 km geometries where southern gyres do not form. This vorticity pattern appears to reflect the 'pinching' effect introduced by Salmon [1992].

Vorticity arising from bottom drag is responsible for permitting gyre circulation by permitting flow to cross geostrophic contours. Figure 4.17 shows the streamfunction, bottom drag and contours of $(f + \overline{\zeta})/h$ for the 1000 km and 2000 km wide ridges with bottom drag coefficient of 0.005. The results have been zoomed to the region in which the additional vorticity dipole appears. Both results show that in general the flow tends to follow the geostrophic contours. As suggested, the additional vorticity mainly arises from the up-slope gyre flow. However, at the point where the gyre flow turns sharply to return downslope, flow is advected across geostrophic contours. Both the jet associated with the ACC and additional vorticity from the gyre flow provide the same sign of vorticity in this zone but

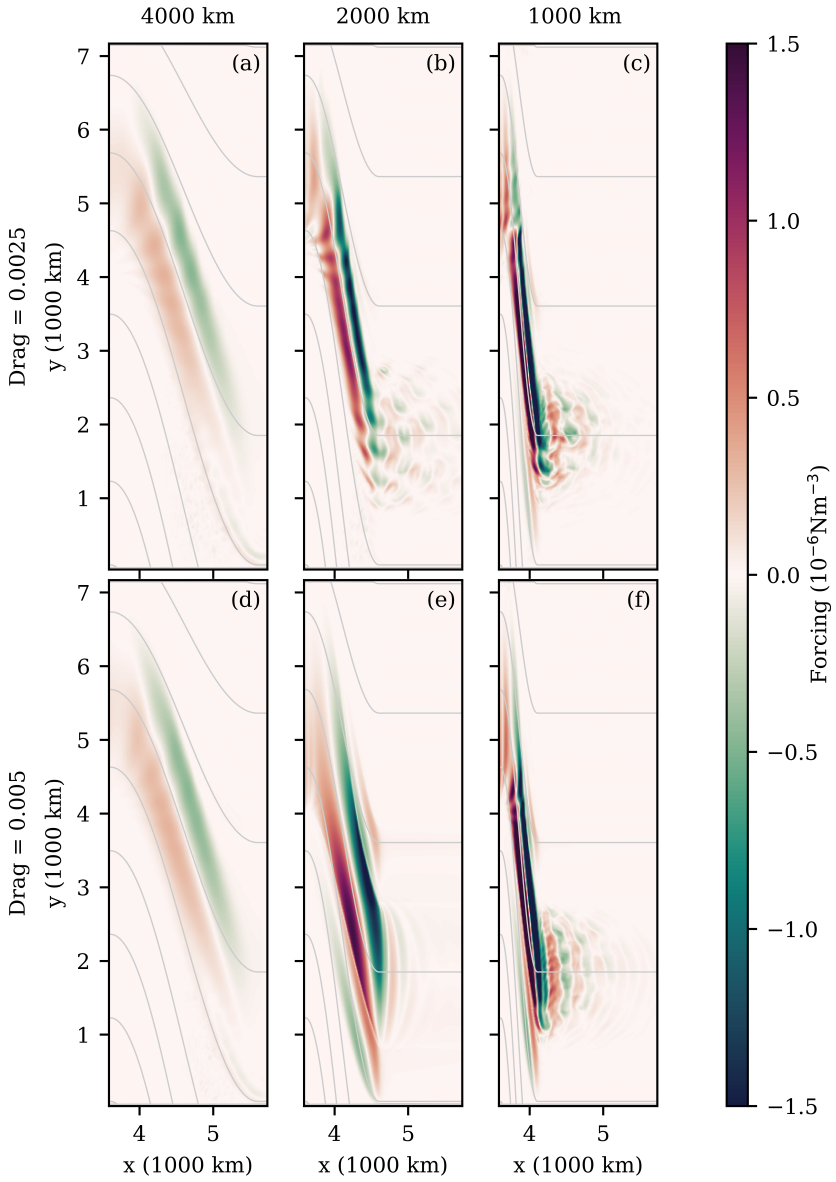

Figure 4.16: $\boldsymbol{k} \cdot \boldsymbol{\nabla} \times \boldsymbol{\tau}_b$ for varying ridge width and bottom drag coefficient, focused on the eastern flank of the ridge. Results are for model simulations 22-27. (a): 4000 km wide ridge, 0.0025 drag coefficient. (b): 2000 km wide ridge, 0.0025 drag coefficient. (c): 1000 km wide ridge, 0.0025 drag coefficient. (d): 4000 km wide ridge, 0.005 drag coefficient. (e): 2000 km wide ridge, 0.005 drag coefficient. (f): 1000 km wide ridge, 0.005 drag coefficient.

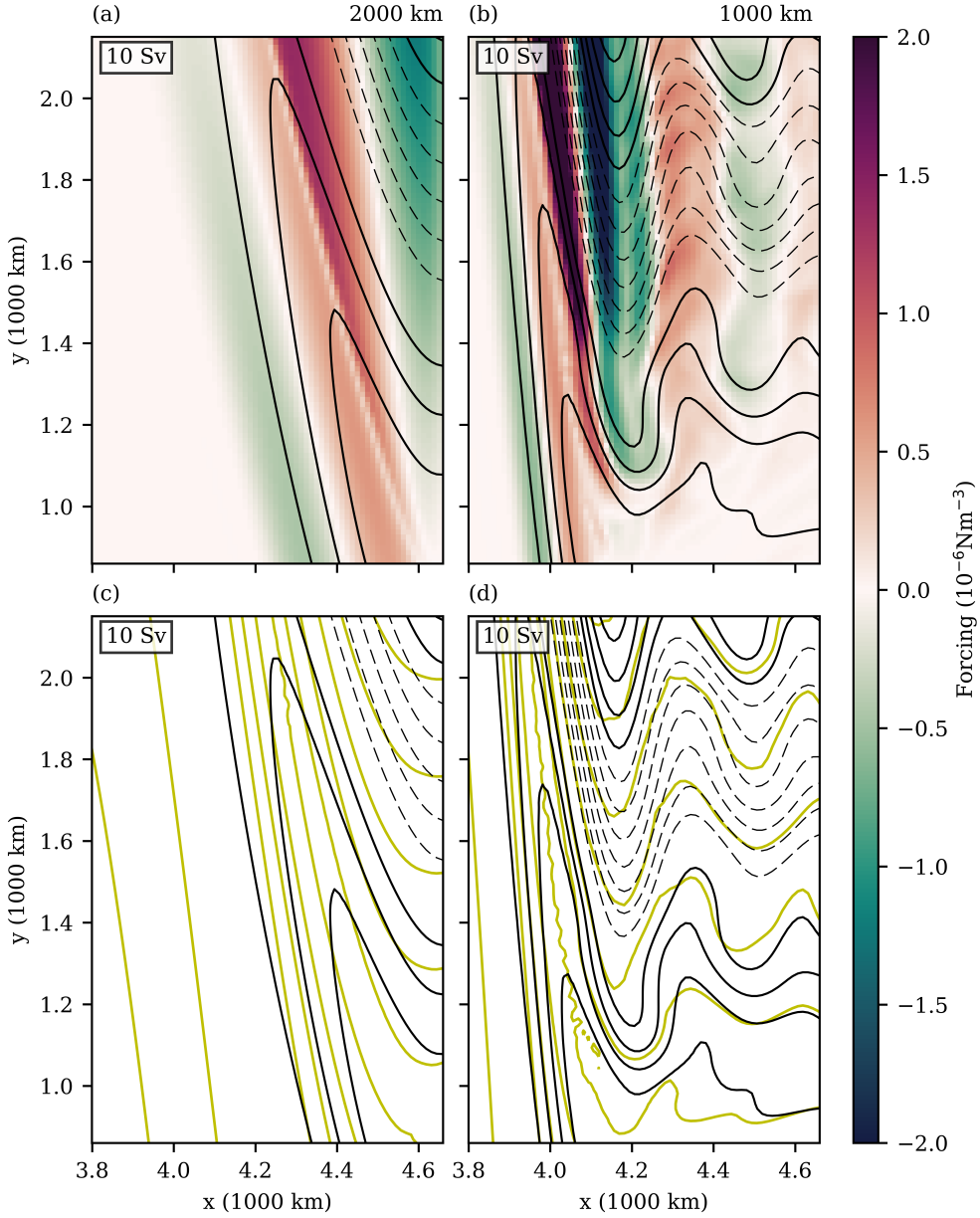

Figure 4.17: Subpolar gyre dynamics over the eastern ridge flank with bottom drag coefficient of 0.005 and varying ridge width. Solid black lines represent gyre streamlines and dashed black lines represent ACC streamlines. The box to the top-left of the plots show the streamline spacing in Sverdrups. Yellow lines show contours of $(f+\overline{\zeta})/h$. The red-green colour-map represents $\boldsymbol{k}\cdot\boldsymbol{\nabla}\times\boldsymbol{\tau}_b$. All panels are focused on the same southern section on the eastern flank of the ridge. Results are for the model simulations 26 and 27. (a) and (c): 2000 km wide ridge. (b) and (d): 1000 km wide ridge.

there is a clear divide in the magnitudes. This flow is supported by the additional positive vorticity contribution from the bottom drag. The bottom drag curl is acting to support gyres in the same sense as the case with blocked geostrophic contours. Vorticity is added to return flow across geostrophic contours, which is initially advected across geostrophic contours in the opposite sense by the wind stress. The difference here being that the vorticity source in the return flow is due to contours of f/h having the necessary spacing.

4.3 Summary

In model simulations, most representations of Southern Ocean gyre formation occur through a mechanism of blocking geostrophic contours. This blocking is achieved through introducing topography that causes the geostrophic contours to intersect with a boundary. This representation may be appropriate for gyres that are bounded by continents such as the North Atlantic gyre. However, gyres that occur in the Southern Ocean, such as the Ross Gyre, form in the presence of unblocked geostrophic contours. Flow along unblocked geostrophic contours is unbounded and preferentially forms a net zonal flow within a gyre. It has been observed here that given a ridge topography with a large enough gradient in f/h, gyres are able to form in a region of unblocked geostophic contours. This gyre formation is attributed to the increased generation of bottom drag that occurs with increase topographic gradient. Once the gradient in f/h reaches a certain threshold, the vorticity generated by bottom drag is large enough to permit flow to return across geostrophic contours and a gyre is formed.

5 Topographic control of the Antarctic Circumpolar Current

The discussion so far has focused on the effects of ridge geometry on gyre dynamics. This chapter will investigate how topography influences net zonal transport through the domain, which corresponds to the ACC. The dynamics of the zonal transport is separated from gyre dynamics by using a wind forcing which exhibits zero curl and therefore creates no gyres.

Previous studies show that increasing topographic height tends to decrease the zonal transport in a channel [Nadeau and Ferrari, 2015]. This relationship is determined by blocking geostrophic contours, shutting off the 'linear free mode' on which net zonal transport can occur [Hughes et al., 1999]. This section reveals that zonal transport has geometric dependencies which are not related to blocked geostrophic contours. The research here considers a different scenario by exploring topographic variations which do not affect the range of blocked f/h. The variations investigated are of ridge width, employing the same topographies presented in Section 4.2.4. Similar simulations involving ridge width variations have been carried out previously by Chen et al. [2015]. However, this study sought to understand eddy-mean flow dynamics and did not investigate the effect of geometric variations on net zonal flow.

Section 4.2.4 introduced experiments in which ridge width was symmetrically varied in a channel. These simulations were forced with a meridionally varying wind stress allowing gyres to develop. Gyres were the focus in Section 4.2.4 and the net zonal transport was not discussed. However, the large areas of unblocked geostrophic contours in these simulations allowed a net zonal flow to develop. A relationship emerged between ridge width and net zonal transport which is opposite to that with the gyres. The gyres were shown to strengthen as the ridge narrows but the net zonal transport became weaker for narrower ridges. It is this relationship of net zonal flow with varying ridge geometry which will be discussed in this chapter.

5.1 Effects of Symmetric Variation of Ridge Width on Zonal Flow

The presence of gyres in results shown in Figure 4.12 makes it difficult to diagnose the dynamics behind the net zonal flow. To address this, the problem is simplified though using a wind forcing which has no meridional variation, thus zero curl. Figure 5.1 shows results with the same topographies used in Figure 4.12 with curl-free wind forcing. In these results, the relationship between net zonal flow and ridge width persists; a decrease in ridge width leads to a decrease in zonal flow. The continued presence of this relationship shows

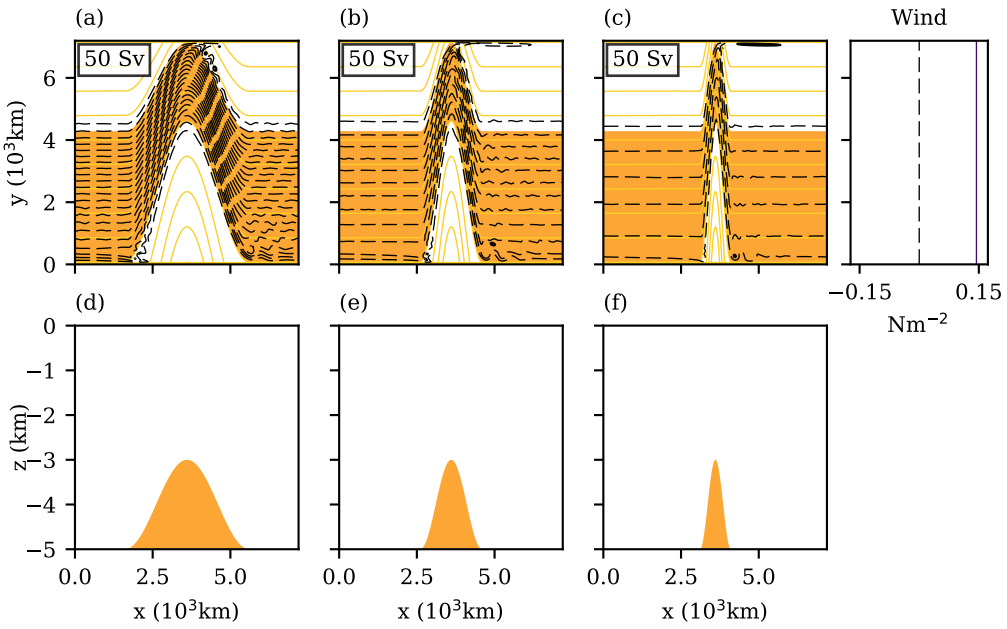

Figure 5.1: Barotropic channel simulations for a 2000 m high ridge with a variation in ridge width. The wind forcing profile is plotted to the right. (a)-(c) shows a plan view of the streamfunction. (d)-(f) show side profiles of the topography in each respective simulation above ((a)-(c)). (a): 4000 km ridge width. (b): 2000 km ridge width. (c): 1000 km ridge width. Results are from model simulations 29, 31 and 35. For colouring and contouring see Figure 4.3.

that it is independent of the gyre dynamics investigated in Chapter 4.

Figure 5.2a shows the net zonal volume transport for an extended range of ridge width variations with uniform wind stress. The relationship between zonal volume transport and ridge width is almost linear.

When flow passes zonally over the ridge there is an associated meridional deflection due to its tendency to follow geostrophic contours. The geostrophic contours also converge as the depth shallows, causing flow to converge at it approaches the ridge crest. Given a constant ridge height, the meridional spacing of these contours remains unchanged at the ridge base and the ridge crest for differing ridge widths. Narrowing the ridge means that contours narrow by the same amount from the base to the crest over a smaller distance. This results in both the gradient and convergence of f/h to be larger for narrower ridges. In past studies, increased gradients in f/h have led to enhanced velocities over topography [Smith and Fandry, 1978]. Higher convergence of the flow would indicate that a narrower

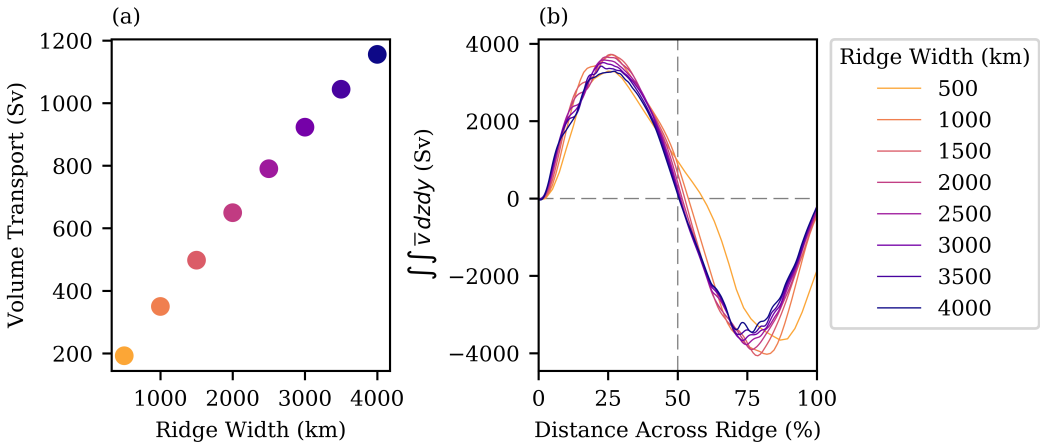

Figure 5.2: Variations in volume transport for different ridge widths. (a) Net zonal volume transport against ridge width. (b) Meridional and depth integral of meridional velocity, $\int\int \overline{v}\, dzdy$, over topography only. Note that the distance across the ridge has been scaled by the ridge width so that the curves overlie. Results are from model simulations 29-35.

ridge gives increased velocities over the ridge.

Figure 5.2b shows the meridional velocities for each simulation, scaled by ridge width. It is found that, contrary to the above indication, meridional velocities are approximately constant in magnitude for all cases. The relationship between volume transport and ridge width is linked to this independence in $\int\int v\, dzdy$. Flow primarily aligns with geostrophic contours and flows at an angle θ to a line of latitude. For $U = \int u\, dz$, $V = \int v\, dz$ and A, the stream-wise velocity,

$$U = A\cos\theta \tag{5.1}$$

$$V = A\sin\theta. \tag{5.2}$$

Substituting (5.1) into (5.2) gives

$$V = U\tan\theta. \tag{5.3}$$

Thus,

$$\int V\, dy = \tan\theta \int U\, dy = \tan\theta \cdot T, \tag{5.4}$$

where T represents the volume transport through the channel. The relationship provided by (5.4) shows that ridge geometry links the meridional velocities to the volume transport.

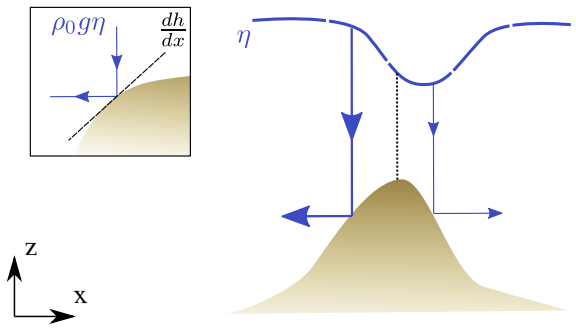

Figure 5.3: Schematic of form stress acting across a ridge shown in the x-z plane. The blue dashed line is the sea surface. The brown shaded area represents the bottom topography. The solid blue lines represent the pressure forces from the fluid overlying the topography. The box to the top left shows how the pressure force is translated by topography.

As ridge width decreases θ increases for flow on the ridge flanks as a result of the change in the path of the geostrophic contours. Thus, a constant $\int V\,dy$ and an increasing θ results in a decreasing volume transport. This means that the net zonal transport in these simulations can be understood through investigating the cause of constant meridional velocity magnitudes over the ridge with variations in ridge width.

5.1.1 Zonal Momentum Budget and Form Stress

The system presented is composed principally of zonal balances. Although v is a meridional term it will be shown that it is governed by zonal dynamics. Since the interest here is in the zonal balances, zonal momentum governs the relevant dynamics. The depth and zonally integrated zonal momentum balance is (see Chapter 2 for derivation):

$$\rho_0\left(\oint \overline{H}(\overline{\zeta}\,\overline{v}+\overline{\zeta' v'})\,dx+\oint \frac{\overline{H}}{2}\frac{\partial(\overline{u}^2+\overline{v}^2)}{\partial x}\,dx+\oint \frac{\overline{H}}{2}\frac{\partial(u'^2+v'^2)}{\partial x}\,dx\right)= \oint \overline{p}_b\frac{\partial h}{\partial x}\,dx+\oint \overline{\tau}^x_w\,dx-\oint \overline{\tau}^x_b\,dx+\mu\oint \overline{H}\boldsymbol{\nabla}^2\overline{u}\,dx, \tag{5.5}$$

where $\oint p_b(dh/dx)\,dx$ is the form stress term.

Form stress arises due to an asymmetric pressure force over the ridge. Figure 5.3 shows a schematic of this asymmetric pressure force. The dip in the sea surface is offset from the peak in the topography which is signified by the black dashed line. This offset results in higher pressure force on the western flank of the ridge versus the eastern flank. The box

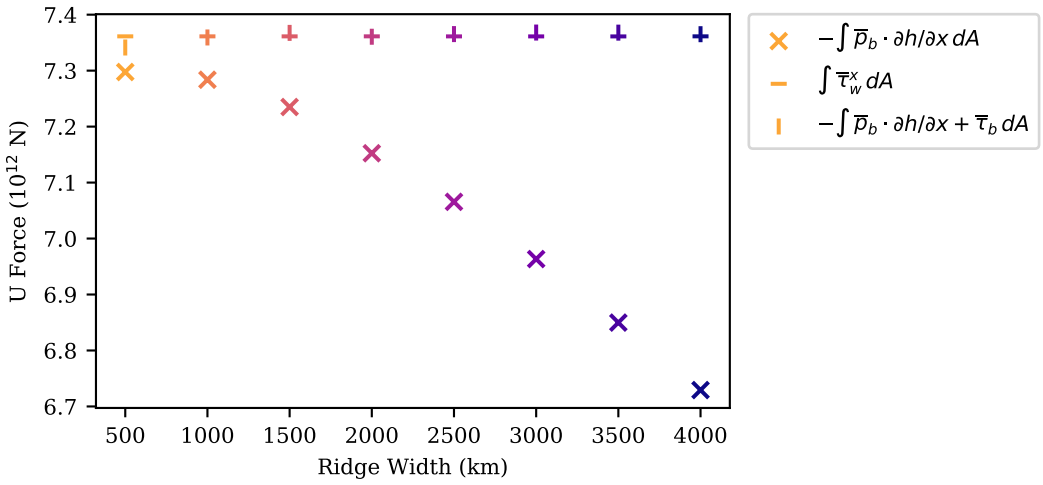

Figure 5.4: Domain integral of terms in the zonal momentum budget for varying ridge width. The momentum terms shown are: the negative of the form stress ($-\int \overline{p}_b \cdot \partial h/\partial x \, dA$); the wind stress ($\int \overline{\tau}_w \, dA$) and the addition of the negative of the form stress and the bottom drag ($-\int \overline{p}_b \cdot \partial h/\partial x + \overline{\tau}_w \, dA$). Results are from model simulations 29-35.

in the top left of Figure 5.3 shows how this vertical pressure force acts in the presence of variable topography. The force from the pressure that lies over the topography is translated into a horizontal force by the gradients in the topography. The pressure lying over the western flank of the ridge is transferred into a westward force by the topography and pressure over the eastward flank results in in an eastward force. This directional force is depicted by the solid blue lines in Figure 5.3. The difference between pressure force over each ridge flank gives form stress. If the dip in the surface pressure were zonally symmetric and lay symmetrically over a symmetric ridge, no form stress would occur. The zonal shift in the surface pressure dip causes a difference in the across-ridge pressure force, creating a form stress.

In the Southern Ocean, form stress is the main balancing term for momentum imparted by the zonal wind stress [Munk and Palmén, 1951, Stevens and Ivchenko, 1997, Masich et al., 2015]. Figure 5.4 shows that the channel simulations run here with ridge width variations concur with this balance. Between all model runs the leading order momentum balance is between wind stress and form stress, with a small contribution arising from bottom drag. The influence of bottom drag increases with ridge width.

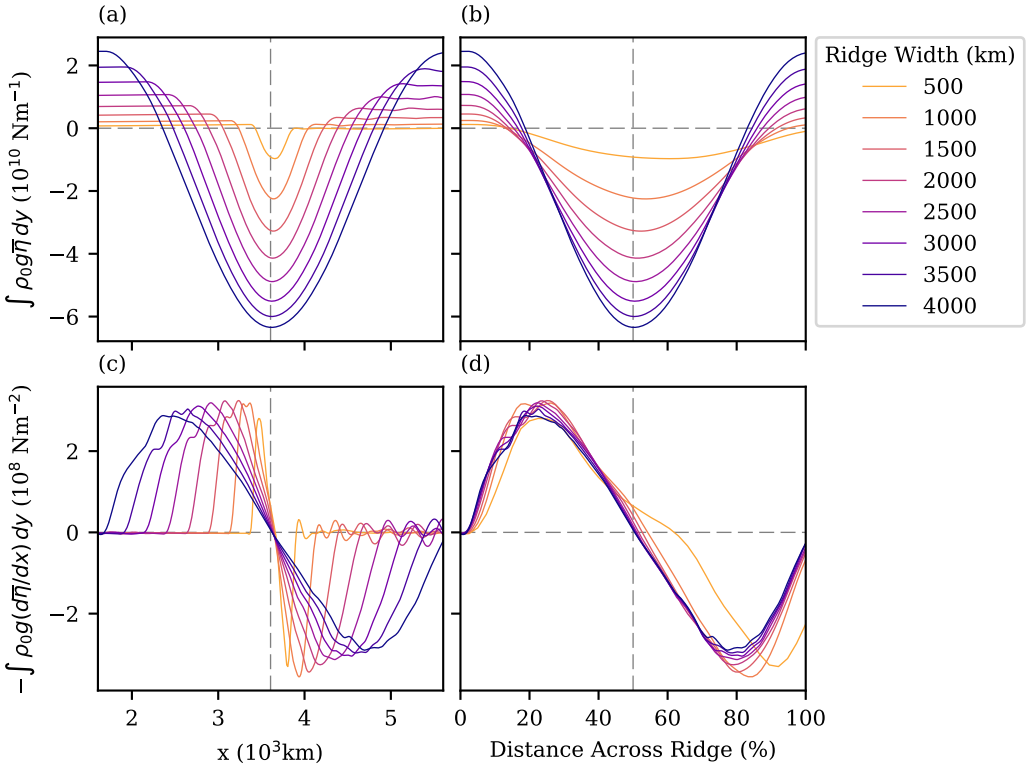

Figure 5.5: Meridionally integrated sea surface pressure and zonal pressure gradients for varying ridge width. (a) Meridionally integrated sea surface pressure. (b) Meridionally integrated sea surface pressure with the x-axis scaled to the ridge width of each simulation. (c) Meridionally integrated zonal sea surface pressure gradient. (d) Meridionally integrated zonal sea surface pressure gradient with the x-axis scaled to the ridge width of each simulation. Results are from model simulations 29-35.

5.1.2 Zonal Pressure Gradients and Zonal Transport

The leading order zonal momentum balance is shown to be between wind stress and form stress. As form stress is given by $\oint p_b(dh/dx)\,dx$, the bottom pressure field plays an important role in zonal momentum dynamics. The dh/dx component dictates that the influence of the pressure field is restricted to regions of variable topography only. Thus, in simulations shown here, bottom pressure only contributes over the ridge.

The bottom pressure term can be separated into two parts, $p_b = \rho_0 gh + \rho_0 g\eta$, a topographic pressure term, $\rho_0 gh$, and a sea surface pressure term, $\rho_0 g\eta$. When zonally integrating over any topography the topographic pressure term has zero contribution to the form stress term, thus giving the relation:

$$\oint p_b \frac{dh}{dx}\,dx = \oint \rho_0 g\eta \frac{dh}{dx}\,dx. \tag{5.6}$$

Figure 5.5a shows the meridionally integrated sea surface pressure term, $\int \rho_0 g\eta\,dy$, for each ridge width. The terms ρ_0 and g are both positive constants, thus, the negative values shown in Figure 5.5a correspond to negative sea surface height with respect to the reference level. All simulations indicate a dip in the surface height over the topography. This dip is associated with the northward deflection of flow over the ridge. On the large scale, to a leading order approximation, the ocean is in geostrophic balance:

$$fv \simeq -g\frac{d\eta}{dx}. \tag{5.7}$$

which would be satisfied exactly under a barotropic, linear approximation and in the absence of forcing, bottom drag and viscosity. The zonal sea surface pressure gradients over the ridge for ridge width variations are shown in Figure 5.5c. Under geostrophy, positive values of the sea surface pressure gradient are associated with northward flow and negative values with southward flow. In all simulations there is a northward flow on the western flank of the ridge and southward flow on the eastern flank. Together, the surface pressure gradients, which are associated with the flow, result in a dip across the ridge in the observed sea surface height.

Figures 5.5a and 5.5b show the sea surface pressure, where the x-axis is scaled with the ridge width for the latter plot. As the ridge width increases the sea surface pressure becomes increasingly negative. There is a relationship between the amount that the sea surface deviates from its resting state and the mean zonal pressure gradients. Figure 5.5d shows the zonal pressure gradients, where the x-axis is scaled with the ridge width for each simulation. This result shows there is a small reduction in the surface pressure gradient

with ridge width. However, this change is relatively small and the surface pressure gradient can be viewed as approximately constant across the different cases. Through (5.7), the insensitivity of the meridional velocities to changes in topography is related to this independence of the zonal surface pressure gradient for the different cases presented. As the pressure gradient remains unchanged, (5.7) gives that v must remain relatively unchanged. Additional to this, the deepening of the sea surface pressure with increased ridge width can be linked to the topography independent surface pressure gradients that appear. For an increased ridge width dx increases. In order to keep $d\eta/dx$ constant $d\eta$ must also increase indicating a deepening of the sea surface pressure.

5.1.3 A Control of Volume Transport Via Form Stress

The form stress contribution changes if the sea surface is altered. Figure 5.5 shows that where $\rho_0 g\eta$ and dh/dx change in concert with changes in ridge width, $d\eta/dx$ is approximately constant. By considering a case with linear topography the following can be written:

$$\begin{aligned}\oint \rho_0 g\eta \frac{dh}{dx}\, dx &= \int_{x_0}^{x_2} \rho_0 g\eta \frac{dh}{dx}\, dx \\ &= \int_{x_0}^{x_1} \rho_0 g\eta \frac{dh}{dx} dx + \int_{x_1}^{x_2} \rho_0 g\eta \frac{dh}{dx}\, dx \\ &= \left|\frac{dh}{dx}\right| \left(\int_{x_1}^{x_2} \rho_0 g\eta\, dx - \int_{x_0}^{x_1} \rho_0 g\eta\, dx \right),\end{aligned} \tag{5.8}$$

with $\{x_0, x_1, x_2\}$ shown in Figure 5.6. If the ridge narrows and hence dh/dx increases $\int_{x_1}^{x_2} \rho_0 g\eta\, dx - \int_{x_0}^{x_1} \rho_0 g\eta\, dx$ must decrease to continue to match the form stress to the wind stress. This pressure difference can be reduced by decreasing both $\int_{x_0}^{x_1} \rho_0 g\eta\, dx$ and $\int_{x_1}^{x_2} \rho_0 g\eta\, dx$ by proportionately equal amounts. One way of achieving this reduction is through the dip in the sea surface height as depicted by the upward shift from the blue to the orange line in Figure 5.6. A reduced dip in the sea surface height reduces both $\int_{x_0}^{x_1} \rho_0 g\eta\, dx$ and $\int_{x_1}^{x_2} \rho_0 g\eta\, dx$, reducing the difference between these terms.

It is shown in Figure 5.4 that form stress remains approximately constant as the ridge width changes in order to match the constant wind stress forcing. Between the different cases the sea surface must respond to the changed topography in order to keep form stress constant. As indicated by (5.8), the sea surface dip reduces with decreasing ridge width to conserve the form stress. In turn, this adjustment in the sea surface height is associated with a constant sea surface pressure gradient with changes in ridge width and an increased volume transport for increased ridge width.

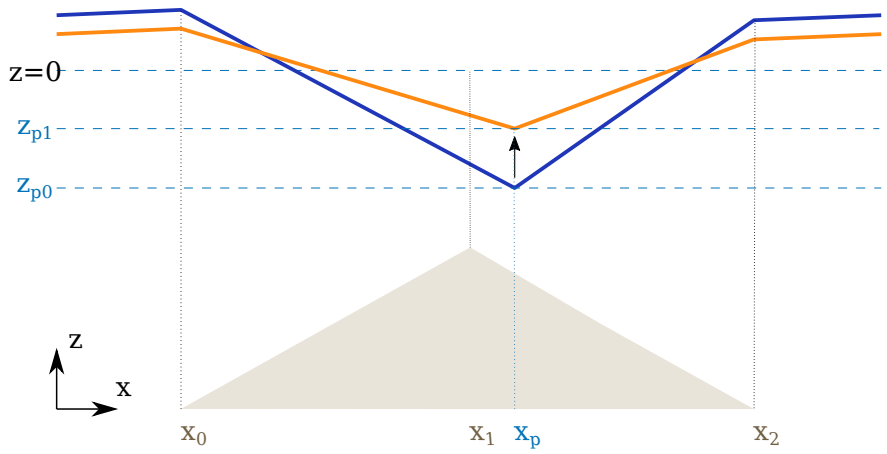

Figure 5.6: Schematic highlighting the form stress response to a change in the ridge width. This is a side profile in the x-z plane. $z = 0$ is the level of the resting ocean. The filled grey triangle represents the side profile of a ridge. The blue line is an example sea surface. The orange line represents the change in sea surface height associated with a narrower ridge.

This mechanism is not the only determinant of the from stress. Form stress arises primarily from the asymmetry of the sea surface trough with respect to topography. Changes to this asymmetry can effect the resulting form stress contribution. This effect is discussed further in the latter half of this chapter.

5.1.4 Summary

Channel simulations are shown with a meridional ridge and an eastward surface forcing via wind stress. In all simulations, form stress is the primary momentum sink balancing the wind stress. Form stress is determined by the seabed topography and the sea surface. The wind stress is constant between simulations so as topography changes the sea surface must respond to keep form stress constant. The ridge height is constant between simulations and the ridge width is varied. The increased topographic gradients corresponding to a narrowing of the meridional ridge and the sea surface depression over the topography decreases in order to conserve form stress.

A deepening of the sea surface trough coupled with a wider ridge leads to an approximately constant $d\eta/dx$ with changes in ridge width. Through geostrophy, a constant $d\eta/dx$

results in meridional velocities which are also approximately constant over the ridge with ridge width variations. A wider ridge width leads to a broader current. Therefore, with approximately constant velocities, the net zonal volume transport increases with an increase in ridge width.

5.2 The Relationship Between Form Stress, Bottom Drag and Inertia

It is shown in Figure 5.4 that with increasing ridge width a larger proportion of the momentum sink is from the bottom drag contribution. The bottom drag contribution increases whilst the form stress contribution decreases. The volume transport in a channel is required to be two orders of magnitude larger when the momentum from the wind stress is balanced by bottom drag rather than form stress. A deviation as small as seen in Figure 5.4 could have noticeable effects on the volume transport.

Accompanying the adjustment in the momentum budget, as ridge width increases there is a zonal shift in the sea surface dip. Figure 5.7 shows the position of the meridionally integrated sea surface pressure minimum for each ridge width simulation over the ridge peak. In Figure 5.7b the x-axis is scaled to the ridge width in each simulation and Figure 5.7a shows the unscaled results. The results which are scaled relative to the ridge width provide a more relevant comparison of the geometric effects as the length scale of the flow scales with the ridge width. Both plots show that as ridge width decreases the minimum of sea surface pressure shifts in the eastward direction.

The following text outlines a link between this shift in sea surface height and the increased contribution of form stress to the zonal momentum budget for decreased ridge width.

5.2.1 The Role of Inertia and Bottom Drag in Overshooting Streamlines

As the dip in the sea surface height is associated with the meridional velocities, the zonal shift in the pressure minimum shown by Figure 5.7 represents an overshoot of the flow over the ridge. On a meridional average, the flow continues northward after passing the ridge crest. Relative to the ridge width, the point at which the flow changes direction and turns south is farther east for wider ridges. The overshoot is related to deviations of the flow from geostrophic contours. As viscosity is negligible and there is no curl in the wind stress for these simulations, deviations must arise from bottom drag or inertia. The steady inertial term and bottom drag act distinctly in the separation of flow from geostrophic contours over topography [Neumann, 1960, Porter and Rattray, 1964, McCartney, 1976]. Over a meridional ridge, both terms act to shift streamlines eastward relative to geostrophic con-

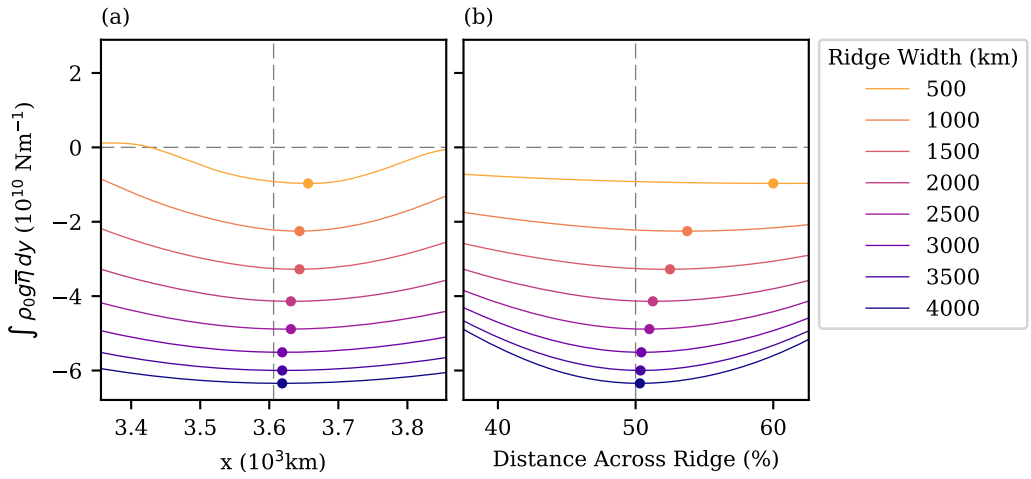

Figure 5.7: Meridionally integrated sea surface pressure over the ridge crest. (a) Meridionally integrated sea surface pressure. (b) Meridionally integrated sea surface pressure with the x-axis scaled to the ridge width of each simulation. The dots represent the minimum of each curve. Results are from model simulations 29-35.

tours. Figure 5.8 gives a schematic representation of the resulting deviation of streamlines provided by each term. This schematic shows the isolated effect of each term relative to a single geostrophic contour. The schematic is intended to reflect the effects over ridge topography and not the entire domain. Figures 5.8a and 5.8b show the deviation in x-y space. Figure 5.8c represents the deviation relative to the geostrophic contour shown in the above x-y space schematics.

The mechanisms for the deviations of streamlines which arise from bottom drag and inertia are best discussed in terms of vorticity. The potential vorticity equation, derived in Section 2.1.8, can be written as:

$$\rho_0 H \frac{D}{Dt}\left(\frac{f+\zeta}{H}\right) = \boldsymbol{\nabla} \times \left(\frac{\boldsymbol{\tau}_w - \boldsymbol{\tau}_b}{H}\right) + \mu \boldsymbol{\nabla}^2 \boldsymbol{\zeta}. \tag{5.9}$$

This equation can be reduced to:

$$\rho_0 H \frac{D}{Dt}\left(\frac{f+\zeta}{H}\right) = -\boldsymbol{\nabla} \times \left(\frac{\boldsymbol{\tau}_b}{H}\right), \tag{5.10}$$

as $\partial H/\partial y$ is small implying $\boldsymbol{\nabla} \times (\boldsymbol{\tau}_w/H) \simeq 0$ and $\mu \boldsymbol{\nabla}^2 \boldsymbol{\zeta}$ is negligible in all simulations presented in this Chapter.

To conserve potential vorticity and satisfy (5.10), to first order flow aligns with con-

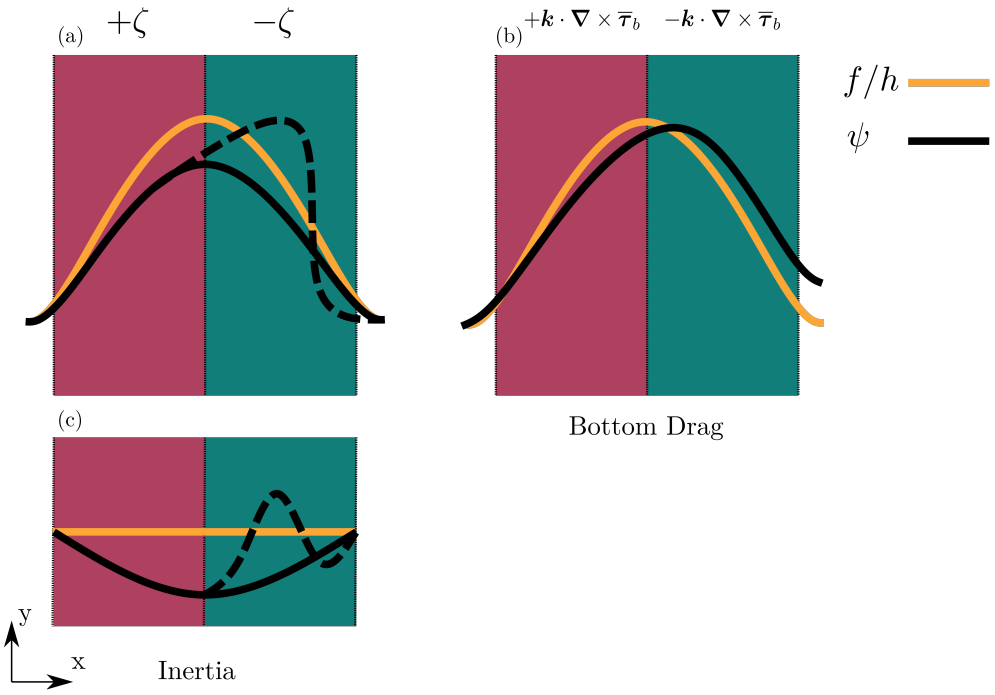

Figure 5.8: Schematic highlighting the mechanism linked with the overshoot of flow over a ridge. (a) the resultant deviation of streamlines due to inertial effects. (b) the deviation of streamlines due to bottom drag effects as shown by Neumann [1960]. (c) the deviation of streamlines due to inertial effects, with respect to geostrophic contours. The yellow lines represent the geostrophic contours and solid black lines are streamlines. The dashed black line shows the additional deviation of streamlines in the presence of Rossby waves. Inertia and bottom drag are associated with an addition of negative and positive vorticity. The deviation of the streamlines arise due to the addition of vorticity. The green and red background signifies the spatial distribution in the addition of positive and negative vorticity respectively along the solid black streamlines. The labels at the top signify the relevant vorticity terms associated with the green and red fill.

tours of f/h (geostrophic contours). Flow can deviate from geostrophic contours through the addition of relative vorticity, ζ, or bottom drag $\boldsymbol{\tau}_b$.

In the Southern Hemisphere f is negative. The addition of positive relative vorticity leads to a more negative f. The magnitude of f increases poleward and a more negative f is associated with a poleward deviation in flow. On the western flank of a ridge, inertia generates an addition of positive relative vorticity on streamlines and on the eastern flank it is associated with the addition of negative relative vorticity, deflecting the streamlines poleward and equatorward respectively [Porter and Rattray, 1964, McCartney, 1976]. The deflection provided by inertia is depicted by the solid black line in Figures 5.8a and 5.8c. This asymmetric vorticity contribution from inertia, deflecting streamlines from geostrophic contours, arises from vortex stretching. As the fluid is advected up slope, the water column thickness reduces. The reduction in the vertical thickness of a vortex leads to a reduced magnitude in its angular velocity. A lowered angular velocity leads to the reduced relative vorticity of the fluid. On a downslope there is then a reversal of this process. The thickness of the vortex is stretched and the magnitude of the relative vorticity is enhanced through the same mechanism.

The asymmetric inertial balance set by vortex stretching is often perturbed by the presence of stationary Rossby waves. Stationary Rossby waves are primarily restricted to the eastern flanks of topographic features and alter the east-west symmetry of streamlines across topography. Rossby waves set an oscillation in the lee of a ridge about geostrophic contours that is dampened downstream and are asymptotic to a value of f/h [McCartney, 1976]. The effect of Rossby waves in the inertial deflection of streamlines is represented by the dashed black line in Figures 5.8a and 5.8c. Rossby waves have virtually no effect on the western flank of the ridge but streamlines become significantly altered downstream [McCartney, 1976]. The combination of both inertial mechanisms together act to shift the northward peak of the streamlines eastward with respect to geostrophic contours. This shift represented in Figure 5.8a.

The steady inertial term gives no net addition of vorticity along a streamline. This means that any source of relative vorticity arising from the steady inertia term is balanced elsewhere by an equal and opposite sink. The addition and removal of vorticity by vortex stretching is balanced across a symmetric ridge. Stationary Rossby waves can contribute to a net deflection between the two bases of a ridge but no net deflection of streamlines arises if the view is extended further downstream [McCartney, 1976]. Stationary Rossby waves can continue to oscillate and extend downstream of a topographic feature. However, given a large enough distance down stream, the waves dampen and flow returns to its original latitude. Ultimately, streamlines which undergo modulation by inertia alone lie at the same

latitude both down and up-stream of a topographic feature.

Bottom drag can have a similar effect to inertia in deflecting flow from geostrophic contours. Through the barotropic vorticity equation (2.51), Neumann [1960] shows that a balance can be observed such that

$$\underbrace{\rho_0 \overline{H} \beta \overline{v}}_{\text{(a)}} + \underbrace{\boldsymbol{k} \cdot \boldsymbol{\nabla} \times \overline{\boldsymbol{\tau}}_b}_{\text{(b)}} = \underbrace{-\frac{\partial \overline{p}_b}{\partial y} \frac{\partial h}{\partial x}}_{\text{(c)}} . \tag{5.11}$$

Neumann [1960] uses (5.11) to show how flow over topography adjusts when (a) and (b) are neglected independently. Neglecting bottom drag from (5.11) leaves an exact balance between (a) and (c) which is associated with flow following geostrophic contours [Jackson et al., 2006]. Flow is northward on the western flank of a ridge and southward on the eastern flank generating the required v velocities for term (a) to balance the bottom pressure torque term (c). Neumann [1960] shows that the streamlines in this situation have a symmetric equatorward deviation over symmetric topography. The inclusion of bottom drag introduces an additional balance between (b) and (c). The vorticity generated by bottom drag in this situation is required to be positive on the western flank and negative on the eastern flank. The generation of vorticity by bottom drag causes a zonal asymmetry in the flow [Neumann, 1960]. There is an eastward shift in the northward peak of the streamlines. This displacement is depicted by Figure 5.8b. Unlike the steady inertial term, bottom drag causes a net displacement of streamlines over topography [Neumann, 1960, McCartney, 1976]. Bottom drag dissipates energy added to the system which creates a net sink of vorticity. The net displacement of streamlines by bottom drag is associated with the net sink of vorticity across the ridge.

The theory presented here indicates that the overshoot observed in Figure 5.7 arises from inertial and/or bottom drag effects.

5.2.2 The Vorticity Budget

The deviation of streamlines from geostrophic contours is associated with sources and sinks of vorticity. The extent to which inertial and bottom drag terms contribute to flow overshooting the ridge peak can be diagnosed in terms of barotropic vorticity. A source of vorticity acts to deflect flow equatorward and sink acts to deflect flow poleward. The deflection of streamlines is not locally confined and Figure 5.7 shows the overshoot associated with an eastward shift in surface pressure is visible in a meridional integral. The two dimensional plots of barotropic vorticity shown previously are relevant for displaying local

balances but are not effective for highlighting global effects which appear in a meridional integral of the results. The meridionally integrated barotropic vorticity equation gives a view of the net contributions to deflection of streamlines across the topography. Meridionally integrating the temporal averaged vorticity budget derived in Section 2.1.5 gives:

$$\rho_0\Big(\int \boldsymbol{k}\cdot\boldsymbol{\nabla}\times\left(\overline{H}\overline{\boldsymbol{u}}\cdot\boldsymbol{\nabla}\overline{\boldsymbol{u}}\right)dy+\int \boldsymbol{k}\cdot\boldsymbol{\nabla}\times\left(\overline{H}\overline{\boldsymbol{u}'\cdot\boldsymbol{\nabla}\boldsymbol{u}'}\right)dy+\int \overline{H}\beta\overline{v}\,dy\Big)= \int \boldsymbol{k}\cdot\boldsymbol{\nabla}\overline{p}_b\times\boldsymbol{\nabla}h\,dy+\int \boldsymbol{k}\cdot\boldsymbol{\nabla}\times\left(\overline{\boldsymbol{\tau}}_w-\overline{\boldsymbol{\tau}}_b\right)dy+\mu\int \overline{H}\boldsymbol{\nabla}^2\overline{\zeta}\,dy. \tag{5.12}$$

The key terms of (5.12) are given in Figure 5.9 for different ridge widths. The x-axis here is scaled with ridge width. The wind stress term has been neglected as it is constant between simulations.

The primary balance in Figure 5.9 is between advection of planetary vorticity, $\int \overline{H}\beta\overline{v}\,dy$, and bottom pressure torque, $\int \boldsymbol{k}\cdot\boldsymbol{\nabla}\overline{p}_b\times\boldsymbol{\nabla}h\,dy$, for all simulations. This concurs with previous results in Section 3.7 where the balance arises in connection with flow following geostrophic contours over topography.

Figure 5.10a shows the sum of the advection of planetary vorticity and the bottom pressure torque. There is less closure between the advection of planetary vorticity and bottom pressure torque for narrower ridge widths. Figure 5.9a shows the advection of planetary vorticity is altered for changing topography. The advection of planetary vorticity deviates increasingly with a decreasing ridge width. Figure 5.9b shows at the same time there is only a relatively small change in the bottom pressure torque which mostly occurs away from the ridge crest. The bottom pressure torque is unchanged over ridge crest as $dh/dx = 0$ at this point regardless of the geometry. As a result, there is a drift in the balance which is most pronounced near the ridge crest.

The changes in the advection of planetary vorticity are associated with an eastward shift in the point at which advection of planetary vorticity changes sign. As this term is determined by meridional velocities, the changes in the balance are linked to the eastward pressure shift shown in Figure 5.7. The eastward shift is associated with an overshoot in the flow. A connection is made in the previous section between flow overshooting over topography and the influence both bottom drag and steady inertia. Vorticity is generated by both bottom drag and steady inertia for these simulations. Figure 5.9 shows that these terms are acting to close the vorticity budget, balancing the deviations in the advection of planetary vorticity. This suggests that bottom drag and steady inertia influence the overshoot.

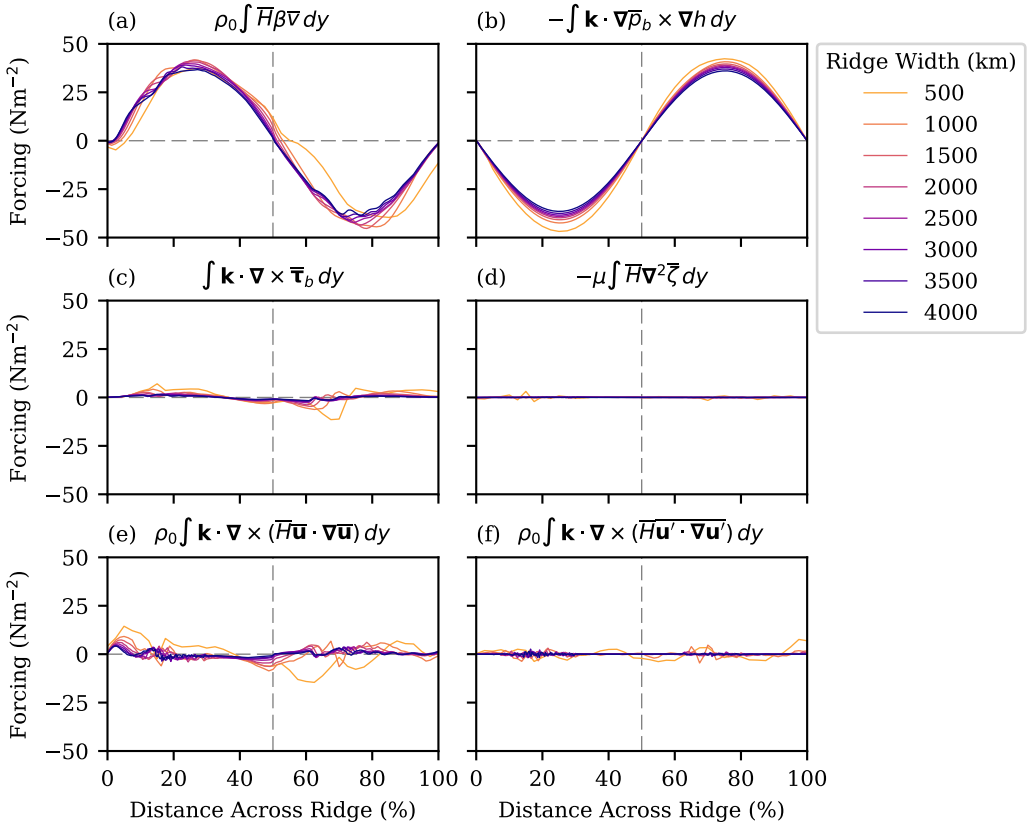

Figure 5.9: The meridionally integrated terms of the barotropic vorticity equation for simulations with differing ridge widths. Only the region over the ridge is shown and the x-axis for is scaled with ridge width for each curve. The titles show the respective terms which are displayed in each panel. Results are from model simulations 29-35.

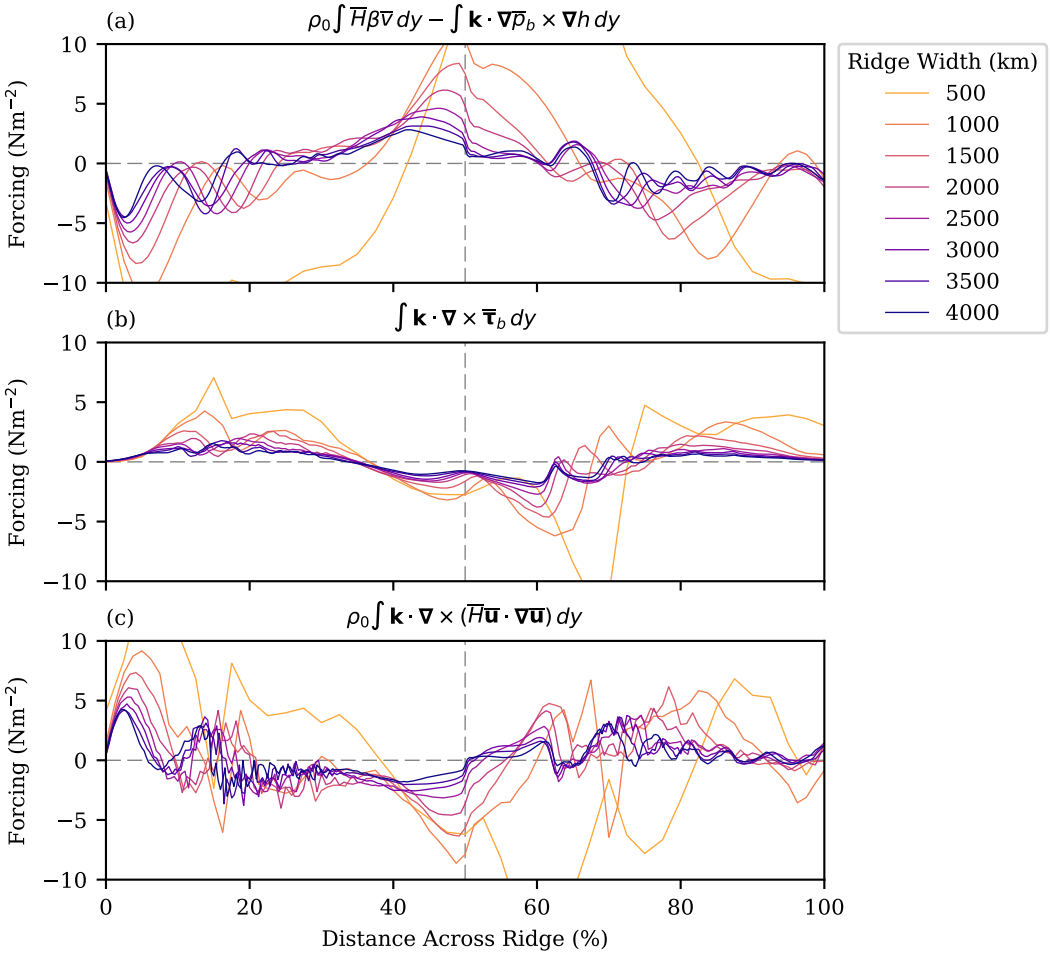

Figure 5.10: The meridionally integrated terms of the barotropic vorticity equation for simulations with differing ridge widths. Only the region over the ridge is shown and the x-axis for is scaled with ridge width for each curve. (a) The residual between the advection of planetary vorticity and the bottom pressure torque. (b) The bottom drag. (c) The steady inertial term. Results are from model simulations 29-35.

5.2.3 Bottom Drag and Inertia

To investigate the role of both inertia and bottom drag in the overshoot Figure 5.10 shows both terms with the y-axis rescaled.

Bottom drag contributes to the overshoot of the flow through an addition of vorticity on the western flank of the ridge and a removal of vorticity on the eastern flank. Figure 5.10a indicates that bottom drag aligns with this pattern, accommodating the overshoot. There is a peak generation of positive vorticity over the western ridge flank and peak negative values to the east of the ridge crest. The magnitudes in the generation of vorticity via bottom drag increase as the surface pressure minimum shifts eastward with the narrowing of the ridge (see Figure 5.7). This further implies a relationship between the bottom drag and the overshoot of the flow.

The increased bottom drag influence in the vorticity budget arises with the decreased contribution of bottom drag in the zonal momentum budget in Figure 5.4, creating an opposing relationship. The increased magnitudes in the vorticity budget arise from geometric effects. As shown in the previous chapter, decreasing ridge width increases gradients in f/h over topography. Where gradients in f/h are enhanced, bottom drag vorticity is increased. On the other hand, the momentum contribution is dependent on zonal velocity magnitudes. As the ridge width is decreased, meridional velocities over the ridge are relatively constant. However, it is shown by the decreased spacing in the streamlines of the flat-bottom region of the simulations in Figure 5.1 that zonal velocities are decreasing. As bottom drag is dependent on velocities, this decrease in velocities is associated with the decrease in bottom drag momentum contribution.

For inertia to contribute to the overshoot in the flow, a removal of vorticity would occur on the western flank of the ridge and much larger addition would occur on the eastern flank. This asymmetric generation of vorticity is present near the ridge crest (between 40-60%) in the results shown for the wider ridges in Figure 5.10c indicating that inertia also has an influence on the observed overshoot. For the narrowest ridges there is no clear spatial pattern and the influence may not hold. Similar to the bottom drag, the magnitudes generally increase with increased shift in the surface pressure minimum. Again, this further implicates inertia as a term responsible for the overshoot.

These results suggest that both inertia and bottom drag are synchronously aiding an eastward shift in the meridional velocity field. From this there is an eastward shift in the surface pressure minimum which increases with decreasing ridge width.

5.2.4 The Boundary Influence

The flow associated with the net zonal transport is almost entirely confined to the region of unblocked geostrophic contours. Flow which is not in this unblocked region is influenced by the northern and southern boundaries. The inertial and bottom drag terms are primary drivers of flow entering regions of blocked geostrophic contours and thus it could be argued that the zonal shift in the meridionally integrated sea surface is due to boundary effects rather than the deflection from streamlines in the centre of the domain.

To investigate this possibility Figure 5.11 shows the same meridionally integrated terms of the barotropic vorticity equation as Figure 5.10 integrated over the central 6700 km of latitude only. This neglects the boundary influences on the vorticity. There is very little difference between results in Figure 5.10 and Figure 5.11. This shows that the boundaries have little influence on the vorticty over the ridge and the streamline deflection is predominantly due to the curvature of the geostrophic contours.

5.2.5 The Bottom Pressure Torque

Figure 5.9b shows a relatively small increase in the bottom pressure torque term as the ridge is narrowed. There is a connection between vorticity and zonally integrated momentum which explains this relationship. Bottom pressure torque and form stress can be linked via an area integral [Hughes and De Cuevas, 2001]. Given that $\boldsymbol{k} \cdot \boldsymbol{\nabla} p_b \times \boldsymbol{\nabla} h = \boldsymbol{k} \cdot \boldsymbol{\nabla} \times (p_b \boldsymbol{\nabla} h)$, through the use of Stokes theorem it holds that

$$\int_A \boldsymbol{k} \cdot \boldsymbol{\nabla} \times (p_b \boldsymbol{\nabla} h)\, dA = \oint_\Gamma p_b \boldsymbol{\nabla} h \cdot d\boldsymbol{\Gamma}, \tag{5.13}$$

where A is an arbitrary surface bounded by a closed curve Γ. This shows that the area integral of the bottom pressure torque is equal to the integral of $p_b \boldsymbol{\nabla} h$ along the bounding curve. It is assumed that $h = 0$ along the bounding curve by defining the bounds as a coastline. Along any segment of the bounding curve there is no value of pressure and $p_b \boldsymbol{\nabla} h = 0$. Hughes and De Cuevas [2001] use this to simplify (5.13) by defining Γ as two lines of latitude to the north and south then coastline lines to the east and west. Taking this approach, the segments to the east and west integrate to zero leaving

$$\int_A \boldsymbol{k} \cdot \boldsymbol{\nabla} \times (p_b \boldsymbol{\nabla} h) dA = \int_{\phi_0} p_b \frac{dh}{dx}\, dx - \int_{\phi_1} p_b \frac{dh}{dx}\, dx, \tag{5.14}$$

where ϕ_0 and ϕ_1 represent arbitrary lines of latitude. This evaluation can be extended to the zonally reentrant domain by observing that integral bounds which lie along the periodic

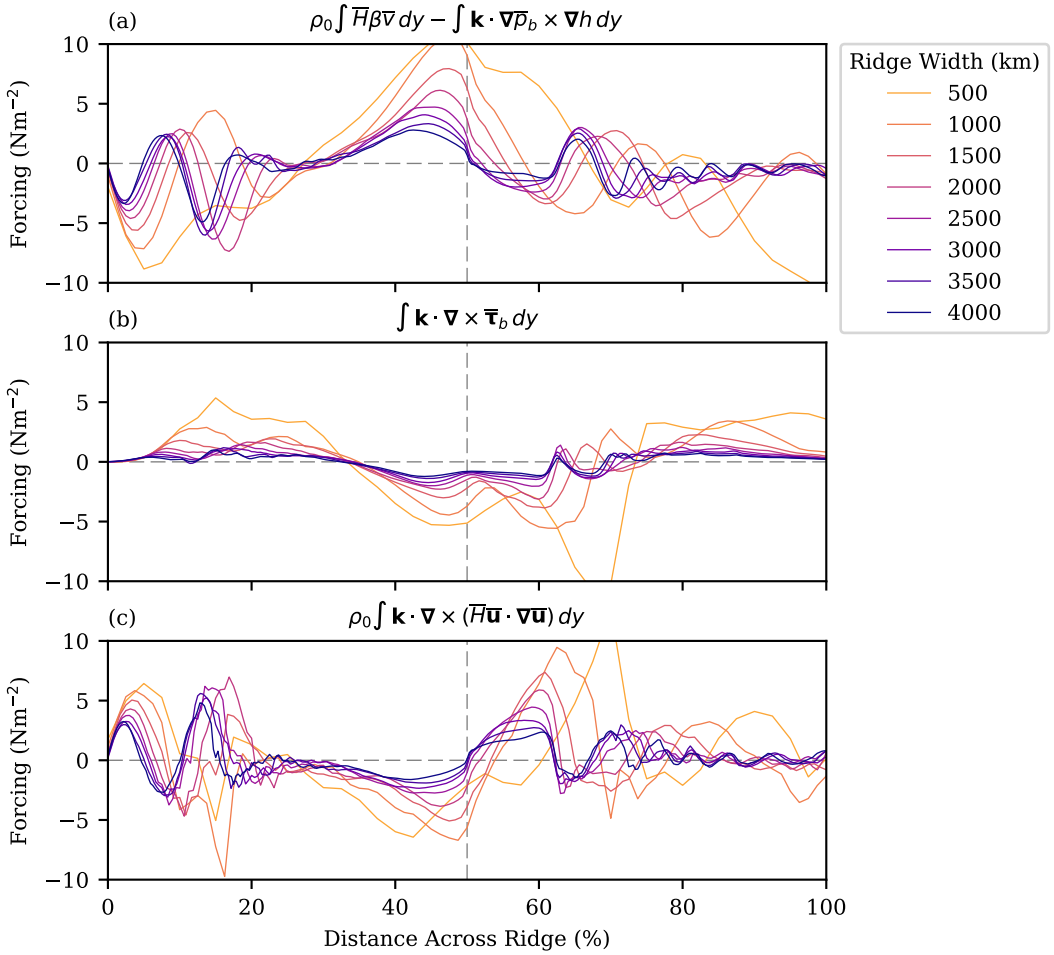

Figure 5.11: The meridionally integrated terms of the barotropic vorticity equation for simulations with differing ridge widths. Only the region over the ridge is shown and the x-axis for is scaled with ridge width for each curve. (a) The residual between the advection of planetary vorticity and the bottom pressure torque. (b) The bottom drag. (c) The steady inertial term. Results are from model simulations 29-35.

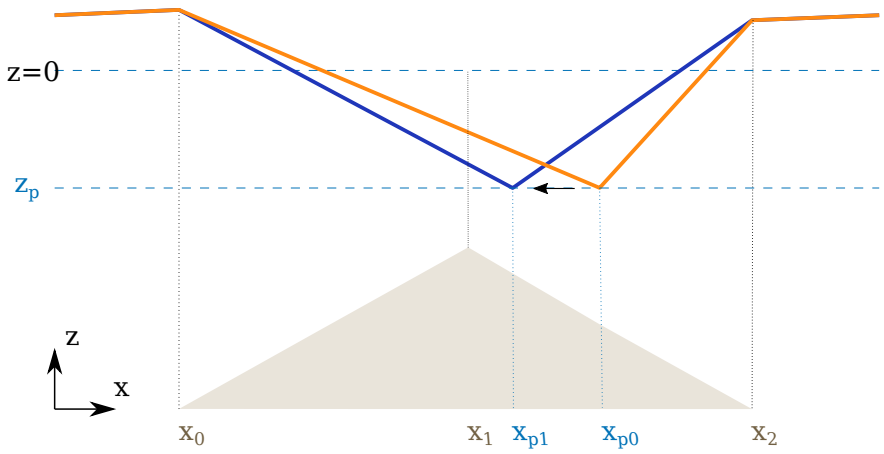

Figure 5.12: Schematic highlighting the form stress response to a change in the ridge width. This is a side profile in the x-z plane. $z = 0$ is the level of the resting ocean. The filled grey triangle represents the side profile of a ridge. The orange line is an example sea surface. The blue line represents a shift in the sea surface minima associated with a wider ridge, relative to the width of the topography.

boundaries are equivalent to bounds positioned along coast lines. First define the east and west bounds of A as Γ_1 and Γ_2 respectively. In the case where Γ_1 and Γ_2 lie along the periodic boundary, these segments share the same path. When calculating the integral around Γ, the integrals along both Γ_1 and Γ_2 are taken in opposing directions. As a result, a complete cancellation occurs in the line integral over these sections and thus (5.14) holds for integrating over a periodic channel.

Equation (5.14) shows that taking the area integral of the bottom pressure torque is equivalent to calculating difference in form stress between two latitudes. This means that the small rise in magnitude of the meridionally integrated bottom pressure torque shown in Figure 5.9b is associated with changes in the form stress. Figure 5.4 shows that an increased contribution from form stress to the domain integrated momentum budget coincides with decreased ridge width. Therefore, the small increase in the meridionally integrated bottom pressure torque is linked to the small increase in form stress.

5.2.6 A Form Stress Mechanism

In Section 5.1.3 a mechanism was given through which a change in sea surface height directly affects the resulting form stress. By equation (5.8) it was shown that a decrease in sea surface trough over topography gives a reduction in form stress. Further to this mechanism, there are many additional ways in which form stress can be affected by the sea surface height. Another example is via a zonal shift in the sea surface height minimum, depicted by Figure 5.12. A westward shift acts decrease the form stress contribution on the upstream side of a ridge and increase it on the downstream side resulting in an overall decrease in form stress.

A westward shift in the surface height minimum is observed in Figure 5.7 to occur with a increase in ridge width. As shown by Figure 5.4, this westward shift corresponds to decrease in the form stress contribution to the domain integrated zonal momentum budget. Thus, this mechanism for the changing sea surface height links form stress contributions to the overshoot of flow over the ridge. An increase in the ridge width is associated with a decrease in both the overshoot in the flow and form stress contribution to the momentum budget.

5.2.7 Summary

In the channel simulations undertaken with uniform wind stress and a meridional ridge, the primary momentum balance is between wind stress and form stress. For increasing ridge width there is a decrease in the closure of these two terms with bottom drag becoming an increasingly important term.

There is an eastward shift of the sea surface pressure minimum with decreasing ridge width. The eastward shift is associated with increased streamline deflections that arise from both bottom drag and inertia. These deflections increase with decreased ridge width causing a larger relative shift in the sea surface minimum. The increased shift in the sea surface pressure is associated with an increased form stress contribution in the momentum budget. Thus, there is a greater contribution from form stress to domain integrated zonal momentum budget for decreased ridge width (see Figure 5.4).

6 Further Topographic Effects on Zonal Flow

So far, all experiments have been implemented with topography which is orientated with strict meridional alignment and zonal symmetry. Here, meridional alignment is used to describe the angle that a ridge makes with a meridian. If a ridge makes an angle of 90° with the meridian its crest has an east-west alignment and if this angle is 0° the crest has a north-south alignment (the alignment of all topography shown so far). The zonal symmetry refers to the position of the ridge crest relative to its two base points. An eastward shift in the peak creates an asymmetry which results in the eastern ridge flank having a higher zonal gradient than the western flank. Figure 4.2 shows that most topographic features deviate from the idealised geometry presented in results thus far. Ridges in Figure 4.2 show zonal asymmetry and alignments that are far from meridional. An example is the Pacific-Antarctic Ridge, which supports the Ross Gyre. It is aligned at an angle which is approximately 45° to the meridian.

This chapter highlights some interesting and highly relevant results but does not explain them in their entirety. Initial results are shown on the relationship between each topographic variation and net zonal transport, and some further analysis is shown to give a broad explanation of the results. However, no clear conclusions are drawn about the causation of the behaviour shown and additional research is required to gain a full appreciation. This is a work in progress.

6.1 Effects of Asymmetric Variation of Ridge Width on Zonal Flow

It has been observed in the previous chapter that ridge width has a significant control on the net zonal volume transport in a channel. It is shown here that, in certain circumstances, the asymmetry of a ridge also exhibits a control on the zonal volume transport. Figure 6.1 shows the barotropic streamfunction for four simulations with varying bottom drag and zonal asymmetry of the topography. When implementing the base model with a bottom drag of 0.0025 there is minimal difference in the zonal transport between the two ridge geometries (Figures 6.1a and 6.1b). The eastward and westward crest shift give zonal volume transports of 415 Sv and 429 Sv respectively, thus, there is a slightly higher transport when the crest is shifted to the west. In setting the bottom drag to a lower value of 0.001, causing inertia to become more influential relative to the bottom drag, the opposite relationship appears (Figures 6.1a and 6.1b). Where $C_d = 0.001$, shifts in the ridge crest to the east and west give zonal volume transports of 487 Sv and 410 Sv respectively. Therefore, the volume transport is lower when the crest is shifted to the west.

To test the robustness of the above relationship, further variations of bottom drag coef-

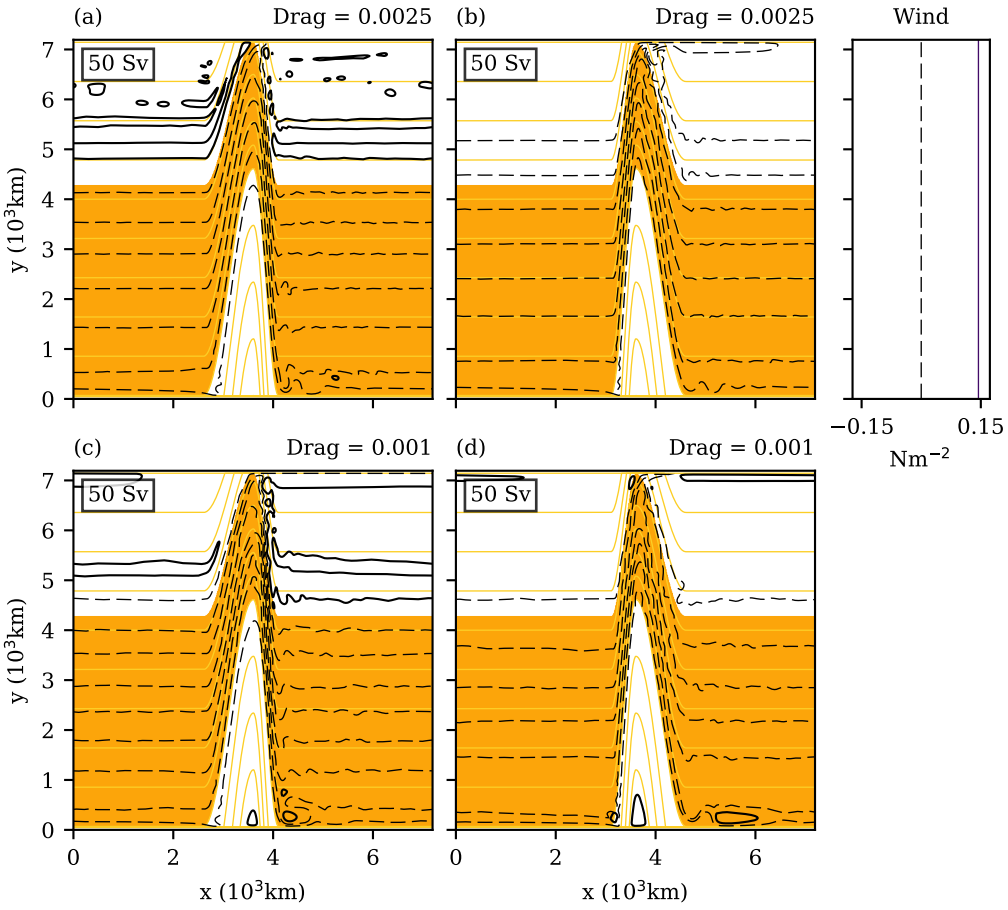

Figure 6.1: Barotropic channel simulations for a 2000 m high and 1000 km wide ridge with a variation in ridge asymmetry and bottom drag coefficient. (a) An eastward shift of the ridge peak where the western flank is 500 km wider than the eastern flank with a bottom drag coefficient of 0.002 (b) An westward shift of the ridge peak where the western flank is 500 km narrower than the eastern flank with a bottom drag coefficient of 0.0025. (c) An eastward shift of the ridge peak where the western flank is 500 km wider than the eastern flank with a bottom drag coefficient of 0.001. (d) A westward shift of the ridge peak where the western flank is 500 km narrower than the eastern flank with a bottom drag coefficient of 0.001. Results are from model simulations 36, 37, 42 and 43. For colouring and contouring see Figure 4.3.

ficients have been used in the same domain topography. Figure 6.2 shows the volume transport for all topographic and bottom drag variants. It is shown that the changes in relationship seen in the volume transports of Figure 6.1 is a result of an asymmetric response of the two geometries to bottom drag variations. For a westward shift, an increase in the bottom drag coefficient leads to a decreased volume transport. Whereas, for the the eastward shift, an increase in the bottom drag coefficient leads to an increased volume transport. It is this asymmetric response which causes the opposing relationship between topographic variations for the high and low bottom drag coefficient.

6.1.1 Form Stress

In the previous chapter, sea surface height was shown to indicate the volume transport and form stress for each simulation and a link emerged between the two. Figure 6.3 shows the sea surface pressure and zonal gradient in sea surface pressure for the asymmetric ridge variations. The trough in the the sea surface pressure is associated with a trough in the sea surface height. Figure 6.3a and 6.3b show that, in agreement with symmetric results, the dip in the sea surface is associated with the zonal volume transport. The minimum point in the sea surface height lowers for increasing volume transport. For the lower bottom drag coefficient, this corresponds to an increased dip for the westward crest shift.

This association of sea surface dip with variations of ridge geometry can be linked to form stress in a similar way to the previous chapter. A simplification is made in (5.8) whereby form stress is approximated by $|dh/dx|(\int_{x_1}^{x_2} \rho_0 g\eta \, dx - \int_{x_0}^{x_1} \rho_0 g\eta \, dx)$. The final step in (5.8) only holds under symmetric variations of topography. In the situation of asymmetric variations the from stress can only be approximated as:

$$\oint \rho_0 g\eta \frac{dh}{dx} \, dx = \int_{x_0}^{x_2} \rho_0 g\eta \frac{dh}{dx} \, dx = \underbrace{\int_{x_0}^{x_1} \rho_0 g\eta \frac{dh}{dx} \, dx}_{\text{(a)}} + \underbrace{\int_{x_1}^{x_2} \rho_0 g\eta \frac{dh}{dx} \, dx}_{\text{(b)}} \tag{6.1}$$

The two integral terms of this equation, (a) and (b), represent the integral across the western and eastern flanks of the ridge respectively. As the wind stress is constant between simulations and the form stress is the main term balancing the wind stress, form stress must remain constant. This means that the difference between integral (a) and (b) on the right-hand side of (6.1) must remain constant between simulations. As the form stress is balancing a positive eastward source of momentum in these simulations the sum of (a) and (b) must remain negative. dh/dx is the gradient in water column thickness and does not include any contribution from sea surface height. This term is of opposite sign on each flank

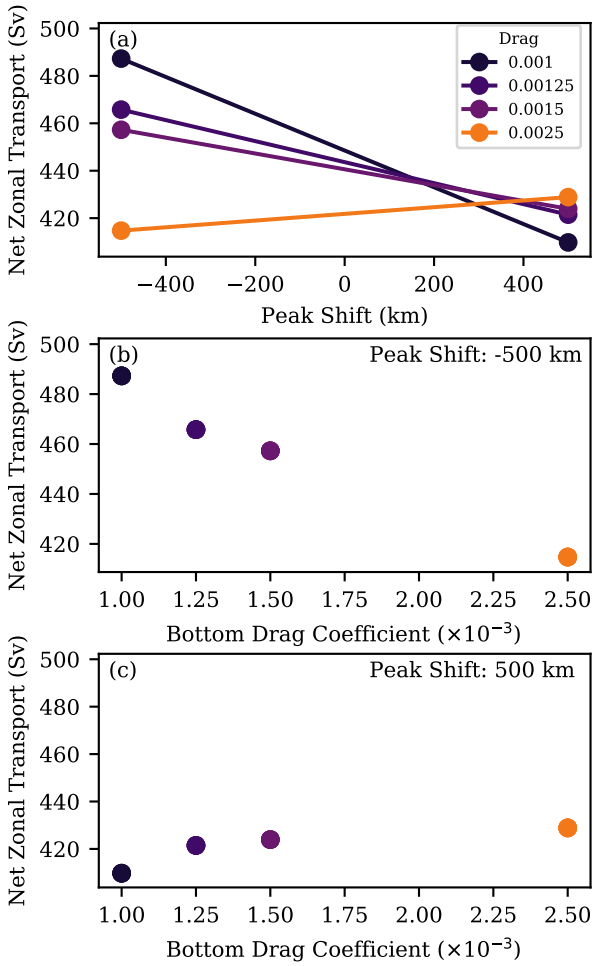

Figure 6.2: The change in net zonal volume transport for variations in both ridge asymmetry and bottom drag coefficient. (a) Ridge asymmetry versus net zonal volume transport for various bottom drag coefficients. The peak shift represents the difference between the zonal length of the east and west ridge flanks. A positive peak shift represents a westward shift of the ridge crest. (b) Net zonal volume transport versus bottom drag coefficients for the eastward shift in the ridge crest. (c) Net zonal volume transport versus bottom drag coefficients for the westward shift in the ridge crest. Results are from model simulations 36-43.

of the ridge, negative on the western flank and positive on the eastern flank. The sign of $\rho_0 g\eta$ generally remains negative across much of the topography. As a result, (a) is negative and (b) is positive for these simulations with (a) larger than (b) causing a negative form stress contribution, generating the required sink of momentum. Therefore, pressure over the western flank contributes to an eastward sink of momentum and pressure over the eastern flank leads to an eastward source of momentum.

6.1.2 Asymmetric Topographic Effects on Form Stress

The integral terms (a) and (b) in (6.1) are dependent on three varying components:

1. The sea surface height, η.
2. The topographic gradients, dh/dx.
3. The integral bounds of the topography, $x_i - x_{i-1}$

The topographic variations presented here represent a shift in the ridge crest with no change in the ridge width. This change in geometry directly affects both dh/dx and the integral bounds. Where the ridge crest is shifted to the east, the distance between integral bounds are reduced on the eastern flank and increased on the western flank. At the same time, dh/dx increases in magnitude on the eastern flank and reduces in magnitude on the western flank. Under this crest shift, these two varying components have opposing effects on both integral terms (1) and (2). The change in the integral bounds for the eastward crest shift enhances the difference between (1) and (2) and the change in dh/dx reduces this difference. If their effects were equal and opposite, form stress would remain unchanged and the profile of η would remain constant between simulations. It is observed, however, that η responds to the changes in geometry. Figure 6.3 shows that the magnitude of η increases uniformly with the eastward crest shift.

The uniform increase of η with the eastward crest shift reflects the change in geometry. The response indicates that the effects of both changing integral bounds and changes in dh/dx are not of equal importance. For the eastward crest shift, η responds by deepening over the ridge relative to the westward crest shift. With all other factors unchanged, this response would cause an increase in the difference between integrals (1) and (2) leading to an increase in form stress. Form stress must remain constant. As dh/dx reduces the difference between integrals (1) and (2) and a change in the integral bounds increases it, this response in η implies that the effects from the change in dh/dx must be larger than the effects of the change of integral bounds.

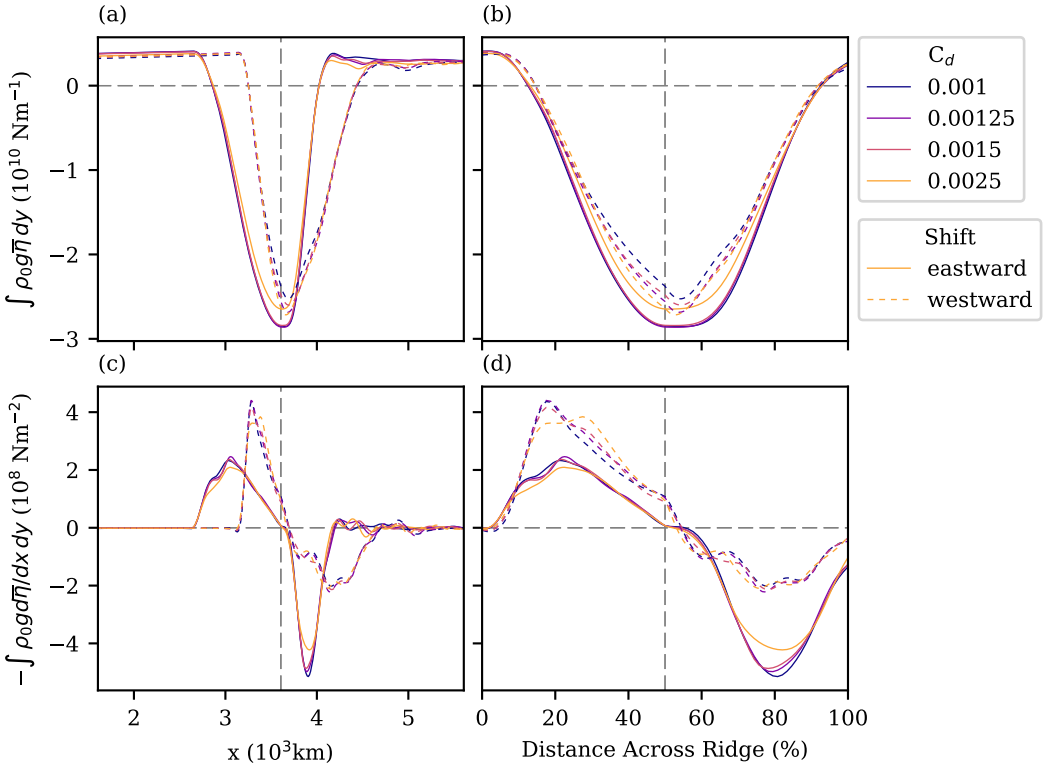

Figure 6.3: Meridionally integrated sea surface pressure and zonal pressure gradients over the ridge crest for variations in bottom drag coefficients (C_d) and ridge asymmetry. Solid lines represent an eastward shift in the ridge crest and dashed lines represent a westward shift. (a) Meridionally integrated sea surface pressure. (b) Meridionally integrated sea surface pressure with the x-axis scaled to the ridge width of each simulation. (c) Meridionally integrated zonal sea surface pressure gradient. (d) Meridionally integrated zonal sea surface pressure gradient with the x-axis scaled to the ridge width of each simulation. Results are from model simulations 36-43.

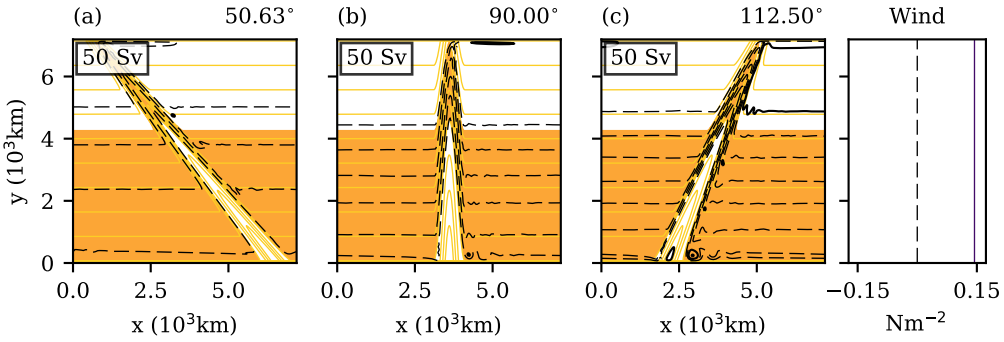

Figure 6.4: The streamfunction for simulations with varying ridge orientation. (a) Ridge alignment of 50.63° with respect to west. The meridional wind stress profile is given to the right. (b) Ridge alignment of 90.00° with respect to west. (c) Ridge alignment of 112.5° with respect to west. Results are from model simulations 29, 44 and 51. For colouring and contouring see Figure 4.3.

The mechanism appears to be the same for a westward shift in the ridge crest. With respect to form stress, both the integral bounds and dh/dx act in the opposite sense in this case. For lower bottom drag coefficients the westward shift leads to a smaller sea surface dip indicating that the sea surface height is responding to the same discrepancy produced by the changing integral bounds and dh/dx.

The above argument holds only for the more inertial simulations with the lower bottom drag coefficient. It is recognised that relationship shown by the simulation with $C_d = 0.0025$ contradicts the above mechanism indicating that the description is incomplete. The asymmetric response with changing bottom drag coefficient is also left unexplained. The two points require further investigation and are left for future study.

6.2 Effects of the Meridional Alignment of Ridge on Zonal Flow

The meridional alignment of a ridge also appears to have a control on the volume transport within a channel. Chen et al. [2015] previously noted that a clockwise rotation of topography tends to increase velocities over the topography. The study by Chen et al. [2015] did not attempt to quantify this effect in terms of net zonal transport and the dynamics behind the trend were not investigated. A rotation of the ridge causes the meridional width of the ridge to vary in each case, with an increase in width for a larger rotation. It is shown in Chapter 5 that a variation of ridge width has implications on zonal volume transport with an increase width causing an increase in transport. In light of this, the effects of

meridional alignment is investigated here by implementing a shear mapping of the base topography instead of a rotation. This type of variation preserves the width and gradients of the topography with respect to the x direction. The shear mapping is given by

$$x' = x + \frac{y}{\tan\theta} \tag{6.2}$$

$$y' = y \tag{6.3}$$

where x' and y' are the new coordinates and θ represents the angle of the shear with respect to west. The base case, with a meridional alignment, is represented by an angle of 90°. Angles greater than 90° represent a positive shear and angles less than 90° represent a negative shear.

Figure 6.4 shows the streamfunction for two differing ridge alignments in comparison to the base alignment used throughout this thesis. The result indicates that a negative shear of the ridge tends to increase net zonal transport and an positive shear tends to decrease the transport. This shows that ridge orientation has a large effect on zonal transport and aligns with the findings of Chen et al. [2015] despite the difference in method used for adjusting the ridge alignment.

To better understand this relationship, simulations with a wider range of orientations have been carried out. Figure 6.5 shows net zonal transport against the ridge orientation for these simulations. The results show an asymmetric trend with ridge orientation. A positive shear from 90° causes a rise in zonal transport before peaking at 112.5° then sharply dropping for angles greater than this. A negative shear causes a drop in transport with minimum at 56.25°. The slight rise in transport between 56.25° and 50.63° suggests that the flow might continue following a quasi-antisymmetric pattern with volume transport sharply rising for angles lower than 50.63°.

6.2.1 Form Stress

Figure 6.6 shows terms of the domain-integrated zonal momentum budget for the ridge rotation simulations with the y-axis on the same scale as Figure 5.4. There is a primary balance between wind forcing and form stress with bottom drag having very little contribution in these simulations. The wind stress is constant between simulations thus form stress is also almost constant. The basis for the change in transport is unlikely to be the same as in the previous arguments. In the previous ridge width and crest shift experiments, the changing volume transport is attributed to the changing ridge geometry. The geometric differences cause an alteration of form stress and the sea surface height adjusts in order

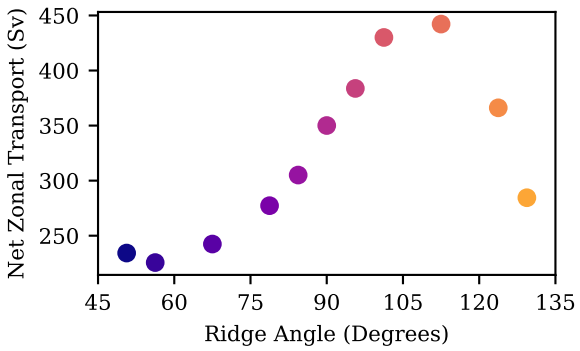

Figure 6.5: Volume transport versus rotational alignment of the ridge in degrees with respect to west. 90° represents a north-south alignment both 0° and 180° represent an east-west alignment. Results are from model simulations 29 and 44-53.

to continue to balance the momentum budget. The adjustments in meridional alignment leave both the meridional gradients and width of the topography unchanged. This means the form stress is only dependent on variations in sea surface height between adjustments in meridional alignment of the ridge. This suggests that the change in volume transport occurs due to an alternative mechanism.

Figure 6.7 shows the sea surface pressure and the zonal gradient in sea surface pressure for differing meridional alignments of the ridge. The integration is done by taking the inverse of the original shear mapping then meridionally integrating. Similar to previous experiments, the trough in the sea surface height is increased where volume transport is larger. What is different here is that, as the width of the ridge is unchanged, the changes in volume transport are associated with an adjustment in the zonal gradients in sea surface height, reflecting the changes in geostrophy. The velocities are increasing over the same distances causing the zonal pressure gradients to increase. In Figure 6.7a the minimum of each curve is signified by dots. The minima of the curves show a significant zonal shift with changing ridge angle. There is a general trend for the peak to shift westward as volume transport drops and to shift eastward as it increases. These zonal shifts occur over far greater distances than observed for the symmetric ridge width variations.

6.2.2 Barotropic Vorticity

The changes due to geostrophy have consequences on the vorticity budget. Figure 6.8 shows terms of the meridional integral of the inverse shear mapping of the barotropic vorticity equation. There is large variance in the bottom pressure torque (Figure 6.8b), with increas-

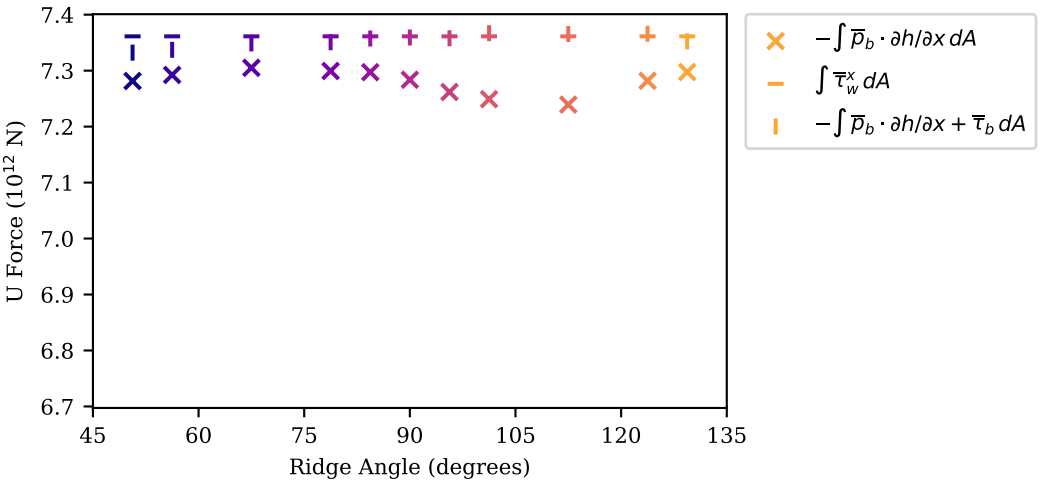

Figure 6.6: The domain integrated zonal momentum terms for varying ridge alignments. The momentum terms shown are: the negative of the form stress ($-\int \overline{p}_b \cdot \partial h/\partial x \, dA$); the wind stress ($\int \overline{\tau}_w \, dA$) and the addition of the negative of the form stress and the bottom drag ($-\int \overline{p}_b \cdot \partial h/\partial x + \overline{\tau}_w \, dA$). Results are from model simulations 29 and 44-53.

ing magnitudes associated with the increasing meridional velocities displayed via the advection of planetary vorticity (Figure 6.8a). Previous topographic variations showed almost no change in the bottom pressure torque. As noted above the bottom pressure torque is associated with form stress. The form stress remains constant between simulations in order to match the constant wind stress. These changes in magnitude of the bottom pressure torque must must be equal and opposite on each side of the ridge in order to preserve form stress. In this case, the increased magnitudes in the bottom pressure torque are associated with the changes in the sea surface trough over the ridge (Figure 6.7a). When the sea surface height is further depressed, pressure gradients rise, increasing the magnitudes in bottom pressure torque. It has been indicated previously that because the sea surface trough is not centred over the ridge peak, a drop in the sea surface is associated with an increase in form stress. This suggests that there must be compensating factor in the sea surface geometry keeping form stress constant. The description of the sea surface height used in the previous chapter is based on changing topography. Topography is fixed here and the previous mechanism does not explain this result. The effect here is still due to a change in the sea surface height geometry and an alternative explanation for the geometric response of the sea surface is required for this change in ridge alignment.

It is shown in Figure 6.8 that, similar to previous results, there is not a complete clo-

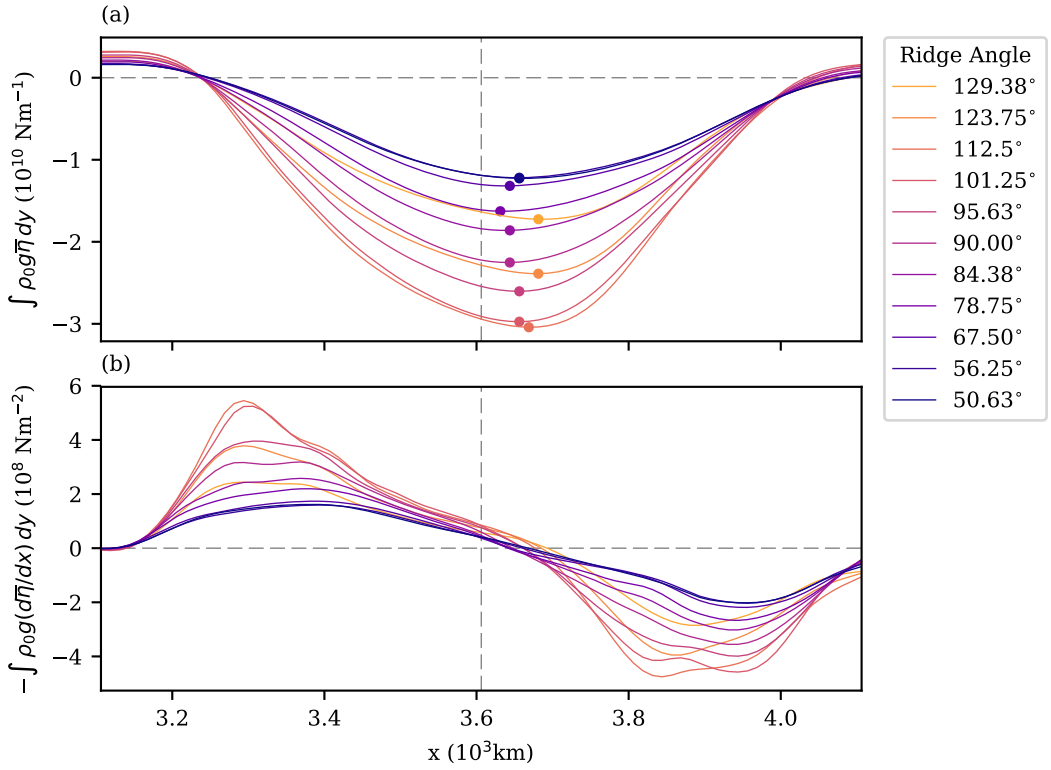

Figure 6.7: Meridionally integrated inverse shear mapping of the sea surface pressure and zonal pressure gradients for varying ridge alignment. (a) Meridionally integrated inverse shear mapping of sea surface pressure. (b) Meridionally integrated inverse shear mapping of zonal sea surface pressure gradient. Results are from model simulations 29 and 44-53.

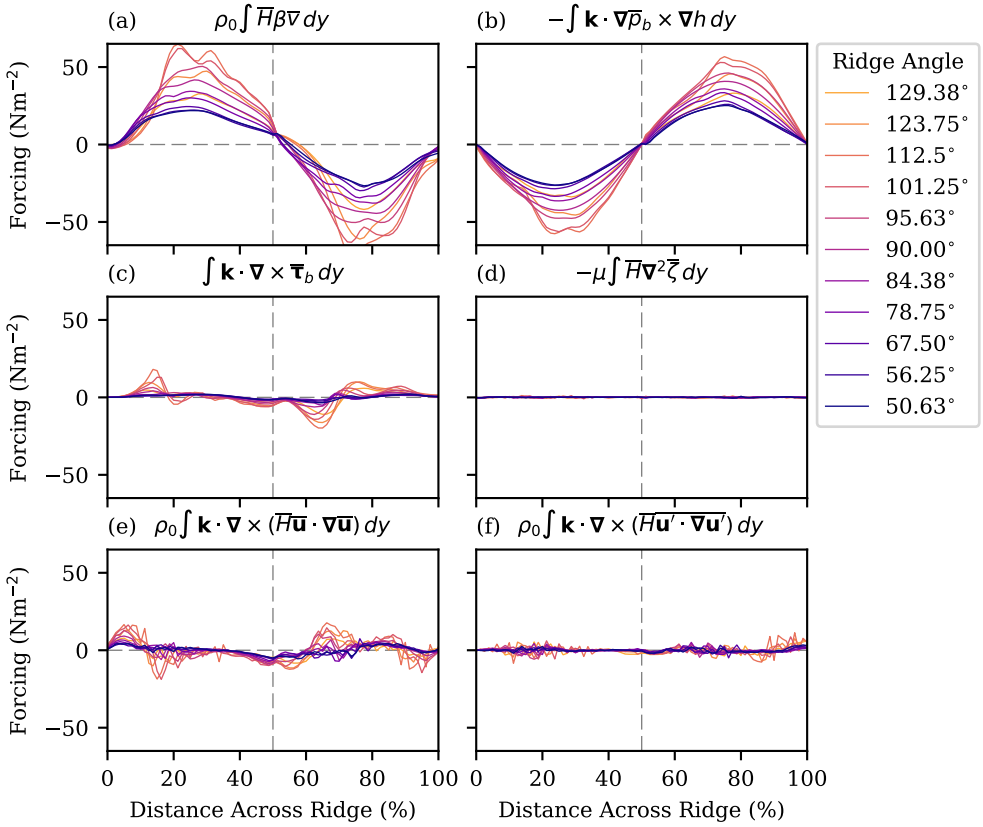

Figure 6.8: Terms of the meridional integral of the inverse shear mapping of the barotropic vorticity equation for simulations with differing ridge alignment. Only the region over the ridge is shown and the x-axis is scaled with ridge width for each curve. The titles show the respective terms which are displayed in each panel. Results are from model simulations 29 and 44-53.

sure between the advection of planetary vorticity and the bottom pressure torque in the vorticity budget. The inertial terms and bottom drag account for the majority of the difference between the advection of planetary vorticity and the bottom pressure torque. Figure 6.9 highlights the closure which occurs due to these terms. As previously outlined, these terms are associated with the overshooting of flow over topography and coincide with the zonal offset of the minimum in the surface pressure shown by Figure 6.7a. The magnitudes of the inertial terms and the bottom drag are associated with the shift, confirming this link. The zonal shift in the sea surface pressure minimum increases as the magnitudes in these terms increase. This shows that both inertial terms and the overshoot in flow is closely linked to the meridional alignment of the ridge. This suggests that there may be a relationship between overshooting of flow and the change in net zonal volume transport in response to a change in ridge alignment.

6.3 Summary

An investigation has been made into the effects of further topographic variations and significant relationships have emerged with respect to net zonal volume transport. Previously in Chapter 5, width variations of a symmetric ridge were undertaken in a channel model with uniform wind stress. These experiments have been extended in this chapter to explore the effect of asymmetry in the geometry of meridional topography and the effects of variation of meridional alignment of a ridge.

The effect of asymmetry is explored by shifting the ridge crest of the base symmetric ridge whilst fixing its two base points. An eastward shift results in the eastern ridge flank being narrower than the western ridge flank and vice versa for the westward crest shift. The results show that, with lower bottom drag coefficients, net zonal volume transport is lower for the westward crest shift compared with the eastward crest shift. As bottom drag coefficient increases there is a transition in the results and the relationship is reversed. A form stress mechanism is outlined as a possible explanation for the low bottom drag results with the sea surface height responding to the changes in geometry, leading to an adjustment in the volume transport. This mechanism does not hold when the bottom drag coefficient is raised and the opposite relationship exists. Further investigation is required to fully understand the dynamics behind asymmetric ridge variation.

The effects of meridional alignment are investigated through a shear mapping of the base geometry used throughout this thesis. The results show that a positive shear mapping leads to an increase in the net zonal volume transport, peaking at 112.5° then decreasing for alignments greater than this angle. Negative shear mappings show the opposite re-

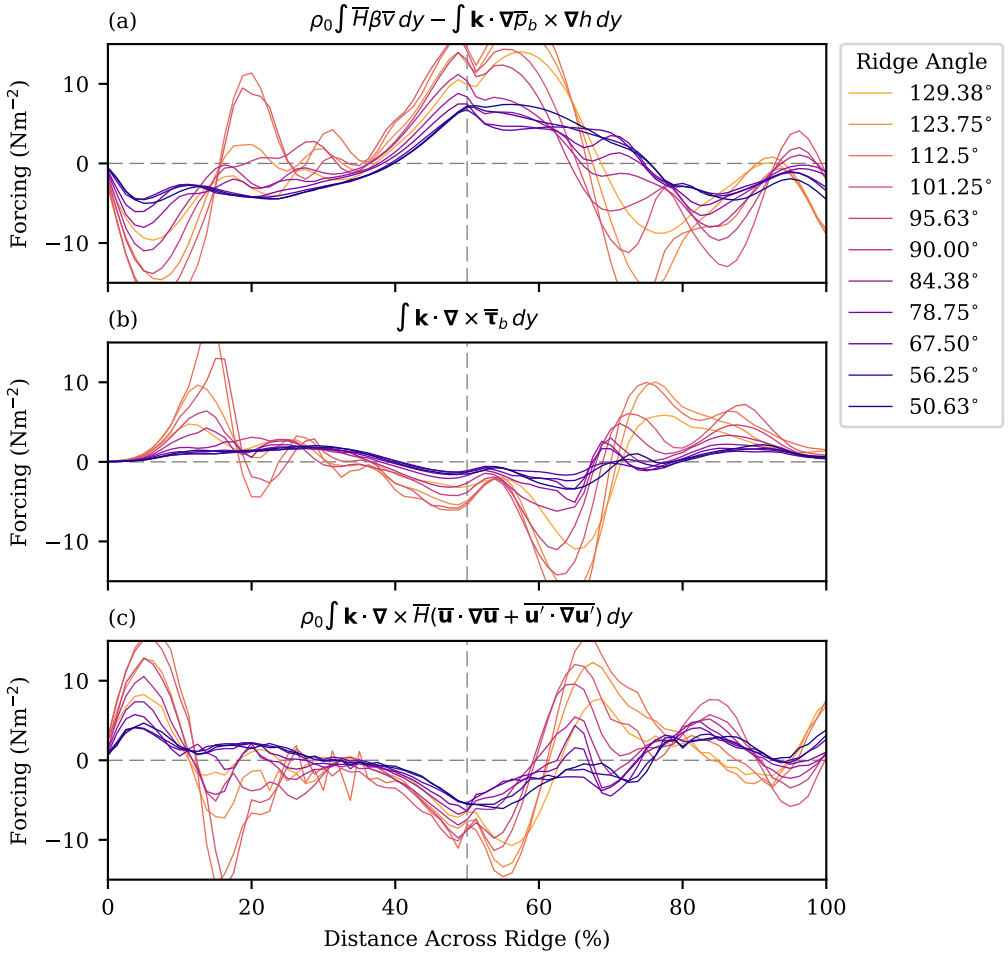

Figure 6.9: Terms of the meridional integral of the inverse shear mapping of the barotropic vorticity equation for simulations with differing ridge alignment. Only the region over the ridge is shown. (a) The residual between the advection of planetary vorticity and the bottom pressure torque. (b) The bottom drag. (c) The sum of the steady inertial term and transient inertial term. Results are from model simulations 29 and 44-53.

sponse, with decreasing net zonal transport down to 56.25° before rising again for angles greater than this. The adjustments in alignment have no effect on the zonal width of the ridges, thus the form stress is unaffected by these variations in topography. Although no firm conclusions are made it is indicated that the change in volume transport with change in ridge alignment could be linked to the overshooting outlined in Chapter 5.

Although progress has been made into the understanding of these two variations in topography, further thought and investigation are required.

7 Conclusions

The Southern Ocean consists of two categories of large-scale flow, the Antarctic Circumpolar Current and a series of subpolar gyres. There is a need to gain insight into the underlying dynamics in order to understand the path and strength of these currents. Both types of flow are largely determined by seabed topography. As a result, topographic interaction of large-scale flow forms the basis for this thesis. The investigation has focused on the role of ridge topography on both ACC and subpolar gyres and it is found that the flow has a strong dependence on the geometry of the seabed. The research undertaken in this thesis is primarily done through numerical simulations with a barotropic model in a simple idealised domain.

7.1 Gyres

There are three main gyre features in the Southern Ocean: the Ross Gyre; the Weddell Gyre; and the Australian-Antarctic Gyre. Each of these ocean circulations form between the Antarctic Circumpolar Current and the Antarctic continent [Gordon et al., 1978, Orsi et al., 1995]. Furthermore, they all exist to the east of large topographic features, either in the form of submarine ridges or continental barriers. Classical gyre theory is based on a western boundary of a gyre forming along on continental land mass. These situations are representative of structures such as the North Atlantic Gyre and western boundaries of gyres which coincide with submarine ridges are unique to the Southern Ocean. The role of submarine topography in gyre formation has had little investigation in the past.

7.1.1 Topographic Control of Closed Basin Gyres

The focus of this study is the topographic effects on Southern Ocean circulation. Nonetheless, a preliminary study given in this thesis into the role of topography in a closed basin yielded some interesting results.

In Chapter 3 an introduction to classical gyre theory is given with an overview of the dynamics of the North Atlantic gyre. The dynamics of gyre formation are introduced in terms of contours of f/h (geostrophic contours). Gyres principally form through a source of vorticity from a curl in the wind forcing, setting Sverdrup balance. The wind stress curl forces flow to a region with a different value of f/h, in the direction orthogonal to geostrophic contours. A closed gyre circulation is formed by a western boundary current advecting the fluid back to a region with its original value of f/h. In order for flow to be returned in this manner, a sufficient sink of vorticity must be generated in the return flow to balance the

basin-wide vorticity input from the wind stress. In the model set-up used in this study, bottom drag takes the role of this required vorticity sink. This is labelled a Stommel-like model, a barotropic model with free-slip boundary conditions and a frictional drag applied at the base (bottom drag).

The most basic closed basin case is a non-inertial system with no topographic variation and a Stommel-like model set-up. With this set-up the vorticity balance is between wind stress curl and the advection of planetary vorticity in the interior, then bottom drag and the advection of planetary vorticity in the western boundary current [Veronis, 1966a]. The extension to the inertial case causes the western boundary current to overshoot and part of the vorticity sink via bottom drag is balanced by time-mean inertia [Veronis, 1966b]. In both the inertial and non-inertial flat-bottom case the flow is able to freely adjust and gyre transport is sensitive to changes in bottom drag coefficient [Veronis, 1966b]. It shown in Chapter 3 that the introduction of variable topography creates a change in this relationship. The western boundary current becomes topographically controlled and adjustments of the bottom drag coefficient have little effect on the gyre strength. Topographic effects have previously been studied in the context of a closed basin representative of the North Atlantic [Holland, 1967, Salmon, 1992] but to the author's knowledge this topographic control has not previously been examined.

In this study, topography is also shown to have a control on the total wind forcing of a gyre. Adjustments in topography change the path of the geostrophic contours and the region of wind forcing that is important for the gyre formation changes. The relevant geostrophic contours can be shifted into regions where the values of the wind curl are different, affecting the area integral of the wind forcing. The adjustment in path due to a change in topography can also change the area over which the wind forcing is able to form a gyre, causing a change in the total wind forcing. This control is shown to have a notable effect on gyre transport and is applicable to the real ocean when considering changes in wind forcing. It indicates that gyres respond to changes in wind forcing over areas bounded by geostrophic contours rather than lines of latitude or arbitrary basin areas.

7.1.2 Southern Ocean Gyre Formation

Prior to this work, gyres in models representative of Southern Ocean dynamics occurred through the intersection of geostrophic contours with a boundary or topography, creating a region of blocked geostrophic contours [Ishida, 1994, Krupitsky et al., 1996, Nadeau and Ferrari, 2015]. The dynamics within a region of blocked geostrophic contours are similar to that of a bounded basin such as the North Atlantic ocean. The formation of gyres

through this mechanism is not necessarily representative of the Southern Ocean, however, with very few locations where geostrophic contours are blocked. Gyres, such as the Ross Gyre, form in the lee of a ridge in a region of unblocked geostrophic contours. It has been shown through idealised model simulations that gyres do not always form under these conditions alone. In order to form gyres in a region of unblocked geostrophic contours there must be the presence of a submarine ridge which has sufficient topographic gradients. One method of varying topographic gradients is through adjusting ridge width. The wide ridge used in simulations of this study are unable to produce gyre formations and a reduction in the ridge width causes gyres to emerge. Large zonal gradients in topography produce large gradients in f/h. When gradients in f/h are great enough, frictional forces occur, inducing a vorticity that permits flow to cross geostrophic contours on the slope. This generation of vorticity is integral to gyre formation. This suggests that the Pacific-Antarctic ridge, which lies to the west of the Ross Gyre, is of sufficient steepness to permit the gyre to form.

As a separate result, changes in ridge width cause an adjustment in the wind forcing which influences the strength of the gyres. A wider ridge results in a weaker gyre. The mechanism for this reduction in gyre strength is similar to the wind forcing response to changes in topography outlined for the closed basin gyre formation. The gyre flow is deflected into regions of opposing forcing over the topography. As ridge width is increased the interior forcing reduces and the area of opposing forcing increases, lowering the total wind forcing of the gyres.

7.2 Antarctic Circumpolar Current

The ACC is a predominantly zonal current, forced by the zonal winds which lie over the Southern Ocean. The ACC forms primarily along unblocked geostrophic contours and is significantly steered by the large submarine ridges which exist in the Southern Ocean [Gordon et al., 1978]. It is found in this study that the ridge topography has a control on the ACC in terms of both its path and volume transport.

7.2.1 Control of Ridge Width on the Antarctic Circumpolar Current

Some important determinants of the volume transport of the ACC are documented to arise from eddy generation [Meredith and Hogg, 2006, Meredith et al., 2012, Langlais et al., 2015], Sverdrup balance [Hughes et al., 1999] and form stress [Munk and Palmén, 1951]. Through investigation of topographic interaction this thesis has shed light on the latter factor, form stress. Form stress is shown to be a primary component involved in the relationship between topographic geometries and volume transport.

Over the Southern Ocean, the wind stress is the primary source of zonal momentum. The submarine topography which is present leads to a sink of momentum via form stress [Munk and Palmén, 1951]. Sea surface height gradients arise over topography in response to the wind forcing and ridge geometry such that topographic form stress is the main balance for the input of zonal momentum by the wind stress [Munk and Palmén, 1951, Stevens and Ivchenko, 1997, Masich et al., 2015]. This thesis shows that in the presence of a meridional ridge, form stress sets a control on the net zonal transport such that zonal gradients in the sea surface height are approximately fixed for a changing width of the ridge. Through geostrophy, the constant zonal sea surface gradients equate to constant meridional velocities. For a decreasing ridge width, the width of the current decreases. The decreasing current width with constant velocities results in a decreasing net zonal volume transport with decreasing ridge width. Thus, the ACC transport is set by ridge flank steepness.

An adjustment in ridge width is also observed to affect the proportional balance between wind stress and form stress. For increasing ridge width there is a decrease in the momentum sink due to form stress and an increase in the momentum sink from bottom drag to account for this change. In all cases there is a zonal overshoot of the flow relative to the ridge crest. This overshoot is associated with the form stress contribution. The narrower ridge widths correspond to a larger overshoot which leads to a increased pressure difference across the meridional ridge and an increased form stress contribution. The overshoot is associated with vorticity contributions from bottom drag and inertia [Neumann, 1960, Porter and Rattray, 1964, McCartney, 1976]. The narrowing of a ridge causes an adjustment in the geostrophic contours which gives a larger vorticity contribution from bottom drag and inertia. These terms cause the flow to deviate from geostrophic contours over topography which leads to an overshoot in the flow.

7.2.2 Extended Geometric Variations

Simulations with extended topographic variations have been carried out and significant relationships have emerged between these variations and net zonal transport.

An asymmetric variation of the gradients in the ridge flanks shows an effect on net transport which is dependent on the choice of bottom drag coefficient. At low bottom drag coefficients, a higher gradient in the eastern ridge flank compared with the western flank produced lower net zonal transport. Whereas at high bottom drag coefficients, the opposite relationship emerges. In Chapter 5 it was observed that changes to the geometry of a ridge in channel simulations affect net zonal transport via a form stress constraints. A similar mechanism could apply to these results.

The meridional alignment of the ridge topography also affects the net zonal transport in the channel with, again, an asymmetric response. A positive shear mapping of the base meridional ridge results in a higher transport for low shear. There is then a point where volume transport decreases as the shear is increased further. The opposite is true for negative shear mappings. The zonal profile of the ridge stays constant in these simulations indicating little effect on the form stress. It is hypothesised that the overshooting described in Chapter 5 plays a key role in the observed changes in volume transport here.

Both types of geometric variations remain to be fully explained and further work is needed to better understand the relationships which occur.

7.3 Implications and Further Work

There is a regional disparity in the Southern Ocean associated with the formation of subpolar gyres and the path of the ACC. It was introduced in Chapter 1 that the distribution of both sea-ice and CDW play a key role in the earth's climate and are closely liked to the regional disparity of Southern Ocean circulation [Jenkins et al., 2016]. The research in this study highlights some important responses of large-scale flow to geometric variations and some of these features have been thoroughly investigated here. As summarised above, the coexistence of both gyres and the ACC are partly determined by the gradients of the submarine topography which are present. Moreover, not only are the existence of these circulations related to these topographic gradients but the geometry also plays a factor the strength of these currents. These factors have a primary influence on the observed regional disparities which occur. This advance in knowledge of the link between topography and Southern Ocean circulation provides an important progression in the understanding of these climate process.

Topography is also shown above to have implications on the relationship between gyre strength and the wind stress field. The ACC volume transport is associated with the wind stress over the Southern Ocean and is proportional to the wind stress over (almost) unblocked geostrophic contours [Hughes et al., 1999]. This theory has been extended here to show that gyre strength is proportional to the wind stress curl between two bounding values of f/h. In an environment with a significant variation in the stress field over time [Marshall, 2003, Langlais et al., 2015] it is implied that topography (and f/h) is an important factor when assessing the response of Southern Ocean gyres to changing winds.

In light of the investigation given by this thesis questions still remain and further avenues of possible research have been unearthed. The final chapter of this thesis shows that both the meridional ridge alignment and asymmetric variation of the flank widths of a

ridge have significant effects on the net zonal transport within a channel. Further work is required to fully understand these results. These varying geometries are simulated with uniform wind stress only. An additional set of simulations could be undertaken to investigate the effects these geometric variations on the gyre circulations by introducing a curl in the wind forcing with is applied.

Lastly, a useful extension to the simulations provided here would be to introduce baroclinic effects. Although the dynamics of the Southern Ocean are predominantly equivalent barotropic, baroclinic instabilities are observed to have a bearing in the volume transport of the ACC through eddy saturation. Introducing baroclinicity would allow for an understanding of the combined effects of the barotropic response to changes in geometry observed in this thesis and the baroclinic instabilities which are thought to modulate volume transport.

Appendix

Model List									
ID	L_x	L_y	Wall	Ridge Height	Ridge Width (West)	Ridge Width (East)	Ridge Angle	Wind	C_d
01	7200 km	3600 km	y	0 m	0 km	0 km	90°	Curl	0.0025
02	7200 km	3600 km	y	250 m	500 km	500 km	90°	Curl	0.0025
03	7200 km	3600 km	y	500 m	500 km	500 km	90°	Curl	0.0025
04	7200 km	3600 km	y	750 m	500 km	500 km	90°	Curl	0.0025
05	7200 km	3600 km	y	1000 m	500 km	500 km	90°	Curl	0.0025
06	7200 km	3600 km	y	1250 m	500 km	500 km	90°	Curl	0.0025
07	7200 km	3600 km	y	1500 m	500 km	500 km	90°	Curl	0.0025
08	7200 km	3600 km	y	2000 m	500 km	500 km	90°	Curl	0.0025
09	7200 km	3600 km	y	2500 m	500 km	500 km	90°	Curl	0.0025
10	7200 km	3600 km	y	3000 m	500 km	500 km	90°	Curl	0.0025
11	7200 km	3600 km	y	0 m	500 km	500 km	90°	Curl	0.0050
12	7200 km	3600 km	y	0 m	500 km	500 km	90°	Curl	0.0075
13	7200 km	3600 km	y	2000 m	500 km	500 km	90°	Curl	0.0050
14	7200 km	3600 km	y	2000 m	500 km	500 km	90°	Curl	0.0075
15	7200 km	3600 km	n	2000 m	500 km	500 km	90°	Curl	0.0025
16	7200 km	3600 km	n	1000 m	500 km	500 km	90°	Curl	0.0025
17	7200 km	3600 km	n	500 m	500 km	500 km	90°	Curl	0.0025
18	7200 km	3600 km	n	0 m	0 km	0 km	90°	Curl	0.0025
19	7200 km	3600 km	n	1000 m	2000 km	2000 km	90°	Curl	0.0025
20	7200 km	3600 km	n	2000 m	2000 km	2000 km	90°	Curl	0.0025

21	7200 km	3600 km	n	2000 m	1000 km	1000 km	90°	Curl	0.0025
22	7200 km	7200 km	n	2000 m	2000 km	2000 km	90°	Curl	0.0025
23	7200 km	7200 km	n	2000 m	1000 km	1000 km	90°	Curl	0.0025
24	7200 km	7200 km	n	2000 m	500 km	500 km	90°	Curl	0.0025
25	7200 km	7200 km	n	2000 m	2000 km	2000 km	90°	Curl	0.0050
26	7200 km	7200 km	n	2000 m	1000 km	1000 km	90°	Curl	0.0050
27	7200 km	7200 km	n	2000 m	500 km	500 km	90°	Curl	0.0050
28	7200 km	7200 km	n	2000 m	250 km	250 km	90°	Flat	0.0025
29	7200 km	7200 km	n	2000 m	500 km	500 km	90°	Flat	0.0025
30	7200 km	7200 km	n	2000 m	750 km	750 km	90°	Flat	0.0025
31	7200 km	7200 km	n	2000 m	1000 km	1000 km	90°	Flat	0.0025
32	7200 km	7200 km	n	2000 m	1250 km	1250 km	90°	Flat	0.0025
33	7200 km	7200 km	n	2000 m	1500 km	1500 km	90°	Flat	0.0025
34	7200 km	7200 km	n	2000 m	1750 km	1750 km	90°	Flat	0.0025
35	7200 km	7200 km	n	2000 m	2000 km	2000 km	90°	Flat	0.0025
36	7200 km	7200 km	n	2000 m	500 km	250 km	90°	Flat	0.0025
37	7200 km	7200 km	n	2000 m	250 km	500 km	90°	Flat	0.0025
38	7200 km	7200 km	n	2000 m	500 km	250 km	90°	Flat	0.0015
39	7200 km	7200 km	n	2000 m	250 km	500 km	90°	Flat	0.0015
40	7200 km	7200 km	n	2000 m	500 km	250 km	90°	Flat	0.00125
41	7200 km	7200 km	n	2000 m	250 km	500 km	90°	Flat	0.00125
42	7200 km	7200 km	n	2000 m	500 km	250 km	90°	Flat	0.0010
43	7200 km	7200 km	n	2000 m	250 km	500 km	90°	Flat	0.0010
44	7200 km	7200 km	n	2000 m	500 km	500 km	50.63°	Flat	0.0025
45	7200 km	7200 km	n	2000 m	500 km	500 km	56.25°	Flat	0.0025
46	7200 km	7200 km	n	2000 m	500 km	500 km	67.50°	Flat	0.0025
47	7200 km	7200 km	n	2000 m	500 km	500 km	78.75°	Flat	0.0025

48	7200 km	7200 km	n	2000 m	500 km	500 km	84.38°	Flat	0.0025
49	7200 km	7200 km	n	2000 m	500 km	500 km	95.62°	Flat	0.0025
50	7200 km	7200 km	n	2000 m	500 km	500 km	101.25°	Flat	0.0025
51	7200 km	7200 km	n	2000 m	500 km	500 km	112.50°	Flat	0.0025
52	7200 km	7200 km	n	2000 m	500 km	500 km	123.75°	Flat	0.0025
53	7200 km	7200 km	n	2000 m	500 km	500 km	129.38°	Flat	0.0025

Table 3: List of all model configurations. The columns represent: model identification number; zonal width of domain; meridional width of domain; existence of central meridional wall; height of submarine topography; width of the topographic feature from peak to basin on western side; width of the topographic feature from peak to basin on eastern side; the angle which the topographic feature makes with the model meridians; curl for the sinusoidal wind forcing and Flat for uniform surface wind forcing; the prescribed bottom drag coefficient.

References

R. Abernathey and P. Cessi. Topographic enhancement of eddy efficiency in baroclinic equilibration. *Journal of Physical Oceanography*, 44(8):2107–2126, 2014.

R. P. Abernathey, I. Cerovecki, P. R. Holland, E. Newsom, M. Mazloff, and L. D. Talley. Water-mass transformation by sea ice in the upper branch of the southern ocean overturning. *Nature Geoscience*, 9(8):596, 2016.

A. Adcroft, C. Hill, and J. Marshall. Representation of topography by shaved cells in a height coordinate ocean model. *Monthly Weather Review*, 125(9):2293–2315, 1997.

D. L. Anderson and A. Gill. Spin-up of a stratified ocean, with applications to upwelling. *Deep Sea Research and Oceanographic Abstracts*, 22(9):583 – 596, 1975.

D. L. Anderson and P. D. Killworth. Spin-up of a stratified ocean, with topography. *Deep Sea Research*, 24(8):709 – 732, 1977.

A. Arakawa and V. R. Lamb. Computational design of the basic dynamical processes of the UCLA general circulation model. *Methods in computational physics*, 17:173–265, 1977.

T. W. K. Armitage, R. Kwok, A. F. Thompson, and G. Cunningham. Dynamic topography and sea level anomalies of the southern ocean: Variability and teleconnections. *Journal of Geophysical Research: Oceans*, 123(1):613–630, 2018.

C. W. Böning. On the influence of frictional parameterization in wind-driven ocean circulation models. *Dynamics of Atmospheres and Oceans*, 10(1):63 – 92, 1986.

C. W. Böning, A. Dispert, M. Visbeck, S. Rintoul, and F. U. Schwarzkopf. The response of the Antarctic Circumpolar Current to recent climate change. *Nature Geoscience*, 1(12): 864, 2008.

K. Bryan. A numerical investigation of a nonlinear model of a wind-driven ocean. *Journal of the Atmospheric Sciences*, 20(6):594–606, 1963.

C. Chen, I. Kamenkovich, and P. Berloff. On the dynamics of flows induced by topographic ridges. *Journal of Physical Oceanography*, 45(3):927–940, 2015.

D. P. Dee, S. Uppala, A. Simmons, P. Berrisford, P. Poli, S. Kobayashi, U. Andrae, M. Balmaseda, G. Balsamo, d. P. Bauer, et al. The ERA-interim reanalysis: Configuration and performance of the data assimilation system. *Quarterly Journal of the royal meteorological society*, 137(656):553–597, 2011.

K. A. Donohue, K. L. Tracey, D. R. Watts, M. P. Chidichimo, and T. K. Chereskin. Mean Antarctic Circumpolar Current transport measured in Drake Passage. *Geophysical Research Letters*, 43(22):11,760–11,767, 2016. 2016GL070319.

T. S. Dotto, A. Naveira Garabato, S. Bacon, M. Tsamados, P. R. Holland, J. Hooley, E. Frajka-Williams, A. Ridout, and M. P. Meredith. Variability of the Ross Gyre, Southern Ocean: Drivers and Responses Revealed by Satellite Altimetry. *Geophysical Research Letters*, 0(0), 2018.

N. Fofonoff. Steady flow in a frictionless homogeneous ocean. *J. mar. Res*, 13:254–262, 1954.

S. T. Gille. The Southern Ocean Momentum Balance: Evidence for Topographic Effects from Numerical Model Output and Altimeter Data. *Journal of Physical Oceanography*, 27(10):2219–2232, 1997.

S. T. Gille. Warming of the Southern Ocean Since the 1950s. *Science*, 295(5558):1275–1277, 2002.

S. T. Gille. Float Observations of the Southern Ocean. part i: Estimating Mean Fields, Bottom Velocities, and Topographic Steering. *Journal of Physical Oceanography*, 33(6): 1167–1181, 2003.

S. T. Gille. Decadal-Scale Temperature Trends in the Southern Hemisphere Ocean. *Journal of Climate*, 21(18):4749–4765, 2008.

S. T. Gille. Meridional displacement of the Antarctic Circumpolar Current. *Philosophical Transactions of the Royal Society of London A: Mathematical, Physical and Engineering Sciences*, 372(2019), 2014.

A. Gordon, D. Martinson, and H. Taylor. The wind-driven circulation in the Weddell-Enderby Basin. *Deep Sea Research Part A. Oceanographic Research Papers*, 28(2):151 – 163, 1981.

A. L. Gordon, E. Molinelli, and T. Baker. Large-scale relative dynamic topography of the Southern Ocean. *Journal of Geophysical Research: Oceans*, 83(C6):3023–3032, 1978.

V. Gouretski. The large-scale thermohaline structure of the Ross Gyre. In *Oceanography of the Ross Sea Antarctica*, pages 77–100. Springer, 1999.

V. V. Gouretski and A. I. Danilov. Weddell Gyre: structure of the eastern boundary. *Deep Sea Research Part I: Oceanographic Research Papers*, 40(3):561 – 582, 1993.

R. M. Graham, A. M. Boer, K. J. Heywood, M. R. Chapman, and D. P. Stevens. Southern Ocean fronts: Controlled by wind or topography? *Journal of Geophysical Research: Oceans*, 117(C8), 2012.

W. R. Holland. On the wind-driven circulation in an ocean with bottom topography. *Tellus*, 19(4):582–600, 1967.

W. R. Holland. Baroclinic and topographic influences on the transport in western boundary currents. *Geophysical & Astrophysical Fluid Dynamics*, 4(1):187–210, 1972.

C. W. Hughes. Nonlinear vorticity balance of the Antarctic Circumpolar Current. *Journal of Geophysical Research: Oceans*, 110(C11), 2005. C11008.

C. W. Hughes and E. R. Ash. Eddy forcing of the mean flow in the Southern Ocean. *Journal of Geophysical Research: Oceans*, 106(C2):2713–2722, 2001.

C. W. Hughes and B. A. De Cuevas. Why western boundary currents in realistic oceans are inviscid: A link between form stress and bottom pressure torques. *Journal of Physical Oceanography*, 31(10):2871–2885, 2001.

C. W. Hughes, M. S. Jones, and S. Carnochan. Use of transient features to identify eastward currents in the Southern Ocean. *Journal of Geophysical Research: Oceans*, 103(C2): 2929–2943, 1998.

C. W. Hughes, M. P. Meredith, and K. J. Heywood. Wind-Driven Transport Fluctuations through Drake Passage: A Southern Mode. *Journal of Physical Oceanography*, 29(8): 1971–1992, 1999.

A. Ishida. Effects of partial meridional barriers on the Antarctic Circumpolar Current - Wind-driven barotropic model. *Dynamics of Atmospheres and Oceans*, 20(4):315 – 341, 1994.

L. Jackson, C. W. Hughes, and R. G. Williams. Topographic control of basin and channel flows: The role of bottom pressure torques and friction. *Journal of Physical Oceanography*, 36(9):1786–1805, 2006.

S. S. Jacobs, A. F. Amos, and P. M. Bruchhausen. Ross sea oceanography and Antarctic Bottom Water formation. *Deep Sea Research and Oceanographic Abstracts*, 17(6):935 – 962, 1970.

B. M. Jamart and J. Ozer. Numerical boundary layers and spurious residual flows. *Journal of Geophysical Research: Oceans*, 91(C9):10621–10631, 1986.

A. Jenkins, P. Dutrieux, S. Jacobs, E. J. Steig, G. H. Gudmundsson, J. Smith, and K. J. Heywood. Decadal Ocean Forcing and Antarctic Ice Sheet Response: Lessons from the Amundsen Sea. *Oceanography*, 29, December 2016.

P. D. Killworth. An Equivalent-Barotropic Mode in the Fine Resolution Antarctic Model. *Journal of Physical Oceanography*, 22(11):1379–1387, 1992.

O. Klatt, E. Fahrbach, M. Hoppema, and G. Rohardt. The transport of the Weddell Gyre across the Prime Meridian. *Deep Sea Research Part II: Topical Studies in Oceanography*, 52(3):513 – 528, 2005. Direct observations of oceanic flow: A tribute to Walter Zenk.

A. Krupitsky, V. M. Kamenkovich, N. Naik, and M. A. Cane. A Linear Equivalent Barotropic Model of the Antarctic Circumpolar Current with Realistic Coastlines and Bottom Topography. *Journal of Physical Oceanography*, 26(9):1803–1824, 1996.

R. Kwok and J. Morison. Sea surface height and dynamic topography of the ice-covered oceans from cryosat-2: 2011–2014. *Journal of Geophysical Research: Oceans*, 121(1):674–692, 2016.

J. LaCasce and P. Isachsen. The linear models of the ACC. *Progress in Oceanography*, 84 (3):139 – 157, 2010.

C. E. Langlais, S. R. Rintoul, and J. D. Zika. Sensitivity of Antarctic Circumpolar Current Transport and Eddy Activity to Wind Patterns in the Southern Ocean. *Journal of Physical Oceanography*, 45(4):1051–1067, 2015.

M. J. Lighthill. Dynamic response of the Indian Ocean to onset of the Southwest Monsoon. *Philosophical Transactions of the Royal Society of London A: Mathematical, Physical and Engineering Sciences*, 265(1159):45–92, 1969. doi: 10.1098/rsta.1969.0040.

R. A. Locarnini. *Water masses and circulation in the Ross Gyre and environs*. Texas A&M University, Office of Graduate Studies, 1994.

D. Marshall. Influence of Topography on the Large-Scale Ocean Circulation. *Journal of Physical Oceanography*, 25(7):1622–1635, 1995a.

D. Marshall. Topographic Steering of the Antarctic Circumpolar Current. *Journal of Physical Oceanography*, 25(7):1636–1650, 1995b.

G. J. Marshall. Trends in the Southern Annular Mode from observations and reanalyses. *Journal of Climate*, 16(24):4134–4143, 2003.

J. Marshall, A. Adcroft, C. Hill, L. Perelman, and C. Heisey. A finite-volume, incompressible Navier Stokes model for studies of the ocean on parallel computers. *Journal of Geophysical Research: Oceans*, 102(C3):5753–5766, 1997a.

J. Marshall, C. Hill, L. Perelman, and A. Adcroft. Hydrostatic, quasi-hydrostatic, and nonhydrostatic ocean modeling. *Journal of Geophysical Research: Oceans*, 102(C3):5733–5752, 1997b.

J. Masich, T. K. Chereskin, and M. R. Mazloff. Topographic form stress in the Southern Ocean state estimate. *Journal of Geophysical Research: Oceans*, 120(12):7919–7933, 2015.

M. McCartney. The interaction of zonal currents with topography with applications to the Southern Ocean. *Deep Sea Research and Oceanographic Abstracts*, 23(5):413 – 427, 1976.

M. S. McCartney and K. A. Donohue. A deep cyclonic gyre in the Australian–Antarctic Basin. *Progress in Oceanography*, 75(4):675 – 750, 2007.

M. P. Meredith and A. M. Hogg. Circumpolar response of Southern Ocean eddy activity to a change in the Southern Annular Mode. *Geophysical Research Letters*, 33(16), 2006. L16608.

M. P. Meredith, A. C. Naveira Garabato, A. M. Hogg, and R. Farneti. Sensitivity of the overturning circulation in the Suthern Ocean to decadal changes in wind forcing. *Journal of Climate*, 25(1):99–110, 2012.

W. H. Munk. On the wind-driven ocean circulation. *Journal of Meteorology*, 7(2):80–93, 1950.

W. H. Munk and E. Palmén. Note on the dynamics of the Antarctic Circumpolar Current. *Tellus*, 3(1):53–55, 1951.

L.-P. Nadeau and R. Ferrari. The Role of Closed Gyres in Setting the Zonal Transport of the Antarctic Circumpolar Current. *Journal of Physical Oceanography*, 45(6):1491–1509, 2015.

G. Neumann. On the effect of bottom topography on ocean currents. *Deutsche Hydrografische Zeitschrift*, 13(3):132–141, May 1960.

W. D. Nowlin, Jr, T. W. III, and R. D. Pillsbury. Structure and Transport of the Antarctic Circumpolar Current at Drake Passage from Short-Term Measurements. *Journal of Physical Oceanography*, 7(6):788–802, 1977.

D. Olbers. Comments on "On the Obscurantist Physics of 'Form Drag' in Theorizing about the Circumpolar Current. *Journal of Physical Oceanography*, 28(8):1647–1654, 1998.

A. H. Orsi, T. Whitworth, and W. D. Nowlin. On the meridional extent and fronts of the Antarctic Circumpolar Current. *Deep Sea Research Part I: Oceanographic Research Papers*, 42(5):641 – 673, 1995.

Y.-H. Park and L. Gamberoni. Large-scale circulation and its variability in the south Indian Ocean from TOPEX/POSEIDON altimetry. *Journal of Geophysical Research: Oceans*, 100(C12):24911–24929, 1995.

B. Peña-Molino, S. R. Rintoul, and M. R. Mazloff. Barotropic and baroclinic contributions to along-stream and across-stream transport in the Antarctic Circumpolar Current. *Journal of Geophysical Research: Oceans*, 119(11):8011–8028, 2014.

G. H. Porter and M. Rattray. The influence of variable depth on steady zonal barotropic flow. *Deutsche Hydrografische Zeitschrift*, 17(4):164–174, Jul 1964.

H. D. Pritchard, S. Ligtenberg, H. Fricker, D. Vaughan, M. Van den Broeke, and L. Padman. Antarctic ice-sheet loss driven by basal melting of ice shelves. *Nature*, 484:502–5, 04 2012.

G. J. Rickard, M. J. Roberts, M. J. Williams, A. Dunn, and M. H. Smith. Mean circulation and hydrography in the Ross Sea sector, Southern Ocean: representation in numerical models. *Antarctic Science*, 22(05):533–558, 2010.

C.-G. Rossby. Relation between variations in the intensity of the zonal circulation of the atmosphere and the displacements of the semi-permanent centers of action. *J. Marine Res.*, 2:38–55, 1939.

R. Sadourny. The Dynamics of Finite-Difference Models of the Shallow-Water Equations. *Journal of the Atmospheric Sciences*, 32(4):680–689, 1975.

J. B. Sallée, K. Speer, and R. Morrow. Response of the Antarctic Circumpolar Current to Atmospheric Variability. *Journal of Climate*, 21(12):3020–3039, 2008.

R. Salmon. A two-layer Gulf Stream over a continental slope. *Journal of marine research*, 50(3):341–365, 1992.

N. R. Smith and C. Fandry. Combined effects of wind stress and topography in a two-layer model of the Southern Ocean. *Deep Sea Research*, 25(4):371 – 390, 1978.

S. Sokolov and S. R. Rintoul. Multiple Jets of the Antarctic Circumpolar Current South of Australia. *Journal of Physical Oceanography*, 37(5):1394–1412, 2007.

S. Sokolov and S. R. Rintoul. Circumpolar structure and distribution of the Antarctic Circumpolar Current fronts: 1. Mean circumpolar paths. *Journal of Geophysical Research: Oceans (1978–2012)*, 114(C11), 2009.

D. P. Stevens and V. O. Ivchenko. The zonal momentum balance in an eddy-resolving general-circulation model of the southern ocean. *Quarterly journal of the royal meteorological society*, 123(540):929–951, 1997.

A. L. Stewart and A. M. Hogg. Reshaping the Antarctic Circumpolar Current via Antarctic Bottom Water Export. *Journal of Physical Oceanography*, 47(10):2577–2601, 2017.

H. Stommel. The westward intensification of wind-driven ocean currents. *Eos, Transactions American Geophysical Union*, 29(2):202–206, 1948.

H. U. Sverdrup. Wind-driven currents in a baroclinic ocean; with application to the equatorial currents of the eastern Pacific. *Proceedings of the National Academy of Sciences*, 33(11):318–326, 1947.

A. F. Thompson and A. C. Naveira Garabato. Equilibration of the Antarctic Circumpolar Current by standing meanders. *Journal of Physical Oceanography*, 44(7):1811–1828, 2014.

A. F. Thompson and K. J. Richards. Low frequency variability of Southern Ocean jets. *Journal of Geophysical Research: Oceans*, 116(C9), 2011.

G. Veronis. Wind-driven ocean circulation—part 1. linear theory and perturbation analysis. *Deep Sea Research and Oceanographic Abstracts*, 13(1):17 – 29, 1966a.

G. Veronis. Wind-driven ocean circulation—part 2. numerical solutions of the non-linear problem. *Deep Sea Research and Oceanographic Abstracts*, 13(1):31 – 55, 1966b.

Z. Wang and M. Meredith. Density-driven Southern Hemisphere subpolar gyres in coupled climate models. *Geophysical Research Letters*, 35(14), 2008.

R. B. Wearn and D. Baker. Bottom pressure measurements across the Antarctic Circumpolar Current and their relation to the wind. *Deep Sea Research Part A. Oceanographic Research Papers*, 27(11):875 – 888, 1980.

T. Whitworth, W. D. Nowlin, and S. J. Worley. The Net Transport of the Antarctic Circumpolar Current through Drake Passage. *Journal of Physical Oceanography*, 12(9):960–971, 1982.

R. G. Williams, C. Wilson, and C. W. Hughes. Ocean and Atmosphere Storm Tracks: The Role of Eddy Vorticity Forcing. *Journal of Physical Oceanography*, 37(9):2267–2289, 2007.

J.-O. Wolff, E. Maier-Reimer, and D. J. Olbers. Wind-Driven Flow over Topography in a Zonal β-Plane Channel: A Quasi-geostrophic Model of the Antarctic Circumpolar Current. *Journal of Physical Oceanography*, 21(2):236–264, 1991.

M. K. Youngs, A. F. Thompson, A. Lazar, and K. J. Richards. ACC Meanders, Energy Transfer, and Mixed Barotropic–Baroclinic Instability. *Journal of Physical Oceanography*, 47(6):1291–1305, 2017.